Author:
Othman, Muhammad F B

Title:
Aeroelastic Tailoring of Composite Aircraft Wings with Uncertainty Quantification for Robust and Reliable Design

University of Bristol

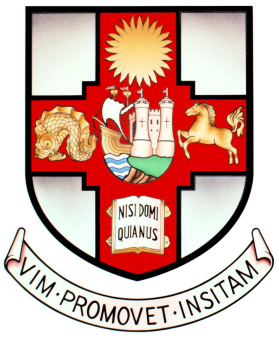

Doctoral Thesis

Aeroelastic Tailoring of Composite Aircraft Wings with Uncertainty Quantification for Robust and Reliable Design

Muhammad Othman

A dissertation submitted to the University of Bristol in accordance with the requirements for award of the degree of Doctor of Philosophy

in the Faculty of

Advanced Composite Centre for Innovation and Science (ACCIS)
Aerospace Engineering Department

September 2019

Seventy eight thousand nine hundred forty one words

Author's declaration

I declare that the work in this dissertation was carried out in accordance with the requirements of the University's Regulations and Code of Practice for Research Degree Programmes and that it has not been submitted for any other academic award. Except where indicated by specific reference in the text, the work is the candidate's own work. Work done in collaboration with, or with the assistance of, others, is indicated as such. Any views expressed in the dissertation are those of the author.

SIGNED: .....DATE: .....

Abstract

Aeroelastically tailored aircraft structures, designed for maximum performance while attaining minimum weight, remain a challenging multidisciplinary optimisation problem. Although the possibility of aeroelastic tailoring has been around since the early 1980s, most of their applications to aircraft structures have been 'black metal' designs, which do not fully exploit the anisotropic properties of the composite materials. This somewhat conservative approach is at odds with the elastic tailoring capabilities offered by composite materials, which, by allowing modification of the bending and torsional stiffness coupling terms, lend themselves to innovative design solutions for improved aeroelastic performance.

Aircraft wing structures have been designed using deterministic approaches for minimum structural weight whilst satisfying multiple constraints for performance and certification. Designers are aware that deterministic optimisation approaches, being unable to account for probabilistic uncertainties in material and structural parameters, may lead to unreliable or unrealistic designs. When dealing with composite structures, uncertainties can be related to geometry, material properties and the manufacturing process. These variabilities should be accurately quantified while designing for reliability and robustness of the structure. Hence, the growing interest in improving or replacing deterministic optimisation approaches for more reliable and robust structural design methods.

The current work aims to develop a novel aeroelastic tailoring framework which can provide a tool for a rapid design process for *robust* and *reliable* composite aircraft wings. The terms *robust* and *reliable* are referred to design sensitivity due to parametric variations in the composite material properties, ply orientation and structural parameters. To incorporate uncertainty in optimal designs requires a *'probabilistic'* optimisation approach with an efficient uncertainty quantification method that can accurately evaluate the effect of parameter variations on the wing performance at a low computational cost. The conventional Monte Carlo Simulation (MCS) method is highly computationally expensive and not practical for solving a robust and reliable design optimisation problem. Polynomial Chaos Expansion and Random Sampling High Dimensional Model Representation methods used in the current work are capable of offering low computational cost for uncertainty quantification analysis. These methods are subsequently used in a

Robust and Reliability-Based Design Optimisation approach in which a robust and reliable design configuration of a composite aircraft wing is obtained. An idealised *'box-like'* Finite Element model representation for a high-aspect-ratio wing of a reference regional jet airliner is used to demonstrate the effectiveness of the approach.

A novel multi-level aeroelastic tailoring framework is introduced to obtain a robust and reliable composite aircraft wing design. The framework is capable of producing an optimised wing design with the best compromise between structural weight, robustness and structural reliability.

Acknowledgements

The author would like to express special gratitude to Prof. Jonathan Cooper and Dr Alberto Pirrera for their guidance, support and encouragement throughout the research.

The financial support from the EPSRC through the funding of the Centre for Doctoral Training in Advanced Composites for Innovation and Science [EP/G036772/1] at the University of Bristol and the Malaysian Ministry of Higher Education and University Science Malaysia for the scholarship awarded are gratefully acknowledged.

Technical support and discussions with Embraer S.A. team members have been constructive throughout the project. Among them are Dr Gustavo Silva, Pedro Cabral and Alex Prado.

The motivation and support from my family, especially my mom is something beyond mentioning. Their endless support and encouragement make me believe that nothing is impossible to achieve.

Finally, the completion of the research work and the thesis would not have been possible without the endless support and love of my wife, Noriah Mat Saed and not to forget my lovely daughter, Nur Aneesa Qaisara, who always makes daddy smile.

Contents

List of Figures

List of Tables

Abbreviations

ACO	**A**nt **C**olony **O**ptimisation
AFOSM	**A**dvanced **F**irst **O**rder **S**econd **M**oment
CLT	**C**lassical **L**aminate **T**heory
CPU	**C**entral **P**rocessing **U**nit
CV	**C**oefficient Of **V**ariance
DLM	**D**ouble **L**attice **M**ethod
DV	**D**esign **V**ariable
EBW	**E**mbraer **B**enchmark **W**ing
FE	**F**inite **E**lement
FORM	**F**irst **O**rder **R**eliability **M**ethod
GA	**G**enetic **A**lgorithm
GP	**G**aussian **P**rocess
GPC	**G**alerkin **P**olynomial **C**haos
GSLB	**G**lobal **S**hared-**L**ayer **B**lending
HDMR	**H**igh **D**imensional **M**odel **R**epresentation
IA	**I**nterval **A**nalysis
LCO	**L**imit **C**ycle **O**scillation
LEV	**L**argest **E**xtreme **V**alue
LHS	**L**atin **H**ypercube **S**ampling
MCS	**M**onte **C**arlo **S**imulation
MPP	**M**ost **P**robable **P**oint
MVFOSM	**M**ean **V**alue **F**irst **O**rder **S**econd **M**oment
PC	**P**robabilistic **C**ollocation
PCE	**P**olynomial **C**haos **E**xpansion
PDF	**P**robability **D**ensity **F**unction
POF	**P**robability **O**f **F**ailure
PSO	**P**article **S**warm **O**ptimisation
RBDO	**R**eliability **B**ased **D**esign **O**ptimisation
RBM	**R**oot **B**ending **M**oment
RDO	**R**obust **D**esign **O**ptimisation
RE	**R**elative **E**rror

RMSE	**R**oot **M**ean **S**quare **E**rror
RRBDO	**R**obust **R**eliability **B**ased **D**esign **O**ptimisation
RS-HDMR	**R**andom **S**ampling **H**igh **D**imensional **M**odel **R**epresentation
SA	**S**ensitivity **A**nalysis
SC	**S**tochastic **C**ollocation
SEV	**S**mallest **E**xtreme **V**alue
SORM	**S**econd **O**rder **R**eliability **M**ethod
SPT	**S**equential **P**ermutation **T**able
VAT	**V**ariable **A**angle **T**ow
WS	**W**eighted **S**um

Nomenclatures

A	in-plane stiffness matrix
B	bending stiffness matrix
C	aerodynamic stiffness matrix
C_{LL}	local lift coefficient of the wing model
D	in-plane-out-of-plane coupling stiffness matrix
d	nodal displacement vector
E	material Young's modulus
EI	flexural rigidity
f	frequency
$f(x)$	output function response
f_{cost}	cost function
f_{obj}	objective function
f_0, $f_i(x_i)$	zeroth and first order HDMR components
$f_{ij}(x_i, x_j)$	second order HDMR components
$f_{1,2,...,n}(x_1, x_2, ..., x_n)$	n^{th} order HDMR components
F_{g}	flight alleviation factor
F'_{PCE}	approximate response obtained from PCE
FI	failure index
g_{rc}	reliability constraint
g_{d}	design constraints
G, g	shear modulus/damping
GJ	torsional stiffness
$h(\mathbf{x})$	analytical function in ratio control variate method in HDMR
H	gust gradient distance
$\mathbf{I}$	identity matrix
K, k	coupling parameter/stiffness matrices
LSL	lower statistical limit
L_{g}	gust wavelength
mac	mean average chord length
$M_{x,y}$	moment in x and y direction
M_{D}	Mach number at dive speed

M_{c}	Mach number at cruise speed
m	element mass
max	maximum
N	number of layers in composite laminate
N_{xy}	force in x and y direction
$N_1, ..., N_4$	shape functions
n_z	load factor
P, p	nodal force applied to the nodes/expansion order of polynomial
P_{cr}	critical buckling load
P_{f},P_{g},P_{allow}	probability of failure for flutter, gust and allowable value
q	flight dynamic pressure
Q_{ij}	reduced stiffness terms in fibre and matrix direction
RE	relative error
RBM	wing root bending moment
S_{i_1}	sensitivity index
SU_i	PC-based Sobol' sensitivity indices
SU_i^T	total PC-based sensitivity indices
T	transformation matrix
t	thickness
t_{panel}	laminate panel thickness
t_{ply}	ply thickness
USL	upper statistical limit
U_j	material invariants
U_{ref}	reference gust velocity
V	flight speed
V_A	partial variance
V_{c}	cruise velocity
V_{D}	dive speed
V_{f}	flutter speed
$V_{\mathrm{f,Benchmark}}$	flutter speed of the benchmark wing model
$V_{\mathrm{f,Design}}$	design flutter speed
w_{g}, w_{g0}	gust velocity/design gust velocity
w_{const}	weighting factor for design constraint

W	structural weight
$W_{\text{benchmark}}$	structural weight of the benchmark wing model
Y	fitted linear regression model
z	transverse displacement
θ	ply orientation/angles
ξ	lamination parameter
$\mathcal{A}$	total order expansion
$a_{i1}, ..., a_{ip}$	deterministic expansion coefficients of PCE
α_r^i	expansion coefficient in HDMR
β,β_i	reliability index/unknown expansion coefficient of PCE
β_{pq}^{ij}	expansion coefficient in HDMR
$u(\theta)$	output response of PCE
σ	standard deviation value
σ_1, σ_2	component stress in longitudinal and transverse direction
σ_{VMS}, $\sigma_{\text{VMS,allowable}}$	von misses stress/allowable von misses stress
Σ	sum function
τ_{12}	shear stress
$\mathcal{E}_1, \mathcal{E}_2$	components strain in longitudinal and transverse direction
γ_{12}	shear strain
$\mathcal{V}_{12}$	poison ratio in fibre and matrix direction
κ	curvature
ρ	density of air
μ	mean value
ΔC_p	sectional pressure coefficient of the wing
$\boldsymbol{X}$	amplitude vector
ω	free vibration frequency
λ	eigenvalue solution
λ_{crit}	buckling critical load factor
ζ	independent random variables
Γ_p	multi-dimensional orthogonal polynomials
ψ	basis function
$\varphi_r(x_i)$, $\varphi_p(x_i)$, $\varphi_q(x_j)$	orthonormal basis function in HDMR

Chapter 1

Introduction

1.1 Introduction

Aeroelasticity is the field of study concerned with the interaction of aerodynamic, inertia and elastic forces, and their influence on a flexible structure [1]. Aeroelasticity can give rise to various instability phenomena not only in aircraft structures but also to bridges, wind turbines, helicopters and racing cars. For example, these instabilities may lead to catastrophic failure if not treated appropriately in the design process. For aircraft structures, the two main components of aeroelasticity are static and dynamic. Static aeroelasticity is concerned with the interaction between aerodynamic forces and elastic forces which may cause instabilities such as divergence. Divergence occurs when the flexible structure's twist increases without limit due to applied torsional forces exceeding the structural restoring forces.

On the other hand, dynamic aeroelasticity deals with the oscillatory effect of the interaction between aerodynamics, inertia and elastic forces. Dynamic aeroelasticity may cause flutter which occurs due to unfavourable coupling between two or more vibration modes with increasing frequency leading to structural failure. The aircraft loads are also affected by aerodynamic, inertia and elastic forces, and therefore it is essential to evaluate the aeroelastic responses of different aircraft loads such as static manoeuvres, gusts and turbulence loads.

The importance of aeroelasticity, especially for aircraft structures, has inspired researchers to look into aeroelastically-tailored structures. Aeroelastic tailoring is a designing method which incorporates the structural directional stiffness into an aircraft design in order to control the static or dynamic aeroelastic deformations in a beneficial way for improved structural and aerodynamic performance [2]. With the increasing use of composite materials for aircraft structures, an aeroelastically-tailored structure is made possible via

material tailoring. This is due to the composite's anisotropic properties and as well as their attractive strength-to-weight ratio.

The tailoring can be achieved by exploring the possibility of stiffness coupling (i.e. bending-torsional stiffness coupling) which alters the static and dynamic aeroelastic responses of the structures. Since the early 1980s, there has been a significant amount of research in aeroelastic tailoring using composite structures which has sought the efficient use of the anisotropic properties for improved aircraft structural designs for multiple load cases [2, 3]. One example of a practical application of aeroelastic tailoring is on the X-29 forward-swept wing demonstrator aircraft in which elastic coupling between bending and twisting was used to allow the wing's bending but limit the twisting in order to eliminate structural divergence within the flight envelope [2].

Previous research into aeroelastic tailoring has looked at the potential benefits to lateral control [4] and drag reduction [5], aileron effectiveness improvement [6–8] , to avoid divergence [9–12] and flutter [9–15] occurring at design airspeeds, and also to alleviate gust load [11, 14–16]. Despite the successful implementation in various design cases, aeroelastically tailored aircraft structures, designed for maximum performance while attaining minimum weight, remain a challenging multidisciplinary optimisation problem. Most of their applications to aircraft structures have been *'black metal'* designs, which do not fully exploit the anisotropic properties of composite materials. This somewhat conservative approach is at odds with the elastic tailoring capabilities offered by composite materials, which provide greater design spaces for bending and torsional stiffness modifications enabling better design solutions with improved aeroelastic performance.

With current modelling capabilities, it is possible to model the aircraft structural behaviour with a high degree of accuracy using different levels of model fidelity. In reality, for composite structures, variability exists through materials, geometry and the manufacturing process, resulting in uncertain structural responses [17]. This parameter variation can be classified as aleatory or parametric uncertainty. Other important sources of uncertainty included epistemic uncertainty and uncertainty due to the human error which are difficult to quantify and not been directly considered in the design process [18]. In a conventional deterministic design approach, these uncertainties are not implicitly accounted for and often treated as worst-case design scenarios by using safety margins which can be overly conservative and therefore limit the potential gains from novel design approaches

such as aeroelastic tailoring [19]. By directly incorporating the parameter variations in the design process will not only allow for robust and reliable designs, which are insensitive to uncertainty, but also maintaining the target performance and satisfying the other design constraints. Such an approach is known as a probabilistic design method [20].

In systems engineering, uncertainty quantification is considered as a tool for quantitative risk analysis with which to provide inputs for design and certification decisions [18]. Uncertainty in aeroelasticity and composite structures can exist due to the variability in the material properties such as material non-homogeneity, fibre misalignment, ply waviness, wrinkling and defects, as well as the manufacturing tolerance and thickness variations [21, 22]. Monte Carlo Simulations (MCS) [23, 24] is a common and straightforward technique to address uncertainty quantification in composite structures. However, MCS often requires extensive sets of simulation data in order to obtain meaningful results. Other quantification methods such as Polynomial Chaos Expansion (PCE) [16, 21], Gaussian Process Emulators (GP) [25], Interval Analysis (IA) [26] and High Dimensional Model Representation (HDMR) [27] are explored by researchers to obtain better efficiency in uncertainty quantification analysis.

The quantification of the uncertainty in composite structure design results in different variability's measures (such as the probability of failure (POF), mean and variance of the responses) of the wing performance which may be used as either the objective function or the constraints in the probabilistic design optimisation. These measures of variability can be utilised to produce a realistic design which accounts for structural robustness and reliability. The probabilistic design methods can be classified into two main categories: 1) Reliability-Based Design Optimisation (RBDO) [21, 28–30] and 2) Robust Design Optimisation (RDO) [29–31]. In a RBDO method, the design is optimised whilst having a particular risk or target reliability as the design objective or constraint. On the other hand, RDO seeks an optimal design about the mean performance by maximising robustness and minimising the sensitivity to uncertainty. In order to optimise a full wing box design through finite element model analysis, both RBDO and RDO require a statically relevant number of stochastic variations for every tentative solution, which is computationally expensive and impractical. For example, the use of a conventional method such as MCS in optimisation procedure requires large sets of simulation data for every iterative solution. To overcome this, the used of surrogate modelling techniques (i.e. PCE, GP and HDMR) allow for improved computational efficiency using a fraction

of the cost of the conventional MCS method. Hence, the goal of this thesis is to develop an aeroelastic tailoring approach with uncertainty considerations as a measure for design robustness and reliability.

1.2 Research Questions and Methodology

Current aeroelastic tailoring approaches for aircraft wing structures employ deterministic optimisation methods to determine the best design for minimum structural weight and optimum performance whilst satisfying aircraft certification requirements. The approach utilises a safety factor to incorporate any uncertainty that may exist in the design which is based on pure assumption rather than statistical data. The deterministic approach, being unable to account for uncertainties in the design directly, may lead to under or over-constrained designs. This limitation leads to the main research question on how to directly incorporate the model/parameter uncertainties into the design process of a composite aircraft wing so that a more reliable, robust and realistic design can be obtained. As such, the main focus of present work is to develop an improved aeroelastic tailoring approach for uncertainty quantification in the design process.

The quantification of uncertainty in the design process requires a probabilistic design method which is often associated with high computational effort. The conventional probabilistic method employs Monte Carlo Simulation as a tool to quantify the uncertainty in the model, and this is highly computationally expensive and not practical for solving design optimisation problems. These requirements lead to another research questions on how the probabilistic design method can be improved, and what are the alternative tools for uncertainty quantification that can accurately evaluate the effect of parameter variation on the wing performance at low computational cost.

The research methodology employed in this work is based on the numerical analysis of a composite aircraft wing to determine the structural and aeroelastic performance. The numerical analysis involves Finite Element modelling and analysis as well as the probabilistic study for uncertainty quantification. The work presented in the thesis can be outlined into two research components - deterministic and probabilistic methods for aeroelastic tailoring. In the first component, an improved optimisation method to obtain a deterministic design solution is developed, which then applied to a detailed

representation of wing structure. In the second research component, the alternative tools for uncertainty quantification are studied for rapid evaluation of wing's response due to random parameters, namely Polynomial Chaos Expansion (PCE) and Random Sampling High Dimensional Model Representation (RS-HDMR) method. The PCE and RS-HDMR are chosen for the study due to their efficiency in determination of model responses due to the uncertainty at minimum computational cost [21, 155].

In order to include uncertainty effect in the design optimisation, a robust and reliability-based design optimisation method is introduced. The method allows for the determination of a robust and reliable design solution for aeroelastic tailoring. The *robustness* and *reliability* of the design are measured in terms of performances sensitivity to the aleatoric uncertainty such as material properties, ply orientation and structural parameters.

1.3 Objective and major contributions

The objective of the current work is to develop a novel aeroelastic tailoring framework which can provide a tool for a rapid design process for the *'robust'* and *'reliable'* design of a composite aircraft wing. Other aims are:

- To evaluate the efficiency of PCE and RS-HDMR methods for uncertainty quantification studies of a composite aircraft wing model.
- To develop an improved method for the optimisation of a composite wing that involves multiple design constraints and loading conditions.
- To develop an optimisation approach for improved robustness and reliability for composite aircraft wing design.
- To develop a multi-level aeroelastic tailoring framework based on a probabilistic design optimisation approach for a composite aircraft wing.

The major contributions of this thesis can be summarised as:

- Use of PCE and RS-HDMR methods to quantify the variation of structural and aeroelastic responses due to parametric uncertainty in the laminate and the composite material properties.

- Development of a design optimisation approach to achieve minimum structural weight with multiple design constraints, including both structural (strain and buckling) and aeroelastic performance (flutter and gusts), for a composite aircraft wing.
- Development of a novel method for a robust and reliable wing design for aeroelastic tailoring using a mixed Robust and Reliability-based Design Optimisation (RRBDO) approach.
- Development of a multi-level aeroelastic tailoring framework for robust and reliable composite aircraft wing design subjected to multiple constraints and parametric variations.
- Demonstration and validation of the above methodologies using an industrial type composite aircraft wing model.

1.4 Dissertation Outline and Publications

The thesis is structured as follows. Chapter 2 contains a literature review of the current state of the art for aeroelastic tailoring. The current approaches and techniques are highlighted, and their effectiveness and application to composite structures are discussed.

Chapter 3 begins with the modelling approach for structural and aeroelastic analysis of an idealised *'box-like'* Finite Element model representation for a high-aspect-ratio wing which is used as the benchmark model in the current work. The modelling work and analyses are performed using MSc. Patran/Nastran with MATLAB being utilised as the model compiler. Lamination parameters are used to represent the composite laminate properties of different sections of the wing. The wing structures are evaluated in terms of their structural and aeroelastic performance that included strength, buckling, aeroelastic instability and gust response. In the structural analysis, different static manoeuvre load cases are introduced in the model, and the structural performance in terms of the strength and critical buckling load is evaluated. For aeroelastic analysis, a simple aerodynamic model is used where the wing planform is divided into two sections - the outer and inner wing. The Doublet-Lattice method (DLM) is used to represent the aerodynamic model, and the flutter analysis is evaluated using a *'p-k'* frequency matching method. The gust analysis for the wing model is performed using a discrete *'1-cosine'* gust load at different

gust wavelengths. The tip deflection and wing root bending moment due to different gust loads are assessed in order to predict the critical gust response.

In Chapter 4, a novel approach for multiple constraint design optimisation approach is presented. The FE wing model is optimised for minimum structural weight when subject to static manoeuvre load cases. The wing is subjected to strength, buckling, dynamic instability and gust constraints. A cost function is introduced in the objective function to quantify the effect of each design constraints on the wing structural weight. A detailed discussion on different algorithms used including Genetic Algorithm (GA) and Particle Swarm Optimisation (PSO) for the optimisation procedures are presented.

In Chapter 5, two approaches are explored to predict the performance behaviour of the wing due to uncertain parameters in the model: 1) PCE method and 2) RS-HDMR method. These approaches are applied on the benchmark model to predict the variation in structural, dynamic and aeroelastic responses with uncertain in material properties and ply thickness. Finally, the results obtained from PCE and RS-HDMR method are compared with MCS to establish the accuracy and efficiency of each method for uncertainty quantification. The advantages and limitations of each method for uncertainty quantification are highlighted and discussed.

In Chapter 6, a probabilistic optimisation approach is introduced, namely Reliability-based Design Optimisation (RBDO) method. The method is applied to the benchmark wing to obtain an optimised design with improved design reliability by minimising the probability of failure of wing's response at target design value.

In Chapter 7, a novel multi-level robust and reliability-based aeroelastic tailoring framework is introduced. The framework is designed to seek for a deterministic and robust/reliable design using the multi-level optimisation approach. The ideal design solution is chosen from the *'Pareto front'*, where the contributions of structural weight, robust and reliable design constraints and other design constraints are quantified.

Finally, Chapter 8 provides the conclusions from the work and the description of the future work related to the topics investigated in the thesis.

The findings from the current work has lead to a journal paper publication.

- Muhammad F. Othman, Gustavo H. C. Silva, Pedro H. Cabral, Alex P. Prado, Alberto Pirrera and Jonathan E. Cooper. *'A robust and reliability-based aeroelastic tailoring framework for composite aircraft wings'.* Composite Structures, 2019. 208: p. 101-113.

In addition, the following peer-reviewed conference publications from the research are also published.

- M.F. Othman, J.E. Cooper, A. Pirrera, P.M. Weaver, G.H.C Silva, *'Robust Aeroelastic Tailoring For Composite Aircraft Wings'*, 5^{th} Aircraft Structural Design Conference, Manchester Conference Centre, Manchester, UK, 4 - 6 October 2016.
- M.F. Othman, J.E. Cooper, A. Pirrera, P.M. Weaver, G.H.C Silva, *'Multilevel Aeroelastic Tailoring For Composite Aircraft Wings'*, ICCS19 19th International Conference on Composite Structures, Porto, Portugal, 5-8 September 2016.

The work presented in Chapter 6 is a continuation from the findings in the conference paper entitled *'Robust Aeroelastic Tailoring For Composite Aircraft Wings'.* The findings in Chapter 7 are based on the work submitted for journal publication entitled *'A robust and reliability-based aeroelastic tailoring framework for composite aircraft wings'.*

Chapter 2

Literature review

2.1 Introduction

This chapter provides a comprehensive review of the scientific literature for subject areas relevant to the work undertaken in this thesis. The current state of the art of several relevant topics is highlighted and critically discussed to identify any significant gaps in the literature.

- Composite structures
- Design methods for composite structures
- Aeroelastic tailoring
- Uncertainty quantification of composite structures
- Uncertainty-based aeroelastic tailoring

In each section, the current approaches and techniques are highlighted, their effectiveness and applications to composite structures analysis and design are discussed.

2.2 Composite materials

Composite materials have become more popular and used increasingly in aircraft structural components. Current aircraft structures incorporated over 50% of composite-based laminates in designs such as the Boeing B787 and A350 XWB aircraft mainly due to their attractive strength-to-weight ratio [20]. The use of composite materials for aircraft wing structures expands the range of options available for designers and promotes innovative design concepts by taking advantage of the unique properties of the composites materials. Unlike conventional metal alloys, composite materials can be tailored

for specific requirements or performance targets by exploiting their anisotropic properties. These unique advantage over metal alloys allows the design of lighter components without compromising the performance of the structures and hence improves the overall efficiency of the aircraft.

The anisotropic properties of the composite materials can be exploited by tailoring the stacking sequence of the composite laminate such that the fibres are oriented in specific directions to provide strength and stiffness in the direction of applied loads. The plies in a composite laminate are arranged at angle from 0° to 90° relative to the primary loading direction (x-y plane) as shown in Figure 2.1 [32]. Different laminate configurations result

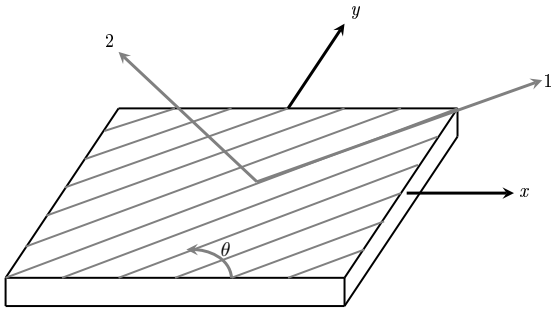

Figure 2.1: Principal axes definition for a composite laminate; Reference (x-y) axes and local material properties (1-2) axes. Note that, 1 and 2 are parallel and transverse direction to the fibre.

in stiffness variations in the structure and potentially beneficial structural coupling such as bending and twist coupling motions [33]. The stiffness of the laminate is represented by the $[A]$, $[B]$ and $[D]$ matrices which describe the response of the laminate to in-plane forces and moments [34]. Different types of coupling may occur when some of the elements in stiffness matrices are not zero. For example, the bending-twist coupling may occur when the $[D]$ matrix elements, D_{16} and D_{26} are not zero, which cause the laminate to twist due to bending moments.

The use of composite materials in aircraft structures introduces a complex design optimisation problem, not only due to numerous design variables but also because of multi-model design space of the ply orientations [35]. In designing a composite structure, certain ply arrangements and rules for laminate configurations must be obeyed to avoid any manufacturing defects such as structural distortion after curing and also to eliminate unnecessary structural coupling in the components [32]. For symmetrical laminates, in which the laminate is symmetrical with respect to the mid-plane, the $[B]$ matrix is zero. Hence, the in-plane / out-of-plane coupling (B_{11}, B_{12} and B_{66} are zero) as well as

extension-twist coupling (B_{16} is zero) are eliminated [34]. On the other hand, the balanced laminate ply arrangement leads to zero extension-shear coupling parameter, A_{16}, which prevents the structure from unexpected deformations [34]. This pre-defined ply arrangement simplifies the design problems and reduces the number of design variables in the optimisation task.

An efficient optimisation procedure is required to optimise the shapes, sizes and the individual ply arrangement (layup) of the structure in questions. Often for aerospace, the objective is to minimise the weight subject to a wide range of constraints. There are many studies related to the optimisation of the composite structures that have been published outlining different techniques to establish the optimum design for the composite structures under different types of loading condition [36–40]. All of these work employed efficient optimisation techniques which utilise the lamination parameters as design variables to obtain the optimum stacking sequence of the laminate.

For many critical composite structures such as aircraft composite structures, additional requirements are often imposed to satisfy all design intents, manufacturing limitations and certification requirements. Due to these constraints, the applications of the composite materials to aircraft structures have been limited to 'black metal' designs, which do not fully exploit the anisotropic properties. Moreover, the designer tends to select readily certified composite materials with limited angle plies (i.e. $0°$, $90°$ and $\pm 45°$) rather than the improved properties due to expense that this would incur over the design stages. Consequently, new technologies or design methods are needed to ensure all the requirements are satisfied at an early stage in the design process, possibly reducing the cost for certification and allowing more innovative design solutions.

Some basic guidelines for designing composite aircraft components have already been published [32] to satisfy both design performances and manufacturing limitations. Examples are the use of balanced laminates in order to avoid warping after cure and in-service loading, the use of a maximum of four adjacent plies in any one direction to avoid splitting on contraction, and the inclusion of drop plies in steps in order to improve load distributions.

A summary of the relevant techniques and approaches for design optimisation of composite structures now follows. A comprehensive discussion is provided particularly for the application of composite material for aircraft structures.

2.3 Design optimisation methods for composite structures

The use of composite materials for primary aircraft structures, such as wings and fuselages, provides significant advantages on the structural weight and performance which are seen with the new generation large aircraft including the Airbus A380 and Boeing 787 Dreamliner. This use is mainly due to the rapid development in the manufacturing capabilities and design methods for the composite structures in recent years. Broadly, the design methods for composite structures can be described in two main categories, deterministic and probabilistic approaches.

In the deterministic approach, the composite structures are designed from a series of optimisation procedures with set requirements such as the weight, strength, stiffness and stability of the structures. The design analysis for simple structures (i.e. composite panel or idealised composite wing plate) involves computation of the governing equations which are derived from mathematical models for different load cases scenario. For more complex structures, the design problems can be solved using computer-based numerical techniques such as finite element (FE) modelling that provide more accurate solutions in comparison with the analytical solutions.

There are many sources of uncertainty [41–44] that exist in composite materials and these are often ignored in the design process, potentially leading to inaccurate design solutions. The performance of the deterministic design can be overestimated, or even underestimated, due to the existence of uncertainty. Henceforth, a probabilistic design method is required to ensure the design reliability has not been compromised due to parametric variation. In reality, the model input parameters can be random. For different samples of composite laminates, the properties such as in-plane/transverse Young's modulus and density vary due to manufacturing defects that included fibre misalignment and mass properties variation, often leading to scatter in the structural performance. Therefore, these uncertainties must be included in the design process to either prevent catastrophic failure in a worst-case scenario or to avoid over-designed inefficient structures.

Detailed reviews on the uncertainty modelling and probabilistic design approaches are discussed in Section 2.5 and Section 2.6. The following sections discuss current approaches for deterministic design methods used for the optimisation of composite structures.

2.3.1 Optimisation using discrete design variables

The deterministic optimisation approach aims to look for the optimum and best combination of composite laminate stacking sequences that satisfy a set of design constraint for specific load cases. The stacking sequence of the composite laminate can be obtained by treating the individual ply angles or the lamination parameters as the design variables. By using ply angles as discrete design variables, the stacking sequence of the optimal design can be directly obtained from the optimisation procedures. However, the optimisation using lamination parameters as continuous design variables require addition optimisation step in order to determine the actual stacking sequence in the form of ply angles. The optimisation approaches using ply angles as discrete design variables are reviewed in this section.

Numerous works [10, 45–47] have been published for optimisation of composite structures using discrete ply angle design variables. All of these works demonstrate the application of different optimisation tools and their effectiveness when using ply angles as design variables. Genetic Algorithms (GA) [45–51], Particle Swarm Optimisation (PSO) [52, 53] and Ant Colony Optimisation (ACO) [10, 54, 55] algorithm are among relatively few examples of optimisation tools use to solve discrete design variable optimisation problems.

GA is a heuristic search method which is based on a directed random search to find the best solution from a *'population'* of randomly generated individuals in a *'generation'*. GA utilises the population of design variables and the probabilistic transition between one solution to another in order to seek for best solution. As GA is randomised search, there is a possibility to lose the best solution in a population due to random chance. Hence, the best solution in the current population is not guaranteed to be selected for recombination [56]. If the best solution from the previous population is lost, there is no guarantee that the solution can be obtained in the subsequent population. Hence, this suggests that several near-optimal solutions can be obtained with GA, but global convergence is not guaranteed. Moreover, as GA randomly searches for a potential solution within a population, the increase in number of design variables leads to increase in the population sizes and hence can be computationally expensive for design problems with greater design spaces.

To improve the computational efficiency of GA, Baluja [56] introduced an improved method known as Population-Based Incremental Learning (PBIL). PBIL employs the generation mechanism of GA and simple competitive learning which results in much simpler algorithm in solving the optimisation problems [56]. In PBIL, the best solutions in the population are described in terms of a probability vector in which samples can be drawn to produce the next generation's population. The probability vector is updated for each generation to represent the current highest evaluation vectors which then use to obtain the bit positions. In a conventional GA, the best solution is encoded into a fixed-length vector consists of strings in form of binary values. The PBIL method minimises the number of steps required in standard GA. Hence, the method is more efficient compared to standard GA.

Another alternative to GA, PSO introduced by Kennedy & Eberhart [57] offers better computational efficiency for discrete design variables optimisation problems. PSO is based on a heuristic search method inspired by simple analogues of the collaborative behaviour and swarming in biological populations [58]. Like the GA, PSO uses a population of random solutions, but each potential solution is assigned with a randomised velocity which makes the algorithm more efficient. A different version of PSO algorithms is available such as the discrete binary PSO [59, 60] and permutation discrete PSO [53]. Similar to PBIL, the discrete binary PSO treats the population members as probabilities instead of potential solutions [59]. The latter version of PSO uses a concept of memory checking, a self-escape idea and valid/invalid exchange to refine the search space for possible solutions [53]. The PSO method offers excellent computational efficiency due to the interaction between the particles and the inclusion of previous best solutions (memory) in the current iteration step. Also, a study performed by Hassan *et al.* [52] showed that the computational effort required to obtain high-quality solutions is less than the effort required by the GA due to reduced number of function evaluation. Moreover, their study suggested that the computational efficiency of the PSO and GA are problem-dependent. Given the fact that the PSO is inherently continuous, the efficient computational PSO is better than GA when dealing with continuous design variables.

The ACO algorithm is another optimisation tool introduced by Dorigo *et al.* [61] and designed for combinatorial optimisation problems such as stacking sequence of composite laminates. ACO is a class of approximate heuristic searches based on the foraging behaviour of real ants to find the shortest path between their nest and the food source

by communicating the best path to take. Ants deposit a chemical substance called *'pheromone'* along the path, and the best path is chosen based on the pheromone concentration. An ACO algorithm employs the same concept by modifying the pheromone variables associated with the problem whilst building solutions to the optimisation problems [62]. The algorithm is initiated by allowing ants to choose their paths at random for each node (ply) as shown in Figure 2.2. Each path represents the possible angle for each node and each time the ants follow a particular path, pheromone is released, and the amount of pheromone is build-up towards the final solution. The best path is chosen based on the concentration of pheromone on each path.

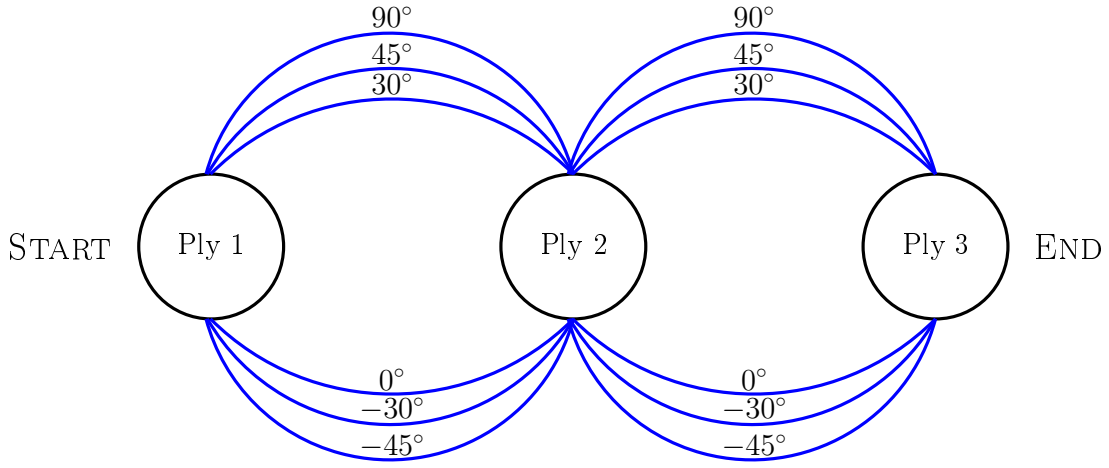

Figure 2.2: The ACO solution paths for symmetrical laminate panel with 0, ±30°, ±45° and 90° plies.

The convergence in ACO depends on the control parameters which influence the selection of the best path and avoid the suboptimal paths, hence allowing for new solution path exploration [10, 39]. The ACO algorithm is also found to be very effective for large parameter design spaces and can be used for both discrete and continuous design problems [10]. Similar to PSO and GA, the global optimum solution in ACO is not guaranteed although the solution's convergence can be obtained due to change in probability values in every iteration.

Harmin & Cooper [10] has demonstrated the first application of ACO in composite design. Their work utilised ACO as the optimisation algorithm to determine the optimal stacking sequences of a simple rectangular composite plate wing for maximum flutter and divergence speed. Later, Bloomfield *et al.* [60] performed a benchmark study using several metaheuristic techniques that included ACO for composite lay-up optimisation.

Other applications of ACO in composite design optimisation problems can be found in [39, 54, 55, 63, 64].

The use of discrete design variables in the optimisation of composite designs allowed designers to directly incorporate additional constraints for feasible lay-ups that satisfied both design and manufacturing constraints [32]. However, most of the design optimisation examples given in the literature consider the composite laminate as stand-alone parts. In reality, the laminate would be a small part of a larger structure. For example, a composite aircraft component such as wing skin is typically designed as multiple panels. Each panel may have different thickness across the wing which may cause high-stress concentrations and manufacturing difficulties.

The Blending method [45, 65, 66] has been introduced to tackle the continuity issues arising in the design of stacking sequences for composite laminates with multiple panels. In this method, the laminate is designed by keeping the thickness changes between two adjacent laminate to a minimum. Two different blending schemes are shown in Figure 2.3 - inner blending, where the inner layers from the mid-plane are continuous from the adjacent panels, and outer blending, where the outer layers of the laminate are continuous [65]. Liu & Haftka [45] incorporated continuity constraints in the structural design optimisation of composite wings by imposing two types of continuity measures - a material continuity measure for global level design and a stacking sequence continuity measure for local level design. Another study by Seresta *et al.* [65] used the two different blending schemes and a guide based GA approach in the optimisation of laminated panels. The method proposed by Seresta *et al.* [65] produced a higher continuity percentage with fewer plies compared to the best design obtained by Liu & Haftka [45] due to a better match in the stacking sequence between adjacent panels. Later, Liu *et al.* [66] performed bi-level optimisation studies to obtain the best stacking sequence of a laminated composite wing structure using blending and manufacturing constraints. A shared-layer blending method is used in the second level of optimisation to satisfy both the global blending requirements and general lay-up design rules. The results from their study highlighted some difficulties in matching the constraint values between two optimisation levels whilst ensuring ply continuity. A table listing sequence [67] and recently, a global shared-layer blending (GSLB) method [68] and a sequential permutation table (SPT) method [40, 69] have been proposed to overcome ply continuity issues for the stacking sequence optimisation of composite structures.

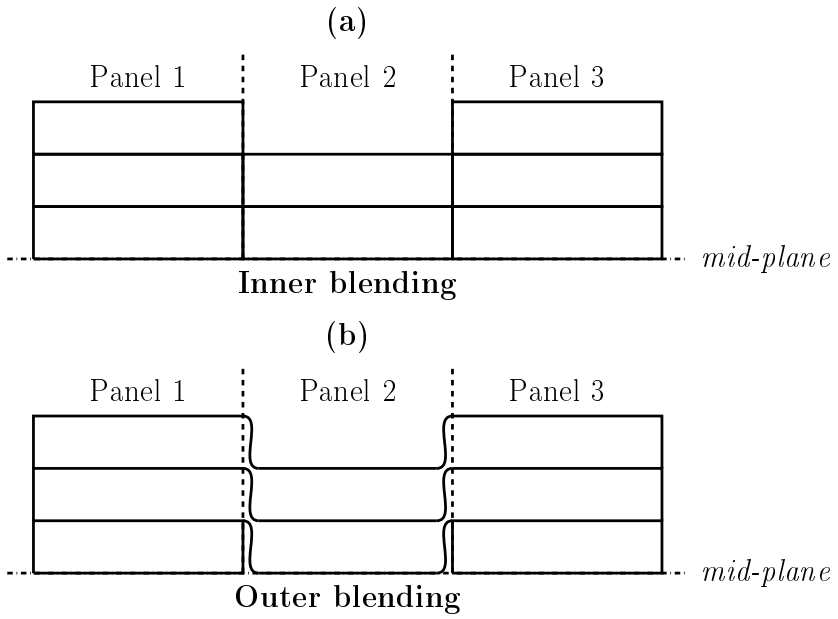

Figure 2.3: Blended laminate configurations; (a) Inner blending, where the inner layers are taken as the guide ply, (b) Outer blending, where the outer layers are taken as the guide ply.

Despite the advantages as mentioned above of an optimisation approach using discrete design variables, the method may not be very efficient for larger structures with multiple panels and a large number of plies. This limitation is due to the massive amount of computational effort required to obtain solution convergence. To overcome this, lamination parameters can be used to represent the stiffness properties of the laminate resulting in a fixed number design variables that are independent of the number of plies in each panel. The following section provides a review of the lamination parameter concept which later is used in the optimisation procedure of the current work.

2.3.2 Lamination parameters

The use of lamination parameters significantly reduces the number of design variables required for the optimisation of composite structures. Tsai *et al.* [70] and Tsai & Hahn [33] introduced the concept of lamination parameters to represent the laminate properties. The lamination parameters, together with material invariants, can be used to represent the laminate stiffness matrices, in-plane $[A]$, coupling $[B]$ and out-of-plane $[D]$ stiffness components as a linear function formulation [33]. There are four lamination parameters associated with each stiffness matrix, where each lamination parameter can be expressed in terms of the ply orientation, θ and material invariants, U_j. The lamination parameters

are not independent and are related to one another by inequality relationships for both in-plane and out-of-plane terms.

Earlier use of lamination parameters in optimisation studies of the composite design was demonstrated by Miki [71] and Miki & Sugiyama [36] for laminated composite plate. Miki introduced an inequality relationship which described the feasible regions of in-plane and out-of-plane stiffnesses for orthotropic laminate using two in-plane or two out-of-plane lamination parameters. Later, Fukunaga & Sekine [72] described the feasible regions of all four in-plane and out-of-plane lamination parameters for symmetrical laminates. Their work examined the relationship between the four in-plane and out-of-plane lamination parameters by considering the extension-shear couplings and the bending-torsion couplings of the laminates. Fukunaga & Sekine suggested that the feasible regions for lamination parameters for a laminate with extension-shear coupling terms (A_{16} and A_{26}) occur within an ellipse for lamination parameters without the coupling terms. An inequality equation governs this relationship for all four lamination parameters. The relationship between two out-of-plane lamination parameters is shown in Figure 2.4 and 2.5, where the feasible regions for two lamination parameters are known when the other two parameters are kept constant. The defined feasible region reduces the design space and hence provide a practical approach for seeking an optimal stacking sequence.

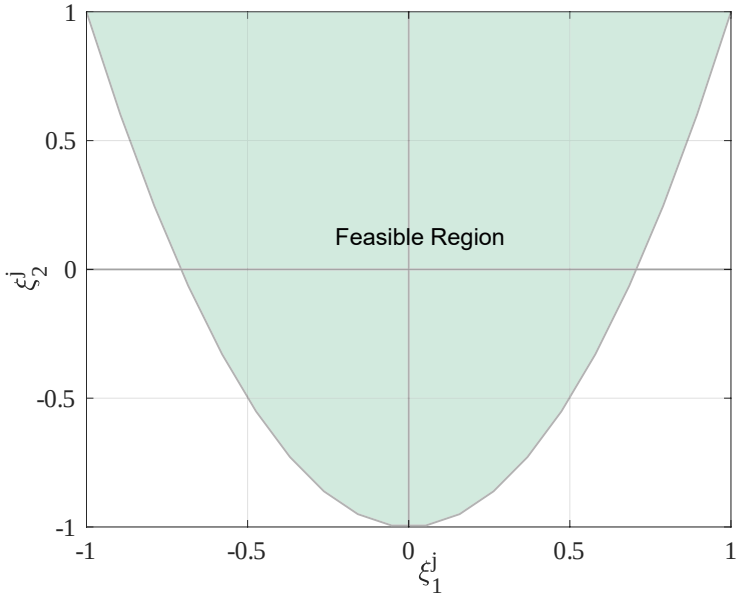

Figure 2.4: Feasible region of lamination parameters, (ξ_1^j, ξ_2^j) when $(\xi_3^j, \xi_4^j) = (0, 0)$ where $j = A, D$.

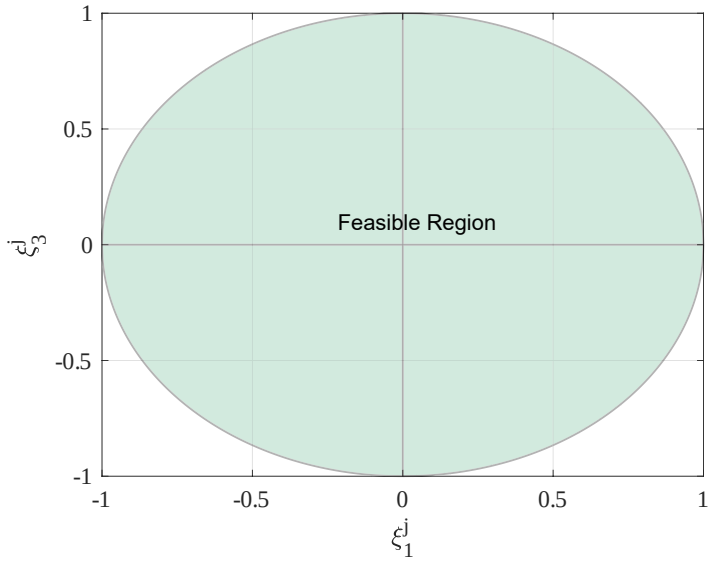

Figure 2.5: Feasible region of lamination parameters, (ξ_1^j, ξ_3^j) when $(\xi_2^j, \xi_4^j) = (0, 0)$ where $j = A, D$.

The feasible regions derived by Miki [71] and Fukunaga & Sekine [72] are applicable only for in-plane and out-of-plane stiffness matrices separately with a restricted ply-orientation. Grenestedt & Gudmundson [73] then introduced an explicit expression using variational approach to link a particular set of in-plane lamination parameters with the out-of-plane parameters such that for a given value of ξ_i^A, there is a range of values for ξ_i^D except when $\xi_i^A = \xi_i^D = \pm 1$. Their work also suggested that the feasible regions for the lamination parameters (design variables) are convex, and the objective function of a design problem is concave. Therefore, local optima can be avoided, and only a global solution exists, which significantly simplifies the optimisation problem.

Using the same approach, Diaconu *et al.* [74] then defined the boundary of the feasible region in the general space of 12 lamination parameters and later, Diaconu *et al.* [75] introduced explicit expressions for feasible regions linking the in-plane, coupling and out-of-plane lamination parameters with a finite set of ply orientations. However, the explicit expression for the feasible region proposed by Diaconu *et al.* gives a larger feasible area compared to a feasible region obtained from the variational approach which suggested that the expression is not sufficient to describe the feasible region in the general design space of all lamination parameters. Other work by Diacanu & Sekine [76] derived an explicit expression relating the nine lamination parameters with restricted ply orientations (0°, 90°, ±45° plies only). The expression proposed by Diacanu & Sekine can be used

efficiently to describe the feasible region for the nine lamination parameter case which is suitable for practical layup design as ply orientations are often restricted to particular set of ply orientations for manufacturing feasibility.

More recently, Setoodeh *et al.* [77] and Bloomfield *et al.* [37] used convex hull methods to determine the feasible region for lamination parameters. Setoodeh *et al.* used a convex hull approximation to refine the feasible region of the lamination parameters by increasing the number of plies and possible ply orientations. The feasible region is approximated in terms of linear inequality constraints by monitoring the convergence of the feasible domain volume. Bloomfield *et al.* proposed an alternative method to determine the exact constraints for the feasible region of any finite set of ply orientation. Their work suggested a two-level method to determine the feasible region of lamination parameters for a pre-defined set of ply orientation. The feasible regions of in-plane, coupling and out-of-plane lamination parameters are determined separately using the convex hull method in the first level. Then in the second level, a non-linear algebraic identity is used to relate all the parameters which are then utilised to determine the constraints on the feasible region of lamination parameters. The method proposed by Bloomfield *et al.* provides a better interpretation of the feasible region of all lamination parameters for a predefined set of ply angles. Moreover, the method suggested by Setoodeh *et al.* only provides an approximation on the feasible region and relatively large number of constraints which may not be computationally efficient. Figure 2.6 and 2.7 shows the boundary of the feasible region with 0, 90, $\pm$30, $\pm$45, $\pm$60 degree plies derived from the hyperplane constraints proposed by Bloomfield *et al.* [37] for in-plane and coupling lamination parameters. The boundary of the feasible region is formed using the hyperplane constraints obtained from the convex hull relationship. Bloomfield *et al.* also suggested that the number of hyperplane constraints that enclosed the feasible regions for coupling lamination parameters is significantly greater than the number of hyperplane constraints for both in-plane and out-of-plane parameters.

The use of a lamination parameter design space in optimisation procedures has been proven to be more effective due to the use of known feasible regions which simplifies the design problems. Furthermore, a maximum of 12 design variables is required for each panel, which is further reduced if a balanced or symmetrical configuration is used. Moreover, the use of lamination parameters can guarantee global optimality for linear

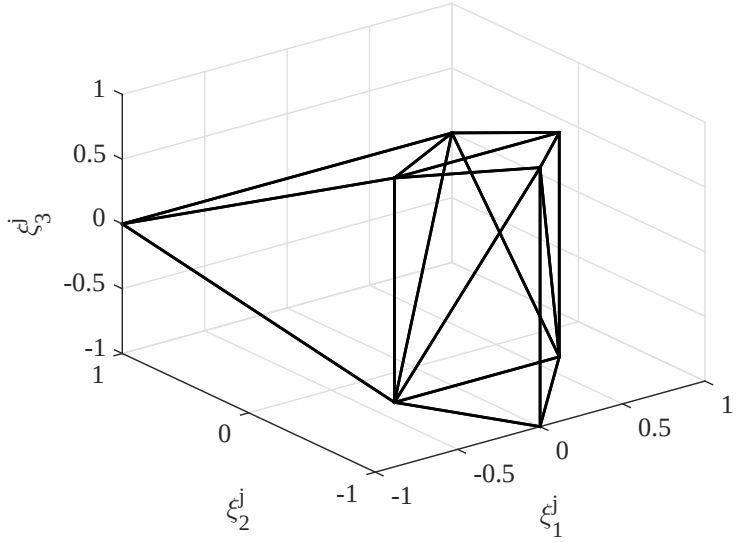

Figure 2.6: Feasible region of lamination parameters, $(\xi_1^j, \xi_2^j, \xi_3^j)$ where $j = A, D$ when $\xi_4^j = 0$ for 0°, 90°, ±30°, ±45° and ±60° plies derived from Bloomfield (2009).

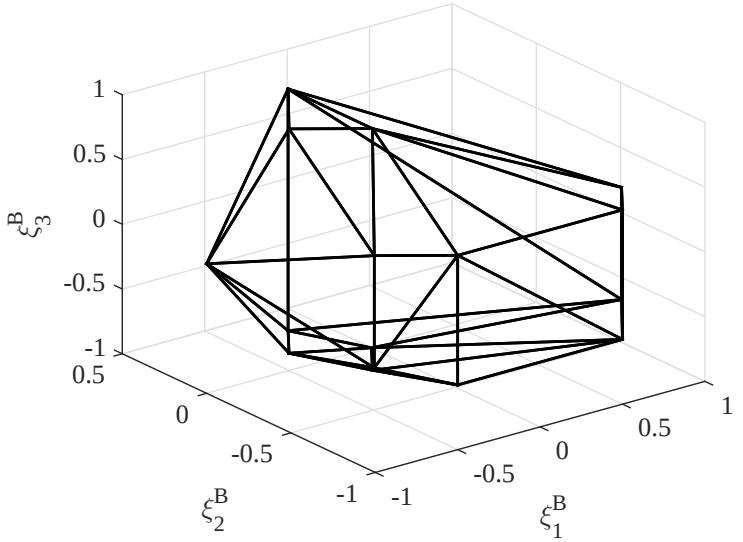

Figure 2.7: Feasible region of lamination parameters, $(\xi_1^B, \xi_2^B, \xi_3^B)$ when $\xi_4^B = 0$ for 0°, 90°, ±30°, ±45° and ±60° plies derived from Bloomfield (2009).

problems which can be solved using standard optimisation tools such as gradient methods. However, an additional optimisation step is required to retrieve the actual stacking sequence for the laminate. The transition between continuous design spaces (lamination parameters) to discrete design space (ply angle) may result in discrepancies in the actual performance of the laminate. The discrete design solution obtained may not correlate with the continuous design solution due to additional constraints for the actual

ply sequence retrieval including ply contiguity, ply-drop and others.

2.3.3 Other optimisation methods

The design optimisation methods in Section 2.3, requires a very efficient optimisation tool to solve the design problems. GAs are often used for composite design problems, either using discrete or continuous design variables. Solving the optimisation problem with a GA may require high computational resources when dealing with complex structural problems and finite element analysis. To overcome this difficulty, a surrogate model can be used to approximate the response surface and provide a rapid evaluation of the design solution. Examples of the surrogate models are the response surface method using polynomial approximation [78–82] kriging model approximation [83], fractal branch and bound method [84, 85], and artificial neural networks [86]. Liu *et al.* [78] used the response surface approximation method to obtain the optimum stacking sequence for buckling design problem of a composite wing. A cubic polynomial response surface with D-optimal criterion was used to represent the optimum buckling load as a function of the loads and number of plies. Another efficient optimisation method for aerodynamic design problem was demonstrated by Jeong *et al.* [83] using a Kriging model as the approximation function for the response surface.

Other optimisation methods using the *variable-stiffness* approach has been used in Refs. [87–91]. In this method, the composite ply is treated as a variable-stiffness panel in which the stiffness properties are varied across the panel. The panel is divided into several regions with the fibre angle at each region optimised for a specific load. Thus, allowing more design space to be explored without a structural weight penalty. Ghiasi *et al.* [92] published a comprehensive review on the variable stiffness design method focusing on the different formulations for the optimisation approach. Ijsselmuiden *et al.* [90] demonstrated the effectiveness of the design method on composite panels subjected to buckling loads. Their study observed significant improvements in buckling resistance for variable stiffness laminate in comparison with quasi-isotropic laminate configurations with similar in-plane stiffness properties.

As mentioned earlier, for composite structures, uncertainty exists from multiple sources through materials, geometry and manufacturing process, resulting in variability in the structural responses. The composite design optimisation methods discussed previously

are proven to be efficient in design problems with the assumption of no parameter variations (uncertainty) in the model. Consequently, the work presented in this thesis focused on the inclusion of uncertainty in design optimisation which should provide better designs with less sensitivity to parameter variations.

2.4 Aeroelastic tailoring

In this section, an overview of aeroelasticity and loads is presented, followed by a discussion of the current aeroelastic tailoring approaches for composite aircraft wing structures. The current state of the art for aeroelastic tailoring is also presented.

2.4.1 Introduction to aeroelasticity and loads

As mentioned earlier in Chapter 1, aeroelasticity is related to the interaction of the aerodynamic, inertia and elastic forces and their influence on the structure performance [1]. The components of aeroelasticity study can be summarised from the Collar's aeroelastic triangle as depicted in Figure 2.8. The figure shows the major components making up aeroelasticity, with each area arising from the interaction of at least two types of force. Static aeroelasticity effects occur due to the interaction of aerodynamic and elastic forces while the stability and control effects result from aerodynamic and inertia forces interaction. In order for dynamic aeroelasticity to occur, all three types of the forces - inertia, aerodynamic and elastic forces are required to interact.

In static aeroelasticity, the deflection of flexible aircraft structures under aerodynamic loads is studied with the forces and motions independent of time [1]. The wing structural deflections due to aerodynamic loads determine the wing bending and twist and are crucial in order to evaluate the structures static aeroelastic behaviour. For steady flight conditions, the static aeroelastic deformation provides an influence on the lift distribution, control surface effectiveness, aircraft trim behaviour as well as the static stability and control characteristics. *Divergence* and *control reversal* are the two critical problems encountered from static aeroelasticity of the aircraft wings. Divergence occurs when the moment due to the aerodynamic forces exceeding the restoring moment from the structural stiffness, which may lead to catastrophic structural failure. Control reversal occurs

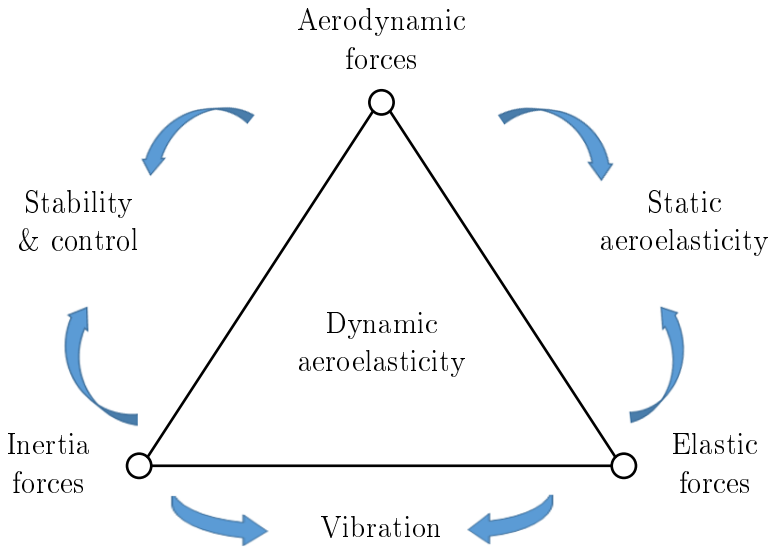

Figure 2.8: Collar's aeroelastic triangle.

when the aircraft speed is higher than the critical speed which leads to the reverse action of the control surface.

Langley's tandem monoplane machine first experienced the structural failure due to wing divergence in 1903, nine days before the Wright brothers' successful flight [93]. The failure was due to insufficient wing-tip stiffness which results in wing torsional divergence. Some years later, the original Langley's machine was flown successfully after a substantial modification on the wing structures and trussing which significantly strengthened and stiffened the original structure. Another example of static aeroelastic related failure of control reversal was experienced by high-aspect-ratio aircraft Bristol Bagshot in 1927 [94]. The aileron effectiveness was decreased to minus value as the speed was increased. Unlike divergence, control reversal is not necessarily leading to disastrous failure. It may affect the aircraft's control response either very slowly or not responsive at speed closes to reversal speed.

Dynamic aeroelasticity is concerned with the oscillatory effects of the interaction between aerodynamics, inertia and elastic forces. One of the major aircraft design concerns related to dynamic aeroelastic is the potential of catastrophic flutter failure. Flutter occurs due to unfavourable coupling between two or more vibration modes which leads to dynamic instability. The flutter analysis is complicated due to the unsteady nature of aerodynamics forces and the moments generated from oscillation motions of the aircraft. The first documented flutter occurrence was observed on Handley-Page O/400 biplane

bomber, where the aircraft experienced violent antisymmetric oscillations of the fuselage and tail section due to insufficient connection between the aircraft's right and left elevators. [93, 94].

In the aircraft design process, consideration of aeroelasticity is one of the critical design criteria towards completing the certification process. For the design flight envelope, the designer must ensure that the aircraft is free from flutter and divergence. Another vital aspect in aeroelasticity study is the influence of loads on the static and dynamic effects [1]. Such influences are illustrated in Figure 2.9. Equilibrium/steady/trimmed manoeuvres loads give influence on the static aeroelasticity effect (i.e. Divergence) whereas gust and turbulence encounter influence the dynamic aeroelastic behaviour. Therefore, loads and aeroelastic considerations are essential for certification in aircraft design.The work in this thesis is concerned with the aeroelastic tailoring of composite aircraft wings considering aeroelastic instabilities, trimmed manoeuvres and gust loads.

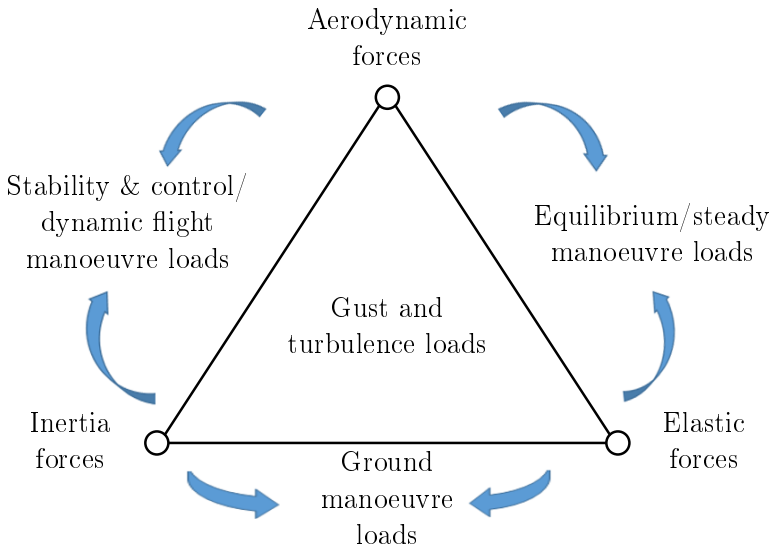

Figure 2.9: Loads triangle.

2.4.2 Introduction to aeroelastic tailoring

In modern aircraft structures, the structural design is driven by the need for minimum weight leading to improved fuel efficiency and flight range. The use of composite materials in the main structural components has proven to be beneficial for light-weight aircraft whilst maintaining the intended performances. This gain is mainly due to their directional stiffness, strength properties and high stiffness-to-weight ratios which allow

for innovative design concepts of load-carrying structures that are not achievable with conventional metallic materials. In the context of aeroelasticity, the use of composite materials allows structures to be tailored for improved static and dynamic aeroelastic performances without penalising the minimum structural weight requirement in the design process.

> *"Aeroelastic tailoring is the embodiment of directional stiffness into an aircraft structural design to control aeroelastic deformation, static or dynamic, in such a fashion as to effect the aerodynamic and structural performance of the aircraft in a beneficial way (Shirk,1986)." [2]*

Krone [95] briefly defined material tailoring (composite) as the use of directional stiffness to offset the aeroelastic instability divergence of forward-swept wings) without abrupt increases in structural weight as compared to an aluminium wing counterpart. Shirk *et al.* [2] provided a proper definition of aeroelastic tailoring as the method of controlling the aeroelastic deformation, static or dynamic by incorporating directional stiffness into an aircraft structures for better aerodynamic and structural performance. Weight minimisation is often treated as the main objective in aeroelastic tailoring with other structural and aeroelastic performances such as flutter, divergence, lift, drag, control effectiveness and buckling treated as additional objectives or design constraints [96]. Aeroelastic tailoring of composite aircraft structures can be explored by introducing directional stiffness into the structure through structural tailoring or material couplings (bending-torsion stiffness coupling) which then alter the static and dynamic aeroelastic behaviour of the wing structures.

Theoretically, aeroelastic tailoring in wing structure can be defined as the modification of the wing's *primary stiffness* direction by changing the bending and torsional stiffness as well as the bending-torsional coupling stiffness of the wing structure for improved aeroelastic performances [4, 96, 97]. The term primary stiffness is defined as *'the locus of points where the structure exhibits the most resistance to bending deformation'* [4]. The primary stiffness direction can be tailored by varying the composite laminate properties, using stiffness or by modifying the rib's position. For composite aircraft structures, the primary stiffness (directional stiffness) can be influenced by number of parameters

that included the laminate thickness, number of plies and the stacking sequence of the composite laminate.

Figure 2.10 (adapted from [4]) shows the aeroelastic tailoring characteristic as results of changing the structure's primary stiffness direction. The wing structure experiences bend-twist coupling when the primary stiffness direction is not coincident with the structural reference axis [98]. The movement of the primary axis forward or aft from the structural reference axis causes the wing to have leading-edge down (wash-out) or leading-edge up (wash-in) behaviour. The wing will experience a wash-in behaviour when positive bending causes a nose-down twist, and wash-out behaviour is governed by nose-up twist deformation from positive bending [2]. Wash-out deformation is useful for divergence prevention, drag reduction and manoeuvre load alleviation while wash-in behaviour is beneficial for delaying the onset of flutter and improving control and lift effectiveness [2, 97, 99]. However, the wing wash-out is undesirable for flutter as an increase in the divergence speed is likely to be accompanied by a lower flutter speed. Conversely, the increase in the flutter speed due to structural wash-in leads to a lower divergence speed [99]. This effect results in aeroelastic objective conflicts and an optimisation procedure must be employed to satisfy all these objectives.

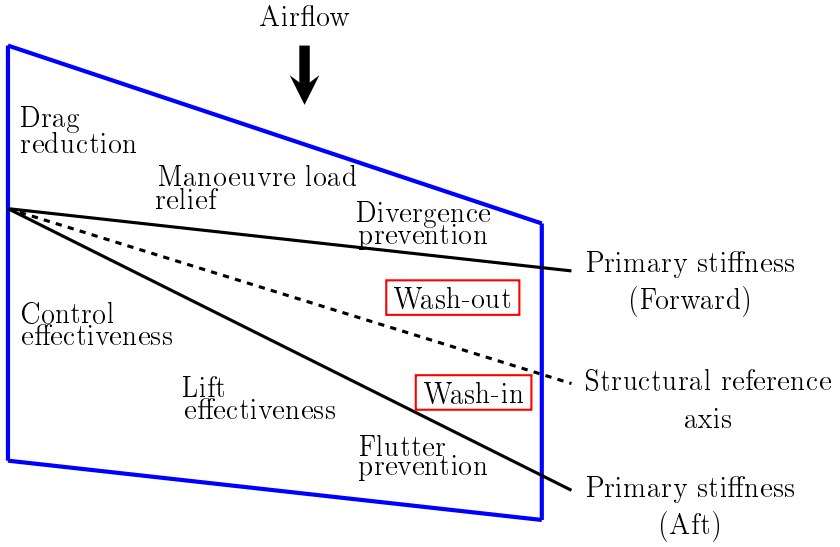

Figure 2.10: Aeroelastic tailoring's concept and the location of primary stiffness with respect to structural reference axis for wing wash-out and wash-in behaviour [4].

2.4.3 Parametric studies in aeroelastic tailoring

The study in aeroelastic tailoring can be broadly classified into two categories - parametric (Section 2.4.3) and optimisation studies (Section 2.4.4). Parametric studies have been conducted by many researchers to establish a better understanding of aeroelastic tailoring for prevention of aeroelastic divergence and flutter.

Housner & Stein [100] performed an earlier parametric study on a swept wing for flutter wing characteristics using a bend-twist beam model. The study evaluated the effect of variation in ply orientation on the flexural rigidity (EI) and torsional stiffness (GJ) of the structure. The results suggested that the flutter speed is increased with increased GJ with the maximum flutter speed attained when GJ was at a maximum ($\pm 45^\circ$ layup). Furthermore, a discontinuity on the flutter boundary was observed when a ply angle increase led to a flutter mode switch.

Krone [95] suggested that divergence on a forward-swept wing can be prevented through aeroelastic tailoring without adding weight to the structures. Through material tailoring, the structural stiffness and wing aerodynamic load are redistributed and hence provide optimum stiffness and strength to the structure. The torsional stiffness of the wing plays a significant role in preventing divergence and controlling the loading distributions of the bending moment close to the root. Another parametric study via a wing tunnel demonstration by Sherrer *et al.* [101] provided similar observations. The composite plate wings were found to be more effective in preventing divergence per unit weight compared to the aluminium counterpart. Sherrer *et al.* also suggested that by simply rotating the composite laminate about the reference line of the wing, the divergence speed can be altered. Moreover, their work also concluded that negative coupling stiffness value produces a wash-out behaviour which is undesirable for divergence, and by increasing the torsional and coupling stiffness reduces the wash-in tendency and is capable of delaying the onset of divergence.

Hollowell & Dugundji [102] also investigated the influence of bending-torsion stiffness coupling on the onset of aeroelastic flutter and divergence. Analytical and experimental studies were performed using an idealised cantilever wing model made of graphite/epoxy with various laminate configurations consisting of $\pm 45^\circ$, 0° and 90° plies. Their work supported the observations made by Krone [95] and Sherrer [101] that bending-torsional

stiffness coupling can be beneficial in delaying or eliminating divergence. Negative stiffness coupling could exhibit divergence while positive coupling values could delay the onset of flutter. Interestingly, the wing model without bending-torsion coupling was found to exhibit bending-torsion flutter at a low angle of attack and torsion-stall flutter at higher angle of attack, whereas the model with large coupling values showed primarily bending-torsion flutter.

Weisshaar & Ryan [99] published a similar observation on the influence of wing sweep and stiffness cross-coupling on the flutter and divergence speed. Their work showed that the forward sweep of the wing caused an increase in flutter speed and a decreased in the divergence speed. The stiffness cross-coupling parameter derived in Ref. [103] was used to analyse the effect of stiffness cross-coupling on flutter and divergence speed. The parameter defined a non-dimensional relationship between the coupling parameter, K, bending stiffness parameter, EI and torsional stiffness parameter, GJ. The positive stiffness cross-coupling parameter leads to wash-in behaviour and undesirable for divergence. While a negative value cause wash-out behaviour and decrease in the flutter speed.

Lottati [104] performed another interesting parametric study of the aeroelastic flutter and divergence characteristic for a composite forward-swept cantilevered wing. The effect of the stiffness coupling terms (D_{16} and D_{26}) on the vibration modes as well as flutter and divergence onset were investigated. The work highlighted that the passive aeroelastic instability enhancement could be achieved by varying the value of the bending-torsional stiffness coupling of the composite wing. It was also found that the coupling terms strongly influenced the divergence speed because of improved rigidity in the torsion mode (warping effect).

More recently, Kameyama & Fukunaga [105] investigated the effect of sweep angles and laminate configurations on the flutter and divergence characteristic of a composite plate wing. The main observation from their work concerned on the discontinuity behaviour of flutter speed due to change in flutter modes. As such, a different laminate configuration may result in the bending-torsional flutter due to coupling between the first torsional and second bending vibration modes (higher-order mode flutter) instead of first torsional and first bending vibration mode (lower-order mode flutter). The flutter speed of higher-order mode is lower than the divergence speed which results in the discontinuity of the contours of flutter speed. Their work also showed that the torsional-bending coupling

lamination parameters (ξ_3^D and ξ_4^D) significantly influence the aeroelastic characteristic of the composite plate wings. The increase in ξ_3^D and ξ_4^D parameters led to an increase in the divergence speed. Conversely, a decrease in the same parameters led to an increase in the flutter speed.

Other parametric study performed by Patil [106] concerned on the effect of bending-twist and extension-twist coupling values on the divergence and flutter speed. The study was carried out using a box-beam wing model. The study suggested that the positive ply angles in the laminate configuration produced bending-twisting coupling, which is beneficial divergence prevention. However, the effect of ply angle variations (negative to positive angles) on the flutter behaviour is more complicated due to mode shape changes.

Another work by Guo *et al.* [107] investigated the effect of bending, torsion and, more importantly, the bending-torsional coupling rigidity on the flutter speed of a composite thin-walled wing box made of laminated carbon-epoxy material. Two types of lay-up - symmetric and asymmetric lay-up (balanced non-symmetric layup) were considered in their work to evaluate the contribution of coupling rigidity, K on flutter speed. For symmetric laminates (K is zero), the flutter speed is mainly influenced by the torsional rigidity, GJ where the maximum flutter speed was obtained when GJ was a maximum. For asymmetric laminates, the flutter speed depends on both GJ and K.

2.4.4 Optimisation in aeroelastic tailoring

In the previous sections, it has been established that the coupling parameters, K, bending stiffness parameter, EI and torsional stiffness parameter, GJ mainly influences the aeroelastic behaviour of composite structures. The bending-torsion coupling parameters (ξ_3^D and ξ_4^D) significantly influence the aeroelastic characteristic of composite plate wings. Numerous works have performed optimisation studies of composite wing structures using different model fidelities and optimisation tools. The main objective for optimisation studies in aeroelastic tailoring is to obtain an optimum design with improved aeroelastic behaviour (i.e. eliminating flutter and divergence behaviour) without affecting other design performances.

Early optimisation studies in aeroelastic tailoring were performed using design tools for flutter and strength optimisation that included Wing Design Optimisation With Aeroelastic Constraints (WINDOWAC) [108], Aeroelastic Tailoring and Structural Optimisation (TSO) [6, 95] and Flutter and Strength Optimisation Program (FASTOP) [109]. The WINDOWAC program was developed to obtain minimum mass designs of wing structures subjected to flutter and strength constraints using finite elements. The TSO is an interdisciplinary program combining aerodynamic, static aeroelasticity, structural and flutter calculations. The program used non-linear programming techniques to obtain optimum composite wing skin thickness distributions and ply orientations subject to flutter and strength constraints for specific aeroelastic load cases [6]. The FASTOP design tool was developed using two major programs - Strength Optimisation Program (SOP) and Flutter Optimisation Program (FOP). The SOP program optimises the structure for minimum weight designs that satisfy the strength requirements while FOP further optimises the design for flutter speed with a minimum weight penalty [109]. FASTOP was used for the preliminary design of the Grumman X-29, a forward-swept experimental aircraft. Later, in early 1990s, an automated multidisciplinary structural design tool known as Automated Structural Optimisation System (ASTROS) was developed for preliminary design of aerospace structures combining concepts of both TSO and FASTOP [110]. The ASTROS program utilised TSO's capability to simultaneously design the structure for multiple constraints and employed FASTOP's concept of incorporating finite element analysis into the optimisation procedure. All these methods proved to be efficient and have been used in practical designs. However, the applications have been limited to flutter and strengths design.

For aeroelastic tailored structures, the optimisation studies focus on the aeroelastic modelling approach and the optimisation techniques. Recent works have employed detailed representations of wing structures in the model to capture the wing performance accurately. However, these will always lead to need for more significant computational resources as a result of the increased model fidelity. Several authors [10, 23, 47, 111] employed numerical methods with simple model representation such as a cantilever wing model in the optimisation procedure to reduce model complexity. The outcomes from such low fidelity model may be sufficient to predict the aeroelastic behaviour of the structure but may lead to inaccurate results for other design items such as the structural strength and buckling.

Harmin & Cooper [10] performed an optimisation study on a simple rectangular composite wing to maximise the flutter/divergence speed by treating the ply orientations as the design variables. In their study, the wing plate was fabricated using a symmetrical laminate (six plies in total). The optimisation was performed using ACO as the design variables (ply angles) are discrete. An optimised wing design with higher flutter speed was obtained from their work at low computational effort. Another study by Attaran *et al.* [111] performed a structural optimisation of a composite flat plate made of woven fibreglass epoxy. The study focused on finding the optimal structural configurations based on the aspect ratio, sweep angle, and stacking sequence of laminated composites. The results indicated that ply orientation angles between 15° and 30° improved the flutter speed. A similar observation was obtained for plates with lower aspect ratios and forward sweep angles.

The use of an idealised wing-box representation in optimisation procedures has been attempted by Refs. [3, 9, 107, 112]. Earlier work by Eastep *et al.* [3] studied the effect of the composite layup orientation on the optimised wing structural weight with strength, roll-reversal velocity and flutter speed. The work analysed the benefits of using ply angles as the design variables in the design optimisation of composite structures. Interestingly, the results showed that the optimum structural weight of the wing was relatively insensitive to the changes in the layup orientation for all design categories. Chang *et al.* [112] and Guo *et al.* [107] performed computational and analytical studies on a swept-back composite wing box. The former work investigated the effect of stiffness distribution on the top and bottom skins across the span of wing boxes with different thickness distributions. The latter work utilised an analytical approach to examine the effect of rigidities on the flutter speed of a laminated composite wing box structure with different layup configurations. The results obtained from both works suggested that significant improvements on the flutter speed were achieved without weight penalty. Guo *et al.* [107] also concluded that the torsional and coupling rigidities have greater influence on the flutter speed of the composite wing box where torsional rigidity is more dominant. Asymmetric layups were found to be more favourable in aeroelastic tailoring optimization.

More recent work by Dillinger & Klimmek [113] investigated the effectiveness of using laminate stiffness matrices for stiffness optimisation of composite wings with mass, strength, buckling, aerodynamic twist, and aileron effectiveness as the design constraints.

The in-plane and bending stiffness matrices and the laminate thickness were used as the design variables. The stiffness optimisation was performed on the upper and lower skins of a composite wing. Lamination parameters were used to represent the laminate stiffness. The results highlighted the advantages of using unbalanced laminate over balanced laminates and reductions in structural mass were obtained from the optimisation procedure. The results also suggested that the structural sizing was predominantly dependent on the effect of buckling loads on the structures. An improvement in the aileron effectiveness was also observed with unbalanced laminates. An unbalanced laminate result in bending-torsion coupling stiffness and hence improves the passive deformation behaviour of the wing structures. The introduction of bending-torsion coupling on the structure induces a more substantial twist and thereby provides an improvement on the aileron effectiveness.

Another optimisation work with multiple design constraints was performed by Guo *et al.* [14]. A multi-level optimisation study was performed on a composite wing structure subjected to structural strength and aeroelastic constraints. Composite laminate ply thicknesses and the ply angles of the wing skins were used as the design variables. In the first level optimisation, the structure was optimised for minimum weight subjected to strength, damage tolerance and flutter speed constraints. In second level, the structure was further optimised to minimise the gust response in terms of wingtip deflection with minimum weight penalty. The optimised design was found to satisfy the aeroelastic design constraints and also the structural performance constraints with reduced structural weight. The work done by Dillinger & Klimmek [113] and Guo *et al.* [14] demonstrated the needs of using multiple design constraints in the aeroelastic tailoring process. The main reason is that the optimised wing for aeroelastic performance may not satisfy the structural performance and vice-versa. The inclusion of the structural analysis in aeroelastic tailoring process allows for an optimum design that satisfies both aeroelastic and structural performance.

2.4.5 Other development in aeroelastic tailoring

In addition to the aeroelastic tailoring works discussed above, there is number of published work that has focused on the optimisation of structural configuration for minimum weight and improved performance (i.e. aeroelastic and structural performances). Harmin

et al. [114] performed aeroelastic tailoring on metallic wing structures to improve the aeroelastic behaviour, flutter/divergence speed and gust loads responses. Two structural tailoring methods were introduced - orientation of the wing ribs and the use of crenellations in the wing skins. A 3% differences in flutter speed were accounted from both design methods. Their work also suggested that the bending-torsion coupling of the wing structures can be controlled by both methods which result in twist and flutter speed variation.

Another work done by Vio *et al.* [15] and Locatelli *et al.* [115] studied the aeroelastic tailoring and weight optimisation of a wing box structures using curvilinear spars and ribs. The findings from Locatelli *et al.* work suggested that the aeroelastic performance of the proposed wing design with curvilinear spars and ribs were improved in terms of the structural mass, flutter speed and wing bending moment. The use of different configurations for ribs and spars resulted in improved wing performance without any structural weight gain. However, the potential gains that can be achieved from structural tailoring are not fully utilised due to manufacturing feasibility constraints and current design practices. More recently, Francois *et al.* [116] carried out experimental study on the aeroelastic tailoring of un-tapered and un-swept wing box using more realistic ribs and spars design orientations for improved aeroelastic performance. Five different ribs orientations were considered in their work which varied from 0° to 45°. The results suggested that the change in the orientation of the ribs altered the structural bend-twist coupling of the wings and hence the static and dynamic aeroelastic response.

Another interesting development in aeroelastic tailoring is the possibility of using a novel manufacturing method to influence the coupling behaviour of the composite wing and hence improve the aeroelastic performance. The introduction of *'tow-steering'* technology to manufacture laminates with variable angle tow (VAT) plies has shown huge potential for the aeroelastic tailoring of composite wing structures. Stodieck *et al.* [11] and Stanford & Jutte [117] studied the use of VAT laminates for aeroelastic tailoring. The work performed by Stodieck *et al.* [11] examined the effect of using VAT laminates on the vibration, flexural axis position, flutter and divergence speeds and gust loads using simple rectangular unswept composite wing model. It was found that a higher flutter speed can be achieved using VAT laminates due to the increase in the design space as compared to traditional unidirectional composite laminates. Stanford & Jutte [117] performed more detailed studies on the possibility of using tow-steering laminate

for aeroelastic tailoring. Simple cantilevered plate and a wing box of a full-scale high aspect ratio wing configuration were used for static aeroelastic and aeroelastic analyses. An interesting finding from their work suggested that although there are limitations on the ply angles that can be used for composite laminate, it is still possible to include the tow steering effect on the wing structure by using a core laminate that was rotated along the defined steering path across the wing semi-span. However, the approach results in a reduction in the aeroelastic performance as compared to fully-steered configuration but beneficial compared to an unsteered laminate configuration.

2.5 Uncertainty quantification in composite structures

Uncertainty quantification is one of the essential aspects of study in aeroelastic tailoring which has drawn much recent research interest. Uncertainty is defined as *'an imperfect state of knowledge or a variability resulting from a variety of factors including, but not limited to, lack of knowledge, applicability of information, physical variation, randomness or stochastic behaviour, indeterminacy, judgement, and approximation'* [118]. In the context of aeroelastic tailoring, uncertainty quantification can be defined as a study of the effects of quantity variations on the system's aeroelastic performances.

Two types of uncertainty can be classified as *'epistemic'* uncertainties or *'aleatory'* uncertainties. As described by Melchers [119], epistemic uncertainty is a type of uncertainty arising from the limitations of knowledge which is often due to lack of understanding about physics and human errors. Epistemic uncertainty can be reduced by improving the understanding of the problems. On the other hand, aleatory uncertainty is an irreducible uncertainty which is inherent in the system or model. The most common example of aleatory uncertainty is randomness in the system's parameter. The effect of aleatory uncertainty on the system can be minimised by acquiring additional data, improving modelling techniques or better parameter estimation.

Aleatory uncertainty is most commonly represented as a probability distribution, using available experimental data of known ranges for determining a distribution [120]. Epistemic uncertainties can be quantified using possibility theory or interval analysis. Possibility theory was introduced by Zadeh [121], in which the theory of fuzzy sets controls the propagation of the uncertainty through the models. The interval analysis is

used when the uncertainties or the data distribution are unknown but only the upper and lower bounds are known [122]. In the occasion where mixed aleatory and epistemic uncertainties exist, evidence theory, also known as Dempster-Shafer theory [123], may be used to quantify the uncertainties. Examples of work on uncertainty quantification using evidence theory are well documented in Refs. [124, 125]. The work in this dissertation deals with parametric uncertainty which is one type of aleatory uncertainty.

Parametric uncertainty can be in the form of variations in the material properties, geometry or the stiffness properties of the model or system. All this information can be represented using randomly distributed data based on the known variation ranges from the historical data (i.e. experimental data). The parametric uncertainty can also be a mix of aleatory and epistemic type of uncertainty [120]. This may become the case when only partial data is available for a system/model, and assumption/correlations are made to link those data for entire system/model.

The uncertainty in composite materials can exist due to the geometry, and material properties scatter. The mechanical properties of composite materials show greater variability compared to conventional metallic material in aircraft structures. The variations are mainly due to the composite manufacturing process which may cause material non-homogeneity (i.e. fibre-rich or resin-rich area), fibre misalignment, fibre waviness, wrinkling, manufacturing tolerance and thickness variation. In a layup process for any composite component, one possible source of uncertainty is the misalignment of ply orientation. Moreover, during the curing process, other causes of uncertainty might include voids, porosity, excess resin or matrix and variations in ply thickness. These so-called manufacturing defects may result in a reduction of the composite material's properties. Studies on the sources of variability that included fibre waviness and misalignment, variability in mass/unit area and geometrical variability of composite materials can be reviewed in Refs. [41–43]. Potter *et al.* [43] reported that fibre waviness and misalignment of the composite plies might result in a reduction of the modulus value of at least 17% of its specification. The effect of fibre wrinkling on the compressive strength is more influential as 15 - 30% is lost in the compression strength. Other sources of variability, such as mass/unit area properties and the fibre straightness that arise from the manufacturing process, may contribute to dimensional variability in composite laminates [42]. Small variations that may exist in the material properties could lead to a loss in the

actual performance of the structure or design. Hence, these need to be accounted for in the early design stages of a composite structure.

The studies on the composite behaviour due to uncertainty at different scales, ranging from micro to structural level, have been performed by Refs. [17, 126, 127]. These study aims to establish the sensitivity of the constituent properties (fibre and matrix) on ply properties and the consequent structural variable. The work performed by Chamis [126] suggested that the ply Young's modulus in the fibre direction E_{11} is most influence by fibre modulus and fibre volume ratio. The variability in the in-plane shear modulus, E_{12} is mainly caused by the scatter in the shear modulus of the matrix and the fibre volume ratio. Chamis also suggested that the traditionally used *'safety factor'* requirement for structural design maybe ultraconservative. By directly incorporating uncertainty quantification into the design allows for a redefinition of the safety factor to be used and potentially more innovative and better design solutions.

At a structural level, the uncertainty quantification analysis focused on the effect of uncertainty and its sensitivity to structural performance. Vinckenroy *et al.* [127] did early work on the uncertainty quantification of the structural behaviour of composite structures. The effect of variability in composite material properties and hole geometry on the maximum stress of a perforated plate was investigated. The sensitivity study revealed that different sets of random parameters influenced the longitudinal, transverse and shear stress. For instance, the longitudinal Young's modulus and the hole's form are the main contributors to the variation in longitudinal stress values. In addition, their work also concluded that each of the parameters in the material properties (longitudinal Young's modulus, Poisson coefficient and others) are best represented by a Largest Extreme Values (LEV) distribution, Weibull or Smallest Extreme Values (SEV) distribution in order to efficiently quantify the contribution of each random parameters.

In the context of aeroelastic tailoring, the primary source of uncertainty was related to the computational model parameters or parametric uncertainty such as material properties, thickness and ply orientation variations. Kuttenkeuler & Ringertz [128] reported that from both experimental and numerical studies, a small variation in material properties results in substantially different in flutter speed. The variation in material properties leads to a variation in the composite stiffness values. For example, the variation in bending-torsional coupling stiffness values results in different flutter behaviour and hence

scatter in the flutter speed values. Moreover, high variability in the material properties or the parametric uncertainty can significantly reduce the aeroelastic performance and may perform very poorly at off-design conditions [18]. The uncertainty quantification can be used as a risk-based design criterion in aeroelastic tailoring. One of the approaches is to use uncertainty in reliability-based design analysis. The reliability-based design analysis allows for direct quantification of the parameter variability in the model and to seek for a reliable design which satisfies all of the design constraints even though uncertainty exists. The inclusion of uncertainty quantification in the design optimisation problem may improve the design confidence for certification and potentially eliminate or replace the traditionally used *safety factor* constraint for designing a composite structure.

There is number of methods available to quantify uncertainty in composite material and structures. The parametric uncertainty or aleatory uncertainty can be quantified using a probabilistic method such as Monte Carlo Simulation (MCS), perturbation technique, Polynomial Chaos Expansion (PCE) and others. In this review, several main tools for uncertainty quantification are presented - MCS, perturbation technique, PCE and High Dimensional Model Representation (HDMR).

2.5.1 Monte Carlo Simulation (MCS) and Perturbation Technique

Monte Carlo Simulation (MCS) is the most common and straightforward technique for uncertainty quantification. MCS uses random input sampling to determine the output of interest. Typically, MCS requires large numbers of sampling data in order to obtain an accurate output distribution. A statistical distribution in the form of a probability density function (PDF) of each of the input parameters is identified. A large number of random inputs are then sampled from these distributions and used as the input parameters. For each set of random input parameters, the corresponding output parameters are determined from a number of simulation runs followed by the statistical analysis to characterise the output distributions [129, 130]. The number of samples for the input parameters in MCS is dependent on the type of problem and often vary. The number of samples or simulation runs required for MCS usually is determined from a convergence study.

In uncertainty quantification of composite material and structures, MCS has been used on many occasions (Refs. [126, 127, 131–133]). Vinckenroy & Wilde [127] performed

a stochastic design study on the structural behaviour of composite material structural components. Their work presented the use of MCS combined with finite element modelling to evaluate the effect of input parameters variation (material properties, structure geometry and loading conditions) on the probabilistic distribution of the structural response. Other work by Jeong & Shenoi [131] applied the MCS method in their study on probabilistic strength analysis of a supported rectangular anti-symmetric laminated plate. MCS was used to quantify the behaviour of the system subjected to variation in the basic design variables that included transverse lateral pressure load, elastic moduli, geometric and ultimate strength value. Their study suggested that the accuracy of the MCS solutions are dependent upon the number of random design variables and increase in the number of samples.

In aeroelastic studies, the MCS method has been used to model the flutter [134] and limit-cycle oscillations (LCO) [135] behaviour of a wing plate subjected to several uncertainty parameters. Castravete & Ibrahim [134] utilised MCS to investigate the influence of the spanwise distribution of bending and torsion stiffness uncertainties on the flutter behaviour. Due to the high number of samples required for MCS to obtain an acceptable accuracy, the MCS output is often used to validate the results from other uncertainty quantification tools. In their work, Castravete & Ibrahim used the results from MCS for comparison with the output from the perturbation method.

The advantage of using MCS is that it is easy to implement on many applications and accuracy is improved as the number of samples increases. However, a few major limitations are being highlighted by researchers on its application. Firstly, a large number of random samples are required to obtain an acceptable level of accuracy. Secondly, the statistical distribution of the random input parameters is needed to be established. A further limitation is that if the random input parameters are not independent then their dependency should be accounted for [24]. These limitations of MCS have lead to the development of other uncertainty quantification tools for better efficiency especially when dealing with complex structures that involve finite element modelling. The work presented in this dissertation employed MCS to evaluate the accuracy of other methods.

The perturbation method was introduced to overcome the limitations of the MCS method. The method employs a first and second-order Taylor series expansion of the random input variables about their mean value to predict the output response of the systems [136].

Early applications of perturbation method in uncertainty quantification can be found in Refs. [134, 137, 138]. Grenestedt [137] utilised the perturbation approach in a sensitivity study of the buckling load due to bending-twisting coupling variations. Their study showed that the perturbation method provides an excellent approximation in comparison with the exact solution obtained from the finite difference approach. Later, Elishakoff *et al.* [138] introduced the improved perturbation method by employing the finite element method for stochastic problems. Their study showed that the improved method provided significant improvements in comparison with the first and second-order perturbation method. Although the perturbation method can produce acceptable results, the random system variations need to be small enough in order to ensure convergence and accuracy of the results.

2.5.2 Polynomial Chaos Expansion (PCE) and related techniques

Due to the limitations of MCS and perturbation methods for uncertainty quantification, a stochastic Polynomial Chaos Expansion (PCE) method is increasingly used and regarded as a more efficient and accurate alternative. PCE is an approach that employs a polynomial based stochastic space to represent the random parameters and their propagation on the model of the system of interest. Norbert Weiner [139] first introduced the concept of polynomial chaos as part of homogeneous chaos. Later, Ghanem & Spanos [140] proposed a simple definition of PCE as a convergent series that included the interaction of individual random variables and the polynomials. For standard Gaussian input random variables, the Hermite polynomial is used for the chaos. The method proposed can achieve exponential convergence for Gaussian distributions but not necessarily for other types of input distribution.

Xiu & Karniadakis [141] then extended the application of PCE to other non-Gaussian distributions of the random input variables using the Askey scheme. According to the scheme, for different types of probability distribution of random input variables, different orthogonal polynomials can be used to represent the polynomial chaos [141, 142]. For example, a continuous Gamma probability distribution can be represented by Laguerre polynomials. The selection of the orthogonal polynomials is based on the inner product weighting function and its corresponding support range that represent the probability density functions of corresponding distributions. The use of an optimal basis ensures an

exponential convergence as it uncouples the variable expansion and allows the polynomial orthogonality properties to be applied on each variable [143].

Early applications of PCE in aeroelasticity study were performed on Limit Cycle Oscillation (LCO) in a nonlinear aeroelastic system [144, 145]. Despite having an advantage in terms of computational efficiency, PCE is found to have difficulties in capturing the uncertain response after a long-time integration and discontinuities in stochastic differential equations [145, 146]. To solve this, Beran *et al.* [145] proposed the use of a two-dimensional Weiner-Haar expansion to obtain the stochastic aeroelastic properties in advanced time. These are done by taking advantage of the Haar's wavelet multiresolution properties. Other solutions were proposed by Wan & Karniadakis [146] with the use of multi-element with generalised Polynomial Chaos (ME-gPC) in which the space of random inputs are decomposed into a sub-domain when the relative error in the variance becomes more significant than the threshold value. The other limitation of PCE is related to dimensionality of the stochastic problem. It is reported that the computational efficiency of PCE drops as the input dimension increase [21, 143].

In general, the PCE methods can be classified into two categories - intrusive and non-intrusive methods [147]. Ghanem and Spanos [148] introduced an intrusive method, the Galerkin Polynomial Chaos (GPC) to model the output responses. The GPC method uses a Galerkin stochastic finite element approach to determine the deterministic coefficients. The method creates a coupled set of deterministic equation resulting from the Galerkin projection on the probability spaces. These deterministic equations need to be solved through altering the deterministic solver which makes the method an unattractive option for industrial applications.

To overcome the limitations of the intrusive method, non-intrusive PCE methods have been developed wherein the deterministic solver is treated as a *'black-box'* as in MCS. Examples of such methods are the Stochastic Collocation (SC) [149, 150], Probabilistic Collocation (PC) [151] and linear regression method [21, 22, 143]. The SC method was introduced by Mathelin & Hussaini [150] in which a stochastic space with known properties is used to enable transformation between the stochastic space and artificial space. The method employs a set of multidimensional Lagrange interpolation polynomials such that each collocation point is represented by one polynomial. These polynomials are equal to one at their particular collocation point and zero at other points. Thus, such

an approach allows for the determination of the coefficient of expansion which is the response value at each collocation point. The method shows significant improvement in computational time compared to the Galerkin Polynomial Chaos approach [150].

The PC method combines the formulation of the chaos transformation as in GPC and the collocation approach from the SC method. In PC, the deterministic coefficients are solved by computing the Galerkin projection in probability space numerically using Gaussian quadrature to decouple the systems of equations [151]. Hence, the method provides a solution to the GPC method since the current deterministic solver can be used to solve for the deterministic equations. The linear regression method, also known as point collocation or stochastic response surface, employs a single linear least-square solution to solve for the expansion coefficient that best matches the set of output responses [143]. The sets of output responses are typically obtained from computational experiments for a particular number of samples. The method requires fewer simulation runs to determine the deterministic coefficients and hence is often used in PCE.

PCE has been used to model uncertainty in aeroelastic models, such as a composite lifting surface. The effects of uncertain material properties, fibre orientation, and ply thickness on the aeroelastic stability (i.e. flutter and divergence) have been studied using PCE [16, 21, 22]. Scarth *et al.* [21] reported on the aeroelastic behaviour of a simple cantilever wing model subjected to uncertainty in the ply orientations using lamination parameters. The use of PCE in their work suggests that the method is significantly more computationally affordable compared to MCS with an acceptable level of accuracy. However, their work is only applicable to simple model representations, and the efficiency of the work is not yet proven for more detailed models. Hence, the work undertaken in this thesis utilised PCE to quantify the uncertainty effect using more detailed FE models and evaluated the efficiency of the method in more practical applications.

2.5.3 High Dimensional Model Representation (HDMR)

High Dimensional Model Representation (HDRM) is another surrogate modelling technique introduced by Rabitz [152] to capture the input-output relationships of high dimensional random input variables. The HDMR method utilised only low order correlations of the random input variables to represent the function response, $f(\mathbf{x})$, with reasonable

accuracy. The advantage of the method over PCE is the capability to include higher dimensional order of the random input variables without significant computational expense. There are three common types in HDMR expansions - ANOVA-HDMR, cut-HDMR and random sampling HDMR (RS-HDMR) [153].

The ANOVA-HDMR expansion method employs the analysis of variance (ANOVA) statistical technique to obtain the variance components of the system responses [154]. The cut-HDMR expansion method primarily depends on the value of $f(\mathbf{x})$ at a specific reference point while the RS-HDMR expansion depends on the average value of the function response over the whole domain [27, 153]. In the cut-HDMR method, the component functions are determined at discrete values of the input variables sampled from the output response function. These component functions are defined along either on cut lines, plane or through a reference point in the input domain [153]. The higher-order component functions in RS-HDMR are typically obtained from a Monte Carlo random sampling. In both cut-HDRM and RS-HDMR methods, the determination of the component functions of the HDMR is straightforward and easy to implement as the components can be obtained from either discrete or randomly sampled points in the input variable domain.

The HDMR method has been used to quantify the effect of random variables in composite materials as in Refs. [155–157]. Dey *et al.* [157] employed the RS-HDMR approach to quantify the free vibration of angle-ply composite plates with uncertain ply angles. A total of 128 sampling data were selected using Sobol's sequence for each random ply angle of a four-plies composite cantilever plate, and 100,000 runs are performed using MCS. The results suggested that the probability density functions (PDF) of the plate's natural frequency displayed a good agreement with the MCS results with mean and standard deviation differences of 0.23% and 2.32%, respectively. Similar results are reported by Murugan *et al.* [155] in the helicopter aeroelastic analysis with spatially uncertain rotor blade properties. The proposed application of the HDMR method provided a significant saving in terms of the computational hours (a few minutes to 1000 CPU hours) in comparison with direct MCS simulations.

In comparison with PCE, the HDMR method provides an alternative tool for uncertainty quantification that requires fewer computational runs and is capable of quantifying a large number of random variables as only low order component functions are formulated to quantify the output responses due to parameter variations sufficiently. Moreover, in

the PCE method the number of samples required for the analysis is increased significantly with higher dimensional order of the random parameters and higher polynomial order used in the model. The HDMR method has been shown to scale favourably with increasing number of design variables. However, the applications of HDMR method in aeroelastic study are not fully explored; hence the current work in the thesis employed HDMR as one of the main tools for uncertainty quantification with higher dimensional input random variables.

2.6 Uncertainty-based aeroelastic tailoring

The current approach of aeroelastic tailoring in composite structures employs a deterministic based design optimisation approach. Although this method has been successfully implemented in many other applications, the validity of the optimised design is in question due to lack of uncertainty consideration in the design process. In reality, when dealing with composite structures, uncertainty can exist due to the multiple sources not only being limited to the material properties variations but also due to the structural geometry variations as a result of the manufacturing process. These uncertainties need to be quantified accurately to produce a realistic design which accounts for design robustness and reliability to parameter variations.

The design approach based on the stochastic variation in the system parameters can be classified into two categories - robust design and reliable design approaches. The former approach aims to optimise the system performance close to target mean value and minimise the variation, without eliminating the source of variability [158]. The reliability-based design approach seeks an optimal design whilst satisfying a reliability requirement defined by the reliability index or the probability of design failure [29].

2.6.1 Robust Design Approach

G. Taguchi [159] first developed the robust design approach in late 1940s for quality improvement. Taguchi suggested three-level steps for a product or a process design - system, parameter, and tolerance designs. The method has been discussed in many references [158, 160–162]. In particular, the Taguchi's parameter design step has been adopted for robust design approach. Within the parameter design step, the optimum

setting for control factors are determined by the designers, and the manufacturing cost will not be influenced by the parameter design as the tolerance are fixed. The ultimate goal in parameter design is the final product to be insensitive to any small changes in parameter value or the noise factors without eliminating the source. Hence, the design variables are considered as the control factors, and the tolerance, as well as the manufacturing process, are the noise factors.

The robust design approach based on Taguchi's method has been expended and implemented in various applications [158, 161–163]. By definition, the robust design approach involves optimising (minimising or maximising) the mean value of response function and minimising the response's variance. Thus, the robust design approach is inherently a multi-objective design problem. The conventional weighted sum (WS) method often used to solve for the multi-objective optimisation problem. The idea is to obtain the trade-off decision between the mean and the variance of the best design solution using a Pareto set. Lee *et al.* [161] used weighting factors to solve for pseudo-objective function in determine the robust design of unconstraint mathematical problems under trust structure designs. A similar approach was used by Hwang *et al.* [162]. Sundaresan *et al.* [164] used a sensitivity index optimisation approach to determine the robust optimum by optimising the weighted sum of the Sensitivity Index and the mean performance. Mulvey *et al.* [165] employed a multi-criteria optimisation approach for robust design to generate a solution set that is less sensitive to variation. The WS method is effective if the Pareto curve which defined the potential solution is convex. Another limitation of this method is that the best solution for the problem is not guaranteed although all the Pareto points are deduced. [166]. Later, Chen *et al.* [167] proposed a Compromise Programming (CP) method (also known as Tchebycheff method) to solve for robust design from a set of efficient solutions or the Pareto points.

The robust design approach has been applied mostly on process system and static design problems, and there are minimal applications of robust design approach in aeroelasticity and dynamic studies. Hwang *et al.* [162] performed a robust optimisation of an automobile rearview mirror for vibration reduction using a modified Taguchi method where the original signal-noise (S/N) ratio was replaced with multi-objective function with the mean and the standard deviation of the vibration displacement. Zhang *et al.* [158] demonstrated the robust design approach based on Taguchi's method on the dynamic responses of a tuned vibration absorber with mass and stiffness properties uncertainty. In

their work, the maximum mean displacement response and the variations caused by the uncertainty parameters were minimised. The results were validated with Monte Carlo Simulation (MCS), and the robust design showed a significant improvement in the mean response and variation when compared to traditional solutions.

The inclusion of uncertainty in the robust design approach requires uncertainty quantification for each iteration step, and the conventional Monte Carlo Simulation is not computationally feasible. An alternative method such as PCE or other uncertainty quantification tools discussed previously can be used in the robust design approach. The non-intrusive Polynomial Chaos (PC) method was used by Dodson & Parks [163] in a robust aerodynamic design optimisation problem to demonstrate the efficiency of the method for uncertainty quantification. The lift-to-drag ratio of a two-dimensional aerofoil was optimised with uncertainty in the leading-edge thickness with reduced computational cost when compared to MCS runs.

2.6.2 Reliability-Based Design Approach

The structural reliability study is concerned on the prediction of the probability of occurrence or failure of limit-state violation of the structure [168]. In the context of reliability design, the aim is to look for design alternatives, so that the structural reliability can be improved and the risk of failure is minimised. Various methods such as simulation methods, first and second-order reliability methods have been used to evaluate the structural reliability by estimating the probability of failure of the design.

The conventional Monte Carlo Simulation (MCS) can be used as a sampling method to determine the probability of failure from a limit state probability distribution. However, the main limitation of this method is that a large number of samples are required to quantify the probability of failure with accepted confidence level and accuracy [168]. Alternatively, other sampling methods such as Latin Hypercube Sampling (LHS) method, capable of producing similar level of accuracy with MCS but with smaller number of samples [142], could be used.

The approximate methods can also be used to obtain structure reliability, such as First-order (FORM) and Second-order reliability methods (SORM). The methods employ either first or second-order Taylor series expansions to estimate the limit state function.

The structural reliability is typically measured in terms of reliability index, β. The mean value first-order second-moment method (MVFOSM) can be used to determine the β value by evaluating the limit state function around the mean value of the random variables [169]. However, the approximated β value can be inaccurate when the random variables are highly non-linear, and the variation (coefficient of variance) is high.

Hasofer & Lind [170] introduced a method called advanced first-order second-moment (AFOSM) method (also referred to as the Hasofer-Lind method) to overcome the limitation of MVFOSM. In this method, the limit state functions are evaluated at a point known as the *'design point'* instead of the mean value. The design point is selected based on the maximum likelihood of occurrence or most probable point (MPP). The reliability index can be obtained from a distance between the origin and MPP in transformed standard normal space of random variables [170]. The FORM method is capable of producing accurate reliability estimations if the limit state function is linear in standard normal space. For non-linear limit state functions, SORM can be used in which a parabolic, quadratic or higher-order surface is fit to the limit state surface in design point as shown in Figure 2.11. The FORM method is considerably more efficient than the SORM since the former only quantifies the first-order derivative. However, both methods may predict poor reliability if the range of the random variables is broad or the response function is non-linear [168].

Lin [133] performed reliability analysis of laminated composite plates with random parameters using FOSM and MCS. The material properties, lamina thickness and strength parameters were treated as random variables with first ply failure as the limit state function of the laminate plates for reliability analysis. Their findings showed that the FOSM method produced reasonably good results compared to experimental data. In aeroelasticity applications, Yang *et al.* [171] employed the AFOSM method to evaluate design reliability of aircraft wings subjected to gust loads. In their work, the second-order Ditlevsen's bound and penalty function were used to account for the statistical correlation between failure modes in predicting system reliability. The AFOSM method was found to perform better compared to the level III method as in the probabilistic design approach.

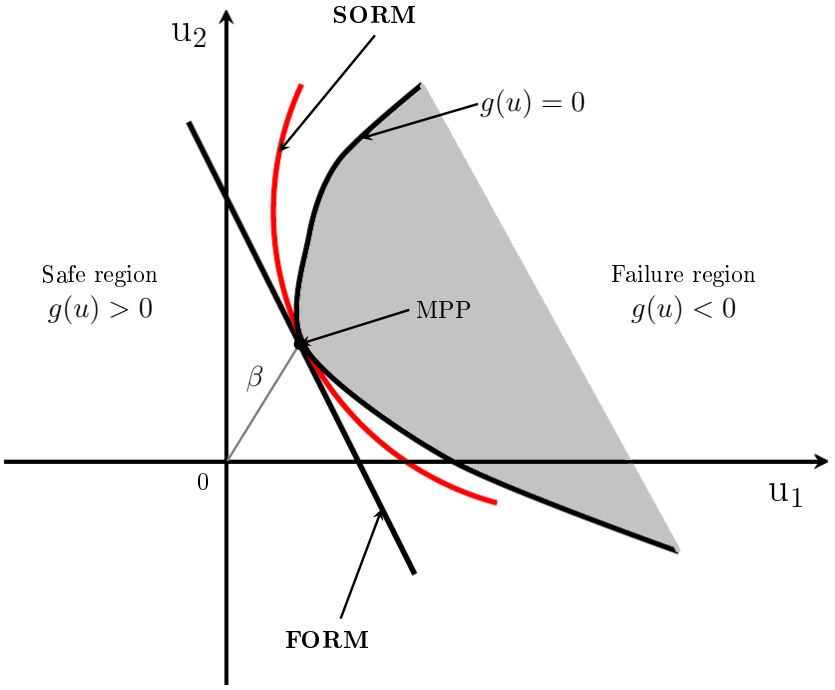

Figure 2.11: Comparison of First-order reliability method (FORM) and Second-order reliability method (SORM).

Allen & Maute [19] provided a detailed study of reliability design approach on aeroelastic structures using FORM. In their work, the wing structure was optimised for maximum likelihood of flight range above the set level with uncertainties in design (wing plate thickness) and operating conditions (angle of attack). A high-fidelity nonlinear aeroelastic simulation method was used together with the FORM to predict the system reliability. The use of FORM method for reliability analysis proved to be efficient when high-fidelity analysis is involved although the accuracy is questionable (under or overestimate) as FORM employs linear limit state surface to approximate the reliability index.

Surrogate modelling techniques such as PCE [142, 172] and HDMR [173] can be used to approximate the limit state function at a reduced computational cost. Manan & Cooper [172] reported that PCE method produced an accurate responses prediction with significantly less number of samples in comparison with MCS. Hence, the method provided an efficient alternative method to MCS in order to predict the limit state function for structural reliability in expense of lower computational cost. In their work, Manan & Cooper employed PCE to obtain an optimum reliable-based design of a composite plate wing for flutter responses. The material properties of the composite material (E_{11} and G_{12})

and ply thickness were selected as the uncertain parameters. At least, a 25.8% reliability improvement was observed compared to the deterministic optimum design. Similar observation was reported by Choi *et al.* [142]. Choi *et al.* performed the structural reliability analysis on a joined-wing model using PCE with LHS. The results from the analysis showed that only 1.25% difference in probability of failure was registered using PCE with 200 samples data in comparison with MCS with 10,000 simulation runs. Other surrogate models such as Gaussian process emulators have been used in a reliable-based design approach for composite plate wings [25].

2.6.3 Design optimisation with Robust and Reliability-based approach

The reliable and robust design approach can be translated into uncertainty-based design optimisation using two primary methodologies: 1) Reliability-Based Design Optimisation (RBDO) [21, 29, 30, 172] and 2) Robust Design Optimisation (RDO) [29, 31]. The RBDO approach seeks for an optimal design whilst having a particular risk or target reliability/performance as a constraint. On the other hand, the RDO approach seeks for optimal designs about a mean target response value, thereby maximising robustness via minimisation of the sensitivity to random parameter variations [29]. Figure 2.12 illustrates the principle of both approaches. A mixed approach, which employs features of both RDO and RBDO is thought to be a more effective means to search for robust optima that also satisfies reliability constraints. Paiva *et al.* [29] used a mixed RDO-RBDO approach for the preliminary design of aircraft wings. Their multidisciplinary approach employs a Kriging surrogate model to account for uncertainties in parameters of the flight conditions.

The application of probabilistic optimisation approaches such as RBDO and RDO for the aeroelastic tailoring of composite structures has been reported by several authors, including refs. [21, 30, 172]. Scarth *et al.* [21] and Manan *et al.* [172] used simplified analytical models for aeroelastic stability with uncertainty arising from composite material properties. Their work employed a PCE model for uncertainty evaluation, together with a singly-constrained RBDO approach, to obtain a reliable design for maximum instability speed. There are minimal applications of this approach on aeroelasticity studies, and to the knowledge of the author, there has been no application to the aeroelastic tailoring

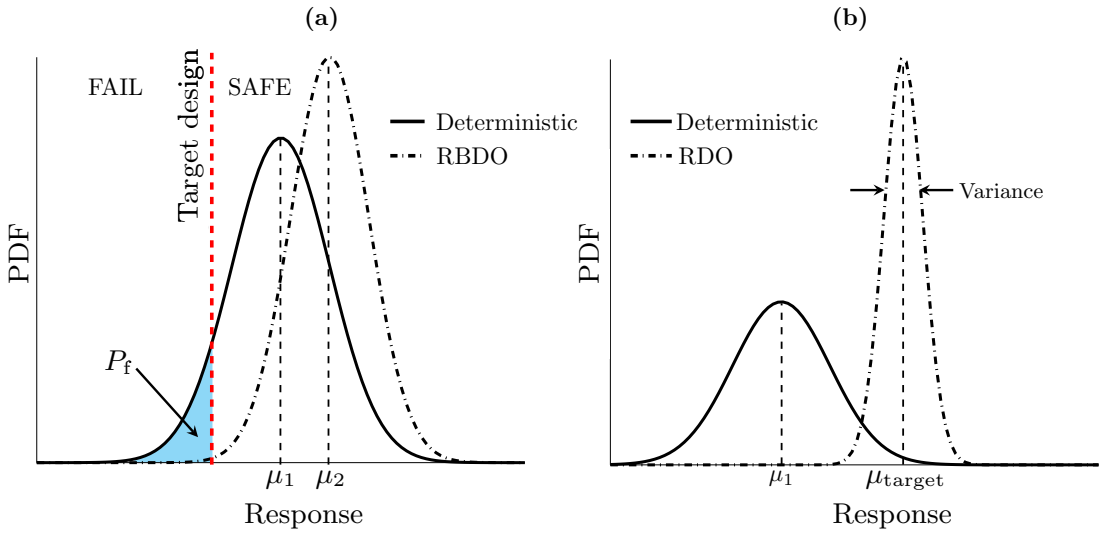

Figure 2.12: Uncertainty-based design optimisation (a) Reliability Based Design Optimisation (RBDO) approach (b) Robust Design Optimisation (RDO) approach for uncertainty-based design optimisation.

using a detailed finite element wing representation. The mixed RBDO and RDO approach is thought to be beneficial for aeroelastic tailoring of composite wings for reliable, robust and efficient composite wing design.

2.7 Summary

The following key points can be drawn from the discussion in this chapter;

1. The unique anisotropic properties of composite materials allow for aeroelastic tailoring and innovative design solutions. However, current applications are limited to *'black metal'* design due to set requirements for manufacturing and certifications. Hence, there is a need for improved and new design approaches to ensure all these requirements can be satisfied at an early stage of the design process. Therefore, the engineer needs to reduce the associated cost of the design process and allow for more innovative design solutions for composite structures.

2. Design methods for composite structures can be classified into deterministic and probabilistic design approaches. Due to inherent variations in the model parameters, it is crucial to include uncertainty quantification in the design process.

3. The optimisation of composite structures can be performed using discrete or continuous design variables. The former approach treats individual ply angles as design variables, and the latter approach uses lamination parameters to represent the laminate properties. GA, PSO and ACO can be used for optimisation of composite structures. PSO offers better efficiency due to better interaction between the possible solution and capability to include previous best solution in current iteration step which is one of the major drawbacks in GAs. ACO is suitable for simple design problems due to discrete formulation in the optimisation algorithm.

4. The use of lamination parameters in optimisation problems minimise the number of design variables to at most 12 variables for each laminate panel assuming the thickness is known. Large composite structures usually consist of multiple laminate panels and a large number of plies in each panel. Hence, the use of lamination parameter in optimisation procedures simplifies the design problem and provides a more efficient solution compared to discrete design variable optimisation procedure.

5. The lamination parameters are not independent and related to one another by inequality relationships for both in-plane and out-of-plane terms. These inequality relationships are used to define the feasible region for design spaces and therefore simplify the design problems. Moreover, the use of lamination parameters can guarantee a global optimum for linear design problems which can be solved using standard optimisation tools such as the gradient method. However, additional optimisation steps may be required to obtain the actual stacking sequence to match the stiffness matrices.

6. Aeroelastic tailoring is a method of controlling the aeroelastic deformation, static or dynamic by incorporating directional stiffness into aircraft structures for better aerodynamic and structural performances. The main objective of aeroelastic tailoring is to minimise the structural weight whilst satisfying structural and aeroelastic design constraints that included aeroelastic stability and gust responses. The aeroelastic behaviour of composite structures are mainly influenced by the coupling parameter, K, bending stiffness parameter, EI and torsional stiffness parameter, GJ.

7. Optimisation in aeroelastic tailoring is mainly concerned on the aeroelastic modelling and optimisation techniques. Various models of aircraft wing have been used

in optimisation approaches with single or multiple design constraints. The optimised solution for simple model like cantilever wing model is useful to predict the aeroelastic behaviour of the structures, but the accuracy is questionable. The use of a detailed wing model representation such as a *'box-like'* wing model can provide a more accurate and realistic response which is crucial for design certification.

8. Uncertainty can be defined as a study of the effects of parameter variations on the model's performances. There are two types of uncertainty - epistemic and aleatory uncertainties. Parametric uncertainty is an aleatory type and can be in the forms of variation in the material properties, geometry variation of the model and stiffness properties variation. The uncertainty may arise from various sources in composite materials such as fibre misalignment, fibre waviness and thickness variation.

9. In reality, when dealing with composite structures, uncertainty may exist due to multiple sources. The current aeroelastic tailoring design approach did not directly consider uncertainty in the design process. The variation in model parameters can significantly reduce the aeroelastic performances and may perform very poorly. Therefore, a new design approach is required to directly consider these uncertainties in the design process for more realistic design which is insensitive to parameter variations.

10. There is number of tools available and suitable for uncertainty quantification. Monte Carlo Simulation (MCS) is the most common tool but require large computational resources in order to provide an accurate prediction. The surrogate model such as Polynomial Chaos Expansion (PCE) and High Dimensional Model Representation (HDMR) are the alternative tools for uncertainty quantification which require fewer number of simulation runs and produce accepted levels of accuracy. The use of surrogate model is beneficial for design analysis that involves finite element analysis on detailed model representation.

11. The uncertainty-based aeroelastic tailoring can be classified into two categories - robust and reliable design approaches. The robust design approach aims to optimise the system performance close to target mean value and minimise the variation in those performances, without eliminating the source of uncertainty. The reliable design approach seeks for optimal design whilst satisfying a reliability requirement defined by the reliability index or the probability of design failure.

12. Reliability-Based Design Optimisation (RBDO) and Robust Design Optimisation are the two main methods for probabilistic design optimisation. The combination of RBDO and RDO approach is thought to be beneficial for aeroelastic tailoring of the composite wing for reliable, robust and efficient composite wing design.

Chapter 3

Structural and Aeroelastic Modelling

3.1 Introduction

As outlined in the introduction to this thesis, in order to evaluate the potential benefits of aeroelastic tailoring with uncertainty quantification, a realistic aeroelastic model representation that incorporated the effect of aeroelastic tailoring is required. Therefore, a detailed structural model is needed that can accurately analyse the performance of composite wing structure subjected to multiple loads and design constraints as well as parameter variations in the model. When dealing with a detailed composite structural model, the design optimisation problem involves typically huge numbers of design variables, especially when working directly with the ply-angle design spaces. The use of lamination parameters to represent the composite stacking sequences of the composite structure provides a significant reduction in the number of design variables. The concept of optimisation using lamination parameters is introduced in this chapter. Posed as a multi-disciplinary design optimisation problem, the composite wing model is evaluated for structural and aeroelastic performance subjected to multiple load cases. The aim for this chapter is to provide the outline of the approach undertaken for structural and aeroelastic analysis on a detailed finite element model of composite aircraft wing structures.

3.2 Modelling Approach

In general, the main objective of aeroelastic tailoring is to optimise the composite wing structure for minimum weight without compromising the structural and aeroelastic performances of the structure. To achieve this, an efficient optimisation approach is required as well as detailed representation of the wing structural model in order to accurately quantify the performance of the wing due to composite tailoring.

Earlier work [10–12, 21, 23, 105, 111] on aeroelastic tailoring of composite wing structures have been performed on a cantilever composite plate wing to quantify the aeroelastic performance of the wing. More recent work [11, 14, 117, 174, 175] on aeroelastic tailoring of composite wing structures utilised a wing box model which allows for quantification of both aeroelastic and structural performances of the wing.

The aircraft structural design process involves multi-disciplinary studies that included linear statics, buckling, dynamic aeroelasticity as well as manufacturing and certification requirements. All these studies require the use of details wing model which can provide more accurate prediction on the aircraft performances. Furthermore, the effect of uncertainty on the actual performance of the wing is not fully understood and hence, the use of details wing model can provide more insight on the matter.

The modelling approach implemented in the current work is summarised in Figure 3.1. The modelling work and the analysis are performed using MSc. Patran/Nastran with the use of MATLAB as the model compiler. The lamination parameters are used to define the composite laminate properties of different sections of the wing. The stiffness matrix (A, B and D matrices) are calculated based on the laminate properties and are input directly into the FE model. The wing structures are evaluated for their structural and aeroelastic performance, including strength, buckling, aeroelastic instability and gust analysis. The wing's performances are quantified in terms of the weight and structural responses as well as aeroelastic characteristics due to different static manoeuvre load cases.

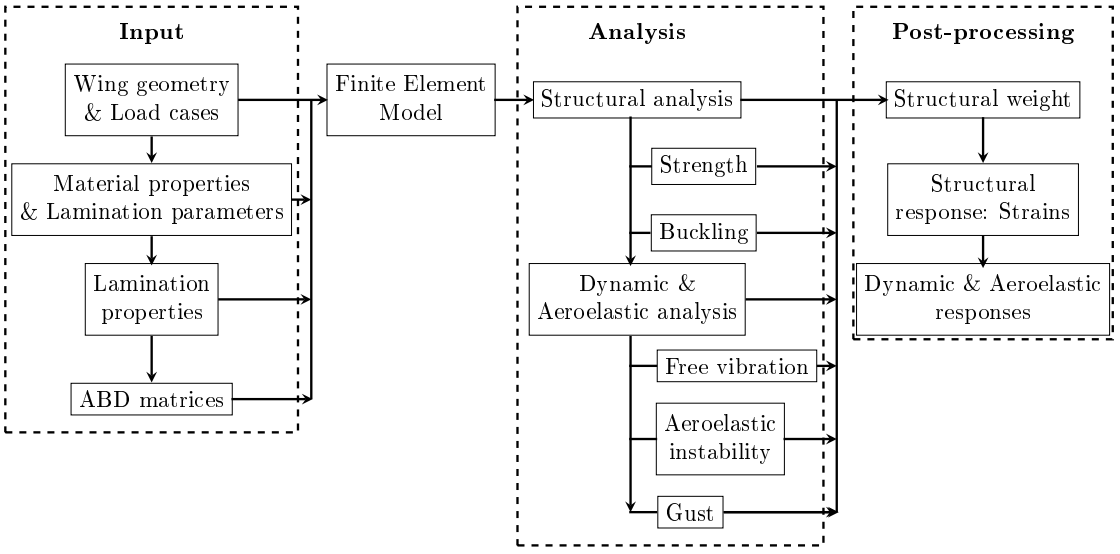

Figure 3.1: Modelling approach for aeroelastic tailoring of composite wing box.

3.2.1 Composite Wing Model Description

An idealised *'box-like'* FE model representation of a high-aspect-ratio wing box model of a reference regional jet aircraft with a single-aisle 120-seats configuration is used as the benchmark model for the analysis as shown in Figure 3.2. The technical details of the similar type of aircraft [176, 177] are presented in Table 3.1 for reference. The benchmark model is referred to as the Embraer Benchmark Wing (EBW) throughout this dissertation.

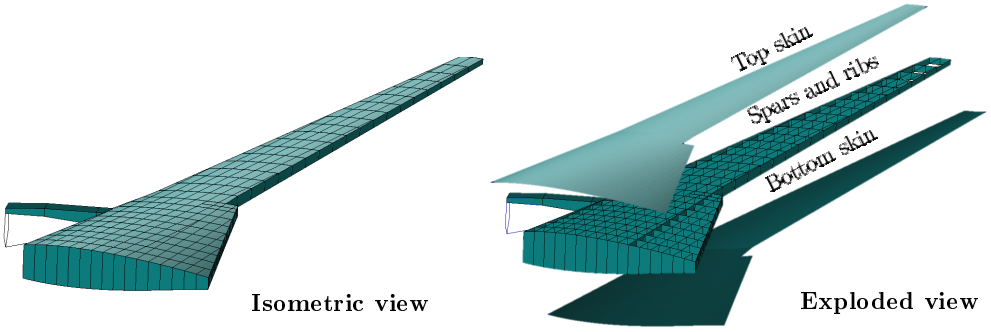

Figure 3.2: Finite element model of the composite wing.

Table 3.1: Technical data for similar type of reference aircraft.

Descriptions	Values
Wing span (m)	28.7
Fuselage length (m)	38.6
Maximum take-off weight (kg)	52 290
Maximum payload (kg)	13 917
Maximum design cruise speed (km/h)	890
Design cruise Mach	0.82
Service ceiling (m)	11 900
Design mission range (nm)	2300

The use of box-like fixtures allows for overall stiffness modelling and hence provides a simplified but detailed representation of the wing structure. The planform and the wing box geometry of the benchmark model are depicted in Figure 3.4 with the dimensions normalised due to confidentiality sensitivity of the data. The FE model of the wing structure was created using MSc. Patran 2013 package. The primary structure of the wing including the skins, spars and the ribs is modelled using `CQUAD4` shell elements, with the stringers along the wingspan created using `CBAR` beam elements. The wing's ribs and stringers elements are depicted in Figure 3.3. Other components of the wing structure such as the engine, pylon and fuel mass are modelled as concentrated masses in the

model. The fuel mass is distributed spanwise along the tank centroid line and modelled using nodal mass points positioned between each spar-rib bay as shown in Figure 3.4. A structural model consists of 25471 elements and 16453 nodes is used to represent the benchmark model.

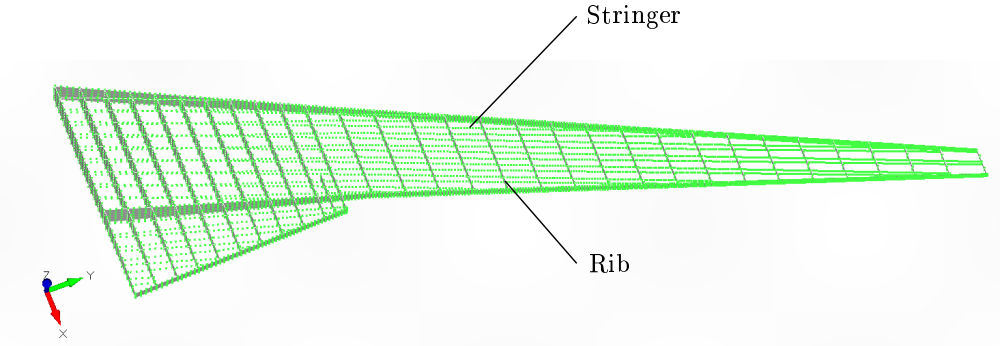

Figure 3.3: The wing's ribs and stringers element of EBW.

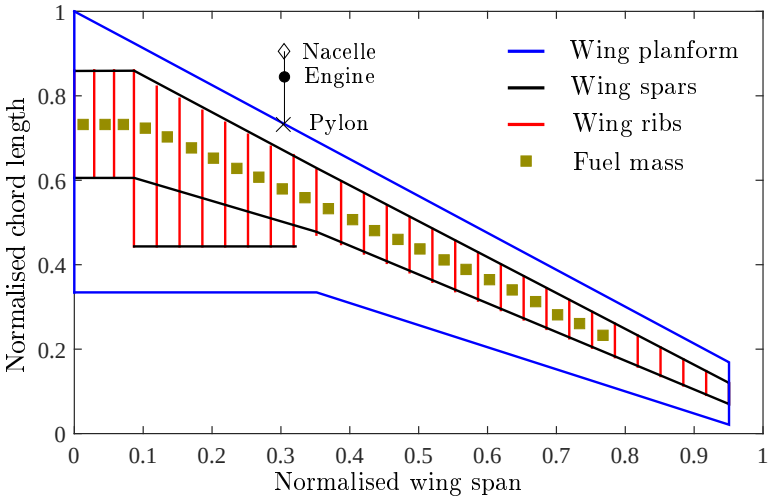

Figure 3.4: Normalised wing geometry of the EBW model with the fuels, pylon, engine and nacelle modelled as concentrated masses.

In the dynamic and aeroelastic analyses, the aerodynamics is modelled using the Doublet-Lattice method (DLM) to represent the lifting surface in the subsonic flow. For the aerodynamic panelling, higher density mesh is used at locations close to the planform edges and regions where significant pressure difference and discontinuous down-wash might occur [14]. In this work, the aerodynamic panels of the wing are divided into two sections - inner wing and outer wing panels as shown in Figure 3.5. The inner wing and outer wing sections consist of 45 and 90 small panels, respectively.

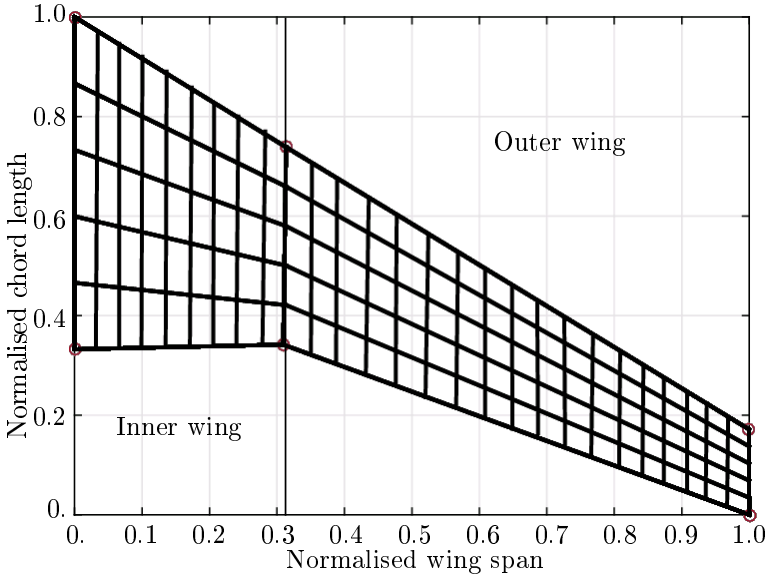

Figure 3.5: The DLM aerodynamic panel (Inner wing and outer wing) for EBW model.

3.3 Aeroelastic Tailoring Modelling

As introduced in Section 2.4.2 (page 25), the aeroelastic tailoring process involves the inclusion of directional stiffness into the structure via passive or active tailoring. The passive tailoring is achieved through structural or material tailoring which then changes the static and dynamic performance of the wing beneficially. For composite wing structures, the aeroelastic tailoring is typically performed via material property tailoring. Due to the anisotropic properties of composite material, the desired directional stiffness can be imparted into the structures by altering the composite laminate properties.

The conventional design approach for composite materials in industrial applications looks typically at a laminate level, where several plies of unidirectional or woven fibres embedded polymer matrix are stacked together in a stacking sequence for desired stiffness properties. Due to the complexity and scale of the aircraft wing structure, it is inefficient to treat the design problem on a ply-level basis which results in a significantly large number of design variables. Conversely, the use of lamination parameters to represent the stacking sequence of the composite lay-up simplifies the design problems which offer a very efficient approach for composite design optimisation. For example, the optimisation of a laminate panel requires only twelve design variables (maximum) given that

the laminate's thickness is known. This section provides an overview of the lamination parameters concept [70] and their application to aeroelastic tailoring.

3.3.1 Concept of Lamination Parameters

The concept of lamination parameters was initially introduced by Tsai *et al.* [70] and Tsai & Hahn [33] where the stacking sequence of any composite laminates can be represented using 12 lamination parameters and laminate thickness. These parameters can be treated as continuous design variables as opposed to individual discrete ply-angle design spaces which lead to efficient gradient-based optimisation. The lamination parameters are formulated based on the constitutive relations of the laminate derived from Classical Laminate Theory (CLT). The derivation of the composite stiffness properties based on CLT given in Appendix A which are also very well documented in many composite design textbooks [34, 178].

From CLT, the constitutive relations of the laminate are given as

$$\begin{Bmatrix} N \\ M \end{Bmatrix} = \begin{bmatrix} A & B \\ B & D \end{bmatrix} \begin{Bmatrix} \mathcal{E} \\ \kappa \end{Bmatrix}, \tag{3.1}$$

where

- $[A]$ is the in-plane stiffness matrix that relate the in-plane forces, $[N]$ to the in-plane deformations, $[\mathcal{E}]$.
- $[D]$ is the bending stiffness matrix that relate the moments, $[M]$ to the curvatures, $[\kappa]$.
- $[B]$ is the in-plane-out-of-plane coupling stiffness matrix that relate the in-plane forces, $[N]$ to the curvatures, $[\kappa]$ and the moments, $[M]$ to the in-plane deformations, $[\mathcal{E}]$.

The in-plane stiffness is important for the structure to resist the in-plane deformation such as extension and shear. The bending stiffness or the out-of-plane stiffness is important for the structure to resist the out of plane bending moments caused by out of plane forces.

The stiffness matrix components, A_{ij}, B_{ij} and D_{ij} can be represent using the invariant properties, $\{U\}$ and the lamination parameters (ξ_k^A,ξ_k^B and ξ_k^D, where $k = 1, 2, 3, 4$) in accordance with the following

$$\begin{Bmatrix} A_{11} \\ A_{12} \\ A_{22} \\ A_{66} \\ A_{16} \\ A_{26} \end{Bmatrix} = t \begin{bmatrix} 1 & \xi_1^A & \xi_2^A & 0 & 0 \\ 0 & 0 & -\xi_2^A & 1 & 0 \\ 1 & -\xi_1^A & \xi_2^A & 0 & 0 \\ 0 & 0 & -\xi_2^A & 0 & 1 \\ 0 & \frac{\xi_3^A}{2} & \xi_4^A & 0 & 0 \\ 0 & \frac{\xi_3^A}{2} & -\xi_4^A & 0 & 0 \end{bmatrix} \begin{Bmatrix} U_1 \\ U_2 \\ U_3 \\ U_4 \\ U_5 \end{Bmatrix}, \tag{3.2}$$

$$\begin{Bmatrix} B_{11} \\ B_{12} \\ B_{22} \\ B_{66} \\ B_{16} \\ B_{26} \end{Bmatrix} = \frac{t^2}{4} \begin{bmatrix} 0 & \xi_1^B & \xi_2^B & 0 & 0 \\ 0 & 0 & -\xi_2^B & 0 & 0 \\ 0 & -\xi_1^B & \xi_2^B & 0 & 0 \\ 0 & 0 & -\xi_2^B & 0 & 0 \\ 0 & \frac{\xi_3^B}{2} & \xi_4^B & 0 & 0 \\ 0 & \frac{\xi_3^B}{2} & -\xi_4^B & 0 & 0 \end{bmatrix} \begin{Bmatrix} U_1 \\ U_2 \\ U_3 \\ U_4 \\ U_5 \end{Bmatrix}, \tag{3.3}$$

and

$$\begin{Bmatrix} D_{11} \\ D_{12} \\ D_{22} \\ D_{66} \\ D_{16} \\ D_{26} \end{Bmatrix} = \frac{t^3}{12} \begin{bmatrix} 1 & \xi_1^D & \xi_2^D & 0 & 0 \\ 0 & 0 & -\xi_2^D & 1 & 0 \\ 1 & -\xi_1^D & \xi_2^D & 0 & 0 \\ 0 & 0 & -\xi_2^D & 0 & 1 \\ 0 & \frac{\xi_3^D}{2} & \xi_4^D & 0 & 0 \\ 0 & \frac{\xi_3^D}{2} & -\xi_4^D & 0 & 0 \end{bmatrix} \begin{Bmatrix} U_1 \\ U_2 \\ U_3 \\ U_4 \\ U_5 \end{Bmatrix}, \tag{3.4}$$

where t is the laminate thickness. The invariant properties, U were introduced by Tsai & Pagano [70] to represent the reduced stiffness terms in transformation equation (see Eqn. (A.9) in Appendix A). The invariant properties of the laminate can be determined from the properties of the lamina constituents irrespective of the lamina orientation. The invariant properties are given by

$$
\begin{aligned}
U_1 &= \frac{1}{8}(3Q_{11} + 3Q_{22} + 2Q_{12} + 4Q_{66}),\\
U_2 &= \frac{1}{2}(Q_{11} - Q_{22}),\\
U_3 &= \frac{1}{8}(Q_{11} + Q_{22} - 2Q_{12} - 4Q_{66}),\\
U_4 &= \frac{1}{8}(Q_{11} + Q_{22} + 6Q_{12} - 4Q_{66}),\\
U_5 &= \frac{1}{8}(Q_{11} + Q_{22} - 2Q_{12} + 4Q_{66}).
\end{aligned} \tag{3.5}
$$

Subsequently, the transformed stiffness properties, $\bar{Q}_{ij}$ of can be put into a more straightforward form using trigonometric identities and material invariant properties, U as

$$
\begin{aligned}
\bar{Q}_{11} &= U_1 + U_2\ \cos\ 2\theta + U_3\ \cos\ 4\theta,\\
\bar{Q}_{12} &= U_4 - U_3\ \cos\ 4\theta,\\
\bar{Q}_{22} &= U_1 - U_2\ \cos\ 2\theta + U_3\ \cos\ 4\theta,\\
\bar{Q}_{16} &= \frac{1}{2}U_2\ \sin\ 2\theta + U_3\ \sin\ 4\theta,\\
\bar{Q}_{26} &= \frac{1}{2}U_2 \sin 2\theta - U_3 \sin 4\theta,\\
\bar{Q}_{66} &= U_5 - U_3\ \cos\ 4\theta.
\end{aligned} \tag{3.6}
$$

The lamination parameters given in Eqns. (3.2) to (3.4) can be expressed in terms of ply orientation, θ as [37]

$$
\xi^{A}_{[1,2,3,4]} = \frac{1}{2}\int_{-1}^{1}[\cos 2\theta(u)\ \cos 4\theta(u)\ \sin 2\theta(u)\ \sin 4\theta(u)]du, \tag{3.7}
$$

$$
\xi^{B}_{[1,2,3,4]} = \int_{-1}^{1}[\cos 2\theta(u)\ \cos 4\theta(u)\ \sin 2\theta(u)\ \sin 4\theta(u)]udu, \tag{3.8}
$$

$$
\xi^{D}_{[1,2,3,4]} = \frac{3}{2}\int_{-1}^{1}[\cos 2\theta(u)\ \cos 4\theta(u)\ \sin 2\theta(u)\ \sin 4\theta(u)]u^2du, \tag{3.9}
$$

where $u(=\frac{2z}{t})$ is the non-dimensional through-the-thickness coordinate.

The conventional approach in the design and optimisation of composite laminates panel restricts the laminate design space to consider only balanced and symmetric lay-ups, ensuring manufacturing feasibility. One of the reason is to eliminate the warping effect due to cooling from the curing temperature. Therefore, the coupling lamination parameters,

$\xi^B_{[1,2,3,4]}$ (Eqn. (3.8)) are zero, which further reduce the number of lamination parameters to eight. Besides, the lamination parameters are not independent, and there exists an inequalities relationship that defines the feasible region of the parameters. The detailed formulation of the relationship for feasible regions of the lamination parameters can be found in Refs. [37, 71, 72, 75]. The work presented in this dissertation uses the inequality relationships derived by Fukunaga & Sekine [72], which describe the feasible regions of the four in-plane and out-of-plane lamination parameters. These are

$$\begin{aligned} -1 \leq \xi^j_k \leq 1, \\ (\xi^j_1)^2 + (\xi^j_3)^2 \leq 1, \\ 2(1+\xi^j_2)(\xi^j_3)^2 - 4\xi^j_1\xi^j_3\xi^j_4 + (\xi^j_4)^2 - (\xi^j_2 - 2(\xi^j_1)^2 + 1)(1-\xi^j_2) \leq 0, \end{aligned} \tag{3.10}$$

where $k = 1, 2, 3, 4$ and $j = A, D$.

The use of lamination parameters as design variables in optimisation problems of composite laminates provide several advantages over using discrete ply angle variables. First of all, lamination parameters are continuous variables allowing efficient gradient-based optimisers to be used. Also, regardless of the number of plies in any composite laminate, the number of lamination parameters required to define the laminate properties is fixed to 12. Whereas, in ply angles design space, the number of design variables increases proportionally with the number of plies. Secondly, lamination parameters are convex and the objective functions to be optimised are concave functions [73]. Therefore, local optima can be avoided, and only a global solution exists.

However, an additional post-processing step is required to obtain the corresponding stacking sequence for a set of lamination parameters. The stacking sequence that exactly matches the lamination parameter values can only be guaranteed in the case of an infinite number of plies and pre-defined set of ply angles.

3.3.2 Aeroelastic Tailoring using Lamination Parameters

The use of lamination parameters to define the laminate properties on wing structures greatly reduces the number of design variables for an optimisation procedure in aeroelastic tailoring. In the current work, only the top skin, bottom skin and the spar section are optimised to obtain an aeroelastically tailored design. The top and bottom skin

panels are divided into 11 small panels, each having their laminate properties definition. Similarly, the three spar sections are also divided into eight small panels for Spar 1 and Spar 2 and three panels for Spar 3 section as shown in Figure 3.6.

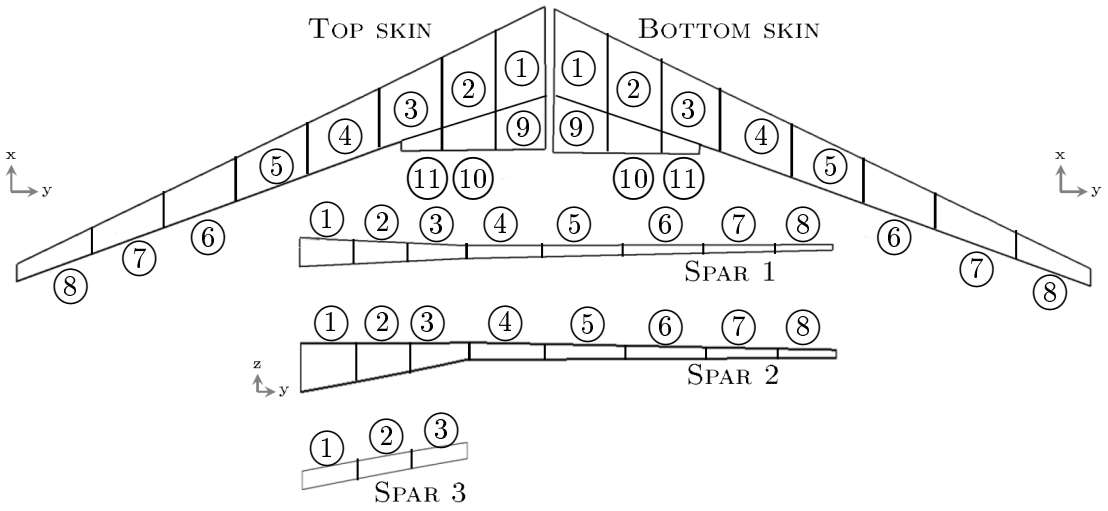

Figure 3.6: Panel partition for skins and spars panel of the wing model.

For each panel, there is maximum of 12 lamination parameters and a laminate thickness value that give a total of 13 design variables assigned to each panel. The current practice in industry restricts the design space to only balanced and symmetric lay-ups, enabling feasible manufacture. Non-symmetric laminates may result in excessive warping upon cooling down from the curing temperature and shear-extension coupling for unbalanced laminates. Due to the balanced and symmetric laminate limitations, the number of lamination parameters for each panel further reduces to six as there is no in-plane-out-of-plane coupling, $[B]$ is zero and the shear-extension coupling stiffness terms, A_{16} and A_{26} are zero.

However, it is known that for unbalanced symmetrical laminates, a bending moment causes wing surface curvature and twisting which then results in wash-out and wash-in deformations [2]. The existence of A_{16} and A_{26} terms results in shearing deformations caused by the in-plane normal stress resultants, N_x and N_y [178]. Similarly, the bending-twisting coupling terms, D_{16} and D_{26} result in surface curvature under applied uniform bending moments. Thus, enforcing a balanced condition limits the full possibility of exploring the potential benefits of aeroelastic tailoring for composite wing structures. In order to take advantage of stiffness tailoring using composite laminates, unbalanced and symmetric laminates are considered in this work which enable us to investigate the

coupling parameters (extension-shear and bending-twist couplng) influence on the wing performance. This approach results in a total of nine design variables for each panel - eight lamination parameters ($\xi^{A}_{1,2,3,4}$ and $\xi^{D}_{1,2,3,4}$) and a laminate thickness value, which gives a cumulative total of 369 design variables for the EBW model.

For the benchmark EBW model, the skin, spars and ribs are modelled as shell elements where the membrane and plate properties (A and D matrices) are specified directly. This allows us to employ lamination parameters in the optimisation procedure. The skin, spars and rib panels are modelled using quasi-isotropic laminate with different thickness values. The layup properties are given in Table 3.2. The panel's thickness variation across the normalised wing-span for the skins and spars of the EBW model are plotted in Figure 3.7. The stringers are also made of composites and modelled as beam elements. Since MSc. Nastran does not support composite beam properties, these are modelled with an equivalent isotropic material. The composite panels are made of intermediate modulus carbon/epoxy composite (Hexcel 8552 IM7) [179] and the properties are summarised in Table 3.3.

Table 3.2: Layup properties for skin and spars panels of the EBW model.

Layup (°)	Angle Percentages (%)			Type
	0	45	90	
$[45/0/\text{-}45/90/45/0/\text{-}45/90]_S$	24%	50%	25%	Quasi-isotropic

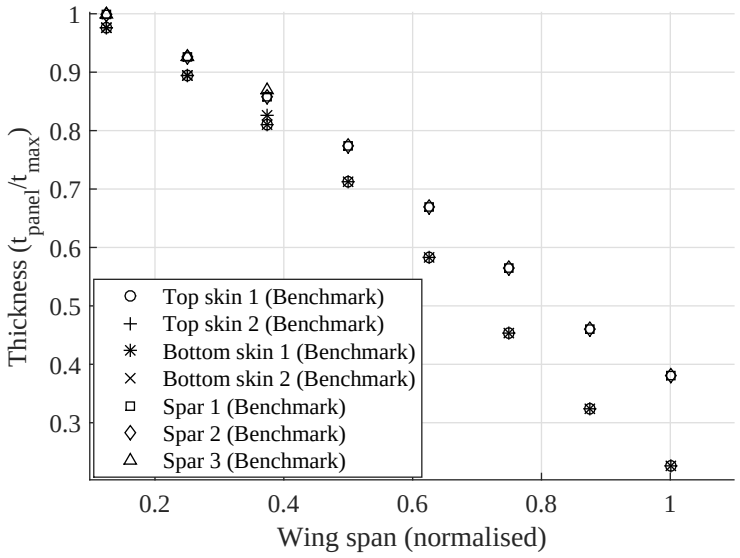

Figure 3.7: Thickness variation for the top and bottom skins and spar sections of the EBW model.

Table 3.3: Material properties of Hexcel 8552 IM7 (Marlett, 2011).

Property	Values
E_1 (GPa)	148.0
E_2 (GPa)	10.3
G_{12} (GPa)	5.90
υ_{12}	0.27
Longitudinal tensile strength (MPa)	2439
Longitudinal compressive strength (MPa)	2013
Transverse tensile strength (MPa)	66
Transverse compressive strength (MPa)	381
Shear strength (MPa)	78
Density, ρ (kgm^{-3})	1580
Ply thickness, t_{ply} (mm)	0.183

In this work, aeroelastic tailoring is performed on the EBW model subjected to multiple load cases and multiple constraints, including aeroelastic and structural constraints. This study is performed using an optimisation procedure to obtain optimal structural and aeroelastic performance whilst minimising the wing structural weight. The optimal design solution is referred to as a deterministic design solution.

The following section presents the structural and aeroelastic analyses performed on the EBW wing which will be used later for comparison with a deterministic aeroelastic tailored wing design.

3.4 Aeroelastic and Structural Analyses

In general, the work presented in this thesis investigated the aeroelastic and structural performances of a composite aircraft wing due to composite tailoring and quantification of uncertainty in the model. Therefore, the optimisation strategy involves deterministic and probabilistic approaches to establish the effect of uncertainty in the design process of composite structures.

The aeroelastic and structural analyses of the EBW model are performed using MSc. Nastran. In the aeroelastic analyses, the free vibration, flutter and gust analysis (dynamic response) is performed with different load cases using `SOL 103` (Normal Mode Analysis), `SOL 145` (Flutter Analysis) and `SOL 146` (Dynamic Aeroelastic Response Analysis), respectively. The structural analyses are performed to quantify the strength and buckling behaviour of the EBW wing subjected to different load cases as summarised in Table 3.4. The static load distributions on the wing structure are obtained from a trim

analysis (`SOL 144`: Static Aeroelastic Response) that included inertial, applied and aerodynamic loads from trim conditions. The load cases are chosen based on the different flight conditions provided by the industrial partner. The load cases with higher load factor ($n_z = 2.50$) were added to evaluate the wing performance under extreme manoeuvre conditions such as a turning manoeuvre.

Table 3.4: Static manoeuvre load cases for the structural analysis.

Static Maneuver Load Cases						
Load ID.	Mass	Mach No.	Altitude, H (m)	EAS (ms^{-1})	Dynamic pressure, P_D (Pa)	n_z (g)
1	Fuel	0.82	10000	146	13038	2.50
2	Fuel	0.88	11887	132	10656	1.88
3	Fuel	0.50	3048	142	12385	2.50
4	Empty	0.82	11887	123	9267	-1.00
5	Empty	0.58	3048	162	16074	-1.00

3.4.1 Boundary conditions

The boundary conditions are applied at a single control node (Node 16453) which is connected to the root section by rigid elements (`RBE2`), as shown in Figure 3.8. The model's global translatory and rotational degrees of freedom (DOF) can be controlled by restricting the DOFs of this single node. Two boundary conditions are implemented on EBW model:

- Active pitch/plunge boundary condition.
  These boundary condition allowing the wing to have pitch and plunge motion by restricting all DOFs except translation in the z-direction (along wing's thickness direction) and rotation in y-direction (along wingspan).
- Fully clamped, where all DOFs are constrained.

The active pitch/plunge boundary condition is used only for manoeuvre loads calculation (static aeroelastic analysis). The fully clamped boundary condition is used for all strain/buckling and flutter/gust analysis. An additional `SUPORT` boundary condition is specified in the model to provide a frame of reference for the rigid-body shape calculations.

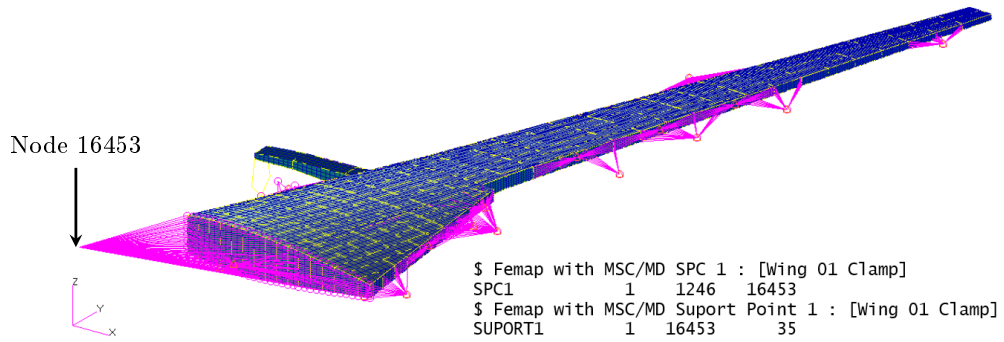

Figure 3.8: The boundary conditions applied on EBW model for aeroelastic analysis. The `SUPORT1` boundary condition is used for the rigid-body shape calculations.

3.4.2 Static Aeroelastic Analysis

The static aeroelastic study concerns the deflection of flexible aircraft structures under aerodynamic loads, where the force and the motion are independent of time. In order to model the static aeroelastic behaviour of the wing structure, it is essential to consider the interaction of the wing structural deflections and the aerodynamic loads which causes the wing bending and twisting at particular flight conditions [1], For example, changing the incidence angle causes the redistribution of the aerodynamic loads and the consequent deflections.

The analysis of static aeroelastic in the current work involves the calculation of the static response, including loads and stresses in the structures at different flight conditions which is necessary for wing structural design. In this section, the basic theories underlying static aeroelastic is presented. The fundamentals for aerodynamic modelling (Doublet Lattice Method (DLM) and geometry interpolation) are briefly explained in Appendix B.1.

In the DLM, the lifting surfaces of the wing model is divided into small trapezoidal panels or *'boxes'* in a manner such that the boxes are arranged in columns (strips) parallel to the flow as shown in Figure 3.9. The aerodynamic panel and the structural geometry are coupled using the surface spline method explained in Appendix B.2.

The static aeroelastic analysis is modelled in MSc. Nastran with `SOL 144`. The aerodynamic pressure and force at n aerodynamic grid points are obtained by specifying `APRES` and `AEROF` in the subcase command. The fight conditions are specified using `TRIM` Bulk Data entries. The trim parameters such as the angle of attack, α and normal acceleration, $\dot{z}$ are defined using `AESTAT` entries. The flight condition Mach number and

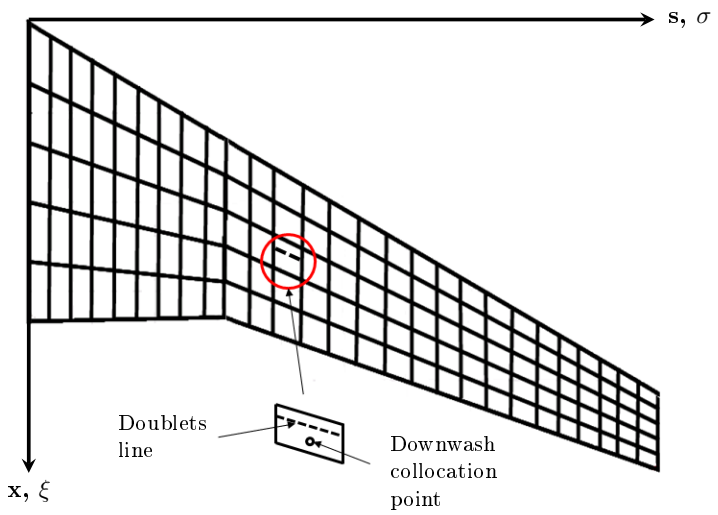

Figure 3.9: Aerodynamic box panels used for the static aeroelastic analysis and location of the doublets and downwash collocation points for DLM.

the dynamic pressure are defined along with the trim parameters in `TRIM` entry. The output forces at the structural grid points are requested by specifying `TRIMF` in subcase command which provides the inertial, applied and the aerodynamic load output at the structural grid points.

Figures 3.10 shows the sectional pressure coefficient (ΔC_p) of the EBW model evaluated for different load cases as given in Table 3.4. The trim analysis was performed with an angle of attack, α of 5 degrees. The chord-wise pressure coefficient evaluated at 25% and 75% aerodynamic panel are plotted in Figure 3.10(a) and (b). From the figure, the resulting pressure difference decreases from the tip to root section of the wing. The pressure coefficient is evaluated at the $\frac{1}{4}$-chord line of each aerodynamic box. The variation of the aerodynamic pressure for different load cases can be observed from the plots. The highest pressure distribution is obtained from load case 5 with the maximum (ΔC_p) is obtained at 75% of the aerodynamic semi-span.

The normalised semi-span lift distributions in terms of local lift coefficient, C_{LL}, chord, c and mean average chord length, mac, $(C_{LL}(c/mac))$ are evaluated using the sectional pressure coefficient distributions and plotted in Figure 3.11. Note that the lift distribution for all load cases is lower at the root section. This is taught due to initial aerodynamic twist and camber data which is not defined in the model. The initial aerodynamic twist and camber can be input in the model as `DMI` entries with user-supplied data of the twist and camber for each aerodynamic panel box.

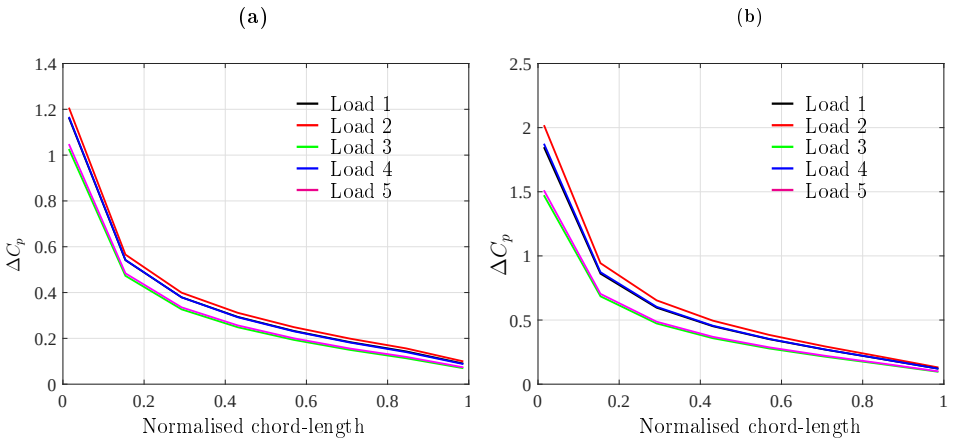

Figure 3.10: Pressure distributions of the EBW at (a) 25% aerodynamic semi-span location (b) 75% aerodynamic semi-span location for different load cases.

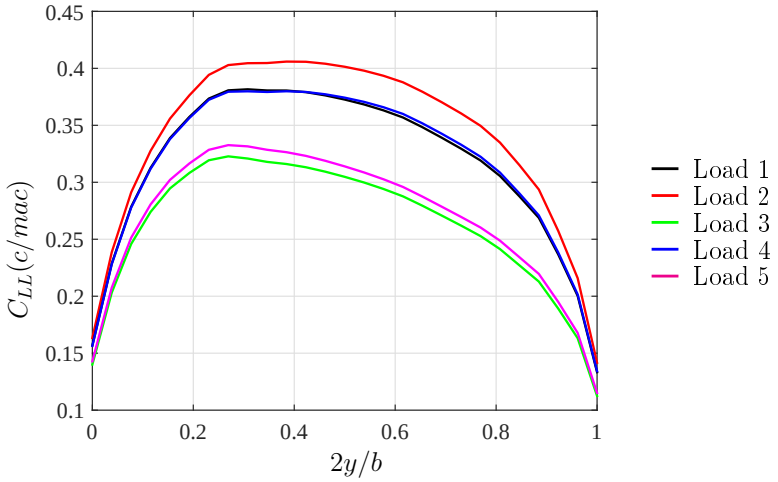

Figure 3.11: Lift distributions obtained from trim analysis of EBW model for different load cases.

In this work, the contribution of the aeroelastic tailoring on the aerodynamic performance of the EBW is not considered, although it is likely that aeroelastic tailoring may provide better aerodynamic performance and maybe the subject for further consideration in future work. However, the resulting load distributions obtained from the trim analysis at different flight conditions are used for structural analysis (i.e. buckling and strength analysis). Examples of the load distributions (nodal forces) at the structural grid points obtained from the trim analysis are shown in Figure 3.12, in this case for load case 1.

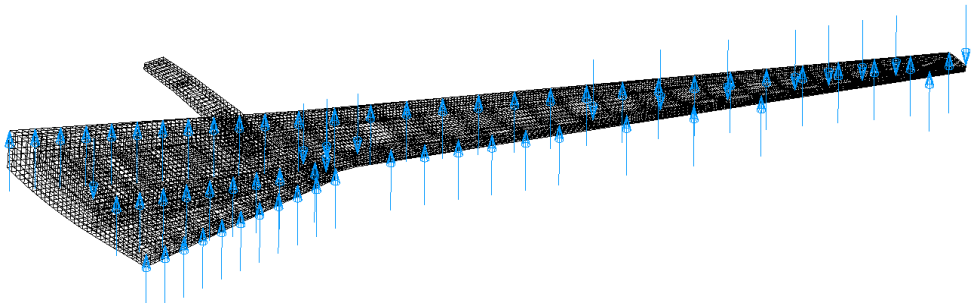

Figure 3.12: Load distributions at structural grid points acquired from trim analysis for load case 1.

3.4.3 Free Vibration Analysis

All parts on an aircraft have a distinctive vibration signature due to the mass distribution and structural stiffness resulting from the vibration modes of the entire structure. Typically, very low-level sources of vibration occur from the normal airflow over the aircraft surface and are regarded as background noise. The vibration resulting from the reaction of the aircraft to turbulence or gusts usually is of a much greater magnitude and is visible. The vibration study of critical components on the aircraft such as the wing structure is crucial in order to assess different vibration modes at specific excitation frequencies as well as the interaction between different vibration modes that might result in catastrophic failure of the structure, for example in the case of aeroelastic instability (i.e. flutter or divergence). The aircraft wing may be considered as an elastic continuum member which can bend and twist [1]. Therefore, the vibration analysis of an aircraft wing is treated as a continuous system which requires a near-infinite number of modes to define them spatially. In practice, only a finite number of modes are of interest. The modelling of a continuous system can be performed using several methods namely; exact approach, approximate approach using the Finite Element method and the approximate approach using assumed mode shapes (Rayleigh-Ritz method) [1, 94, 180].

In the exact approach, the exact mode shapes and natural frequencies are determined by solving the partial differential equation and is applicable for systems with simple geometries such as slender members under bending and torsion. The Rayleigh-Ritz approach uses a series of assumed shapes to represent the continuous systems with simple geometry such as uniform cantilever wings. The method allows systems to be modelled using a small number of generalised equations of parametric variables.

The finite element method allows modelling of continuous systems for more complex system in which the system is sub-divided into the number of elements and joined together at a node point. In this work, the free vibration analysis of EBW model was performed using the finite element method. The stiffness and the mass matrices of each element are evaluated and assembled into global matrices for evaluation (i.e. normal mode solution). In this section, the general formulation for free vibration analysis of a continuous system is introduced based on the finite element method.

3.4.3.1 Finite Element Method

In the Rayleigh-Ritz method, the displacement variation of the entire continuous system is determined using a finite series of known assumed deformation shapes [1]. In finite element method, a form of displacement variation is assumed for each element. As such, the finite element method is essentially a piece-wise Rayleigh-Ritz. The element mass and stiffness matrices are obtained using an energy approach and assembled to determine the overall structural mass and stiffness matrices. Consider a two-node uniform beam element with length, L, mass per unit length, μ and flexural rigidity, EI as shown in Figure 3.13, the nodal displacement are denoted as a vector, $\boldsymbol{d} = [d_1\, d_2\, d_3\, d_4]^T$. In this case, an in-plane bending problem is considered. The transverse displacement, $z(y)$ can be expressed as a cubic polynomial in y such that

$$z = a_0 + a_1 y + a_2 y^2 + a_3 y^3, \tag{3.11}$$

where $a_0, ...a_3$ are the unknown coefficients that can be obtained such that the polynomial matches the nodal displacement at $y = 0$, L. Hence, Eqn. (3.11) can be rewritten as

$$z = N_1 d_1 + N_2 d_2 + N_3 d_3 + N_4 d_4 = \underline{\mathbf{N}}^{\mathbf{T}} \underline{\mathbf{d}}, \tag{3.12}$$

where $N_1, ...N_4$ are the shape functions.

The equation of motion for the beam element can be determined by employing Lagrange's equation with the nodal displacement, d representing the coordinates so that equilibrium is applied. The elastic potential energy for the element is given as

$$U = \frac{1}{2}\int_0^L EI\Big(\frac{\partial^2 z}{\partial y^2}\Big)^2 dy = \frac{1}{2}\int_0^L EI(\underline{\mathbf{d}}^{\mathbf{T}}\underline{\mathbf{N}}'')(\underline{\mathbf{N}}''^{\mathbf{T}}\underline{\mathbf{d}})dy. \tag{3.13}$$

Thus,

$$U = \frac{1}{2}\underline{\mathbf{d}}^{\mathbf{T}}\Big[\int_0^L EI(\underline{\mathbf{N}}''\underline{\mathbf{N}}''^{\mathbf{T}})dy\Big]\underline{\mathbf{d}}, \tag{3.14}$$

where $'' = \partial^2/\partial y^2$. The kinetic energy for element is

$$T = \frac{1}{2}\int_0^L \mu\dot{z}^2 dy = \frac{1}{2}\int_0^L \mu(\dot{\underline{\mathbf{d}}}^{\mathbf{T}}\underline{\mathbf{N}})(\underline{\mathbf{N}}^{\mathbf{T}}\dot{\underline{\mathbf{d}}})dy \tag{3.15}$$

Thus,

$$T = \frac{1}{2}\dot{\underline{\mathbf{d}}}^{\mathbf{T}}\Big[\int_0^L \mu(\underline{\mathbf{N}}\underline{\mathbf{N}}^{\mathbf{T}})dy\Big]\dot{\underline{\mathbf{d}}} \tag{3.16}$$

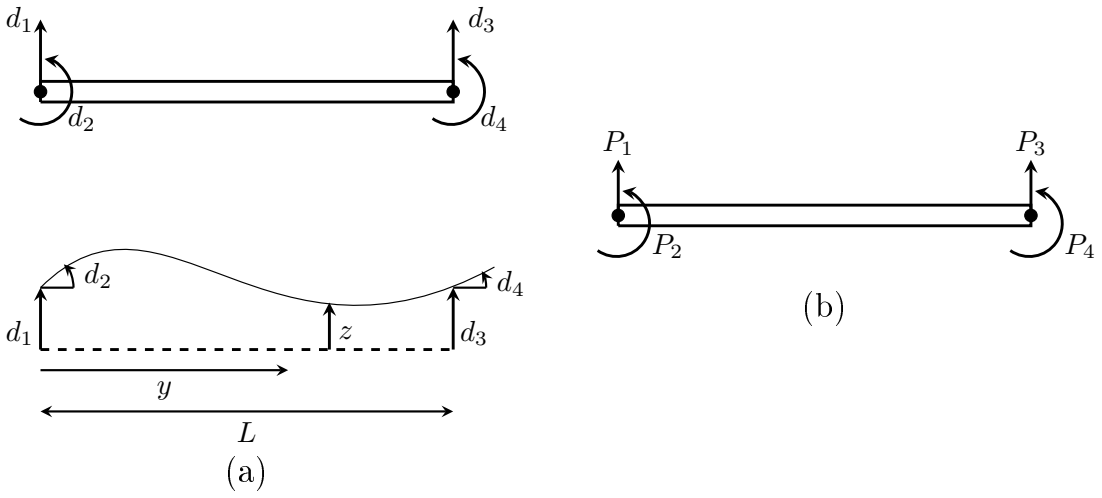

Figure 3.13: Beam element representation (a) Two-node beam bending element with nodal displacement defined (b) Nodal forces applied on two-node beam element.

The forces or moments may only be applied to the element at the nodes, as shown in Fig. 3.13(b) where $\mathbf{P} = [P_1\, P_2\, P_3\, P_4]^T$. Hence, the incremental work done by the applied load is given as

$$\delta W = P_1\delta d_1 + P_2\delta d_2 + P_3\delta d_3 + P_4\delta d_4 = \underline{\mathbf{P}}^{\mathbf{T}}\delta\underline{\mathbf{d}}. \tag{3.17}$$

By applying Lagrange's equation, the differential equation of motion for a two node beam element is given as

$$\mathbf{m}\ddot{\underline{\mathbf{d}}} + \mathbf{k}\underline{\mathbf{d}} = \underline{\mathbf{P}}, \tag{3.18}$$

where $\mathbf{m}$ and $\mathbf{k}$ are the element mass and stiffness matrices, respectively and are given as

$$\mathbf{m} = \Big[\int_0^L \mu(\underline{\mathbf{N}}\underline{\mathbf{N}}^{\mathbf{T}})dy\Big] \qquad \text{and} \qquad \mathbf{k} = \Big[\int_0^L EI(\underline{\mathbf{N}}''\underline{\mathbf{N}}''^{\mathbf{T}})dy\Big] \tag{3.19}$$

To obtain the global/structural matrices, an assembly process is required which involves element matrices *'mapping'* onto global matrices by means of the element topology. Thus, the global/structure equation of motion can be written as

$$\mathbf{M}\ddot{\underline{\mathbf{x}}} + \mathbf{K}\underline{\mathbf{x}} = \mathbf{f} \tag{3.20}$$

where $\mathbf{M}$, $\mathbf{K}$ are the structural mass and stiffness matrices, and $\mathbf{x}$, $\mathbf{f}$ are the structure/-global displacement and forces. By using the direct or eigenvalue approaches, the natural frequencies and the corresponding mode shapes can be obtained. In the former approach, the free vibration motion is given by

$$\boldsymbol{x}(t) = \boldsymbol{X}\sin\omega t, \tag{3.21}$$

where $\boldsymbol{X}$ and ω are the amplitude vector and free vibration frequency, respectively. By substituting Eqn. (3.21) into Eqn. (3.20), yields

$$[\boldsymbol{K} - \omega_j^2\boldsymbol{M}]\boldsymbol{X}_j = 0 \qquad \text{for} \qquad j = 1, 2, ..., N. \tag{3.22}$$

The solution can be obtained by setting the determinant of $|\boldsymbol{K} - \omega^2\boldsymbol{M}|$ to zero which gives an Nth-order polynomial in ω^2. Solving this polynomial yields roots ω_j which are the *'undamped natural frequencies'* of the system. In MSc. Nastran, normal mode analysis is available in `SOL 103` of the structured solution sequence. The eigenvalue approach is defined using `EIGR` or `EIGRL` Bulk Data entries. The Lanczos method is specified using `EIGRL` entry and all other method are speficied using `EIGR` entry. The computed eigenvectors from the Lanczos method are normalised using a `MASS` method where the eigenvectors are normalised to a unit value of the generalised mass.

The mode shapes of the EBW model obtained from the normal mode analysis in `SOL 103` are shown in Figure 3.14. A total of ten-mode shapes are evaluated in the analysis. The first seven mode shapes are shown with the corresponding frequency values. The first

and second bending modes are obtained from Mode 1, and Mode 2 and the first two torsion modes are acquired from Mode 3 and Mode 4.

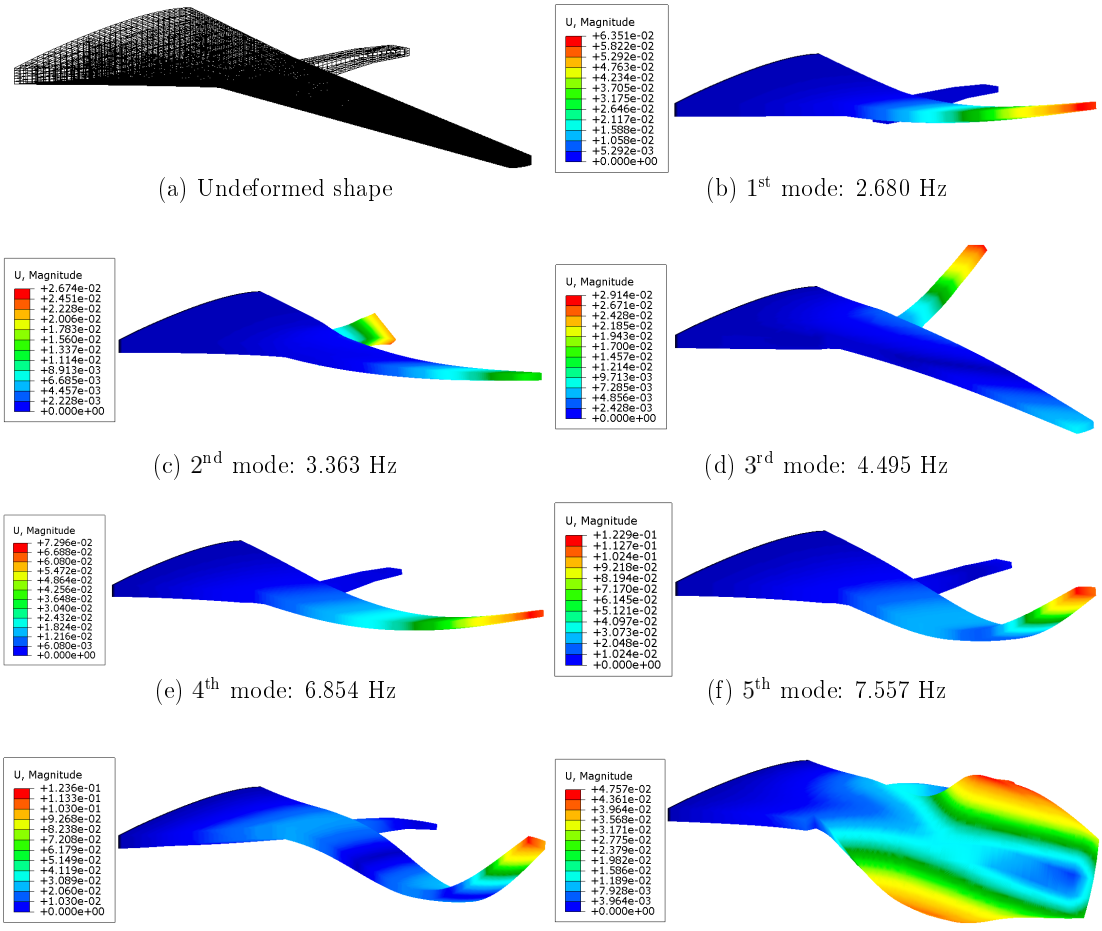

(a) Undeformed shape

(b) 1st mode: 2.680 Hz

(c) 2nd mode: 3.363 Hz

(d) 3rd mode: 4.495 Hz

(e) 4th mode: 6.854 Hz

(f) 5th mode: 7.557 Hz

(g) 6th mode: 12.946 Hz

(h) 7th mode: 15.591 Hz

Figure 3.14: The mode shapes of EBW model obtained from normal mode analysis (SOL. 103 MSC. NASTRAN) for (a) Undeformed (b) 1st bending (c) 2nd bending (d) 1st torsion (e) 2nd torsion (f) 3rd bending (g) 4th bending (h) 3rd torsion. The colour contours show the magnitude of deflection, U in metre.

3.4.4 Dynamic Aeroelasticity - Flutter Analysis

The aeroelastic stability analysis of the wing structure for flutter and divergence is crucial in the design process. Flutter is the most important phenomena that are undesirable and difficult to predict which often results in catastrophic structural failure. Flutter occurs when two or more vibration modes are coupled and cause unstable oscillation. The flutter speed is defined as the critical speed in which the structure sustains the oscillations caused by the initial disturbance. Below this speed, the structure is safe

from flutter in which the oscillations are adequately damped. Above this speed, the oscillations become negatively damped which lead to structural failure.

The aeroelastic stability evaluation is critical for aircraft certification requirement process (CS 25.629) that includes flutter and divergence. The validation of the flutter behaviour is required and must be designed, so the aircraft is free from aeroelastic instabilities over all configuration and design conditions [181]. Figure 3.15 shows the typical flutter envelope for large aircraft at different combinations of altitude and speed. The solid green line from the figure shows the boundary in which for all design configuration and flight condition, the critical flutter speed must be outside the envelope. From the aircraft certification requirement (CS 25.335), the dive speed, V_{D} and dive Mach number, M_{D} are determined such that $V_c/M_c \leq 0.8V_{\mathrm{D}}/M_{\mathrm{D}}$ where V_{c} and M_{c} are the cruising speed and Mach number. Based on the requirement, the critical flutter speed should be outside the flutter envelope such that $V_{\mathrm{D}} = 1.25V_{\mathrm{c}}$. In this work, an additional safety margin of 15% is enforced for flutter stability evaluation. Thus, the flutter speed, V_{f} obtained from all design configuration should be greater than $1.15V_{\mathrm{D}}$. In this case, the V_{D} gives the limit load, and V_{f} is the ultimate load. However, the work presented in the thesis concerns with the flutter behaviour of the wing rather than the static load case; thus, V_{f} is set as the flutter requirement.

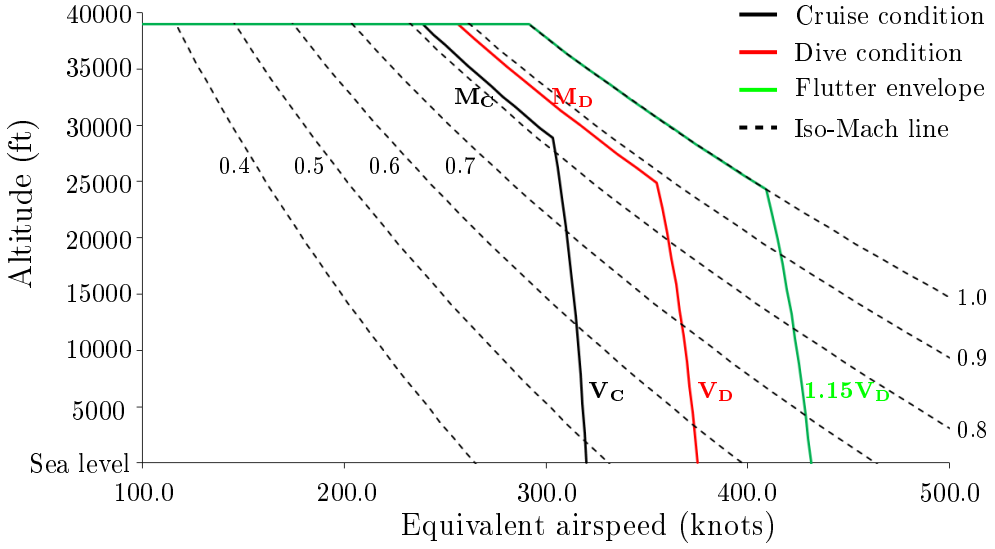

Figure 3.15: Typical flutter clearance envelope for aircraft structure certification at different flight altitude and Mach number.

Having properly defined the certification requirements for aeroelastic stability of the aircraft wing structure, it is beneficial at this stage to introduce the aeroelastic model

and flutter evaluation method employed in this work. In order to evaluate the flutter response, the analysis of the aerodynamic surface under dynamic motion using unsteady aerodynamics is required. The analysis evaluates the time or frequency effect on the lift and pitching moment of the aerodynamic surface. The equation of motion for the full aeroelastic model that included the aerodynamic forces and the structural equation is given in Eqn. (3.23). The derivation of the equation of motion is not presented here and can be found from published literature [1, 94].

$$\mathbf{A_m}\ddot{\boldsymbol{q}} + (\rho V \mathbf{B_m} + \mathbf{D_m})\dot{\boldsymbol{q}} + (\rho V^2 \mathbf{C} + \mathbf{E})\boldsymbol{q} = 0, \tag{3.23}$$

where $\mathbf{A_m}$, $\mathbf{B_m}$, $\mathbf{C}$, $\mathbf{D_m}$, $\mathbf{E}$ and $\boldsymbol{q}$ are the structural inertia, aerodynamic damping, aerodynamic stiffness, structural damping, structural stiffness matrices and generalised coordinates (modal coordinates), respectively. The flutter solution in terms of the frequencies and the damping ratios at a flight condition can be determined using an eigenvalue solution such that

$$\begin{bmatrix} \mathbf{I} & 0 \\ 0 & \mathbf{A_m} \end{bmatrix} \begin{Bmatrix} \dot{\underline{\mathbf{q}}} \\ \ddot{\underline{\mathbf{q}}} \end{Bmatrix} - \begin{bmatrix} 0 & \mathbf{I} \\ -(\rho V^2 \mathbf{C} + \mathbf{E}) & -(\rho V \mathbf{B_m} + \mathbf{D_m}) \end{bmatrix} \begin{Bmatrix} \underline{\mathbf{q}} \\ \dot{\underline{\mathbf{q}}} \end{Bmatrix} = \begin{Bmatrix} \underline{0} \\ \underline{0} \end{Bmatrix}, \tag{3.24}$$

where $\mathbf{I}$ is the $N \times N$ identity matrix. By rewriting Eqn. (3.24) in first order form gives

$$\begin{Bmatrix} \dot{\underline{\mathbf{q}}} \\ \ddot{\underline{\mathbf{q}}} \end{Bmatrix} - \begin{bmatrix} 0 & \mathbf{I} \\ -\mathbf{A_m}^{-1}(\rho V^2 \mathbf{C} + \mathbf{E}) & -\mathbf{A_m}^{-1}(\rho V \mathbf{B_m} + \mathbf{D_m}) \end{bmatrix} \begin{Bmatrix} \underline{\mathbf{q}} \\ \dot{\underline{\mathbf{q}}} \end{Bmatrix} = 0 \tag{3.25}$$

or in simplified form,

$$\dot{\boldsymbol{x}} - \mathbf{Q}\boldsymbol{x} = 0 \tag{3.26}$$

Equation (3.26) can be solved by assuming $\boldsymbol{x} = \boldsymbol{x_0} e^{\lambda t}$, thus the equation can be written in the classical eigensolution form $(\mathbf{A_m} - \mathbf{I}\lambda)\boldsymbol{x} = 0$ as follows

$$(\mathbf{I}\lambda - \mathbf{Q})\boldsymbol{x_0} = \mathbf{0} \qquad \text{or} \qquad (\mathbf{Q} - \mathbf{I}\lambda)\boldsymbol{x_0} = \mathbf{0}. \tag{3.27}$$

The eigenvalue solutions, λ are given in complex conjugate pairs and are written as

$$\lambda_j = -\xi_j \omega_j \pm i\omega_j \sqrt{1 - \xi_j^2}, \qquad j = 1, 2, ..., N \tag{3.28}$$

where N is the number of mode shapes, ξ_j are the damping ratios and w_j are the natural frequencies. However, the aerodynamic stiffness ($\mathbf{C}$) and the damping matrices ($\mathbf{B_m}$) are reduced frequency dependent. As the results, Eqn. (3.24) can only be solved if $\mathbf{B_m}$ and $\mathbf{C}$ are known. $\mathbf{B_m}$ and $\mathbf{C}$ can only be found if the reduced frequency is known. In order to solve this, frequency matching methods namely, *'k'* method or *'p-k'* are used. In *'k'* method, the general form of the aeroelastic equation (Eqn. 3.23) are formulated with $\mathbf{B_m}$ and $\mathbf{C}$ matrices as function of reduced frequency, $k = \omega b/V$ and also with the structural damping, $\mathbf{D_m}$ in terms of structural stiffness matrices, $\mathbf{E}$ given by $\mathbf{D_m} = ig\mathbf{E}$, where g is the structural damping coefficient. For each reduced frequencies of interest, the frequencies and damping coefficient are determined and the consequent air speed. The flutter speed is determined by joining up these values to form $V-f$ and $V-g$ plots.

In the *'p-k'* method, the reduced frequency for each airspeed of interest is calculated using the initial guess of the frequency for the mode. The aerodynamic stiffness and damping matrices $\mathbf{B_m}$, $\mathbf{C}$ are determined using the calculated reduced frequency. The corresponding frequencies for the system are determined from Eqn. (3.26) and the process is repeated until convergence is achieved. The sets of frequency, damping ratio and airspeed values for all modes of interest are plotted, and the corresponding flutter speed can be deduced when the damping is zero.

The flutter analysis is available in MSc. Nastran using `SOL 145`. In this work, the flutter solution is obtained using the *p-k* method with matched-method calculation. In the matched-method, the flutter solution is obtained at fixed Mach number and different flight altitude. The governing equation for *p-k* method in MSc. Nastran is expressed as [182].

$$[-M_{hh}p^2 + (B_{hh} - 0.25\rho cVQ^I_{hh}(M,k)/k) + (K_{hh} - 0.5\rho V^2 Q^R_{hh}(M,k))]\{u_h\} = 0, \tag{3.29}$$

where M_{hh} is the modal mass, B_{hh} is the damping, K_{hh} is the stiffness matrix, and M, k and u_h are the Mach number, reduced frequency and modal amplitude vector, respectively. Q^I_{hh} and Q^R_{hh} are the imaginary and real part of the eigenvalues, Q_{hh}. The frequency and damping are obtained from the analysis as functions of airspeed and relative modal amplitudes. The corresponding output of frequency, damping and the airspeed for all modes are used in $V-g$ and $V-f$ plots. The flutter speed is determined

when the damping value is zero. A total of 12 modes are considered in the flutter analysis to allow for mode switching during the optimisation process [177]. Figure 3.16 shows typical $V-g$ and $V-f$ plots used to determine the flutter points. The critical flutter speed obtained from benchmark EBW model is $V_{\text{f,Benchmark}} = 1.95V_{\text{D}}$ which is well above the requirement value of $1.15V_{\text{D}}$. A higher flutter speed may suggest that the structural stiffness is more than sufficient to prevent flutter in design flight condition and satisfies the certification requirements. However, this may also result in heavier wing design. Therefore, aeroelastic tailoring aims to obtain a minimum structural weight while satisfying the aeroelastic stability requirements.

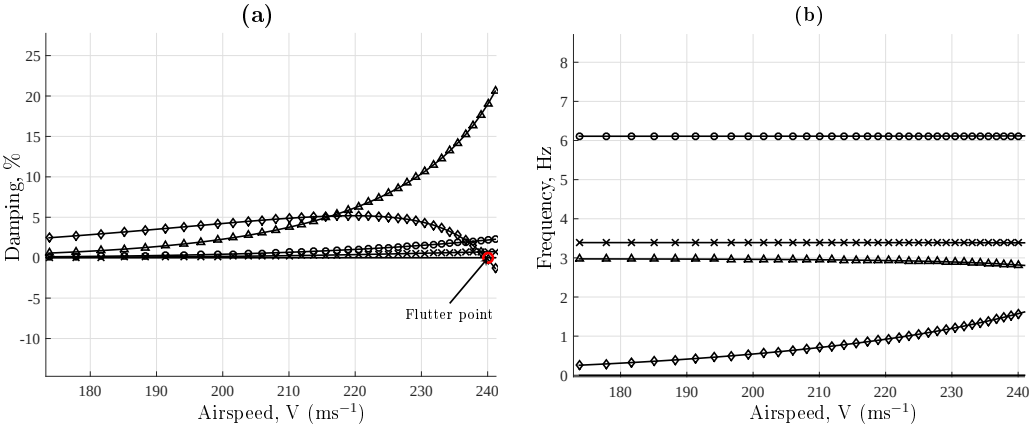

Figure 3.16: Typical damping vs. velocity (V-g) and frequency vs. velocity (V-f) plots used to determine the flutter points and the corresponding frequencies.

3.4.5 Gust Analysis

In the aircraft wing design process, the structural response to a gust encounter is listed as one of the main critical design criteria for certification. There are numbers of work that have been done in wing design optimisation for gust load alleviation [14, 23, 183, 184]. The wing structure must be designed in a way to sustain certain levels of deformation due to gust load. As specified by aeronautical authorities (CS-25) [181], the response to atmospheric turbulence or gust are analysed as either idealised discrete gusts or continuous turbulence. The current work used a discrete gust representation which is represented using *'1-cosine'* gust profile. In addition to that, the level 1g flight loads are included in the analysis defined by the aircraft speed, altitude, weight and the fuel load. The steady

1g flight loads distribution is calculated from the static aeroelastic analysis and input in the gust model.

For discrete gusts, the expression governing the *temporal* variation of *'1-cosine'* gust velocity is given as

$$w_g(t) = \frac{w_{g0}}{2}(1 - \cos\frac{2\pi V}{L_g}t), \tag{3.30}$$

where w_{g0} is the peak or design gust velocity, L_g is the gust wavelength and V is the flight speed. A set of gust gradient distance, H (half of the gust wavelength) between 9 m to 107 m, is evaluated to capture the gust load variation. The design gust velocity is formulated in terms of a reference velocity, U_{ref}, a flight alleviation factor, F_g and the gradient distance, H as

$$w_{g0} = U_{ref}\, F_g \left(\frac{H}{107}\right)^{\frac{1}{6}}, \tag{3.31}$$

where the $F_g = 1$. The reference gust velocity, U_{ref} is decreases linearly with the altitude. At sea level, U_{ref} is 17.07 ms^{-1}, 13.41 ms^{-1} at 4572 m and 6.36 ms^{-1} at 18 288 m [1]. The flight speed is set to 253 ms^{-1}. The corresponding input data for gust analysis at different gust wavelength and reference gust velocity are summarised in Table 3.5.

Table 3.5: The relative gust design velocity, w_{g0} data at different gust wavelengths, L_g and reference gust velocity, U_{ref}.

	Reference gust velocity, U_{ref}					
	U_{ref}=17.07 ms^{-1}		U_{ref}=13.41 ms^{-1}		U_{ref}=6.36 ms^{-1}	
L_g (m)	w_{g0} (ms^{-1})	f (Hz)	w_{g0} (ms^{-1})	f (Hz)	w_{g0} (ms^{-1})	f (Hz)
18	11.314	7.028	8.888	7.028	4.215	7.028
56	13.670	2.259	10.739	2.259	5.093	2.259
96	14.955	1.318	11.748	1.318	5.572	1.318
136	15.848	0.930	12.450	0.930	5.905	0.930
176	16.544	0.719	12.997	0.719	6.164	0.719
214	17.092	0.591	13.427	0.591	6.368	0.591

In this work, the analysis of the wing box dynamic aeroelastic response to discrete gusts is performed using MSc. Nastran's `SOL 146`. For a gust analysis, MSc. Nastran uses direct and inverse Fourier transforms methods to allow for a frequency response analysis [185]. The gust velocity variation over time for different gust wavelengths are input in `SOL 146` as a load-frequency table (`TLOAD1` and `TABLED1`). The set of frequencies used to obtain the frequency response solution is defined using `FREQ1` input command. The `TSTEP` input command defines the time step intervals at which the transient responses are required; in this case, the time step is eight seconds. Figure 3.17 shows the gust velocity

variation over time for different gust wavelengths used in the analysis at reference gust velocity, U_{ref} of 13.41 ms^{-1} at 4572 m.

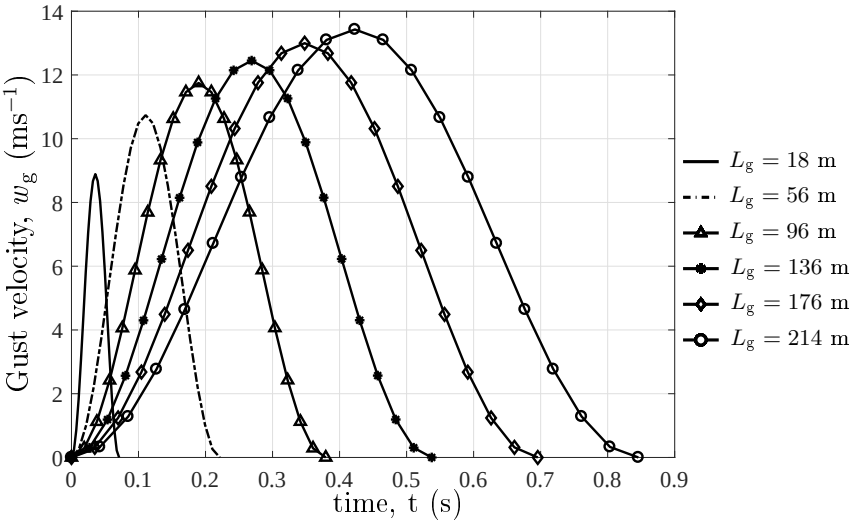

Figure 3.17: The variation plot of gust velocity as a function of time evaluated at reference gust velocity, U_{ref} of 13.41 ms^{-1} at 4572 m.

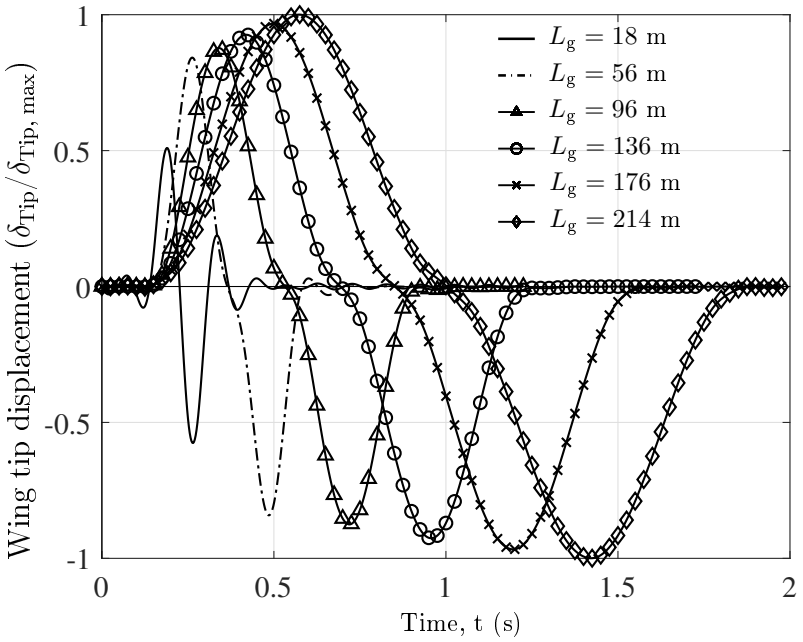

Figure 3.18: The wing tip displacement vs. time response of EBW model evaluated at different critical gust wavelength, L_g from 18 m to 214 m.

Figures 3.18 and 3.19 show the time responses of wingtip displacement and the wing root bending moment (RBM) for EBW model evaluated at different gust wavelengths, L_g of 18 m, 56 m, 96 m, 136 m, 176 m and 214 m. The results shown are obtained

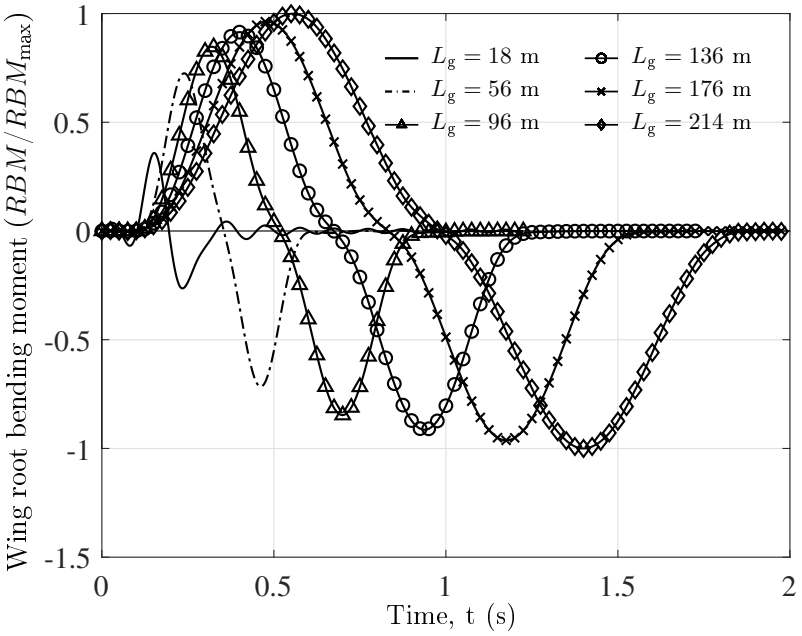

Figure 3.19: The wing root bending moment vs time response of EBW model evaluated at different critical gust wavelength, L_g from 18 m to 214 m.

at reference gust velocity, U_{ref} of 13.41 ms^{-1}. For the wingtip displacement, a higher response is obtained at a shorter wavelength with maximum tip displacement is obtained at a gust load with $L_g = 214$ m. A similar pattern of output responses are obtained for the wing root bending moment, where higher RBM responses are obtained at gust load with $L_g = 18$ m. Note that, the output response value is normalised against the maximum value obtained from all gust length and reference gust velocity combination for each output response.

The minimum and maximum value of the RBM and tip displacement obtained at each gust wavelength and different reference gust velocities of the EBW model are plotted in Figure 3.20 and 3.21. It is observed that for the wingtip displacement, the maximum displacement of each gust wavelength increases linearly as the wavelength increases. A higher increase in the value is observed at lower gust wavelength of below 50 m. Different reference gust velocity also results in different output responses. For instance, at $U_{ref} = 17.07$ ms^{-1}, the overall wingtip displacement is higher compared to the response obtained at lower U_{ref}. The critical tip displacement is found when $L_g = 214$ m and $U_{ref} = 17.07$ ms^{-1}. The critical value is the maximum value obtained from all gust wavelength and U_{ref}. Similarly, the minimum and maximum RBM values of the EBW

model also varied linearly with respect to the gust wavelength and reference gust velocity. The critical RBM value is obtained at $L_g = 214$ m and $U_{ref} = 17.07$ ms^{-1}

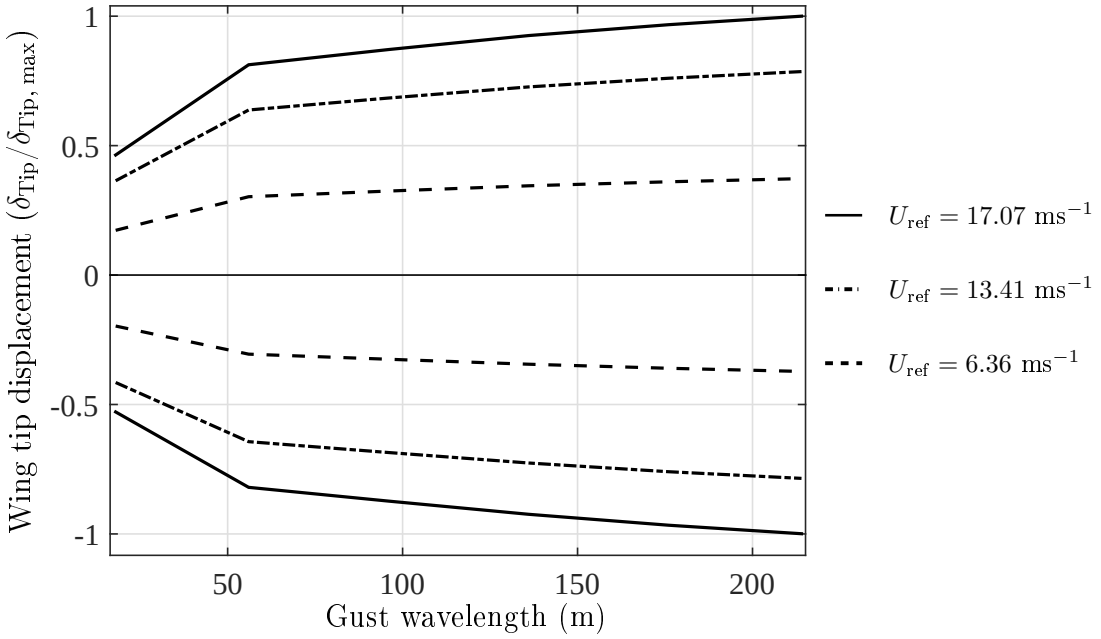

Figure 3.20: Minimum and maximum wing tip displacement at different gust wavelength, L_g with respect to different reference gust velocity, U_{ref}.

3.5 Structural Analysis

The aeroelastic tailoring performed in this work incorporates the dynamic and structural analyses of the EBW model. The structural performance in terms of the strength and buckling are included in the tailoring framework as additional design constraints. The strength and buckling analyses are performed in MSc. Nastran using `SOL 105`. The aerodynamic load distributions obtained from the static aeroelastic analysis (Section 3.4.2 (page 66)) are included in the model as nodal forces. The strength of the laminate panels (top, bottom skin and spars) are evaluated in terms of the laminate stress and strength. The stress and strain limit is defined in terms of failure index to quantify the strength performance by not exceeding a set allowable value. The stress failure index, FI_{stress} is formulated as

$$FI_{\text{stress}} = \max\Big(\frac{\sigma_{\text{VMS}}}{\sigma_{\text{VMS,allowable}}}\Big), \tag{3.32}$$

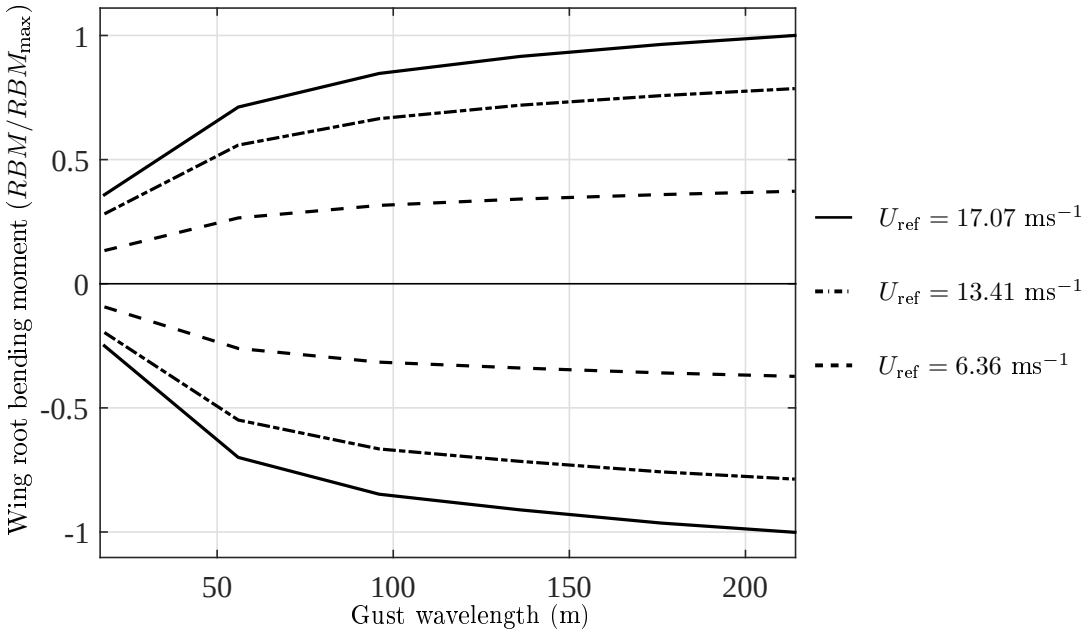

Figure 3.21: Minimum and maximum wing root bending moment at different gust wavelength, L_g with respect to different reference gust velocity, U_{ref}.

where $\sigma_{VMS,allowable}$ is the von Mises stress calculated using the strength properties given in Table 3.3 (page 65).

Since no information is yet available on the stacking sequences, the strain limit is applied in terms of strain failure index, FI_{strain} based on homogenised strain values, i.e. maximum and minimum principle and shear strain.

$$FI_{strain} = \max\Big(\frac{\epsilon_{min}}{\epsilon_{min,allowable}}, \frac{\epsilon_{max}}{\epsilon_{max,allowable}}, \frac{\gamma_{min}}{\gamma_{min,allowable}}, \frac{\gamma_{max}}{\gamma_{max,allowable}}\Big), \tag{3.33}$$

where ϵ_{min} and ϵ_{max} are the principal strains for laminate under compression and tension, respectively. The allowable values are set to $\epsilon_{min,allowable} = -5900\mu\epsilon$ and $\epsilon_{max,allowable} = 7100\mu\epsilon$. The shear strains limit is defined in terms of maximum and minimum shear strains, with allowable values set to $\gamma_{min,allowable} = -4500\mu\epsilon$ and $\gamma_{max,allowable} = 4500\mu\epsilon$.

3.5.1 Stress and Strain Analysis

An initial structural design analysis was performed on the EBW model to evaluate the stress and strain distributions on the laminate panels of top skin, bottom skin and the spars section. Figure 3.22 and 3.23 show the laminate stress and strain distribution

of the wing sections. Note that the stress and the strain values are normalised with the maximum stress and strain value. From the analysis, the higher stress and strain distributions are found on the bottom skin panel at the junction of inboard and outboard wing. The higher stress and strain values at this location were due to the high load concentrations caused by the engine and pylon attachment. On the wingtip, the stress and strain values are at minimum for all panels. For the spar and rib panels, high stress and strain distribution were observed at the *'kink'* area. This high stress and strain concentration area are critical and thicker sections may be required in order to satisfy the strength constraints. Moreover, the FE results suggest that improvement on the wing design can be achieved via composite tailoring by allowing optimum stress and strain distribution on the wing panels.

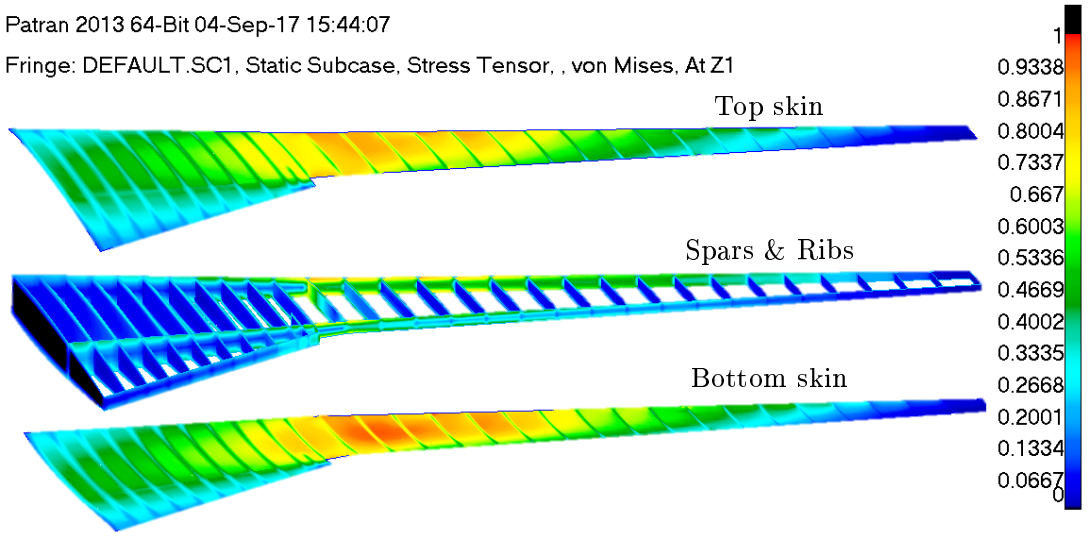

Figure 3.22: von Mises stress (normalised scale) distribution for EBW model at spars, ribs, top and bottom skins subjected to Load 1.

The strain values for the top and bottom skins of the EBW model at different load cases (as given in Table 3.4 (page 66)) plotted in Figure 3.24 and 3.25. It is noticed that the maximum strain for the top and bottom skin were evaluated at 1/3 of the wing-span with higher strain value obtained for the bottom skin panel. The maximum strain of 27% of $\epsilon_{\text{allowable}}$ was obtained at the bottom skin panels. Higher strain values are obtained for load case 1 and 5 and are thought to be critical load cases for the strength constraint. Lower strain values close to zero are observed at the wing tip for top and bottom skin panels.

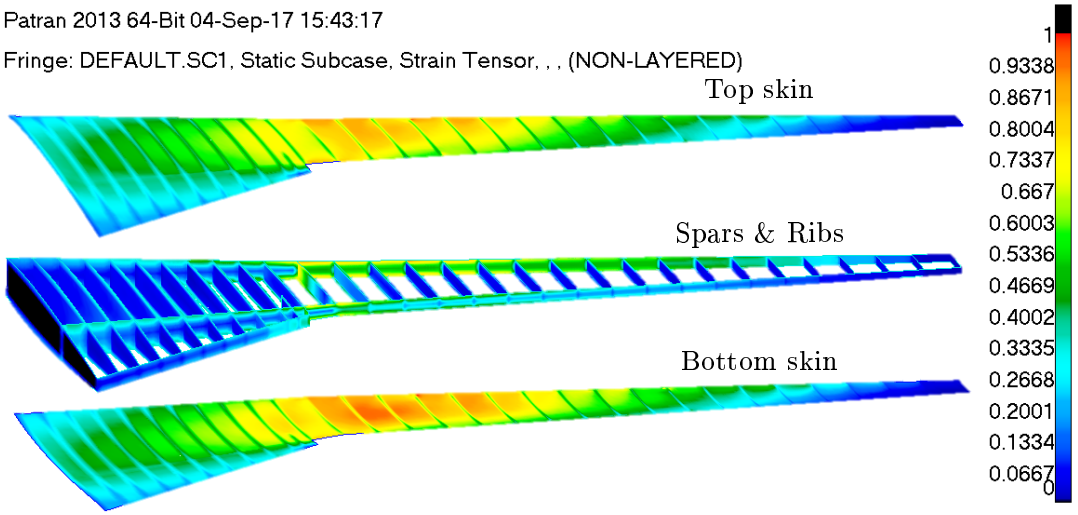

Figure 3.23: Longitudinal strain (normalised scale) distribution of the laminate for EBW model at spars, ribs, top and bottom skins subjected to Load 1.

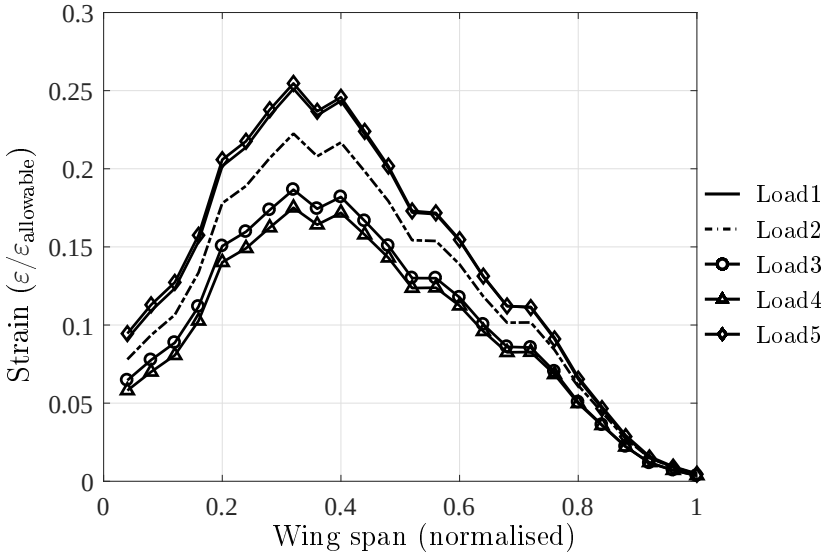

Figure 3.24: Top skin's strain (von Mises) distributions across the span length of EBW model for different static manoeuvre load cases.

The strain values for the top skin, bottom skin and the spar sections obtained from load case 1 are plotted in Figure 3.26. For all sections, higher strain values are obtained at the middle wingspan with the maximum value found on the bottom skin panel. The strain values for Spar 1 and 2 sections are significantly lower compared to the top and bottom skin section. Overall, the strain values evaluated for EBW model are significantly below the allowable strain value. Hence, the results suggest that there is ample safety margin for the benchmark model to be optimised through aeroelastic tailoring.

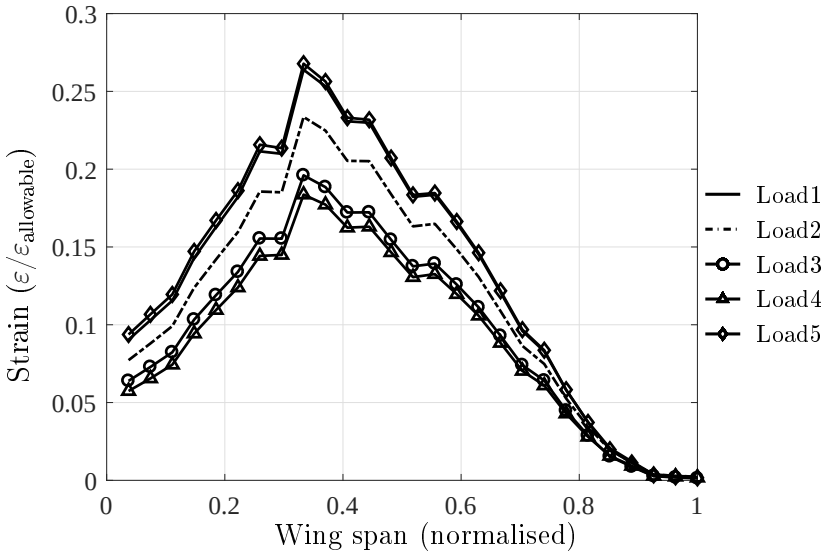

Figure 3.25: Bottom skin's strain (von Mises) distributions across the span length of EBW model for different static manoeuvre load cases.

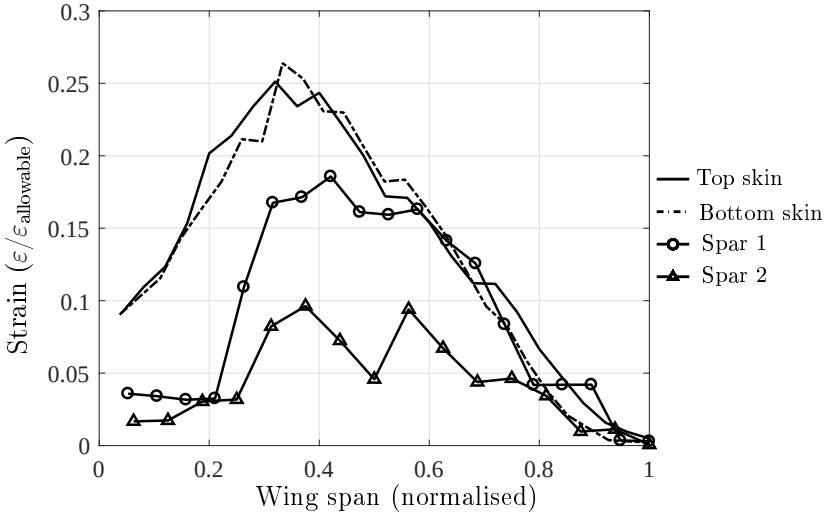

Figure 3.26: Strain (von Mises) values measured at top skin, bottom skin and spars across the span length of EBW model for the first load case (Load1).

3.5.2 Buckling Analysis

The buckling performance of the composite structure is one of the main requirements in structural design. The composite structures must be free from buckling under the applied load. The buckling performance of the composite wing structures can be evaluated as global or local buckling. For global buckling, the whole structure is considered in the analysis and the structural performance to buckling is assessed using the critical buckling load which defines the upper limit of load that can be applied before the structures

buckle. On the other hand, the local buckling analysis is usually performed on a panel level of the wing structures (i.e. small panel of top skin section). In this work, global buckling analysis was performed on the wing model, and the critical buckling load factor is determined from the entire structures. The structure is buckled when

$$\lambda \leq 1 \qquad \text{and} \qquad \lambda = \frac{P}{P_{\text{cr}}}, \tag{3.34}$$

where, P and P_{cr} are the applied load and the critical buckling load, respectively. The first ten buckling modes for EBW model are evaluated at each load cases, and the results are given in Table 3.6. For all load cases, the buckling load factor values are greater than one which suggests that the EBW design is sufficient for buckling consideration. It is also observed that the critical load cases for buckling are load case 1 and 5, which support the previous findings from structural strength analysis. The first buckling mode for load case 1 is shown in Figure 3.27, where the structure buckled at the top skin panel under applied load with critical buckling load factor of 2.02. The buckling behaviour of the wing panel is thought depends on how the wing's stiffeners are modelled. For the EBW model, the stiffeners are modelled using multiple ribs and stringers positioned in the wing thickness and span length direction. It can be seen from the Figure 3.27, the buckling mode shape formed within small patches between the stringers and ribs, hence, suggests that the wing's bucking behaviour depends on the arrangement of the wing's stiffeners.

Table 3.6: The buckling load factors, λ for the first ten buckling modes at each load cases obtained from FE analysis on EBW model.

	Load 1	Load 2	Load 3	Load 4	Load 5
Mode	λ	λ	λ	λ	λ
1	2.020	2.263	2.601	2.601	2.003
2	2.029	2.274	2.673	2.673	2.012
3	2.107	2.381	2.695	2.847	2.074
4	2.127	2.404	2.708	2.861	2.094
5	2.249	2.515	2.830	3.023	2.234
6	2.255	2.521	2.858	3.054	2.239
7	2.311	2.574	2.995	3.156	2.279
8	2.317	2.582	3.002	3.165	2.309
9	2.324	2.601	3.054	3.199	2.316
10	2.358	2.608	3.063	3.209	2.323

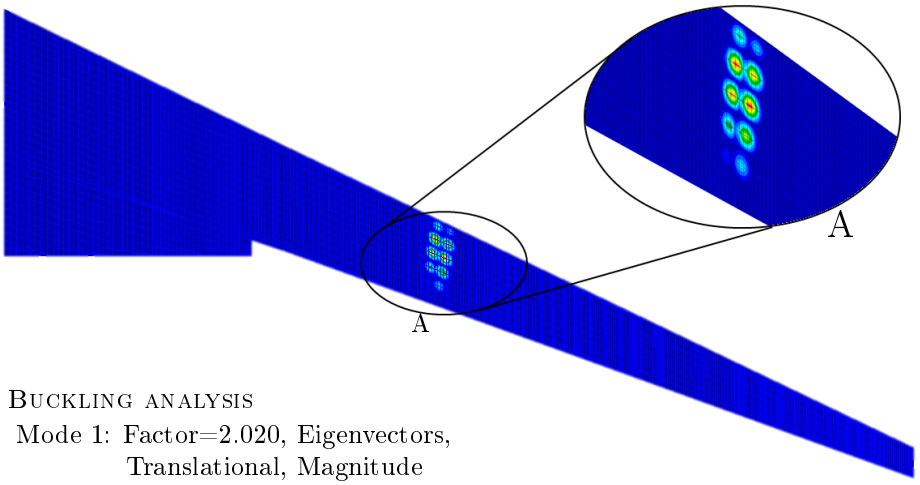

Figure 3.27: Translation deformation of EBW model for buckling analysis with critical buckling load factor (Mode 1) of 2.020.

3.6 Model Validation

The composite wing model used in the current work is based on the reference jet aircraft, and hence direct comparison with previous work from the published literature is not possible. Based on the technical data of the reference aircraft as given in Table 3.1 (page 56) and the initial analyses on EBW model show that the model is sufficient to provide an accurate estimation of the performance for similar aircraft type and design range. Furthermore, the structural and aeroelastic analysis performed on the EBW model suggested that the model satisfied all the structural (strength and buckling) and aeroelastic (flutter) requirement imposed on the design. These are evidence for flutter analysis such that the flutter speed obtained for the EBW model is above the flutter requirement of $V_{\mathrm{f}} = 1.15V_{\mathrm{D}}$.

To further validate the accuracy of the model, six different models of similar wing configuration with different structural mesh seed are modelled and used for mesh convergence analysis. The modal analysis is performed to obtain the natural frequency of the composite wing. The number of structural elements chosen for the analysis is between 7609 elements to 118259 elements. The purpose of the analysis is to determine the optimal mesh size for the EBW wing, which can provide accurate results with a reasonable computational cost.

The outcomes from the mesh sensitivity study are summarised in Table 3.7. By comparing Model 1 and Model 2, the natural frequency value reduced from 2.6843 Hz to

2.6799 Hz, which is equivalent to 0.16% differences. The change in frequency value is insignificant (0.0037%) when finer mesh seed (Model 3 and Model 4) is used for the analysis. The results suggest that the convergence has been achieved with Model 3. The convergence plot for the mesh sensitivity study is depicted in Figure 3.28. The 3rd model (Model 3), modelled with 25471 elements, is opted for the current work.

Table 3.7: The wing's natural frequency obtained from the mesh sensitivity study.

Model No.	Total Elements	Frequency, f (Hz)	% difference
1	7609	2.6843	-
2	16865	2.6799	0.1600
3	25471	2.6798	0.0037
4	58975	2.6797	0.0037
5	79949	2.6797	0.0000
6	118259	2.6797	0.0000

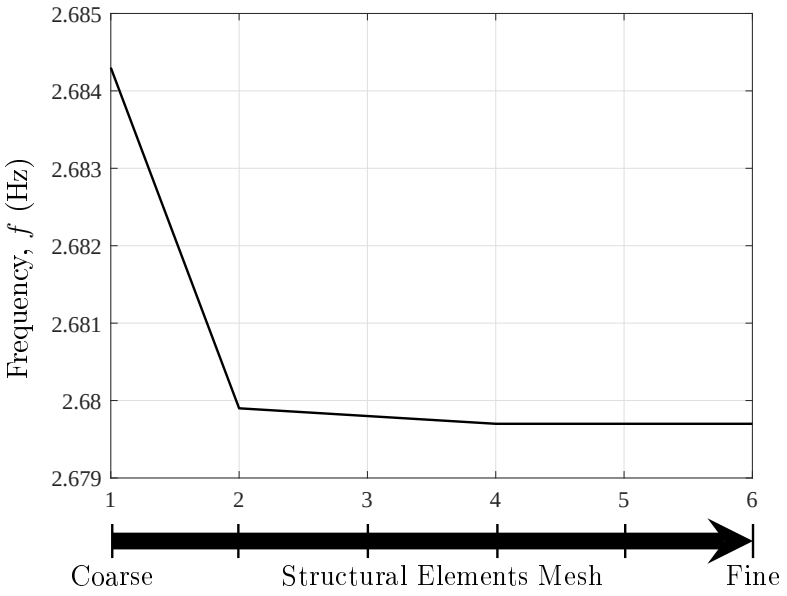

Figure 3.28: Convergence plot of the the natural frequency (modal analysis) with varying structural mesh density from coarse to fine mesh seed of the EBW model

3.7 Summary

1. A very efficient approach and detailed finite element wing model to represent the complex aircraft structure are required to quantify the wing's performances for aeroelastic tailoring accurately. Aeroelastic tailoring is an efficient design method

to obtain an optimised design that satisfied the minimum structural weight requirement as well as the structural and aeroelastic performances.

2. The idealised box-like finite element model used in the current work capable of producing a realistic approximation of the wing's performance. A high-aspect-ratio of a reference regional jet aircraft is chosen as the benchmark wing model (EBW). MSc. Patran/Nastran is used for modelling and analysis.

3. The use of lamination parameters greatly reduced the number of design variables require for the optimisation procedures in aeroelastic tailoring. The assumption of using a specific type of ply configuration such as non-balanced and symmetric laminate in this study further reduce the number of variables.

4. The aerodynamics in the model is represented using the Doublet Lattice Method (DLM). The static aeroelastic analysis is performed to obtain the load distributions on the wing due to multiple static manoeuvre load cases. The free vibration analysis is performed to determine the wing's mode shapes and modal frequencies.

5. The aeroelastic instability behaviour of the wing structures is determined from the dynamic aeroelastic analysis in MSc. Nastran using frequency-matching *'p-k'* method. Flutter is determined as the critical instability mode, while divergence occurs at a higher airspeed. The assessment of flutter is performed to match the aircraft certification requirement such that for all design conditions, the flutter speed must be greater than $1.15V_{\mathrm{D}}$, where V_{D} is the design dive velocity.

6. The wing's responses due to atmospheric turbulence is one of the main design requirements for certification as provided by the aeronautic authority. The wing structures must be designed in a way to sustain a certain level of deformation due to gust load. In the current work, the wing's response due to discrete *'1-cosine'* gust loads are quantified in terms of root bending moment at the root and wingtip displacement at critical gust wavelength and velocity.

7. The structural responses of the wings due to multiple static manoeuvre load cases are quantified in terms of structural strength and buckling responses. These are specified as design constraints in aeroelastic tailoring procedures in order to obtain a feasible design solution with both aeroelastic and structural performances are satisfied.

8. Preliminary analyses on the benchmark model (EBW model) show that the model has a potential for design improvement and structural weight saving via aeroelastic tailoring due to ample margin between the design values and the actual responses of the wing model.

Chapter 4

Aeroelastic Tailoring and Optimisation Methods

4.1 Introduction

Aeroelastic tailoring is an approach in which the directional stiffness is incorporated into the aircraft structural design in order to control the static or dynamic aeroelastic behaviour as to affect the aircraft's aerodynamic and structural performance in a beneficial way [2]. In composite structures, aeroelastic tailoring can be performed by tailoring composite's fibre orientation to obtain the desired structural and aerodynamic performance. The static and dynamic aeroelastic behaviour of the composite structures are controlled by various coupling terms in the composite stiffness matrix and tailoring the fibre orientation alters the coupling terms and hence provides design flexibility, as well as challenges, in the optimisation process.

Numerous studies have been performed in aeroelastic tailoring particularly concerned with the aeroelastic modelling and optimisation approaches. Various approaches have been adapted for modelling a wing structures in order to obtain the desired performances. The numerical method and low computational model such as *'idealised'* simple wing model have been used by many researchers [10, 23, 47, 111] because of low computational cost. Other authors [3, 9, 107, 112] employed an idealised wing-box representation in aeroelastic tailoring to obtain an accurate prediction of the wing performance. In the present work, a composite wing-box model of a reference jet aircraft is aeroelastically tailored by altering the wing's composite panels ply orientation.

The objective of the present work is to obtain an aeroelastically-tailored wing design subjected to multiple design constraints that include structural and aeroelastic performance. The wing structure is subjected to multiple static manoeuvre load cases and evaluated in terms of the strength and buckling as well as the flutter/divergence and gust response.

An improved optimisation approach is introduced to account for the multiple constraint design problem. Genetic Algorithm (GA) and Particle Swarm Optimisation (PSO) are employed as the optimisation algorithms. In this work, three types of design optimisation problems are defined:

- Optimisation of a composite wing for minimum structural weight subjected to flutter/divergence design constraints.
- Optimisation of a composite wing for minimum structural weight subjected to multiple constraints that included flutter/divergence and wing root bending moment due to gust load.
- Optimisation of a composite wing for minimum structural weight subjected to structural and aeroelastic design constraints.

4.2 Optimisation approach

The complexity of the design optimisation problems coupled with finite element analysis requires an efficient optimisation tool to produce a design solution in a rapid manner. When dealing with the multi-variable optimisation problem, a direct or gradient-based techniques is often employed to seek for a global optimised solution but it requires a longer solving time for large parameter space solutions. Other optimisation techniques, such as an exhaustive search method, in which equally spaced points are used to search for new points for the next iteration step. These techniques offer global optimum solution; however, higher computational costs may results if large design spaces are involved.

Alternatively, a heuristic algorithm can be used to solve the optimisation problem in a faster and more efficient fashion than the aforementioned methods by sacrificing the accuracy, precision or completeness for speed. Two heuristic optimisation techniques, namely, Genetic Algorithm (GA) and Particle Swarm Optimisation (PSO) are presented herein and employed in the current work. GA is an iterative process of finding the best solution from a *'population'* of random generated individuals in a *'generation'*. Using GA, multiple near-optimal solution can be found as GA is based on the population of the design variables and the probabilistic transition between the optimal solutions [48]. In PSO, the search is based on random population (particles) of the solution and each

potential solution is assigned with a randomised velocity. The ability of the particles to compete and communicate between each other and to exchange their position and speed effectively, results in a better efficiency compared to gradient method or exhaustic search method.

The general flow of the aeroelatic tailoring approach employed in the current work is illustrated in Figure 4.1. The reference benchmark wing introduced in Chapter 3 is used as the initial design. GA or PSO technique is used in the optimisation procedures. Initially, the objective function (minimum structural weight), design variables and design constraints are defined. In this case, the design variables are the lamination parameters and panel thickness. The structural and aeroelastic performances are set as the design constraints. For each set of design variables, the wing model is evaluated for set constraint/constraints using MSc. Nastran's solver. The outcomes are then fed into the optimisation algorithm. The process is repeated until convergence is achieved. The underlying concepts of GA and PSO are presented in next section.

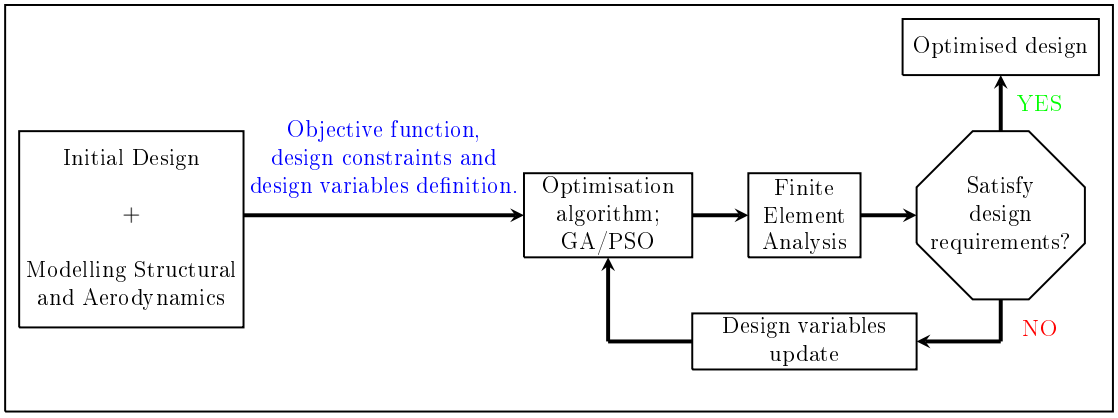

Figure 4.1: The general flow of the optimisation process for aeroelastic tailoring of the composite wing.

4.2.1 Genetic Algorithm (GA)

A Genetic Algorithm is a heuristic search method for solving both constrained and unconstrained optimisation problems based on Darwin's theory of natural selection process that mimics biological evolution. The algorithm initiates by creating a random initial population. The algorithm then uses the current population to produce the *'children'* for the next generation. Each member of the current population are evaluated in terms of their fitness value. The algorithm selects individuals in the current population, called

'parents' to contribute their *'genes'* to their children. The individuals that have better fitness values are selected as parents. There are three types of children in the next generation's population:

- *'Elite'* children - Individuals with the best fitness value in the current generation.
- *'Crossover'* children - The crossover children are formed by using the vectors of a pair of parents.
- *'Mutation'* children - The mutation children are formed by random changes or mutation to a single parent.

Over successive generations, the population *'advances'* toward an optimal solution. The stopping condition can be specified to govern the solution's convergence. The function tolerance can be used in which the algorithm runs until the average relative change in the fitness function value is less than the function tolerance value.

In the current work, the design variables are continuous, which defined by the upper and lower limit as well as the feasible region constraints. The upper and lower limit is set to -1 and 1, respectively. In GA, the algorithm generates an initial population based on the upper and lower limit. The population is checked against the feasible region constraint such that any value (lamination parameters) outside the feasible region is considered invalid. In MATLAB optimisation toolbox, GA optimisation tool is available and calling a built-in `ga` function file. The user-defined parameters for the optimisation such as the generations, population size, convergence tolerance and others can be specified using `gaoptimset` function. Example of GA script as follows;

```
% GA optimisation

fun=@ObjFunction;            % Define objective function
nvars = 328;                 % Specify numbers of design variables
lb=-1;                       % Lower bound of design variables
ub=1;                        % Upper bound of design variables
% Option definition
options = gaoptimset('Generations',50,'PopulationSize',20,...
```

```
'StallGenLimit',20,'TolFun',1e-6,'PlotFcns',gaplotbestf,gaplotbestindiv);
[x,fval] = ga(fun,nvars,lb,ub,options)
```

4.2.2 Particle Swarm Optimisation (PSO)

PSO is a heuristic search method introduced by Kennedy & Eberhart [57] which is inspired by simple analogues of collaborative behaviour and swarming in biological populations [58]. In PSO, a population of random solution or *'particles'* is defined and each particle is assigned with a randomised velocity. Each particle in the swarm has a memory and capable of interacting with each other. For every iteration, the particles' position and velocity are updated using the previous best value from each particle and swarm. The velocity, v_i and position, x_i of the particles in the n^{th} iteration are given by [186];

$$v_i(n+i) = wv_i(n) + c_1\phi_{1d}[p_i(n) - x_i(n)] + c_2\phi_{2d}[g_i(n) - x_i(n)] \tag{4.1}$$

and

$$x_i(n+1) = x_i(n) + v_i(n), \tag{4.2}$$

where

- p_i and g_i are the best position obtained from each particle and the entire population.
- ϕ_{1d} and ϕ_{2d} are the independent uniformly distributed random numbers. These numbers are generated independently.
- w, c_1 and c_2 are the inertia factor, particle belief factor and swarm belief, respectively. These factors can be either constant or variable and are defined by the user.

Higher w values allow for a greater distance for the next particle's position and hence promotes the chance to miss the near-optimum value. However, the lower w value leads to an exhaustive search for an optimum solution. c_1 and c_2 can be increased throughout the iterations, which increase the belief in swarm results.

Similar to the GA, PSO is also available from MATLAB optimisation toolbox. A built-in function `particleswarm` is called to initiate PSO for optimisation procedure. User-defined parameters that included a maximum number of iteration, swarm size, stopping

criterion and others can be specified using `optimoptions` function. An example of a PSO script as follows

```
% Particle swarm optimisation (PSO)

fun=@ObjFunction;            % Define objective function
nvars = 328;                 % Specify numbers of design variables
lb=-1;                       % Lower bound of design variables
ub=1;                        % Upper bound of design variables
% Option definition
options = optimoptions('particleswarm','MaxIter',50,'SwarmSize',20,...
'StallIterLimit',20,'TolFun',1e-6,'PlotFcns',@pswplotbestf);
[x,fval,eflag,output] = particleswarm(fun,nvars,lb,ub,options);
```

4.3 Model Description and Design Optimisation Problem

The benchmark composite wing (EBW) model presented in Chapter 3.2 (page 54) is used as the initial design for the optimisation procedure. In the current work, only the top skin, bottom skin and spars section are tailored for a minimum structural weight which gives a total of 41 composite laminate panels, as depicted in Figure 3.6 (page 63).

The lamination parameter and panel thickness are chosen as the design variables. It is assumed that the laminate panels are made of unbalanced and symmetric laminate configurations. With this assumption, only nine design variables are defined (eight lamination parameters and a laminate thickness) for each panel and a total of 369 design variables for the entire wing model. An additional set of optimisation constraints is introduced to establish the feasible region of the lamination parameter and hence ensure convergence to the solution.

The feasible region constraints for lamination parameters used in this work are derived from Fukunaga & Sekine [72]. To recall, the feasible region of the four in-plane and

out-of-plane lamination parameters are given by

$$
\begin{aligned}
&-1 \leq \xi_k^j \leq 1, \\
&(\xi_1^j)^2 + (\xi_3^j)^2 \leq 1, \\
&2(1+\xi_2^j)(\xi_3^j)^2 - 4\xi_1^j\xi_3^j\xi_4^j + (\xi_4^j)^2 - (\xi_2^j - 2(\xi_1^j)^2 + 1)(1-\xi_2^j) \leq 0,
\end{aligned} \tag{3.10}
$$

where ξ_k^j are the lamination parameters with $k = 1, 2, 3, 4$ and $j = A, D$. The above inequality relationships provide the feasible regions in the design space for each lamination parameters and hence simplify the design problem.

In an actual industrial application, aeroelastic tailoring of aircraft structures focused on minimising the structural weight while optimising the aeroelastic performance of the structures [2]. The use of composite materials allows for better design solutions through material tailoring and to achieve the target performance at lower structural weight. Moreover, for a complex structural design such as aircraft's wing requires detailed consideration of multiple design constraints and not limited to aeroelastic performance. The structural performance of the design is equally important to obtain a realistic aeroelastically-tailored design.

Therefore, the aeroelastic tailoring work presented in this chapter aims to minimise the wing structural weight subjected to multiple design constraints that include structural and aeroelastic responses. A penalty function with weighting factors are introduced to account for various constraints in the optimisation. An optimal solution for the optimisation is chosen based on averaging principle and *'pareto front'*.

The work presented in this chapter uses lamination parameters as the design variables. However, the work only considers the unbalanced and symmetric laminates configuration; hence, only in-plane, $\xi^A_{1,2,3,4}$ and out-of-plane, $\xi^D_{1,2,3,4}$ lamination parameters are chosen as design variables rather than a full set of lamination parameters. Additionally, all the lamination parameters considered are governed by the feasible region (inequality) relationship given by Fukunaga & Sekine [72]. The design variables are treated as continuous parameters which allow the use of heuristic search methods such as GA and PSO.

Both GA and PSO are used in the optimisation for the aforementioned design problems. GA offers an efficient technique but often requires a significant computational effort to

obtain converged solution. On the other hand, PSO offers better computational efficiency for optimisation problems with large design spaces. Twenty populations/particles are assigned in GA/PSO with the maximum number of generation/iteration is set to 50 to ensure convergence. The stopping criterion is configured such that the fitness function of the best design did not vary for 20 repetitions. In subsequent sections, the aeroelastic tailoring of a composite aircraft wing is presented for aeroelastic and structural constraints. The optimisations were conducted on a quad-core Intel Core i7-3770S-CPU @ 3.10 GHz with 32 GB RAM.

4.4 Aeroelastic tailoring for flutter/divergence and gust responses

In this section, the benchmark model of the composite wing (EBW model) as presented in Section 3.2.1 (page 56) is optimised for minimum structural weight with flutter/divergence and gust responses are treated as active design constraints. Two types of design problems were investigated:

1. Aeroelastic tailoring to minimise the structural weight subject to flutter/divergence.
2. Aeroelastic tailoring to minimise the structural weight subject to both flutter/divergence and gust response.

In the first design problem, the wing structure is optimised to satisfy the flutter/divergence requirements as given in Section 3.4.4 (page 74). In the second design problem, the optimisation aims at minimising the structural weight with both flutter/divergence and gust response constraints. The gust response was quantified in terms of the wing root bending moment (RBM) due to discrete *'1-cosines'* gust profile.

The model analysis (flutter and gust analysis) are performed with MSc. Nastran's solvers. Both the GA and PSO methods are employed for the optimisation and are available from MATLAB global optimisation toolbox.

4.4.1 Optimisation for flutter/divergence response only

The first design problem aims to establish the possibility of structural weight saving from aeroelastic tailoring with aeroelastic instability as the design criteria. The composite wing box is optimised for minimum structural weight while satisfying the requirement for flutter/divergence speed. The lamination parameters and the panel thickness of top skin, bottom skin and spar panels are selected as the design variables (DV). The lamination parameters are set to be continuous and varied between -1 to 1. In addition to that, no more than two plies were allowed to be dropped between adjacent panels to prevent sharp changes in thickness variation. Finally, the lower bound for panel thickness is set to be no less than 20 plies to avoid unrealistic thickness value due to lack of structural constraints (strength constraints).

To evaluate the effectiveness of the chosen optimisation method, both GA and PSO are used to solve the design problems. A comparison study on the optimised solution and the resulting computational expenses are studied. The benchmark wing model is used as the initial design for the optimisation. The optimised solution was selected based on the convergence/stopping criteria such that the fitness function value is not changing for subsequent 20 iterations or the difference in fitness function value is less than 10^{-6}.

The aeroelastic behaviours of the composite wing box are evaluated in terms of the flutter/divergence occurrence at each iteration. The frequency matching, *'p-k'* matched-method (`PKNL` method in MSC. NASTRAN's `SOL 145`: Flutter analysis) is used to predict the flutter/divergence speed of the wing model. The frequencies and the damping output as a function of airspeed and relative model amplitude were extracted from the analysis and used to predict the flutter/divergence points. A total of 12 modes are predicted in the model analysis to allow for mode switching.

The design optimisation problem can be described as

$$\begin{aligned} \underset{\mathbf{x}}{\text{minimize}} \quad & f_{1,\text{obj}}(W(\mathbf{x}), f_{1,\text{cost}}(\mathbf{x})), \\ \text{subject to:} \quad & \text{Flutter speed}, \quad V_\text{f}(\mathbf{x}) \geq 1.15 V_\text{D} \\ & \mathbf{x} = [\xi_1^A, ..., \xi_4^A, \xi_1^D, ..., \xi_4^D \quad \text{and} \quad t_{\text{panel},1}, ..., t_{\text{panel},41}], \end{aligned} \tag{4.4}$$

where

- $\mathbf{x}$ is vector containing design variables.
- ξ is the lamination parameters. For each panel, there are eight lamination parameters chosen as the design variables. Only unbalanced and symmetrical laminates are considered in this work.
- t_{panel} is the thickness of the composite laminate panels. A total of 41 panels are considered in this work; 11 top skin panels, 11 bottom skin panels and 19 spar panels.
- The flutter speed, V_{f} is calculated from conventional $V-g$ plot, assuming Mach 0.82 and flight dive velocity, V_{D} at 10000m. V_{f} is assumed to be the lowest of 12 values (from 12 modes) at which the damping factor equals zero.

Additional constraints for the feasibility region of lamination parameters as given in Eqn. (3.10) were included in the optimisation procedures. The ply drops constraint is enforced in the optimisation algorithm such that the thickness reduction for the adjacent panel is limited to $2 \times t_{\text{ply}}$.

The objective function in Eqn. (4.4) is formulated as a function of structural weight (skins and spars) and the cost function, $f_{1,\text{cost}}$ such that

$$f_{1,\text{obj}} = \frac{W(\mathbf{x})}{W_{\text{benchmark}}} + f_{1,\text{cost}}(\mathbf{x}), \tag{4.5}$$

where W and $W_{\text{benchmark}}$ are the structural weight of the current design and the benchmark model, respectively. Note that the components of Eqn. (4.5) are equally weighted in order to obtain an optimised design with minimum structural weight at optimum flutter speed. The cost function, $f_{\text{cost},1}$ is introduced to account for the flutter/divergence constraint contribution on the overall objective function and formulated as

$$f_{1,\text{cost}} = \left| \frac{V_{\text{f}} - V_{\text{f,Design}}}{V_{\text{f,Design}}} \right|, \tag{4.6}$$

where the subscript '*Design*' denotes allowable or desired value for the flutter speed.

Table 4.1 provides a summary of the deterministic optimised design for the flutter/divergence constraint only. The itemised structural weight of the composite panels was given for comparison with the benchmark model. The results are normalised with the benchmark data due to the design confidentiality. In general, the optimised designs obtained

are much lighter in comparison with the benchmark model. A 42.5% weight saving was accounted from the optimised model obtained from GA, and a 48.9% reduction was obtained from PSO. For GA's optimised solutions, the highest weight saving of 47.2% is obtained from Spar 3 panel. The top and bottom skin panels contributed to percentage weight saving of 42.2% and 45.2%, respectively.

Table 4.1: Deterministic optimised design for flutter/divergence constraint using GA and PSO method.

Items	Benchmark	GA	% difference	PSO	% difference
Flutter speed, $V_f/V_{f,Design}$	1.5600	1.0000	0.0	1.0000	0.0
Structural weight, $W/W_{Benchmark}$					
Top skin	0.4033	0.2332	42.2	0.2091	48.2
Bottom skin	0.4050	0.2220	45.2	0.2099	48.2
Spar 1	0.0959	0.0544	43.3	0.0463	51.7
Spar 2	0.0746	0.0538	27.9	0.0359	51.9
Spar 3	0.0212	0.0112	47.2	0.0097	54.2
Total	1.0000	0.5746	42.5	0.5109	48.9
No. of runs	-	780	-	460	-

Table 4.2: The extension-shear coupling terms (A_{16} and A_{26}) and bending-twisting coupling terms (D_{16} and D_{26}) deduced from the optimised model and benchmark EBW model for top skins panels.

Top skin panels								
	Benchmark EBW model				Optimised Model			
	A_{16} (N/m)	A_{26} (N/m)	D_{16} (N.m)	D_{26} (N.m)	A_{16} (10^7 N/m)	A_{26} (10^7 N/m)	D_{16} (N.m)	D_{26} (N.m)
Panel 1	0	0	-255.12	291.29	-3.95	-8.71	-45.76	-95.60
Panel 2	0	0	446.53	474.65	1.80	-2.95	-88.35	-24.67
Panel 3	0	0	-216.08	100.00	-0.48	0.55	-66.76	-18.39
Panel 4	0	0	151.38	341.50	-0.98	-2.28	-46.05	-12.74
Panel 5	0	0	-240.60	-98.80	4.01	0.21	-19.98	-47.04
Panel 6	0	0	-14.62	21.46	-6.44	-2.43	-4.28	-1.26
Panel 7	0	0	-18.86	-39.66	-3.97	-1.38	-22.10	-7.77
Panel 8	0	0	2.30	5.67	3.43	2.65	13.76	10.62
Panel 9	0	0	26.90	-557.93	-3.42	2.52	-43.51	-39.03
Panel 10	0	0	-695.53	-443.14	25.30	4.00	-46.09	-95.27
Panel 11	0	0	246.37	479.97	-5.30	-1.74	-23.36	-30.51

Moreover, the total percentage weight-saving obtained from PSO's optimised design is 48.9% which is 6.4% differ to GA's optimised design. The highest weight saving of 54.2% is obtained from Spar 3 panel. Furthermore, the structural weight of the optimised top and bottom skin panels are 48.2% lighter than the benchmark model. In terms of the computational time, PSO is more efficient as compared to the GA for the current design problem. Note that the same convergence/stopping criterion is used for both methods. The total iteration runs required to achieve the convergence for the PSO is 460 runs

Table 4.3: The extension-shear coupling terms (A_{16} and A_{26}) and bending-twisting coupling terms (D_{16} and D_{26}) deduced from the optimised model and benchmark EBW model for bottom skins panels.

Bottom skin panels								
	Benchmark EBW model				Optimised Model			
	A_{16} (N/m)	A_{26} (N/m)	D_{16} (N.m)	D_{26} (N.m)	A_{16} (10^7 N/m)	A_{26} (10^7 N/m)	D_{16} (N.m)	D_{26} (N.m)
Panel 1	0	0	-1153.11	-428.64	-4.29	-8.38	24.65	88.44
Panel 2	0	0	-314.95	-738.21	-9.08	-3.14	31.88	-21.20
Panel 3	0	0	-321.23	-560.33	-3.09	-6.74	-27.62	20.74
Panel 4	0	0	220.43	57.33	2.76	5.34	16.29	41.61
Panel 5	0	0	-209.74	-57.59	-7.44	-2.69	-9.85	-11.51
Panel 6	0	0	-16.30	13.40	-2.77	-6.10	-18.13	-25.40
Panel 7	0	0	-35.93	-10.55	-4.20	-0.63	8.43	7.79
Panel 8	0	0	-5.87	-8.19	-2.26	-4.29	-2.21	1.36
Panel 9	0	0	-553.95	-81.12	-4.92	-7.57	41.37	65.19
Panel 10	0	0	519.06	80.52	0.64	-3.49	-78.78	-33.61
Panel 11	0	0	145.09	-210.77	-2.56	-3.28	-51.06	-49.58

Table 4.4: The extension-shear coupling terms (A_{16} and A_{26}) and bending-twisting coupling terms (D_{16} and D_{26}) deduced from the optimised model and benchmark EBW model for Spar 1 panels.

Spar 1 panels								
	Benchmark EBW model				Optimised Model			
	A_{16} (N/m)	A_{26} (N/m)	D_{16} (N.m)	D_{26} (N.m)	A_{16} (10^7 N/m)	A_{26} (10^7 N/m)	D_{16} (N.m)	D_{26} (N.m)
Panel 1	0	0	-883.76	-95.44	-5.25	-7.41	64.69	13.87
Panel 2	0	0	360.41	-140.10	0.23	-4.52	-20.49	43.52
Panel 3	0	0	-678.22	-180.66	3.67	0.004	-72.34	-30.71
Panel 4	0	0	-352.96	13.79	0.78	4.67	-50.92	-19.49
Panel 5	0	0	-185.09	-328.12	0.23	4.89	-17.10	-41.13
Panel 6	0	0	52.05	194.46	0.29	4.44	-26.74	-13.15
Panel 7	0	0	-56.34	-40.53	2.16	2.84	15.11	6.64
Panel 8	0	0	-46.39	-29.46	1.77	4.31	-8.38	5.95

as opposed to the GA, which requires 780 runs. The flutter speed for both optimised designs are closed to $V_{\text{f,Design}}$ (less than 0.0001% difference) which is the only active design constraint for this problem. From the 12 modes predicted in the analysis, flutter is the critical mode of failure whereas divergence was observed at higher airspeeds.

Tables 4.2 to 4.6 provide the comparison between the optimised model and the benchmark EBW model in terms of the extension-shear (A_{16} and A_{26}) and bending-twisting coupling (D_{16} and D_{26}) parameters. For each laminate panels, the resultant lamination parameters are translated into the stiffness matrix components (A_{ij} and D_{ij}) to provide a meaningful comparison. Since the EBW model is made up from quasi-isotropic laminates, the extension-shear coupling terms (A_{16} and A_{26}) are zero. However, in this work,

Table 4.5: The extension-shear coupling terms (A_{16} and A_{26}) and bending-twisting coupling terms (D_{16} and D_{26}) deduced from the optimised model and benchmark EBW model for Spar 2 panels.

Spar 2 panels								
	Benchmark EBW model				Optimised Model			
	A_{16} (N/m)	A_{26} (N/m)	D_{16} (N.m)	D_{26} (N.m)	A_{16} (10^7 N/m)	A_{26} (10^7 N/m)	D_{16} (N.m)	D_{26} (N.m)
Panel 1	0	0	392.28	972.25	-6.82	-0.93	20.95	87.30
Panel 2	0	0	233.19	822.42	-5.41	-2.83	-72.92	-6.88
Panel 3	0	0	-773.43	-304.04	-8.20	-2.92	27.32	39.94
Panel 4	0	0	132.59	330.58	5.27	2.84	36.67	17.19
Panel 5	0	0	-233.09	0.05	0.11	3.14	-52.17	-20.21
Panel 6	0	0	-137.87	-128.53	-4.17	-4.01	-10.09	-28.29
Panel 7	0	0	-94.51	-72.09	-0.28	-3.13	-9.29	0.00
Panel 8	0	0	-16.50	23.57	-3.23	-3.54	16.80	5.34

Table 4.6: The extension-shear coupling terms (A_{16} and A_{26}) and bending-twisting coupling terms (D_{16} and D_{26}) deduced from the optimised model and benchmark EBW model for Spar 3 panels.

Spar 3 panels								
	Benchmark EBW model				Optimised Model			
	A_{16} (N/m)	A_{26} (N/m)	D_{16} (N.m)	D_{26} (N.m)	A_{16} (10^7 N/m)	A_{26} (10^7 N/m)	D_{16} (N.m)	D_{26} (N.m)
Panel 1	0	0	-457.27	225.27	1.35	-2.55	-98.10	-31.75
Panel 2	0	0	470.35	65.44	2.43	1.75	-97.25	-31.97
Panel 3	0	0	573.76	227.07	-7.48	-3.92	-6.30	8.04

the optimisation procedures opted for unbalanced and symmetric laminates, which results in non-zero A_{16} and A_{26}. The presence of extension-shear coupling in the laminate, allowing the laminate panels to shear and elongate under normal and twist forces.

Additionally, due to a balanced laminate, the existence of bending and twist moment cause the twist of the laminate and in-plane curvatures. In combination, the presence of these coupling parameters causing the structures to bend and twist due to the moment forces in the structures (weight) and shear as well as elongation due to the aerodynamic forces. However, the comparison of the bending-twisting parameters (D_{16} and D_{26}) of the optimised design with the EBW model shows reduction in the magnitude which suggests that optimised structure is stiffer which helps to resist the bending and twist deformation and hence reduce the flutter speed, V_f closer to the set target value in the optimisation procedure such that $V_f = 1.15V_D$.

Figure 4.2 provides the thickness variation plots of the optimised top skin, bottom skin

and spar panels obtained using GA and PSO method. Figure 4.2(a) compares the thickness of the top skin panel for the benchmark model and the optimised design. The optimised designs have thinner panel sections compared to the benchmark model which leads to a lower structural weight. The thickest panel was obtained at the root section and allowed to drop across the wingspan for better weight distributions and to maintain ply contiguity. The bottom skin and the spar panels show similar thickness variation as the top skin panel.

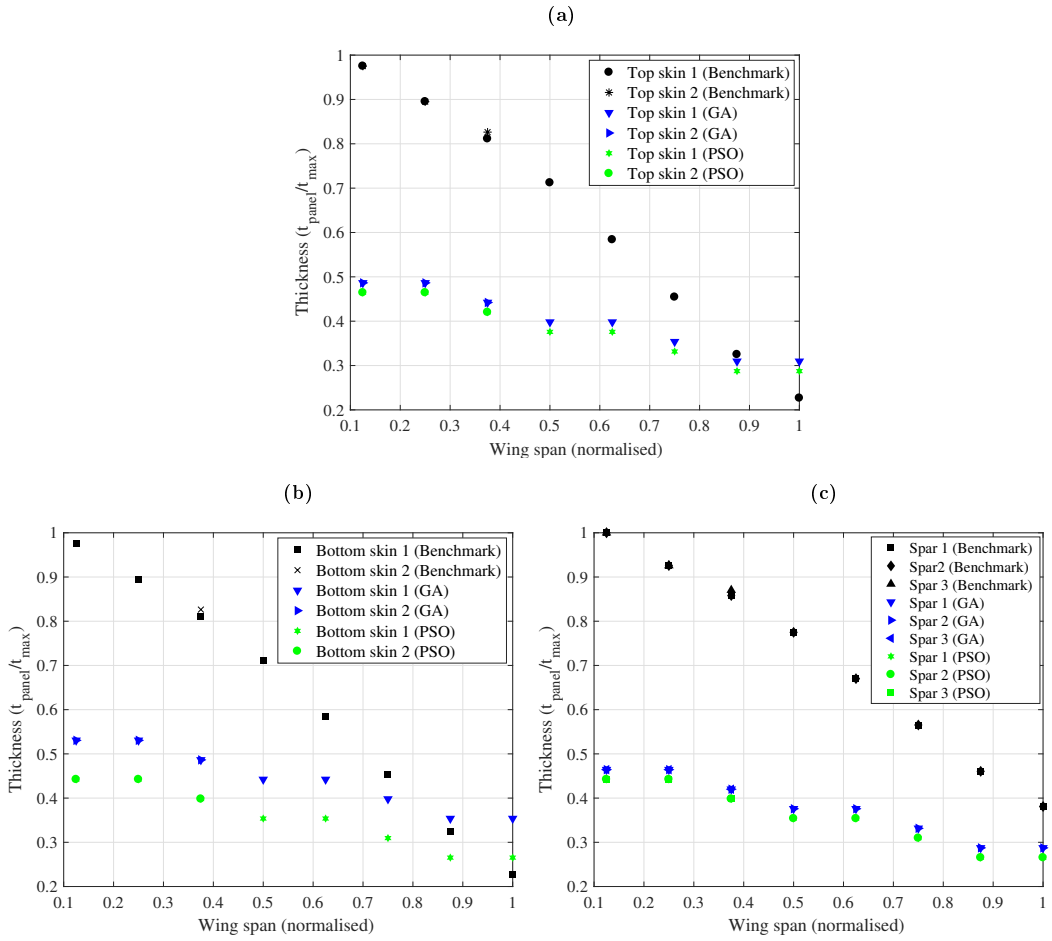

Figure 4.2: Panel thickness of the deterministic optimised design (flutter/divergence constraint only) obtained from GA and PSO; (a) Top skin panels, (b) Bottom skin panels and (c) Spar panels.

The efficiency of PSO over GA is evidenced in the plots as PSO is capable of solving the design problem with smaller thickness values as compared to the GA without violating the design constraints. These findings are due to multiple design solutions available in the design problem, and the PSO is capable of selecting the best design solution with fewer iteration steps. Given that the nature of the design variables is continuous in current problem, PSO shows good promise and is more efficient in solving design problems with

large design spaces. Henceforth, the PSO optimised design can be regarded as the best solution for deterministic flutter design problem.

4.4.2 Optimisation for flutter and gust responses

The second design problem aims to establish the possibility of structural weight saving from aeroelastic tailoring in the presence of multiple aeroelastic design constraints; flutter/divergence and gust response. In the previous problem, a total weight saving of 48.9% was achieved with flutter/divergence as the only active design constraint. In reality, the optimisation of any aircraft structure involves consideration of multiple design constraints which require multi-constraints or a multi-objective optimisation process. The inclusion of multiple design constraints often increases the complexity of the design problem, hence requiring an effective and efficient optimisation approach to obtain reliable solutions.

Herein, the benchmark wing model is optimised for minimum structural weight subjected to flutter/divergence and gust response constraints. The response due to the gust is measured in terms of minimum strain energy governed by the wing root bending moment induced against discrete gust load as proposed by [47]. The discrete gust is idealised as *'1-cosines'* gust profile given by the expression in Eqn. (3.31) (page 79).

The aeroelastic response for flutter/divergence is evaluated using frequency matching, *'p-k'* matched-method (`PKNL` method in MSc. Nastran's `SOL 145`. The frequency and damping output from the analysis are post-processed to determine the flutter/divergence speed. The mode switching behaviour was monitored by acquiring the first 12 modes in the model analysis.

The wing box dynamic aeroelastic response to discrete gust was performed using MSc. Nastran's `SOL 146`: Dynamic Aeroelastic Analysis. The gust velocity variation over time for different gust wavelengths are input in `SOL 146` as load-frequency table (`TLOAD1` and `TABLED1`). The gust wavelength are selected between 18 m to 214 m to represent the range of critical gust wavelength [1]. The set of frequencies used to obtain the frequency response solutions are defined with `FREQ1` input command. The time step intervals for the transient responses are defined using `TSTEP` input command. For this study, the time step response is eight seconds. The reference gust velocity, U_{ref} of 17.07 ms^{-1} at sea level

is used in the gust analysis. The relative gust design velocity, w_{go} and the frequency data at different gust length were given in Table 3.5 (page 79). Figure 4.3 provides the variation of gust velocity as function of time evaluated at reference gust velocity, U_{ref} of 17.07 ms^{-1} (at sea level).

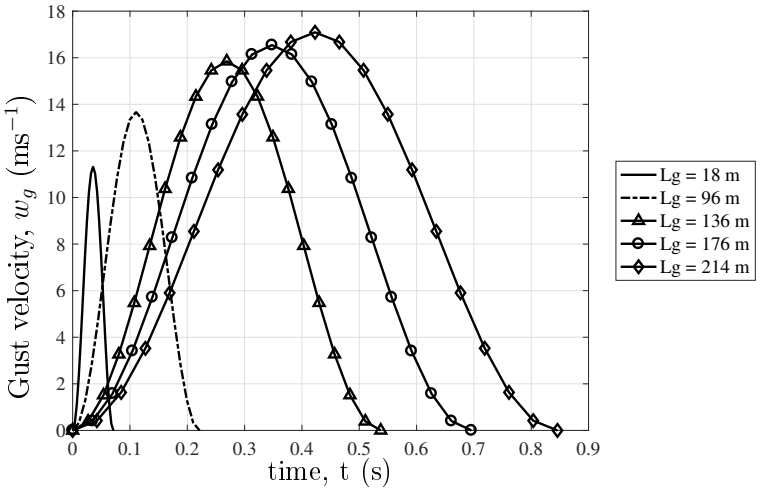

Figure 4.3: The plot of gust velocity variation against time evaluated at reference gust velocity, U_{ref} of 17.07 ms^{-1} at sea level.

The second design problem can be formulated as

$$
\begin{aligned}
\underset{\mathbf{x}}{\text{minimize}} \quad & f_{2,\text{obj}}(W(\mathbf{x}), f_{2,\text{cost}}(\mathbf{x})), \\
\text{subject to:} \quad & \text{Flutter speed}, \quad V_{\text{f}}(\mathbf{x}) \geq 1.15 V_{\text{D}}, \\
& \text{Wing Root Bending Moment}, \quad \max(RBM(\mathbf{x}, L_{\text{g}})) \leq \max(RBM_{\text{Benchmark}}(L_{\text{g}})), \\
& \mathbf{x} = [\xi_1^A, ..., \xi_4^A, \xi_1^D, ..., \xi_4^D \quad \text{and} \quad t_{\text{panel},1}, ..., t_{\text{panel},41}],
\end{aligned}
\tag{4.7}
$$

where

- $\mathbf{x}$ is a vector containing the design variables.
- ξ is the lamination parameters. For each panel, there are eight lamination parameters chosen as the design variables. Only unbalanced and symmetrical laminates are considered in this work.
- t_{panel} is the thickness of the composite laminate panels. A total of 41 panels are considered in this work; 11 top skin panels, 11 bottom skin panels and 19 spar panels.

- The flutter speed, V_{f} is calculated from conventional $V-g$ plot, assuming Mach 0.82 and flight dive velocity, V_{D} at 10000m. V_{f} is assumed to be the lowest of 12 values (from 12 modes) at which the damping factor equals zero.
- For gust response constraint, six different values of gust wavelength, L_{g} are used to determine the maximum RBM. The values are given in Table 3.5 (page 79).

The objective function in Eqn. (4.7) is given as

$$f_{2,\mathrm{obj}} = \frac{W(\mathbf{x})}{W_{\mathrm{Benchmark}}} + f_{2,\mathrm{cost}}(\mathbf{x}), \tag{4.8}$$

where W is the wing structural weight (skins and spars only); $f_{2,\mathrm{cost}}$ is a cost penalty function introduced to account for aeroelastic constraints violation as

$$f_{2,\mathrm{cost}} = w_{\mathrm{f}} \times \left|\frac{V_{\mathrm{f}} - V_{\mathrm{f,Design}}}{V_{\mathrm{f,Design}}}\right| + w_{\mathrm{g}} \times \left|\frac{RBM}{RBM_{\mathrm{Benchmark}}}\right|, \tag{4.9}$$

and where

$$w_{\mathrm{constr}} = \{w_{\mathrm{constr}_i} \in [0,1] : \sum_{\mathrm{constr}_i} = 1, \mathrm{constr}_i \in \{\mathrm{f},\mathrm{g}\}\} \tag{4.10}$$

is the set of weighting coefficients for flutter and gust response constraints. By variation of the weighting coefficients, a Pareto front of the optimised solution can be obtained. The weighting coefficients for flutter and gust are given in Table 4.7.

Table 4.7: The values of the weighting factor specified in the optimisation procedures to obtain minimum structural weight subjected to flutter and gust design constraints.

Run	Weighting factors	
ID	w_{f}	w_{g}
1	1.000	0.000
2	0.900	0.100
3	0.800	0.200
4	0.700	0.300
5	0.600	0.400
6	0.500	0.500
7	0.400	0.600
8	0.300	0.700
9	0.200	0.800
10	0.100	0.900
11	0.000	1.000

The overall best deterministic design solution is chosen as the best Pareto point according to the averaging principle proposed in Ref. [187]. The best Pareto point is deduced by

minimising the expression ($|\Sigma - 1|$), where

$$\Sigma = a_1 \frac{W}{W_{\min}} + a_2 \frac{V_{\mathrm{f}}}{V_{\mathrm{f,max}}} + a_3 \frac{RBM}{RBM_{\min}}, \tag{4.11}$$

and

- The subscript 'min' and 'max' denote the minimum and maximum values obtained for flutter and gust constraints from all possible weighting combinations.
- a_1, a_2 and a_3 are the constant parameters and the sum is equal to 1.

Equation (4.11) is used to determine the best Pareto solution out of possible optimised designs (at different weighting factors) obtained from the optimisation. The equation is calculated using the output response of the possible optimised design (i.e. post-processing) and not directly incorporated into the optimisation algorithm. The intention is to obtain an ideal design with optimum wing's responses. For example, from Eqn. (4.11), the best optimum Pareto solution is selected when $|\Sigma - 1|$ is at minimum, such that a design with minimum weight, maximum flutter speed and the minimum wing root bending moment is attained. The denominators of every component in the equation are deduced from the responses of all possible optimised design solutions.

The design variables consist of lamination parameters ($\xi^{A}_{1,2,3,4}$ and $\xi^{D}_{1,2,3,4}$) and panel thickness of skins and spars. The lamination parameters are varied between -1 to 1 and governed by the feasible region constraints as in Eqn. (4.3). The lower bound for the panel thickness is set to be 20 plies as in Section 4.4.1 (page 99). Finally, a contiguity constraint is included in the optimisation algorithm to ensure no more than two plies were allowed to be dropped between adjacent panels to prevent unnecessary sharp changes in thickness variations.

The current design problem was solved using GA and PSO. For results convergence, 20 populations/particles and a maximum number of generation/iteration of 50 was specified in the optimisation procedures. Similar convergence criteria as in Section 4.4.1 (page 99) was defined in the optimisation.

Table 4.8 provides a summary of the structural weight and the responses for the optimised design for different combinations of the weighting factors. The weighting factors are assigned such that the sum of each factor equals unity. The contribution of the design

constraints on the optimised solution can be assessed based on the weighting of each constraint. For example, if $w_f = 1$, the optimised solution is contributed only by the flutter constraint.

Table 4.8: The deterministic optimised solutions for design problem subjected to flutter and wing root bending moment constraints. GA and PSO algorithms are used for optimisation procedures.

Run	GA				PSO			
ID	$\frac{W}{W_{\text{Benchmark}}}$	$\frac{V_f}{V_{f,\text{Design}}}$	$\frac{RBM}{RBM_{\text{Benchmark}}}$	$\lvert\Sigma - 1\rvert$	$\frac{W}{W_{\text{Benchmark}}}$	$\frac{V_f}{V_{f,\text{Design}}}$	$\frac{RBM}{RBM_{\text{Benchmark}}}$	$\lvert\Sigma - 1\rvert$
1	0.918	1.033	0.415	0.655	0.588	1.000	0.119	0.468
2	0.918	1.034	0.293	0.396	0.588	1.001	0.071	0.142
3	0.932	1.044	0.257	0.329	0.588	1.000	0.079	0.196
4	0.679	1.026	0.165	0.005	0.588	1.000	0.063	0.087
5	0.679	1.026	0.164	0.003	0.588	1.002	0.053	0.020
6	0.679	1.026	0.164	0.003	0.588	1.000	0.057	0.047
7	0.679	1.026	0.164	0.003	0.588	1.001	0.062	0.081
8	0.679	1.026	0.164	0.003	0.588	1.000	0.052	0.013
9	0.679	1.026	0.164	0.003	0.588	1.000	0.058	0.053
10	0.679	1.026	0.164	0.003	0.588	1.003	0.050	0.000
11	0.679	1.026	0.160	0.006	0.588	1.003	0.054	0.027

Overall, in terms of the structural weight, it can be said that the optimised solutions obtained from the second design problem are slightly heavier as compared to the deterministic flutter solution (Det-V_f) as given in Table 4.8. An increase of 16.81% in structural weight was measured for GA optimised solution in comparison with deterministic flutter solution. It is also noticed that higher increases in the structural weight is measured when $w_g \leq 0.2$ for GA solutions. A smaller increase in structural weight was observed for PSO solution with 7.71%. The increases were expected due to additional gust constraint in the optimisation. Despite that, the optimised designs provide a weight saving of 32.1% for GA solution and 41.2% for PSO solution in comparison with the benchmark model. Furthermore, it is also noticed that the weighting factors provide no influence on the optimised weight in both optimisation approaches (GA and PSO). These are thought to be due to the limit set on the minimum number of plies allowed on each panel.

For the GA optimised solution, the lowest $V_f/V_{f,\text{Design}}$ and $RBM/RBM_{\text{Benchmark}}$ is 1.026 and 0.160, respectively. For PSO optimised solution, the lowest $V_f/V_{f,\text{Design}}$ of 1.000 is obtained when $w_f = \{1.0, 0.8, 0.7, 0.5, 0.3, 0.2\}$. The minimum $RBM/RBM_{\text{Benchmark}}$ value is 0.05; obtained when $w_g = 0.8$. The flutter speed obtained from PSO is closer to the target design speed with 95% reduction in RBM value. Note that the benchmark

wing model is an initial model provided by the industrial partner and not optimised. Hence, a higher percentage of RBM reduction is expected when a comparison is made with the benchmark model. Also, the results suggest that PSO is more efficient than GA due to effective communication between the particles and lesser function evaluation in the algorithm, which results in less computational effort to obtain high-quality solutions.

The contribution of each design constraints can be efficiently quantified in the optimisation using the cost function and weighting factors. Figure 4.4 provides the Pareto front for the optimised solutions with each design constraints are plotted against the weighting factors. It can be seen that at higher weighting factor ($w_\mathrm{f} \approx 1$ or $w_\mathrm{g} \approx 1$), the response constraints determined are converged to the target design value. For example, from Figure 4.4(a), the $V_\mathrm{f}/V_{\mathrm{f,Design}}$ seem to converge to $V_{\mathrm{f,Design}}$ as $w_\mathrm{f} \approx 1$ (GA optimised designs). While for PSO design, the $V_\mathrm{f}/V_{\mathrm{f,Design}}$ seem to be closed to the target design value ($V_\mathrm{f}/V_{\mathrm{f,Design}} = 1$). Higher weighting factor results in a higher value of cost function (for a particular design constraint), hence lower objective function value is attained. Similar observations can be said for the RBM, as the w_g increase to unity, the RBM values are converged to $RBM_{\min}$ for both GA and PSO optimised designs. Furthermore, it can be seen that lower $RBM_{\min}$ is obtained from PSO in comparison to GA solutions.

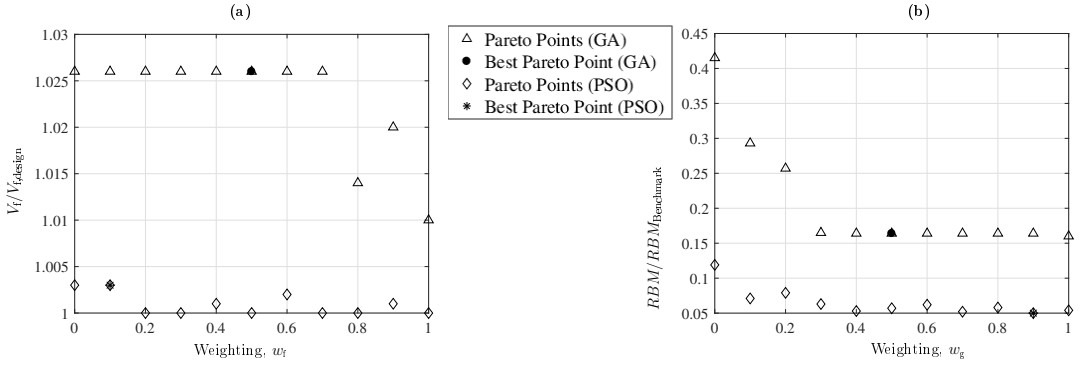

Figure 4.4: Pareto plots for (a) Flutter constraint against weighting, w_f and (b) RBM constraint against weighting, w_g for optimised design obtained from GA and PSO.

The best Pareto point for the current design problem can be determined based on the averaging principle (Eqn. (4.11)). The best solution is deduced when the expression $|\Sigma - 1|$ is at minimum as given in Table 4.8. For GA, the best Pareto point is obtained when $w_\mathrm{f} = 0.5$ and $w_\mathrm{g} = 0.5$ with $|\Sigma - 1| = 0.003$. For PSO, the best Pareto point is deduced when $w_\mathrm{f} = 0.1$ and $w_\mathrm{g} = 0.9$ with $|\Sigma - 1| = 0.000$. The thickness variation

for the optimised panels (skins and spars) are plotted against the benchmark model and the deterministic flutter solution as shown in Figure 4.5. In general, the top skin panel's thickness values obtained for GA optimised solution are slightly lower compared to the deterministic flutter design. However, the top skin panel's thickness values for PSO solution are slightly higher compared to both GA solution and the deterministic flutter. Similar observations are remarked for the bottom skin panels. On the other hand, the spars panel's thickness values for PSO optimised solution are lower compared to the GA solution which results in a lower structural weight. In comparison with the benchmark model, the panel's thickness values for the optimised solutions (GA and PSO) are significantly lower which contributed to at least 32.1% weight saving.

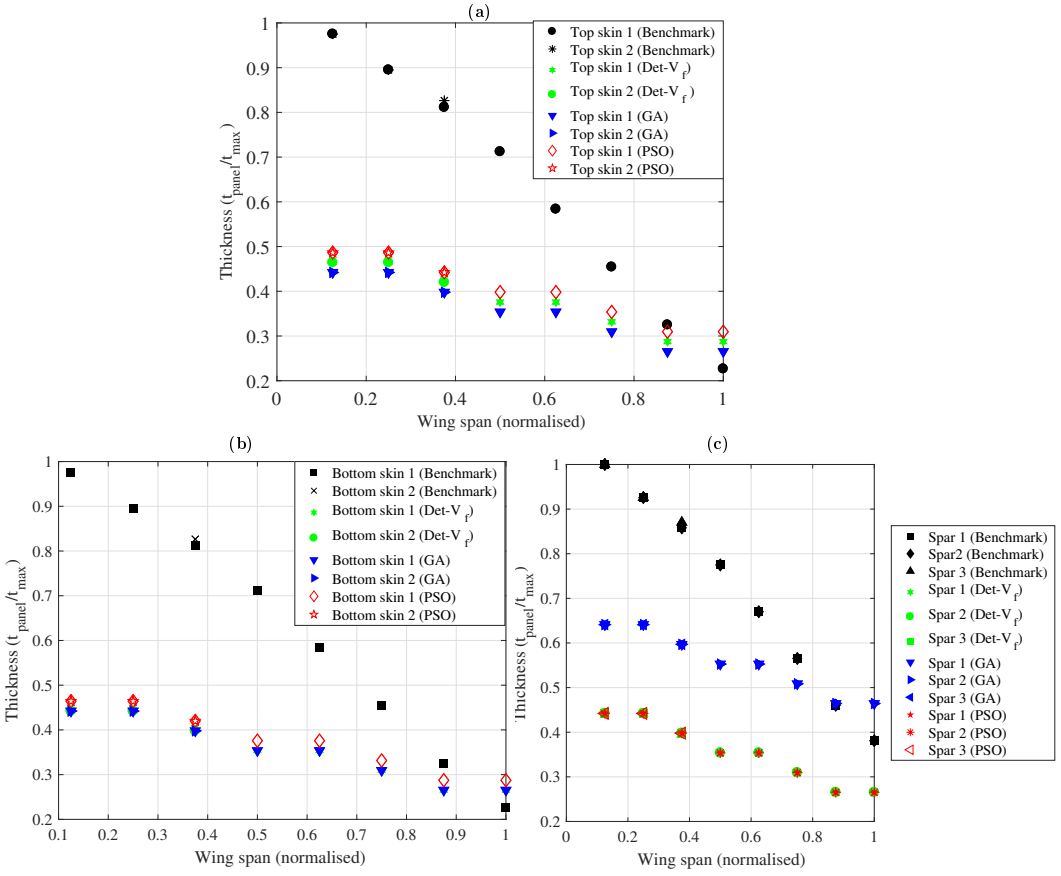

Figure 4.5: Thickness variation for skins and spars of the benchmark and optimised designs; (a) Top skin panel's thickness, (b) Bottom skin panel's thickness and (c) Spar panel's thickness. Thickness variation for deterministic flutter (Det-V_f) optimised design is plotted together with current optimised design solution.

4.5 Aeroelastic tailoring due to structural and aeroelastic responses

In this section, the benchmark composite wing is optimised for minimum structural weight subjected to multiple constraints that included structural and aeroelastic response constraints. The structural constraints are evaluated in terms of the laminate strains and buckling resistance due to static manoeuvre loads. In addition to this, the wing is evaluated in terms of the aeroelastic instability behaviours (flutter/divergence) and wing root bending moment response due to gust load. Two types of design cases were analysed as follows;

1. Aeroelastic tailoring to minimise the structural weight subject to **a static manoeuvre load** condition with structural and aeroelastic constraints (Single-point optimisation).
2. Aeroelastic tailoring to minimise the structural weight subject to **multiple static manoeuvre load** condition with structural and aeroelastic constraints (Multi-point optimisation).

In the first design case, the wing structure was optimised due to a static manoeuvre load. The structural design constraints that included strain and buckling are evaluated as well as the flutter and RBM response. In second design case, the wing was optimised for similar objectives and constraints; however, the structural design constraints are evaluated subjected to multiple static load cases. The static manoeuvre loads are deduced from various aerodynamic conditions as given in Table 3.4 (page 66).

MSc. Nastran was used for model analysis throughout the optimisation process coupled with MATLAB's global optimisation toolbox for PSO method. Only the PSO method is employed in this design problem as it has been proven to be more efficient than GA method in Section 4.4.2 (page 104).

4.5.1 Design Optimisation Formulation

For both design cases described above, the optimisation problem is formulated as follows;

$$\begin{aligned}
&\underset{\mathbf{x}}{\text{minimize}} \quad && f_{3,\text{obj}}(W(\mathbf{x}), f_{3,\text{cost}}(\mathbf{x})), \\
&\text{subject to:} && \text{Strain Failure Index,} \quad FI(\mathbf{x}) \leq 1 \quad \text{(Max. Strain)}, \\
& && \text{Buckling critical load factor,} \quad \lambda_{\text{crit}}(\mathbf{x}) \geq 1, \\
& && \text{Flutter speed,} \quad V_{\text{f}}(\mathbf{x}) \geq 1.15 V_{\text{D}} \quad (V_{\text{D}} = \text{Design dive speed}), \\
& && \text{Wing Root Bending Moment,} \quad \max(RBM(\mathbf{x}, L_{\text{g}})) \leq \max(RBM_{\text{Benchmark}}(L_{\text{g}})), \\
& && \mathbf{x} = [\xi_1^A, \ldots, \xi_4^A, \xi_1^D, \ldots, \xi_4^D, t_{\text{panel},1}, \ldots, t_{\text{panel},41}],
\end{aligned} \tag{4.12}$$

where $\mathbf{x}$ and L_{g} are the vector containing the design variables and gust wavelength, respectively. A total of eight lamination parameters per panel is assigned as design variables. Only unbalanced-symmetrical laminate is considered in the optimisation. The optimisation is performed on the top (11 panels) and bottom skin (11 panels) panels as well as the spar panels (19 panels) of the composite wing model.

The objective function in Eqn. (4.12) is given as

$$f_{3,\text{obj}} = \frac{W(\mathbf{x})}{W_{\text{Benchmark}}} + f_{3,\text{cost}}(\mathbf{x}), \tag{4.13}$$

where W is the structural weight of the skin and spar panels; $f_{3,\text{cost}}$ is the cost function introduced to account for multiple design constraints as

$$f_{3,\text{cost}} = w_{\text{f}} \times \left| \frac{V_{\text{f}} - V_{\text{f,Design}}}{V_{\text{f,Design}}} \right| + w_{\text{g}} \times \left| \frac{RBM}{RBM_{\text{Benchmark}}} \right| + w_{\text{EIG}} \times \left| \frac{\lambda_{\text{crit}} - \lambda_{\text{Design}}}{\lambda_{\text{Design}}} \right| + w_{\text{FI}} \times \left| \frac{FI - FI_{\text{Design}}}{FI_{\text{Design}}} \right|, \tag{4.14}$$

and where

$$w_{\text{constr}} = \{ w_{\text{constr}_{\text{i}}} \in [0,1] : \sum_{\text{constr}_{\text{i}}} w_{\text{constr}_{\text{i}}} = 1, \ \text{constr}_{\text{i}} \in \{\text{f}, \text{g}, \text{EIG}, \text{FI}\} \} \tag{4.15}$$

is the set of weighting coefficients relative to each of the constraints. The subscripts 'EIG', 'FI' and 'Design' denote the buckling, strain failure index and allowable design values. The values of the weighting factors are chosen at random such that the sum equals one and are given in Table 4.9. averaging principle, the best-optimised solution

is determined as a Pareto point minimising the expression, $|\Sigma - 1|$, where

$$\Sigma = b_1 \frac{W}{W_{\min}} + b_2 \frac{V_{\mathrm{f}}}{V_{\mathrm{f,max}}} + b_3 \frac{RBM}{RBM_{\min}} + b_4 \frac{\lambda_{\mathrm{crit}}}{\lambda_{\mathrm{crit,min}}} + b_5 \frac{FI}{FI_{\max}}, \tag{4.16}$$

and

- The subscripts 'min' and 'max' denote the minimum and maximum values obtained for each constraint for all possible weighting combination.
- b_1, b_2, b_3, b_4 and b_5 is the constant parameters, each having a value of 0.2.

Equation (4.16) is calculated using the output responses from all ten possible solutions, where the summation of all constant parameters is equal to 1. The best pareto point is determined such that $|\Sigma - 1|$ is at minimum.

Table 4.9: Weighting factors for the single point and multi-point optimisation runs.

Run	Weighting factors			
ID	w_{f}	w_{g}	w_{EIG}	w_{FI}
1	1.000	0.000	0.000	0.000
2	0.000	1.000	0.000	0.000
3	0.000	0.000	1.000	0.000
4	0.000	0.000	0.000	1.000
5	0.250	0.250	0.250	0.250
6	0.500	0.250	0.125	0.125
7	0.250	0.500	0.125	0.125
8	0.250	0.125	0.125	0.500
9	0.125	0.250	0.500	0.125
10	0.100	0.300	0.300	0.300

4.5.1.1 Structural responses

The structural responses of the composite wings are measured in terms of the laminate strain and buckling resistance. The laminate strain and the critical buckling load factor of the skins and spars panels are evaluated when subjected to static manoeuvre loads. The static load distributions are obtained from the static aeroelastic analysis (see Section 3.4.2 (page 66)) and are included in the model as nodal forces. The strength performance of the composite panels is evaluated in terms of the maximum and minimum strain limit. The strain failure index is introduced to quantify the strength performance by not exceeding

a set allowable value and formulated as

$$FI_{\text{strain}} = \max\Big(\frac{\epsilon_{\text{min}}}{\epsilon_{\text{min,allowable}}}, \frac{\epsilon_{\text{max}}}{\epsilon_{\text{max,allowable}}}, \frac{\gamma_{\text{min}}}{\gamma_{\text{min,allowable}}}, \frac{\gamma_{\text{max}}}{\gamma_{\text{max,allowable}}}\Big), \tag{4.17}$$

where ϵ_{min} and ϵ_{max} are the principle strains for laminate under compression and tension, respectively. The allowable values are set to $\epsilon_{\text{min,allowable}} = -5900\mu\epsilon$ and $\epsilon_{\text{max,allowable}} = 7100\mu\epsilon$. The shear strains limit is defined in terms of maximum and minimum shear strains, with allowable values set to $\gamma_{\text{min,allowable}} = -4500\mu\epsilon$ and $\gamma_{\text{max,allowable}} = 4500\mu\epsilon$. The upper boundary for FI is set as 1.0.

The buckling performance is evaluated in terms of the critical buckling load factor, λ_{crit}. The wing composite structure is optimised such that $\lambda_{\text{crit}} > 1$ to prevent the structure from buckling. Ten buckling modes are computed to account for mode switching. The strength and buckling analyses are performed in MSc. Nastran's `SOL 105`.

4.5.1.2 Aeroelastic behaviour

The aeroelastic stability of the composite wing is evaluated using MSc. Nastran's `SOL 145`, which employs the frequency matching, *'p-k'* matched-method to predict the flutter/divergence speed. The analysis is performed assuming Mach 0.82 and the flight dive velocity, V_{D} at 10000m. The structural frequencies, as well as the modal amplitudes and damping, are obtained from the analysis as a function of airspeed. The flutter speed at each mode is determined from the $V-g$ plot at which the damping becomes negative. A total of 12 modes are considered to ensure adequate representation of the aeroelastic behaviour. Further details on the flutter analysis can be found in Section 3.4.4 (page 74).

The wing aeroelastic response to the atmospheric turbulence, idealised as discrete *'1-cosines'* gust is evaluated in terms of the wing root bending moment (RBM). The gust wavelength, reference gust velocity and other parameters are previously defined in Section 4.4 (page 98).

4.5.1.3 Single-point optimisation

In the single-point optimisation approach, the reference jet aircraft (benchmark model) is optimised for minimum structural weight subjected to a static manoeuvre load case with multiple design constraints that included strain, buckling, aeroelastic stability and gust response. The aim of the study is to solve for a realistic optimised design by considering a single load case - single-point optimisation approach. The current practice in design process for aeroelastically-tailored wing structures involves consideration of multiple load cases which often computationally expensive. In this work, the method is thought to be sufficient in order to provide a realistic preliminary design for aircraft wing structure.

The load case is chosen from five static manoeuvre load condition provided by the industrial partner. Table 4.10 provides the parameters for the load condition employed in current analysis. The aerodynamic load distribution is obtained from the static aeroelastic analysis, and it is used as nodal forces for strength and buckling analysis.

Table 4.10: The parameters for the static manoeuvre condition. The load distributions obtained from the static aeroelastic analysis is used in the single-point optimisation procedure.

Parameters	Values	Parameters	Values
Mach no.	0.82	Dynamic pressure, P_{D} (Pa)	13038
Altitude, H (m)	10000	Acceleration, n_{z} (g)	2.5
Equivalent airspeed, EAS (ms^{-1})	146	Mass	Fuel

4.5.1.4 Multi-point optimisation

In the multi-point optimisation approach, the benchmark model is optimised for minimum structural weight subjected to multiple static manoeuvre loads with structural and aeroelastic design constraints. The case study aims to provide an alternative method and design solution for multi-constraints optimisation approach.

In this study, the design solution is obtained whilst satisfying all the design constraints at different load cases. Five different load cases are considered with different Mach number, flight altitude, fuel mass and acceleration. The load cases details are given in Table 3.4 (page 66). The same design constraints as in single-point optimisation method were used in this case study in order to obtain a meaningful comparison from the optimised designs.

4.5.2 Single-point vs. Multi-point optimisation

In Section 4.4.2 (page 104), it has been established that a significant structural weight saving is achieved via aeroelastic tailoring with aeroelastic design constraints. In addition to that, the wing root bending moment due to gust was minimised for the optimised design solution. Herein, the structural design constraint is added to the previous design problem. The aim is to obtain an optimised design with both structural and aeroelastic constraints satisfied. Two methods are introduced; Single-point and Multi-point optimisation approach. In the Single-point method, the wing is optimised subjected to a static manoeuvre load case while in latter method, the wing is optimised subject to multiple static manoeuvre load cases.

Table 4.11 and 4.12 summarised the results obtained from both optimisation procedures. The structural weight and the response constraint are tabulated together with $|\Sigma - 1|$ values. A total of ten optimisation runs are performed for each method with a different combination of weighting factors, w_i which are chosen at random. For the Single-point method, the lowest structural weight, $W/W_{\text{Benchmark}}$ is 0.620, obtained from RUN 7 with $w_{\text{f}} = 0.25$, $w_{\text{g}} = 0.5$, $w_{\text{EIG}} = 0.125$ and $w_{\text{FI}} = 0.125$. In comparison with the best-optimised design for multiple aerelastic constraints, an increase of 5.44% is observed in terms of the structural weight due to the additional structural design constraints.

Table 4.11: The deterministic optimised solution obtained with Single-point method. Particle Swarm Optimisation (PSO) algorithm is used for the optimisation procedures.

Run	Responses					
ID	$\frac{W}{W_{\text{Benchmark}}}$	$\frac{V_{\text{f}}}{V_{\text{f,Design}}}$	$\frac{RBM}{RBM_{\text{Benchmark}}}$	FI	λ_{crit}	$\lvert\Sigma - 1\rvert$
1	0.651	1.015	0.250	0.575	1.017	0.312
2	0.733	1.024	0.079	0.817	1.125	0.120
3	0.713	1.001	0.471	0.649	1.002	0.949
4	0.774	1.042	0.107	0.995	1.056	0.038
5	0.679	1.001	0.071	0.919	1.001	0.189
6	0.641	1.021	0.107	0.977	1.023	0.092
7	0.620	1.011	0.082	0.896	1.001	0.176
8	0.725	1.045	0.293	1.000	1.203	0.500
9	0.689	1.009	0.091	0.789	1.079	0.113
10	0.652	1.030	0.196	0.853	1.007	0.161

For the Multi-point method, the lowest structural weight, $W/W_{\text{Benchmark}}$ of 0.632 is obtained from RUN 7 with weighting factors; $w_{\text{f}} = 0.25$, $w_{\text{g}} = 0.5$, $w_{\text{EIG}} = 0.125$ and $w_{\text{FI}} = 0.125$. It is noticed that there is a slight increase in the lowest structural weight

Table 4.12: The deterministic optimised solution obtained with Multi-point method. Particle Swarm Optimisation (PSO) algorithm is used for the optimisation procedures.

Run	Responses					
ID	$\frac{W}{W_{\text{Benchmark}}}$	$\frac{V_{\text{f}}}{V_{\text{f,Design}}}$	$\frac{RBM}{RBM_{\text{Benchmark}}}$	FI	λ_{crit}	$\lvert\Sigma - 1\rvert$
1	0.651	1.016	0.247	0.598	1.014	0.459
2	0.733	1.022	0.178	0.821	1.114	0.344
3	0.713	1.001	0.512	0.641	1.005	1.273
4	0.798	1.055	0.068	0.957	1.164	0.080
5	0.671	1.018	0.325	0.990	1.041	0.782
6	0.649	1.023	0.108	0.996	1.053	0.132
7	0.632	1.014	0.091	0.946	1.001	0.054
8	0.672	1.035	0.259	0.914	1.194	0.604
9	0.795	1.014	0.278	0.805	1.005	0.636
10	0.856	1.041	0.067	0.995	1.030	0.074

in comparison to Single-point solution. This is due to the presence of multiple load cases which leads to a different design solution. Moreover, the results suggest that the design solution obtained from Single-point method might not be feasible as the analysis only consider a single manoeuvre load case, whereas, in reality, the aircraft wing is subjected to multiple load conditions. However, the optimised design obtained from Single-point method can be used as a preliminary design solution.

The distribution of the structural weight against each design constraints is plotted in Figure 4.6. For all design constraints, the lowest structural weight is obtained from the Single-point method. In addition to that, it is observed that a higher flutter speed can be obtained but with additional weight penalty as to increase the rigidity of the structure as shown in Figure 4.6(a). The flutter speed for all the optimum designs are less than $1.06V_{\text{f,Design}}$. The RBM values obtained from lightest design solutions (Single-point and Multi-point) are below 0.1, which is 90% reduction from the benchmark model. Similarly, for buckling constraint, the critical load factor, $\lambda_{\text{crit}} > 1$ is obtained for both solutions. Conversely, the analysis on the resultant FI values for the optimised design suggested that most of the design points show higher FI value due to the optimum panel thickness and the ply configurations of the optimised solution.

The contribution of each of the design constraints on the optimised solutions is evaluated with the use of weighting factors, w_i in the cost function as in Eqn. (4.14) (page 113). The effectiveness of the approach is evidenced such that the optimum response constraint is obtained when w_i of particular constraints ($i = \{\text{f,g,EIG,FI}\}$) is dominant. For example, consider the FI responses of the Single-point's optimised solution given in Table 4.11,

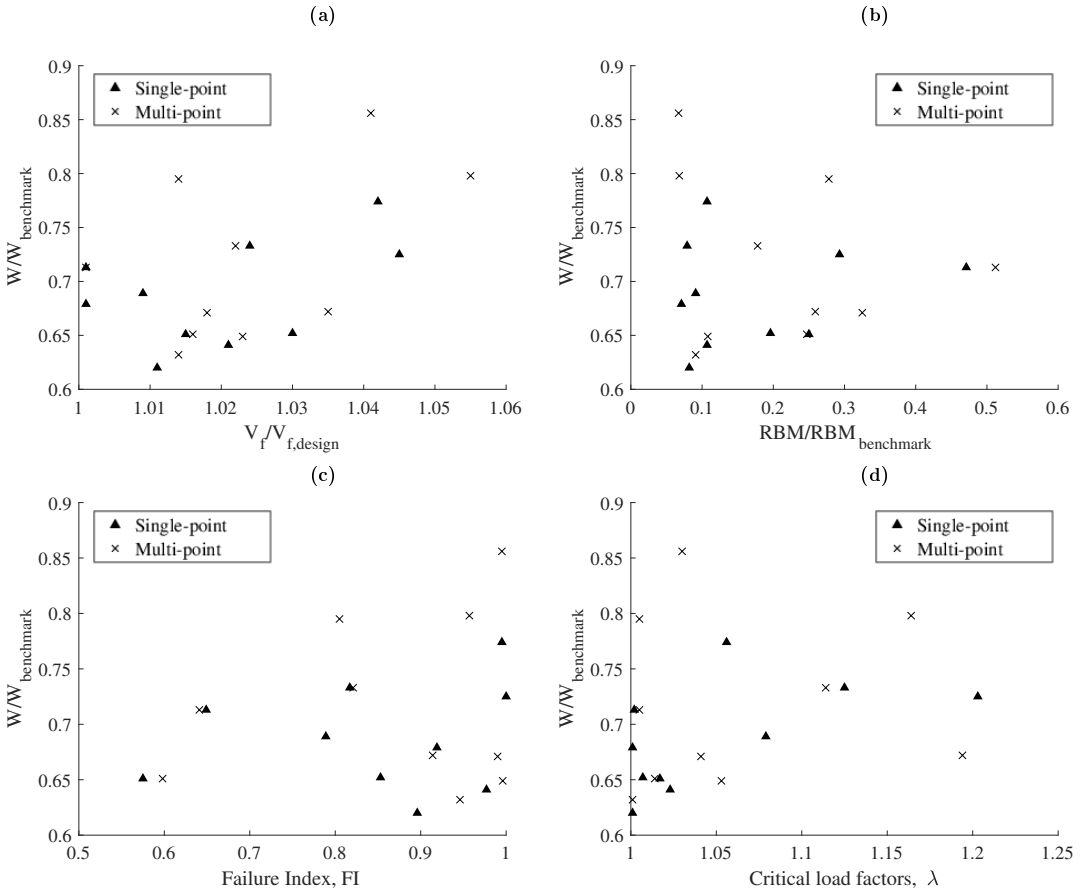

Figure 4.6: The plots of structural weight, $W/W_{\text{Benchmark}}$ against design constraints; (a)Structural weight, $W/W_{\text{Benchmark}}$ vs. Flutter speed, $V_{\text{f}}/V_{\text{f,Design}}$, (b)Structural weight, $W/W_{\text{Benchmark}}$ vs. Wing root bending moment, $RBM/RBM_{\text{Benchmark}}$, (c) Structural weight, $W/W_{\text{Benchmark}}$ vs. Strain Failure Index, FI and (d) Structural weight, $W/W_{\text{Benchmark}}$ vs. Buckling Critical Load Factor, λ_{crit}.

from RUN 8, weighting factors of $w_{\text{f}} = 0.25$, $w_{\text{g}} = 0.125$, $w_{\text{EIG}} = 0.125$ and $w_{\text{FI}} = 0.5$ results in optimised design with FI value equalled to FI_{Design} (FI_{Design}=1).

The distribution of the constraints responses against the weighting factors is plotted in the form of Pareto front as depicted in Figure 4.7. A clear convergence pattern can be seen from the RBM, FI and λ_{crit} plots where the Pareto points seem to converge to the target design value when w_i is increased to one. For the flutter response, the convergence pattern is not evidence despite the increase in w_{f} value. This finding is due to the small difference in the flutter speed value obtained from all combination of weighting factors.

The best-optimised design for Single-point and Multi-point methods are selected based on the averaging principle given in Eqn. (4.16) (page 113). The best design is chosen with a minimum $|\Sigma - 1|$ calculated from all possible optimised design solutions. For

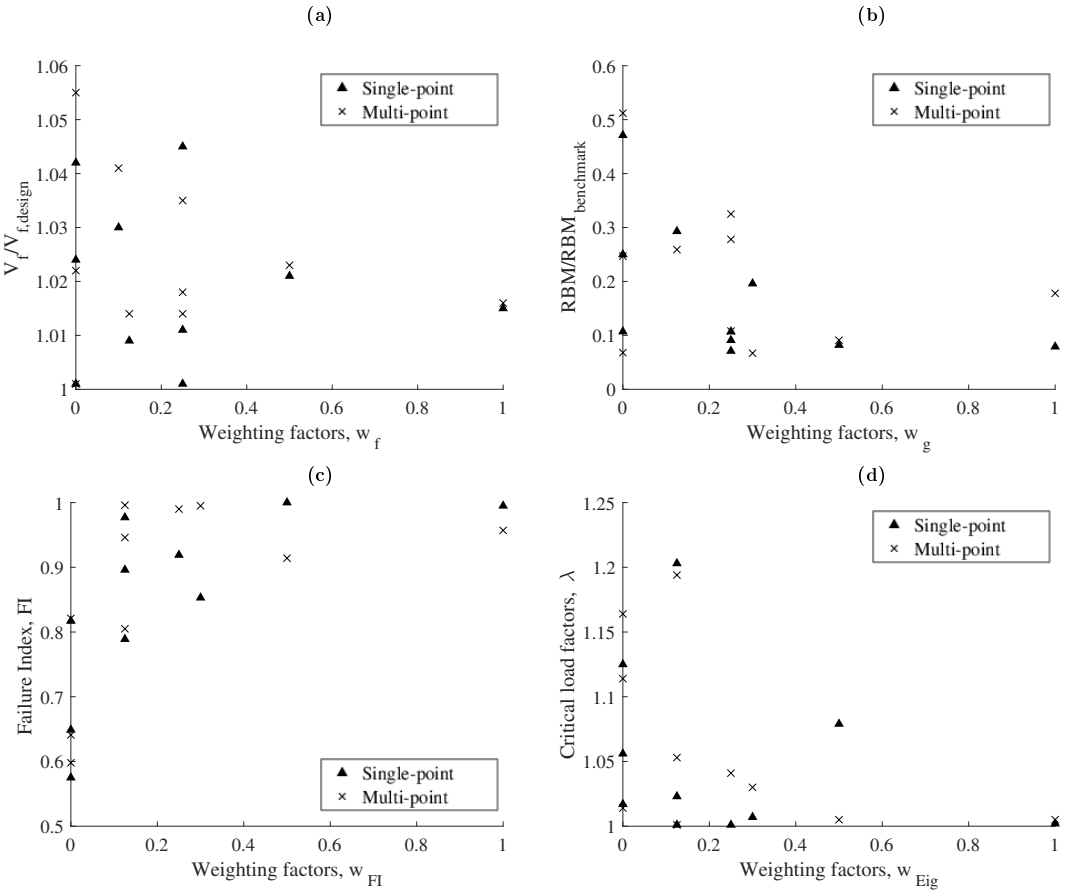

Figure 4.7: The pareto plots for (a) Flutter constraint against weighting factors, w_{f}, (b) Wing root bending moment, RBM constraint against weighting factors, w_{g}, (c) Strain constraint against weighting factors, w_{FI} and (d) Buckling constraint against weighting factors, w_{EIG}.

the Single-point method, the best deterministic optimum is obtained from RUN 4 with $|\Sigma - 1| = 0.038$ and weighting factors of $w_{\mathrm{f}} = 0.00$, $w_{\mathrm{g}} = 0.00$, $w_{\mathrm{EIG}} = 0.00$ and $w_{\mathrm{FI}} = 1.00$. The constraints values obtained are $W/W_{\mathrm{Benchmark}} = 0.774$, $V_{\mathrm{f}}/V_{\mathrm{f,Design}} = 1.042$, $RBM/RBM_{\mathrm{Benchmark}} = 0.107$, $FI = 0.995$ and $\lambda_{\mathrm{crit}} = 1.056$.

The best optimum design for Multi-point method is obtained from RUN 7 with $|\Sigma - 1| = 0.054$. The constraints values obtained for the optimum solution are $W/W_{\mathrm{Benchmark}} = 0.632$, $V_{\mathrm{f}}/V_{\mathrm{f,Design}} = 1.014$, $RBM/RBM_{\mathrm{Benchmark}} = 0.091$, $FI = 0.946$ and $\lambda_{\mathrm{crit}} = 1.001$. It is noticed that there are slight differences in the structural weight and the response constraints values between Single-point and Multiple=point optimum design. Higher structural weight and RBM values are observed for the best Multiple-point optimum design. For the structural constraint, higher FI value is obtained for the best Multiple-point optimum design, hence suggests that the design is subjected to maximum strain as results from multiple loading conditions.

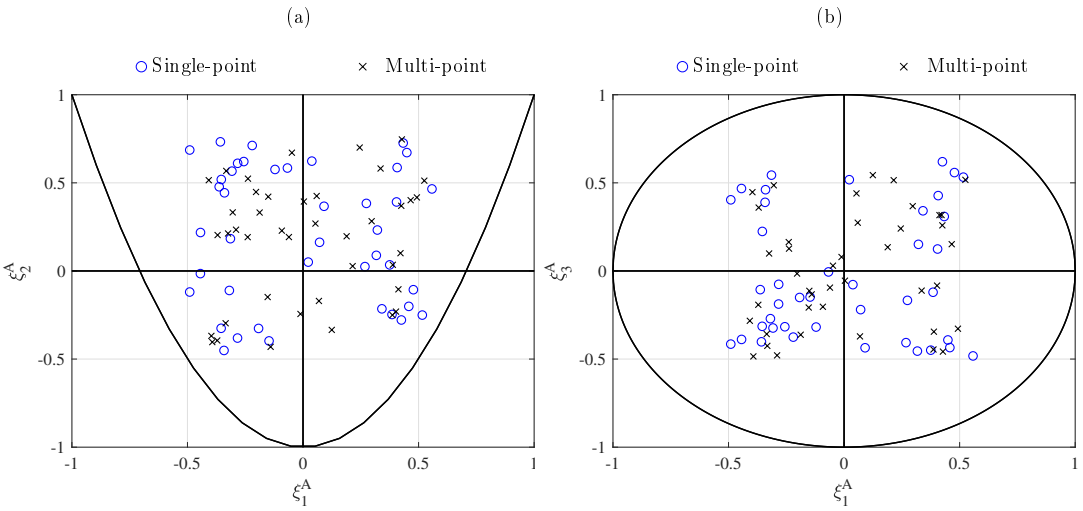

Figure 4.8: The lamination parameters (ξ_1^A, ξ_2^A and ξ_3^A) distribution obtained from the Single-point and Multi-point optimised design. The feasible regions for lamination parameters are plotted for comparison.

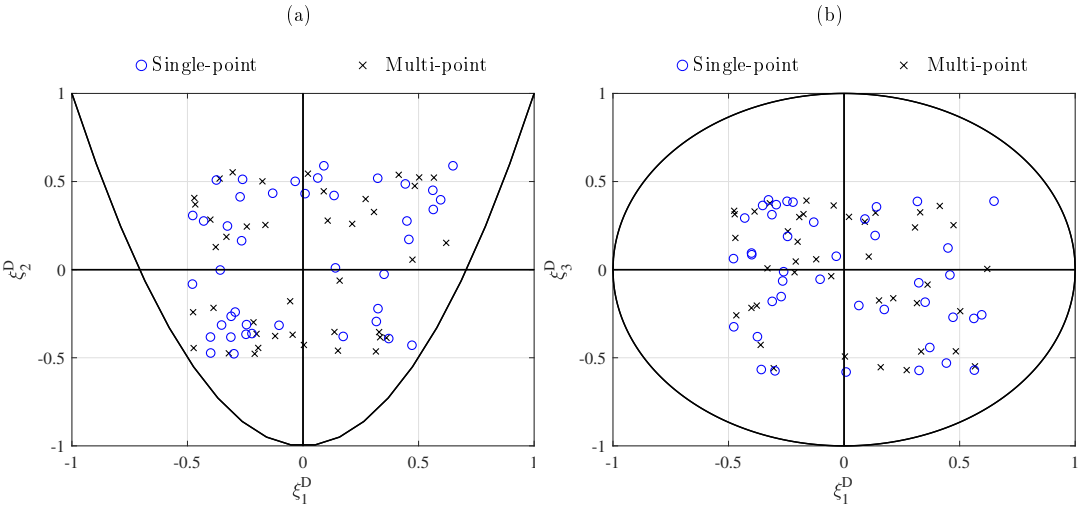

Figure 4.9: The lamination parameters (ξ_1^D, ξ_2^D and ξ_3^D) distribution obtained from the Single-point and Multi-point optimised design. The feasible regions for lamination parameters are plotted for comparison.

Figures 4.8 and 4.9 provide the distributions of the lamination parameters obtained from the Single-point and Multi-point best optimum design. In general, the resulting lamination parameters are within the feasible regions specified in the optimisation procedures. There is a small difference in the lamination parameters when a comparison is made between the single and multi-point design. In the Multi-point method, the algorithm seeks for alternative solutions for the design but within the set feasible regions. Further calculation on the coupling parameters; A_{16}, A_{26}, D_{16} and D_{26} show that the bend-twist coupling parameters increased going from Single-point to Multi-point design. The increase results in higher structural bending stiffness to resist bending and twisting

deformation, which evidenced in the higher flutter speed value for Multi-point design. However, it is noticed form the lamination parameter distribution that there is a significant gap between the possible solution (feasible region) and the optimised solution. This is thought due to continuous nature of the design variables, where the optimisation algorithm seeks for any combination of lamination parameters. The design solutions can be improved using a predefined stacking sequence governed by discrete lamination parameters which are not considered in the present work.

The strain distribution for both best optimum designs are shown in Figure 4.10 and 4.11. For the Single-point optimised design, high strain distribution was observed at the bottom skin with the maximum value obtained at the kink section of the wing (at the trailing edge close to engine-pylon attachment). A similar observation is noted for the Multiple-point optimised design. High strain distribution was observed at the kink section due to high load concentration from the engine and the pylon components.

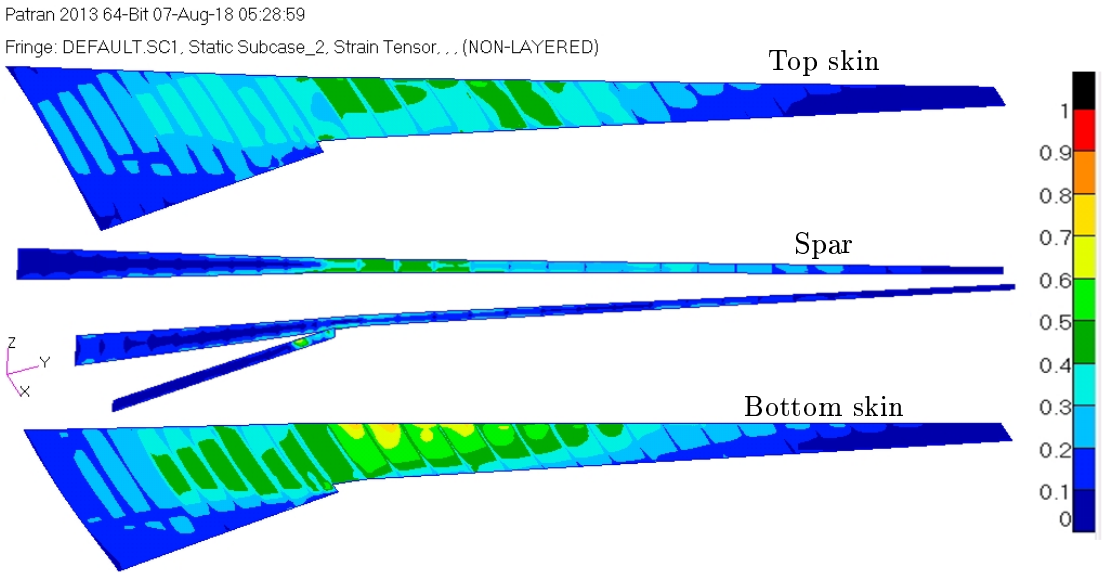

Figure 4.10: The von Mises strain (normalised scale) distribution at the skin and spar panels of the best-optimised design obtained from Single-point method.

Overall, both of the optimised designs (Single and multi-point method) provide a significant structural weight saving via aeroelastic tailoring. The Multi-point design solution provides a realistic design solution due to multiple load case has been considered in the optimisation method. Moreover, multi-point method requires longer time to solve as opposed to Single-point method. Nevertheless, single-point method is preferable, provided that a pre-established critical load case is available.

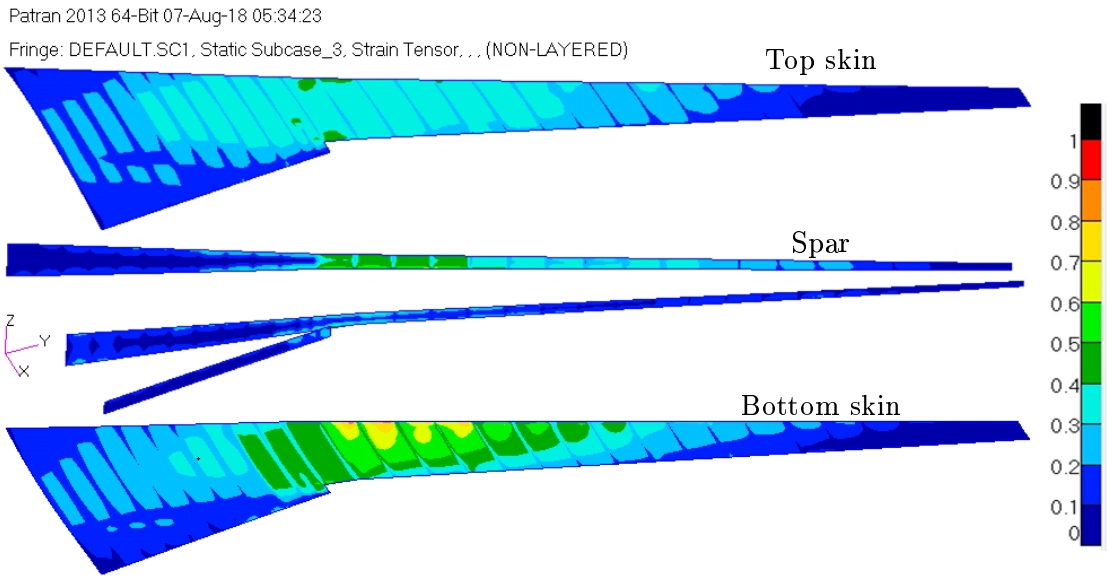

Figure 4.11: The von Mises strain (normalised scale) distribution at the skin and spar panels of the best-optimised design obtained from Multi-point method.

The contribution of each design constraint are effectively evaluated using the weighted cost function in the objective function, hence provide an optimum design solution which satisfied the structural and aeroelastic performances as well as minimum structural weight requirement.

4.6 Summary

The following conclusions can be drawn:

1. The proposed aeroelastic tailoring procedure on a composite wing of a reference jet aircraft provides a significant structural weight saving without compromising the structural and aeroelastic design constraints. The composite wing is subjected to multiple static manoeuvre load cases with strength and buckling constraints as well as flutter/divergence and wing root bending moment due to gust load.

2. In the aeroelastic tailoring study with flutter/divergence constraint, the total percentage weight saving (from benchmark model) of 42.5% and 48.9% are obtained from GA and PSO's optimised design. The highest weight saving was obtained from Spar 3 panel in both cases.

3. PSO is more efficient than the GA for design optimisation problem subjected to flutter/divergence constraint. The PSO's optimised solution is obtained with less number of iteration runs of 460 as compared to GA, which requires 780 runs. Note that flutter is the critical mode of failure whereas divergence was observed at higher airspeeds. Hence, the results suggest that PSO is more efficient in solving a design problem with large design spaces.

4. In the aeroelastic tailoring with both flutter and gust constraints, an increase of 7.71% in the structural weight is obtained from the PSO's optimised solution in comparison with deterministic flutter solution. An increase in weight is necessary to compensate the gust constraint in the design problem. PSO's optimised design is 41.2% lighter than the benchmark model while GA's solution produces a weight saving of 32.1%.

5. The contributions of multiple design constraints on the outcome of the optimisation procedure are effectively measured using a weighted cost function introduced in the objective function. The more considerable value of weighting factor for a particular design constraint promotes the solution response towards target design value.

6. The inclusion of additional structural design constraints in the optimisation process results in higher structural weight in comparison with optimised design with only aeroelastic design constraints. However, a significant weight saving is accounted in comparison with the benchmark model.

7. The Single-point and Multi-point optimisation methods provide an alternative procedure to obtain an optimised design while satisfying the set design constraints. The optimised designs obtained from both of the methods show variation in terms of the structural weight and constraints responses. These are due to additional static load cases in the Multi-point method. The optimised solution obtained from Multi-point method is more realistic as it included more critical load cases in the optimisation procedures. The Single-point method is preferable if pre-established critical load cases are available.

8. The best-optimised design obtained from Single-point method provides a percentage weight saving of 38.0% in comparison with the benchmark model. The best Multi-point's optimised design is 36.8% lighter than the benchmark model.

9. The use of weighted cost function in the objective function enables the quantification of all the design constraints contribution towards the optimised solution in effective manner.

Finally, an aeroelastically-tailored composite wing can be obtained from the proposed method with improved structural weight while satisfying all design constraints that included structural and aeroelastic responses.

Chapter 5

Uncertainty Quantification on Composite Wings

5.1 Introduction

In composite materials, uncertainty may exist through material properties, geometry and manufacturing processes which can cause variations in the structural response. In conventional deterministic aeroelastic design approaches, these uncertainties are not implicitly accounted for and often treated in a qualitative sense by using safety margin to define the worst-case scenario. Therefore, the deterministic design approach can often lead to conservative, overcompensating or unknowingly dangerous designs due to the inherent uncertainty in composite materials [19]. Moreover, the method may limit the potential gains from a novel design approach such as aeroelastic tailoring. The shortcoming of the deterministic design approach can be addressed by directly incorporating the uncertainty into the design process through the use of either probabilistic or non-probabilistic design methods.

The probabilistic design approach requires uncertainty to be modelled as distribution functions with their effects on the system characterised from the probabilistic distribution of output responses. Therefore, an efficient tool is required to quantify the uncertainty accurately and can be used efficiently for the probabilistic design approach. A variety of methods, as presented in Section 2.5 (page 35), can be employed to quantify uncertainties in composite structures. Monte Carlo Simulation (MCS) is the most common tool for uncertainty quantification but is too expensive for a probabilistic design application.

Herein, the work aims to efficiently determine the wing's structural and aeroelastic response variation due to uncertainties in the model parameters at minimum computational costs. Two methods namely (1) Polynomial Chaos Expansion (PCE) method and (2) High Dimensional Model Representation - Random Sampling (RS-HDMR) method are

presented herein, and their efficiency in predicting the wing's response due to uncertainty is evaluated.

These approaches are applied on the detailed finite element model of the EBW to predict the variation in structural and aeroelastic behaviour due to the uncertain in material properties, ply angle and thickness. Results obtained from these approaches are compared with MCS for validation. The efficiency of the approaches for low and high dimensional orders of random input parameters are explored which then used for probabilistic design optimisation approaches.

5.2 Model Description and Analysis Methods

The work presented in this chapter employs a detailed FE composite wing model, as described in Section 3.2.1 (page 56). The deterministic design configuration of the model which is obtained in Section 4.5 (Single-point method) (page 111) with equal weighting coefficient the flutter, wing root bending moment (RBM) due to gust and strength constraints are used for the analysis.

The buckling, flutter and RBM responses are evaluated as results from material properties and composite ply thickness variations. The effect of individual uncertain parameters and their combination on the wing responses are analysed using both PCE and RS-HDMR methods. To demonstrate the effectiveness of both methods, the parameter variations are introduced via use of the coefficient of variance (CV) [28], which is the measure of the dispersion of the parameter. The CV is defined as the ratio of standard deviation to the mean of the random variable. Due to lack of published data, the parameter variables are defined in terms of Gaussian distribution using different CV values.

For the work presented in this thesis, the selected random variables are the laminate material properties that included the longitudinal Young Modulus, E_{11}, transverse Young Modulus, E_{22}, shear modulus, G_{12} and the ply thickness, t_{ply}. These parameters are selected for uncertainty quantification study due to their direct contribution on the structural stiffness via A, B and D matrices. Hence, by varying these parameters, the global wing's responses variation can be evaluated using the purpose method. In addition to

that, the ply thickness is included in the study, but the variation in the parameter is treated globally.

The localised parameter variation, such as ply angle requires each of the ply angles in the laminated wing panels to be quantified individually. The proposed method, such as PCE and RS-HDMR require a sufficient number of sampling data in order to quantify the effect of uncertainty accurately. The quantification of ply angle variation leads to a more significant number of random variables and hence require a more extensive number of sampling data. Manan & Cooper [28] have done a study on the effect of ply angle variation on flutter speed using a simple composite plate. Their work suggests that the variation in individual ply angle results in significant variation in the flutter speed. However, their study was performed on a simple rectangular plate consists of six composite plies. In the current work, the effect of uncertainty is quantified on a large scale wing model consists of multiple panels, each with different laminate configuration. Thus, the study on individual ply angle variation is not covered in this thesis and subject to future work.

Other localised parameter variation such as individual ply thickness may result in localised effects such as local buckling in addition to the global effect of wing's flutter or gust responses. In order to quantify the effect of localised parameter variation such as ply angles or the individual ply thickness, a localised model is required to represent the local area of interest and treated as a sub-model to the full model of aircraft wing. By using a sub-model, the localised parameter variation can be modelled, and the effects can be evaluated in efficient manners. In this work, ply angle variation is included in the uncertainty quantification analysis but it has been modelled in global sense rather than individual ply thickness variation. The study on the effects of localised parameter variation is not covered in the current work.

In this work, the random variables are summarised in Table 5.1 with the coefficient of variations (CV) in material properties are assumed as 0.1 and 0.01 for ply thickness. The CV values are chosen to represent the worst-case condition in properties variation. For example, the CV value of 0.1 for the longitudinal Young Modulus, E_{11} represent $\pm 30\%$ of the properties variation. The effect of different level of uncertain parameters dispersion (different CV value) on the wing response is assessed. The results obtained from the proposed methods are compared with MCS for validation.

Table 5.1: The mean and standard deviation of E_{11}, E_{22}, G_{12} and t_{ply} used in the uncertainty quantification analyses.

	E_{11} (GPa)	E_{22} (GPa)	G_{12} (GPa)	t_{ply} (m)
Mean, μ	148.0	10.3	5.90	1.83×10^{-4}
Std Dev., σ	14.8	1.03	0.59	1.83×10^{-6}

The flutter behaviour due to uncertain variables are assessed using MSc. Nastran's `SOL 145`, which relies on the frequency matching *'p-k'* method to predict the flutter speed, V_{f}. In Nastran, a matched flutter analysis is specified (`PKNL` in `FLUTTER` input command) with constant Mach number 0.82 at varying altitude. A total of 12 modes are considered in the flutter analysis to account for the mode switching. The flutter speed for each set of uncertainty parameters is determined from the damping-airspeed ($V-g$) and frequency-airspeed ($V-f$) plots using the modal amplitude frequencies and the damping output at different airspeeds. Details on the flutter analysis using `SOL 145` are given in Section 3.4.4 (page 74).

The wing responses to discrete *'1-cosine'* gusts are evaluated in terms of the RBM at the wing's root section. In the current work, the reference gust velocity, U_{ref} of 17.07 ms^{-1} with the flight speed of 253 ms^{-1} are specified. Only one critical gust length, $L_{\text{g}} = 216\,\text{m}$ is considered in the analysis. MSc. Nastran's `SOL 146` is used to evaluate the wing box dynamic aeroelastic response to discrete gust and the details on the gust analysis are explained as per Section 3.4.5 (page 78).

The critical buckling load factors, λ_{crit} subjected to a static manoeuvre load case and uncertain parameter are evaluated with MSc. Nastran's `SOL 105`. The first ten buckling modes are computed for each set of random parameters. Details on the buckling analysis in `SOL 105` are given in Section 3.5.2 (page 86).

5.3 Polynomial Chaos Expansion (PCE) Method

Polynomial Chaos Expansion (PCE) method uses a polynomial based stochastic space to represent the random parameters in the system and their propagation. Norbert Weiner [139] originally introduced the concept of Polynomial Chaos as part of homogeneous chaos formulations. The concept was extended by Ghanem & Spanos [140] and they proposed a simple definition of PCE which account for interaction of individual random

variables and its polynomials as a convergent series in following form

$$u(\theta) = a_0\Gamma_0 + \sum_{1}^{\infty} a_{i1}\Gamma_1(\zeta_{i1}(\theta)) + \sum_{i1=1}^{\infty}\sum_{i2=1}^{i1} a_{i1i2}\Gamma_2[\zeta_{i1}(\theta), \zeta_{i2}(\theta)] + \sum_{i1=1}^{\infty}\sum_{i2=1}^{i1}\sum_{i3=1}^{i2} a_{i1i2i3}\Gamma_3[\zeta_{i1}(\theta), \zeta_{i2}(\theta), \zeta_{i3}(\theta)] + ... \tag{5.1}$$

where $\{\zeta_{i1}(\theta)\}_1^\infty$ denotes a set of independent random variables (standard Gaussian), $\Gamma_p[\zeta_{i1}(\theta), ..., \zeta_{ip}(\theta)]$ is a set of multi-dimensional orthogonal (Hermite) polynomials of order p, $a_{i1}, ..., a_{ip}$ are the deterministic expansion coefficients and θ is the random characters of the quantities involved.

Equation (5.1) is often written as

$$u(\theta) = \sum_{i=0}^{\infty} \beta_i \psi_i(\zeta(\theta)), \tag{5.2}$$

where there is a one-to-one correlation between $\Gamma_p[\zeta_{i1}(\theta), ..., \zeta_{ip}(\theta)]$ and $\psi_i(\zeta(\theta))$ also between β_i and $a_{i1}, ..., a_{ip}$ where $i = 1, 2, 3, ..., \infty$. Hence, the PCE expression with a variable parameter can also be written as

$$u = \beta_0 + \beta_1\zeta + \beta_2(\zeta^2 - 1) + \beta_3(\zeta^3 - 3\zeta) + \beta_4(\zeta^4 - 6\zeta^2 + 3) + ... \tag{5.3}$$

The formulation of PCE depends on the type of probability distribution function (PDF) of the uncertain variables. The above expression is formulated based on the assumption that the random variables are Gaussian, hence Hermite Polynomials can be used to represent these variables. For standard Gaussian random variables, the output distribution of the system is assumed to be Gaussian provided that only lower terms (β_0 and β_1) are included in the PCE. If higher terms are included in the formulation, the output responses may not be in the form of a Gaussian distribution.

The PCE formulation provides a complete polynomial basis which is orthogonal to the PDF of the random variables and hence guarantees exponential with increasing expansion order for Gaussian random variables [143]. For other types of random input distributions, other orthogonal polynomials may be used such as Laguerre and Jacobi's polynomials given in Ref. [141]. The orthogonality is defined such that

$$\psi_i(\zeta)\psi_j(\zeta) = \int_S \psi_i(\zeta)\psi_j(\zeta)W(\zeta)d\zeta = \psi_i^2\delta_{ij}, \tag{5.4}$$

where

$$\delta_{ij} = \begin{cases} 0 & \text{if } i \neq j, \\ 1 & \text{if } i \neq j. \end{cases} \tag{5.5}$$

$W(\zeta)$ is the weighting for the polynomials and S is the support range given in Table 5.2 [141].

Table 5.2: Type of continuous random variables and their corresponding Askey polynomials (Xiu & Karniadakis, 2002).

Random variables	Polynomial	Support	Weighting
Gaussian	Hermite	$(-\infty, \infty)$	e^{-x^2}
Gamma	Laguerre	$[0, \infty]$	1
Beta	Jacobi	$[a, b]$	$e^{-x}x^{\alpha}$
Uniform	Legendre	$[a, b]$	$(1-x)^{\alpha}(1+x)^{\beta}$

5.3.1 *n*-Dimension Polynomial Chaos Expansion

The formulation for PCE models for any output responses can be defined for any dimension and polynomial order. The dimensional order of the PCE model is related to the number of random variables. For n number of random variables, the PCE model is derived from n-dimensional polynomial chaos. Herein, Gaussian input random variables are assumed, and hence Hermite polynomials are used for the PCE formulation. The n-dimensional Hermite polynomials, Γ_p can be expressed as [141]

$$\Gamma_p[\zeta_{i1}(\theta), ..., \zeta_{in}(\theta)] = (-1)^p e^{\frac{1}{2}\zeta^T\zeta} \frac{\partial^p}{\partial\zeta_{i1}(\theta), ..., \partial\zeta_{in}(\theta)} \left[e^{-\frac{1}{2}\zeta^T\zeta}\right], \tag{5.6}$$

where $\{\zeta\}$ contains a vector of n-variables, *i.e.* $\{\zeta_k\}_{k=1}^n$; $(k = 1, 2, 3, ..., n)$ and p is the order of the polynomial. For example, consider the 1-Dimensional Polynomial Chaos model with second-order polynomial $(p = 0, 1, 2)$, the polynomials can be determined as

$$\Gamma_0 = 1,$$

$$\Gamma_1 = (-1)^1 e^{\frac{1}{2}\zeta_1^T\zeta_1}\frac{\partial}{\partial\zeta_1}e^{-\frac{1}{2}\zeta_1^T\zeta_1} = (-1)^1 e^{\frac{1}{2}\zeta_1^2}\frac{\partial}{\partial\zeta_1}e^{-\frac{1}{2}\zeta_1^2} = (-1)^1 e^{\frac{1}{2}\zeta_1^2}(-\zeta_1)(e^{-\frac{1}{2}\zeta_1^2}) = \zeta_1,$$

$$\Gamma_2 = (-1)^2 e^{\frac{1}{2}\zeta_1^T\zeta_1}\frac{\partial^2}{\partial^2\zeta_1}e^{-\frac{1}{2}\zeta_1^T\zeta_1} = -e^{\frac{1}{2}\zeta_1^2}\Big(\frac{\partial}{\partial\zeta_1}\zeta_1 e^{-\frac{1}{2}\zeta_1^2}\Big) = -e^{\frac{1}{2}\zeta_1^2}\Big[\zeta_1\frac{\partial}{\partial\zeta_1}e^{-\frac{1}{2}\zeta_1^2} + e^{-\frac{1}{2}\zeta_1^2}\frac{\partial}{\partial\zeta_1}\zeta_1\Big]$$

$$= -e^{\frac{1}{2}\zeta_1^2}\Big[-\zeta_1^2 e^{-\frac{1}{2}\zeta_1^2} + e^{-\frac{1}{2}\zeta_1^2}\Big] = \zeta_1^2 - 1. \tag{5.7}$$

Similarly, the calculated higher order polynomial terms are $\Gamma_3 = \zeta_1^3 - 3\zeta_1$, $\Gamma_4 = \zeta_1^4 - 6\zeta_1^2 + 3$, $\Gamma_5 = \zeta_1^5 - 10\zeta_1^3 + 15\zeta_1$, and $\Gamma_6 = \zeta_1^6 - 15\zeta_1^4 + 45\zeta_1^2 - 15$.

In a 1-D polynomial chaos model, there are no interaction terms since only one random variable considered. For the case where there are two random variables (ζ_1 and ζ_2), there will be interaction terms to capture the combined effects of both random variables (for 2-D polynomial chaos) on the output response of the systems. The contributions of the interaction terms towards the overall response are likely to be minimal. Similarly, the polynomial chaos terms up to second order ($p = 0, 1, 2, 3$) can be determined using Eqn.

(5.6) where

$$
\begin{aligned}
&\Gamma_0 = 1,\\
&\Gamma_1(\zeta_1) = (-1)^1 e^{\frac{1}{2}(\zeta_1^2+\zeta_2^2)} \frac{\partial}{\partial \zeta_1} e^{-\frac{1}{2}(\zeta_1^2+\zeta_2^2)} = -e^{\frac{1}{2}(\zeta_1^2+\zeta_2^2)}(-\zeta_1)e^{-\frac{1}{2}(\zeta_1^2+\zeta_2^2)} = \zeta_1,\\
&\Gamma_1(\zeta_2) = (-1)^1 e^{\frac{1}{2}(\zeta_1^2+\zeta_2^2)} \frac{\partial}{\partial \zeta_2} e^{-\frac{1}{2}(\zeta_1^2+\zeta_2^2)} = -e^{\frac{1}{2}(\zeta_1^2+\zeta_2^2)}(-\zeta_2)e^{-\frac{1}{2}(\zeta_1^2+\zeta_2^2)} = \zeta_2,\\
&\Gamma_2(\zeta_1) = (-1)^2 e^{\frac{1}{2}(\zeta_1^2+\zeta_2^2)} \frac{\partial^2}{\partial^2 \zeta_1} e^{-\frac{1}{2}(\zeta_1^2+\zeta_2^2)} = -e^{\frac{1}{2}(\zeta_1^2+\zeta_2^2)} \frac{\partial}{\partial \zeta_1} \zeta_1 e^{-\frac{1}{2}(\zeta_1^2+\zeta_2^2)}\\
&\qquad = -e^{\frac{1}{2}(\zeta_1^2+\zeta_2^2)} \Big[\zeta_1 \frac{\partial}{\partial \zeta_1} e^{-\frac{1}{2}(\zeta_1^2+\zeta_2^2)} + e^{-\frac{1}{2}(\zeta_1^2+\zeta_2^2)} \frac{\partial}{\partial \zeta_1} \zeta_1 \Big]\\
&\qquad = -e^{\frac{1}{2}(\zeta_1^2+\zeta_2^2)} e^{-\frac{1}{2}(\zeta_1^2+\zeta_2^2)} \Big(-\zeta_1^2 + 1 \Big) = \zeta_1^2 - 1,\\
&\Gamma_2(\zeta_1,\zeta_2) = (-1)^2 e^{\frac{1}{2}(\zeta_1^2+\zeta_2^2)} \frac{\partial^2}{\partial \zeta_1 \partial \zeta_2} e^{-\frac{1}{2}(\zeta_1^2+\zeta_2^2)} = -e^{\frac{1}{2}(\zeta_1^2+\zeta_2^2)} \frac{\partial}{\partial \zeta_1} \zeta_2 e^{-\frac{1}{2}(\zeta_1^2+\zeta_2^2)}\\
&\qquad = -e^{\frac{1}{2}(\zeta_1^2+\zeta_2^2)} \Big[\zeta_2 \frac{\partial}{\partial \zeta_1} e^{-\frac{1}{2}(\zeta_1^2+\zeta_2^2)} + e^{-\frac{1}{2}(\zeta_1^2+\zeta_2^2)} \frac{\partial}{\partial \zeta_1} \zeta_2 \Big]\\
&\qquad = -e^{\frac{1}{2}(\zeta_1^2+\zeta_2^2)} \Big[\zeta_2 (-\zeta_1) e^{-\frac{1}{2}(\zeta_1^2+\zeta_2^2)} \Big] = \zeta_1 \zeta_2,\\
&\Gamma_2(\zeta_2) = (-1)^2 e^{\frac{1}{2}(\zeta_1^2+\zeta_2^2)} \frac{\partial^2}{\partial^2 \zeta_2} e^{-\frac{1}{2}(\zeta_1^2+\zeta_2^2)} = -e^{\frac{1}{2}(\zeta_1^2+\zeta_2^2)} \frac{\partial}{\partial \zeta_2} \zeta_2 e^{-\frac{1}{2}(\zeta_1^2+\zeta_2^2)}\\
&\qquad = -e^{\frac{1}{2}(\zeta_1^2+\zeta_2^2)} \Big[\zeta_2 \frac{\partial}{\partial \zeta_2} e^{-\frac{1}{2}(\zeta_1^2+\zeta_2^2)} + e^{-\frac{1}{2}(\zeta_1^2+\zeta_2^2)} \frac{\partial}{\partial \zeta_2} \zeta_2 \Big]\\
&\qquad = -e^{\frac{1}{2}(\zeta_1^2+\zeta_2^2)} \Big[e^{-\frac{1}{2}(\zeta_1^2+\zeta_2^2)} (-\zeta_2^2) + e^{-\frac{1}{2}(\zeta_1^2+\zeta_2^2)} \Big] = \zeta_2^2 - 1,\\
&\Gamma_3(\zeta_1) = \zeta_1^3 - 3\zeta_1,\\
&\Gamma_3(\zeta_1,\zeta_2) = \zeta_2(\zeta_1^2 - 1),\\
&\Gamma_3(\zeta_1,\zeta_2) = \zeta_1(\zeta_2^2 - 1),\\
&\Gamma_3(\zeta_2) = \zeta_2^3 - 3\zeta_2,
\end{aligned}
\tag{5.8}
$$

where $\Gamma_2(\zeta_1,\zeta_2)$ and $\Gamma_3(\zeta_1,\zeta_2)$ are the interaction terms (ζ_1 aand ζ_2) for the polynomial chaos. Note that there are two terms for $\Gamma_3(\zeta_1,\zeta_2)$ due to the differential order (*i.e.* $\frac{\partial^3}{\partial^2\zeta_1\partial\zeta_2}$ and $\frac{\partial^3}{\partial^2\zeta_2\partial\zeta_1}$). Using the calculated polynomials, the 2-D PCE model of two standard Gaussian inputs $\zeta = \{\zeta_1, \zeta_2\}$ can be formulated by multiplying each polynomial by the unknown expansion coefficients, β_i as follows

$$
\begin{aligned}
u_{1^{st}} &= \beta_0 + \beta_1\zeta_1 + \beta_2\zeta_2 \\
u_{2^{nd}} &= \beta_0 + \beta_1\zeta_1 + \beta_2\zeta_2 + \beta_3(\zeta_1^2 - 1) + \beta_4\zeta_1\zeta_2 + \beta_5(\zeta_2^2 - 1) \\
u_{3^{rd}} &= \beta_0 + \beta_1\zeta_1 + \beta_2\zeta_2 + \beta_3(\zeta_1^2 - 1) + \beta_4\zeta_1\zeta_2 + \beta_5(\zeta_2^2 - 1) + \beta_6(\zeta_1^3 - 3\zeta_1) + \\
&\quad \beta_7(\zeta_1^2\zeta_2 - \zeta_2) + \beta_8(\zeta_2^2\zeta_1 - \zeta_1) + \beta_9(\zeta_2^3 - 3\zeta_2).
\end{aligned} \tag{5.9}
$$

5.3.2 Latin Hypercube Samping (LHS) Technique

The determination of unknown expansion coefficient, β_i requires a large number of data samples to achieve global accuracy in the approximation, and this could be a major drawback if higher dimensions of random variables are involved. Latin Hypercube Sampling (LHS) is employed to provide an efficient approach for sampling. The LHS method ensures all samples of input random variables cover the ranges represented while being capable of achieving small response variances with a relatively few numbers of samples [188]. A detailed explanation of the LHS method can be found in Ref. [189].

The use of LHS method within the PCE model allows for better sampling selection (for PCE model) as it acquires the sample points from a distribution based on equal probability rather than random selection. Figure 5.1 shows the sampled distribution and the corresponding PDF plot of the longitudinal Young's Modulus, E_{11} of 8552/IM7 with the coefficient of variance (CV) of 0.1 obtained from LHS method. From Figure 5.1(a) consider five points in a distribution, LHS ensures that all these points are sampled with equal probability (0.2) on the PDF [189], so that the responses are captured on all PDF's points, hence minimising the response variances.

5.3.3 Determination of Unknown Expansion Coefficients, β_i

The unknown expansion coefficients β_i can be obtained by fitting a linear regression model on a series of computed test data. The purpose of the linear regression analysis is to provide functional relationships between two or more input random variables [188]. The fitted linear regression model for stochastic process, $u(\theta)$ (from Eqn. (5.2)), denoted by Y is expressed as

$$
Y = \beta_0 + \beta_1\psi_1(\boldsymbol{\zeta}) + ... + \beta_k\psi_k(\boldsymbol{\zeta}) + \varepsilon, \tag{5.10}
$$

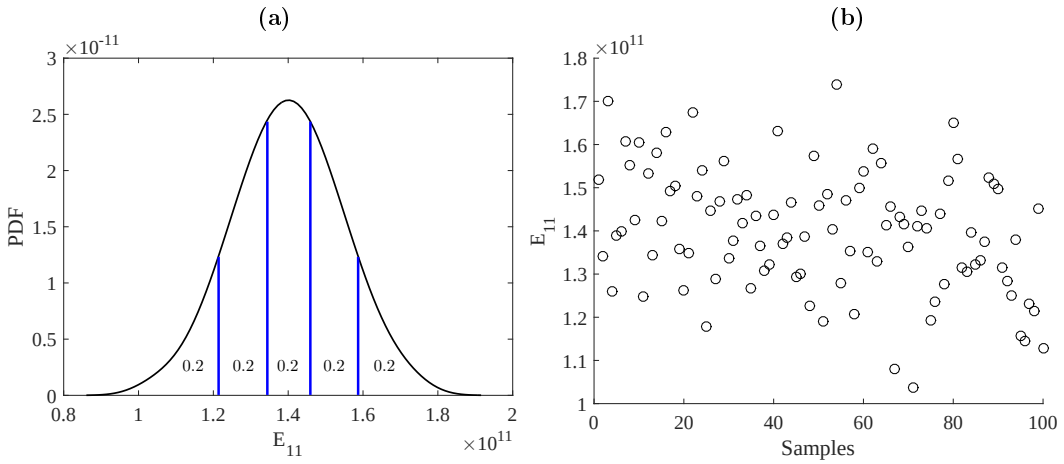

Figure 5.1: Data samples for longitudinal Young's Modulus (E_{11} obtained from LHS method (a) The corresponding probability density function (PDF) (b) Samples data distribution.

where β_i, $i = 0, 1, 2, \ldots k$, are the regression/expansion coefficients and ε is the error in the regression model. The error is assumed to be normally distributed with zero mean and variance σ_ϵ^2. The linear regression model requires a set of N input samples, $[\zeta^{(1)}, \zeta^{(2)}, \ldots \zeta^{(N)}]$ generated using LHS method and the corresponding basis function, ψ for each sample. These set of data is used as training samples for the PCE model. Equation (5.10) can be rewritten to obtain N simultaneous linear equations as

$$\begin{Bmatrix} Y(\zeta^{(1)}) \\ \vdots \\ Y(\zeta^{(N)}) \end{Bmatrix} = \begin{bmatrix} \psi_0(\zeta^{(1)}) & \ldots & \psi_k(\zeta^{(1)}) \\ \vdots & \ddots & \vdots \\ \psi_0(\zeta^{(N)}) & \ldots & \psi_k(\zeta^{(N)}) \end{bmatrix} \begin{Bmatrix} \beta_0 \\ \vdots \\ \beta_k \end{Bmatrix} + \begin{Bmatrix} \varepsilon^{(1)} \\ \vdots \\ \varepsilon^{(N)} \end{Bmatrix}, \tag{5.11}$$

alternatively, in the simplified matrix form

$$\Big\{Y\Big\} = \Big[\psi\Big] \Big\{\beta\Big\} + \Big\{\varepsilon\Big\}. \tag{5.12}$$

For example, consider a 2-D second-order PCE, Eqn. (5.12) can be expressed as

$$\begin{Bmatrix} Y^{(1)} \\ \vdots \\ Y^{(N)} \end{Bmatrix} = \begin{bmatrix} 1 & \zeta_1^{(1)} & \zeta_2^{(1)} & (\zeta_1^2-1)^{(1)} & (\zeta_1\zeta_2)^{(1)} & (\zeta_2^2-1)^{(1)} \\ \vdots & \vdots & \vdots & \vdots & \vdots & \vdots \\ 1 & \zeta_1^{(N)} & \zeta_2^{(N)} & (\zeta_1^2-1)^{(N)} & (\zeta_1\zeta_2)^{(N)} & (\zeta_2^2-1)^{(N)} \end{bmatrix} \begin{Bmatrix} \beta_0 \\ \beta_1 \\ \beta_2 \\ \beta_3 \\ \beta_4 \\ \beta_5 \end{Bmatrix} + \begin{Bmatrix} \varepsilon^{(1)} \\ \vdots \\ \varepsilon^{(N)} \end{Bmatrix}. \tag{5.13}$$

The unknown vector of expansion coefficient, β_i can be solved using the method of least square such that

$$\{\beta\} = (\psi^T\psi)^{-1}\psi^T\{Y\}, \tag{5.14}$$

where ψ^T is the transpose of the matrix ψ. The fitted model and the error of the approximation are given by

$$\hat{Y} = \psi\beta \qquad \text{and} \qquad \varepsilon = Y - \hat{Y}. \tag{5.15}$$

The simultaneous linear equation for unknown expansion coefficients, β_i can be solved efficiently using a backslash operator in MATLAB. The backslash operator uses `QR` decomposition with pivoting to ensure $(\psi^T\psi)^{-1}$ give acceptable rounding errors [143]. The *total-order expansion*, $\mathcal{A}$ in an expansion of order p involving d-dimensional order of random variables can be determined by [143]

$$\mathcal{A} = \binom{d+p}{p} = \frac{(d+p)!}{d!p!}. \tag{5.16}$$

Note that $\mathcal{A}$ increases exponentially with d and p. Thus, the number of expansion terms increase dramatically when d is large, say $d > 10$, which is referred as *'curse of dimensionality'* [190]. If 4^{th} order PCE is employed, when $d = 4$, $\mathcal{A}$ is $\binom{8}{4} = 70$ and for $d = 10$, $\mathcal{A}$ is $\binom{14}{4} = 1001$.

5.3.4 Sensitivity Analysis using Polynomial Chaos Expansion

Sensitivity analysis (SA) is one of the main components in the probabilistic study of a model. SA aims at quantifying the relative importance of the input parameters on the model responses. Global SA is often employed in many studies in order to quantify the output response due to single or multi-variable uncertainty in the model parameters [191]. There are two main groups for global SA method, namely: Regression-based methods and variance-based methods. In the latter method, the variance of the output responses is decomposed as a total contribution of each input random variable or the combination of them. Sobol' indices are typically used in the variance-based method as it

uses direct interpolation of the sampling data. Sobol' indices are computed using Monte Carlo Simulations (MCS) which is a computationally expensive method, particularly when involving detailed finite element models.

Herein, the application of PC-based Sobol' Indices on the sensitivity analysis of a composite wing model due to uncertainty in model parameters is presented. The aim is to provide an alternative approach in order to obtain sampling data efficiently and less computationally expensive in comparison to conventional MCS method.

5.3.4.1 Statistics of PCE

The fitted PC expansion, $\hat{Y} = f^{\mathrm{PCE}}(\zeta) = \sum_{\alpha \in \mathcal{A}} \beta_\alpha \psi_\alpha(\zeta)$, provides all the statistical properties of the random output, $Y = f(\zeta)$, where α is the expansion terms order. Due to the orthogonality of the polynomial basis (Eqn. (5.4)), the mean and standard deviation of $\hat{Y}$ can be computed directly from the expansion coefficient β. Therefore, the mean value of $\hat{Y}$ is given as the first term of the PC expansion such that

$$\mathbb{E}\Big[\hat{Y}\Big] = \mathbb{E}\left[\sum_{\alpha \in \mathcal{A}} \beta_\alpha \psi_\alpha(\zeta)\right] = \beta_0. \tag{5.17}$$

Similarly, the variance of $\hat{Y}$ is given as

$$\sigma^2_{\hat{Y}} = \mathrm{Var}\Big[\hat{Y}\Big] = \mathbb{E}\left[\Big(\hat{Y} - \beta_0\Big)^2\right] = \sum_{\alpha \in \mathcal{A}, \alpha \neq 0} \beta^2_\alpha. \tag{5.18}$$

In other words, the statistical properties of the random response can be obtained directly using the computed PC expansion coefficients.

5.3.4.2 PC-based Sobol' Indices

The global sensitivity analysis of a random response can be evaluated based on Sobol' decomposition of the computational model, G such that [190]

$$G(\zeta) = G_0 + \sum_{i=1}^{d} G_i(\zeta_i) + \sum_{1 \leq i < j \leq d} G_{ij}(\zeta_i, \zeta_j) + \cdots + G_{12\ldots d}(\zeta), \tag{5.19}$$

where G_0 is a constant, $G_i(\zeta_i); 1 \leq i \leq d$ are the univariate functions, $G_{ij}(\zeta_i, \zeta_j); 1 \leq i < j \leq d$ are the bivariate functions and $G_{12\ldots d}(\zeta)$ are the multivariate functions.

By comparing Eqns. (5.10) and (5.19), both PCE and Sobol's decomposition are formulated as sums of the orthogonal functions. Hence, it is possible to derive a analytical expression for Sobol' indices using PCE as proposed by Sudret [191]. Consider a set of multivariate polynomial basis, ψ_α which depends only on a subset of random parameter $A = \{i_1, \ldots, i_s\} \subset \{1, \ldots, d\}$ such that

$$\mathcal{A}_A = \{\alpha \in \mathcal{A} : \alpha_k \neq 0 \quad \text{if and only if} \quad k \in A\}. \tag{5.20}$$

where the sums of all these set is equal to $\mathcal{A}$. Thus, the terms in the PCE's formulation can be reordered to exhibit the Sobol' decomposition such that

$$f^{\mathrm{PC}}(\zeta) = \beta_0 + \sum_{A \in \{1,\ldots,d\}, A \neq 0} f_A^{\mathrm{PC}}(\zeta_A) \quad \text{where} \quad f_A^{\mathrm{PC}}(\zeta_A) = \sum_{\alpha \in \mathcal{A}_A} \beta_\alpha \psi_\alpha(\zeta) \tag{5.21}$$

Accordingly, due to the orthogonality of the basis function, the partial variance, V_A is given as

$$V_A = \mathrm{Var}[f_A^{\mathrm{PC}}(\zeta_A)] = \sum_{\alpha \in \mathcal{A}_A} \beta_\alpha^2. \tag{5.22}$$

In other words, the Sobol' indices at any order for a given PCE can be obtained by evaluating the square-summed of the expansion coefficients. Therefore, the PC-based Sobol' sensitivity indices are formulated as

$$SU_i = \frac{\sum_{\alpha \in \mathcal{A}_i} \beta_\alpha^2}{\sum_{\alpha \in \mathcal{A}, \alpha \neq 0} \beta_\alpha^2} \quad \text{where} \quad \mathcal{A}_i = \{\alpha \in \mathcal{A} : \alpha_i > 0, \alpha_{i \neq i} = 0\}, \tag{5.23}$$

Similarly, the total *PC-based sensitivity indices*, SU_i^T is given as the summation of the PCE-based Sobol indices of each random parameter

$$SU_i^T = \frac{\sum_{\alpha \in \mathcal{A}_i^T} \beta_\alpha^2}{\sum_{\alpha \in \mathcal{A}, \alpha \neq 0} \beta_\alpha^2} \quad \text{where} \quad \mathcal{A}_i^T = \{\alpha \in \mathcal{A} : \alpha_i > o\}. \tag{5.24}$$

5.4 Polynomial Chaos Expansion Case Study

The efficiency of the PCE method to evaluate the effect of parameter variations on the detailed FE composite wing responses are studied. The results from MCSs are used to validate the results obtained with the PCE model. The wing responses due to uncertain material properties (E_{11}, E_{22} and G_{12}) and ply thickness, t_{ply} are evaluated using different orders of the PCE formulation. The accuracy of the PCE results is calculated in terms of its relative error, RE with respect to the results obtained from MCSs. The relative error is formulated as;

$$RE(\%) = \frac{|F - F'_{\text{PCE}}|}{F} \times 100, \tag{5.25}$$

where F is the actual response (MCS) and F'_{PCE} is the approximate response obtained from PCE. The convergence study for MCSs are performed, and the results are shown in Figure 5.2. The Root-Mean Square Error (RMSE) of the responses are calculated using the sampled data and the actual response values to obtain the minimum number of samples required for convergence. The RMSE is formulated as

$$RMSE = \sqrt{MSE} \qquad \text{and} \qquad MSE = \frac{1}{N}\sum_{i=1}^{N}(Y_i - Y_{\text{actual}})^2, \tag{5.26}$$

where MSE is the mean square error, N and Y are the number of sample and responses of interest (i.e. flutter speed), respectively. The results show in Figure 5.2 indicated the convergence could be obtained with at least 500 samples data for most cases, although it appears that the RMSE plot for 3-Dimensional order of random variables shows slight fluctuations between 750 to 1000 data samples. In this work, 1200 data samples are generated for MCSs to predict the response variation due to uncertainty.

A case study is presented here to evaluate the accuracy and the efficiency of the PCE method over the conventional MCSs method for uncertainty quantification of the composite wing model. The effects of random input parameters on flutter, gust and buckling responses are assessed. The mean and standard deviation of the random parameters are given in Table 5.1 with coefficient of variance (CV) of 0.1 for stiffness properties and 0.01 for ply thickness.

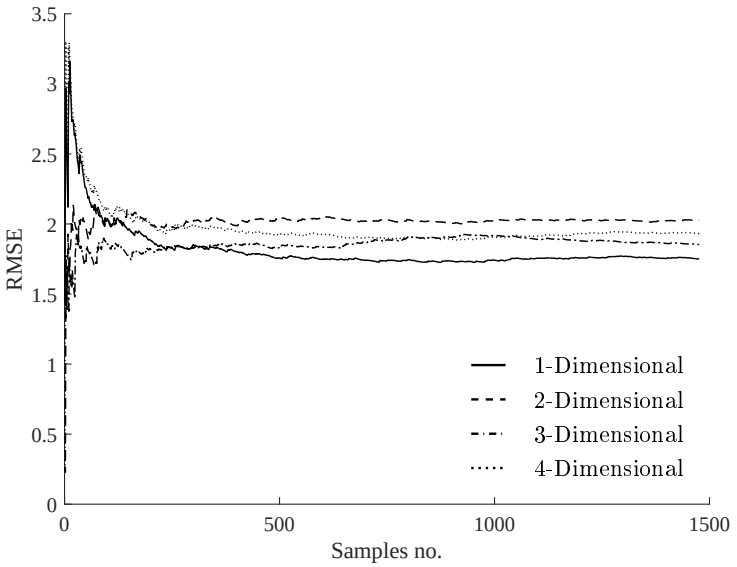

Figure 5.2: The Root-Mean Square Error (RMSE) obtained from MCS. The data is generated using different dimensional order of random variables.

5.4.1 Polynomial Chaos Expansion for Flutter Response

The flutter speed variation due to uncertainty in the composite material properties (longitudinal stiffness, E_{11}, transverse stiffness, E_{22} and shear modulus, G_{12}) and the ply thickness, t_{ply} are evaluated using a PCE model. The effect of these parameter variations are assessed individually, and their collective contribution on the wing response is then studied.

The flutter responses of the composite wing are evaluated using 1-Dimensional, 2-Dimensional, 3-Dimensional and 4-Dimensional PCE models. For the 1-D model, the effects of longitudinal stiffness, E_{11} on flutter speed are evaluated. For 2-D model, the longitudinal stiffness, E_{11} and the transverse stiffness, E_{22} are treated as the random variables. In 3-D PCE analysis, the shear modulus, G_{12} is added as the random parameters together with E_{11} and E_{22} and in 4-D PCE analysis, the ply thickness variation, t_{ply} is also considered.

As the polynomial order of the PCE model and the dimensional order of the random parameters increases, the number expansion coefficient, β_i increases and can be determined using Eqn. (5.16). For example, consider a 1^{st} order 4-D PCE model, the number of expansion coefficients, $\mathcal{A}$ is five and increase to 70 for 4^{th} order 4-D PCE. Generally, the number of LHS samples required for PCE is $3 \times \mathcal{A}$ to obtain accurate approximation [168], which means for 1^{st} order 4-D PCE model, 15 LHS data are needed and for 4^{th}

order 4-D PCE, 210 LHS data are required. However, the convergence study on the number of LHS requires for different polynomial order PCE for flutter responses showed convergence with samples less than $3\mathcal{A}$ as shown in Figure 5.3. The log (RMSE) plot for 4^{th} order 4D-PCE (Figure 5.3 (d)) shows that the convergence is obtained at 80 LHS. In order to include uncertainty quantification in the optimisation procedure (i.e. probabilistic optimisation), it is important to keep the number of samples as small as possible with reasonable accuracy. Hence, the convergence study is required to establish the minimum number of sample for PCE model. Based on the convergence study, the number of LHS data ($3 \times \mathcal{A}$) used in this case study is sufficient to provide an accurate estimation of the flutter response due to random parameters.

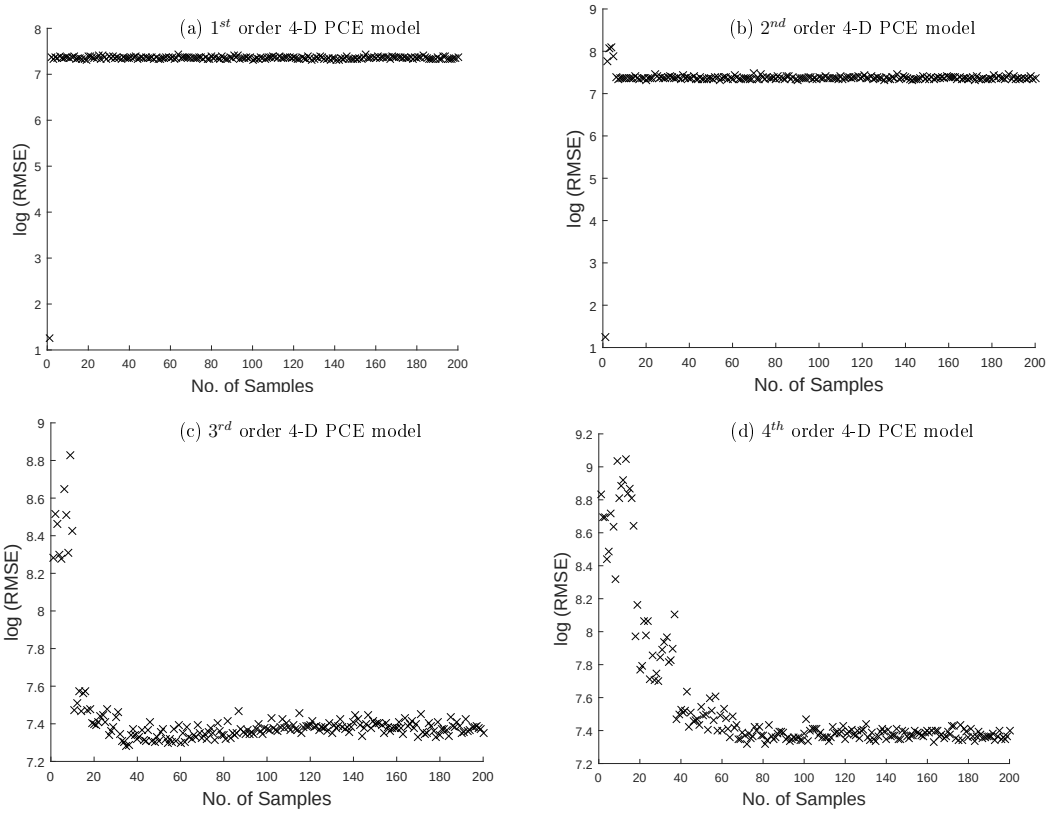

Figure 5.3: The convergence study of PCE model for wing flutter response with uncertain material properties (E_{11}, E_{22}, G_{12}) and ply thickness (t_{ply}) (a) 1^{st} order PCE (b) 2^{nd} order PCE (c) 3^{rd} order PCE and (d) 4^{th} order PCE.

Table 5.3 to 5.6 provides the mean and standard deviation of the flutter speed obtained using 1-D, 2-D, 3-D and 4-D PCE model and MCS with 2500 simulation runs. The flutter response due to uncertainty in longitudinal stiffness, E_{11} is plotted in Figure 5.4(a) and

the statistic are summarised in Table 5.3. The analysis are performed with 1st, 2nd, 3rd and 4th order PCE model.

Table 5.3: The mean, $\frac{\mu_{V_f}}{V_{f,design}}$ and standard deviation,σ of flutter speed approximated with PCE and MCS for 1-dimension order of random parameters.

	MCS (2500)	Order of PCE			
		$p=1$	$p=2$	$p=3$	$p=4$
Mean, $\frac{\mu_{V_f}}{V_{f,design}}$	0.9986	0.9996	0.9947	0.9964	0.9959
Std. dev, σ	4.0338	4.6194	4.7002	4.2018	4.4634
RE (%) (μ)	-	0.1001	0.3905	0.2203	0.2704
$\mathcal{A}$	-	2	3	4	5
N_{LHS}	-	6	9	12	15

Table 5.4: The mean, $\frac{\mu_{V_f}}{V_{f,design}}$ and standard deviation,σ of flutter speed approximated with PCE and MCS for 2-dimension order of random parameters.

	MCS (2500)	Order of PCE			
		$p=1$	$p=2$	$p=3$	$p=4$
Mean, $\frac{\mu_{V_f}}{V_{f,design}}$	0.9963	1.0018	0.9956	0.9977	0.9832
Std. dev, σ	4.3013	4.6568	4.5454	4.1921	6.7438
RE (%) (μ)	-	0.5520	0.0703	0.1405	1.3149
$\mathcal{A}$	-	3	6	10	15
N_{LHS}	-	9	18	30	45

Table 5.5: The mean, $\frac{\mu_{V_f}}{V_{f,design}}$ and standard deviation,σ of flutter speed approximated with PCE and MCS for 3-dimension order of random parameters.

	MCS (2500)	Order of PCE			
		$p=1$	$p=2$	$p=3$	$p=4$
Mean, $\frac{\mu_{V_f}}{V_{f,design}}$	0.9994	1.0023	0.9959	0.9964	0.9965
Std. dev, σ	4.2011	5.2343	5.0925	4.6985	5.3902
RE (%) (μ)	-	0.2902	0.3502	0.3002	0.2902
$\mathcal{A}$	-	5	15	20	35
N_{LHS}	-	15	45	60	105

The probability density function (PDF) plots of the flutter speed show a very good correlation with the MCS data with little discrepancy observed for 2nd, 3rd and 4th polynomial order. The relative error, RE of the mean flutter speed with respect of the MCS results are less than 0.4%, with the lowest RE obtained from 1st order PCE.

Similar observations can be made for the 2-D PCE model with uncertainty in E_{11} and E_{22} as shown in Figure 5.4(b). An excellent agreement between PCE and MCS results are obtained with lowest RE (mean value) of 0.07% for 2nd order PCE as given in Table

Table 5.6: The mean, $\frac{\mu_{V_f}}{V_{f,design}}$ and standard deviation,σ of flutter speed approximated with PCE and MCS for 4-dimension order of random parameters.

	MCS (2500)	Order of PCE			
		$p=1$	$p=2$	$p=3$	$p=4$
Mean, $\frac{\mu_{V_f}}{V_{f,design}}$	0.9981	1.0120	0.9935	0.9954	0.9965
Std. dev, σ	4.3186	4.8933	5.1753	5.0923	5.2424
RE (%) (μ)	-	0.3052	0.4607	0.2736	0.1592
$\mathcal{A}$	-	5	15	35	70
N_{LHS}	-	15	45	105	210

5.4. Higher RE of 1.32% of the mean value is observed for PCE with 4^{th} polynomial order in comparison with the MCS.

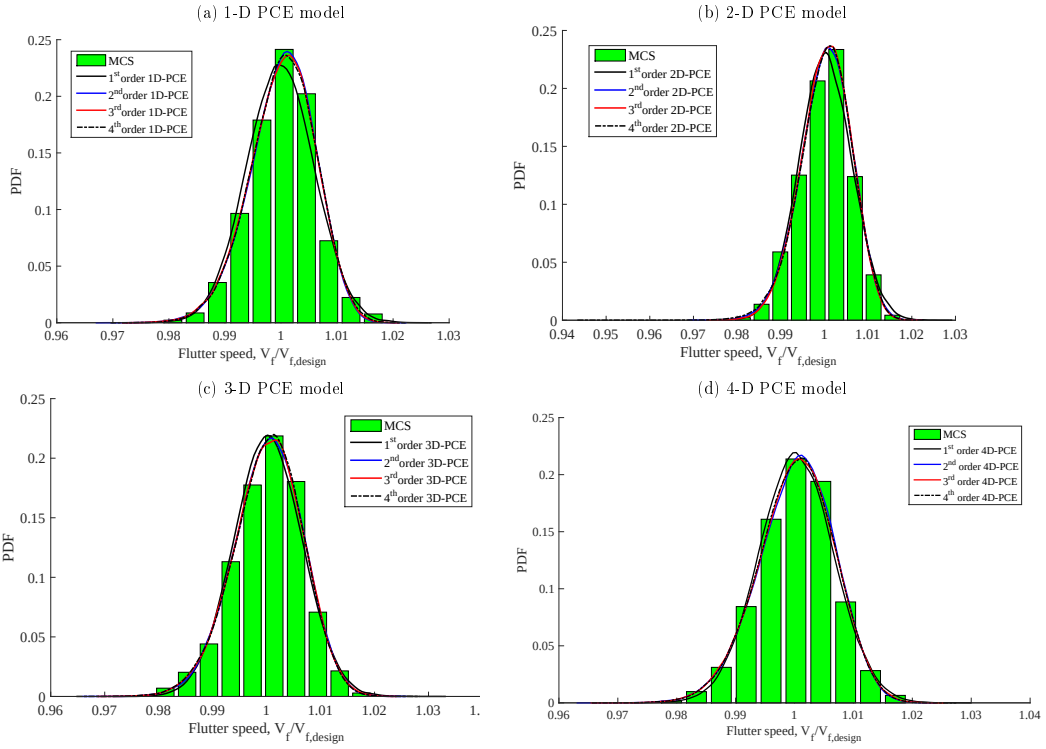

Figure 5.4: The flutter speed variation obtained with PCE model using different polynomial order in comparison with MCSs results (a) 1-D PCE model (b) 2-D PCE model (c) 3-D PCE model (d) 4-D PCE model.

For a 3-D PCE model with uncertainty in E_{11}, E_{22} and G_{12}, a small difference in the mean value is obtained compared to MCS for different orders of PCE with the highest RE of 0.35% obtained for second-order PCE. A higher number of LHS data (105 sample data) is required for 4^{th} order 3-D PCE to obtain a reasonably accurate flutter speed approximation.

Similarly, for a 4-D PCE model with uncertainty in E_{11}, E_{22}, G_{12} and t_{ply}, an excellent agreement with MCSs data was observed as shown in Figure 5.4(d) with the highest RE of 0.46% obtained for 2^{nd} order PCE. The lowest RE of 0.16% is obtained with 4^{th} order PCE. However, at least 210 training data points are required for 4^{th} order PCE, which is very expensive when involving a computationally demanding model. For flutter responses with higher dimensional order of random variables, 2^{nd} or 3^{rd} PCE model is sufficient to provide an accurate prediction with less computational expense.

Again, looking at Figure 5.4, all the PCE model except for the 1^{st} order PCE show similar distribution at the lower end tail and matched well with the MCS which suggests that the PCE model can capture the response variations accurately. In terms of design sensitivity to random parameters, the inclusion of multiple random parameters in the model results in different distribution properties which are evidenced from the skewness and the variance of the distribution. For example in Figure 5.4(b), when both E_{11} and E_{22} variations are quantified, the flutter speed distribution exhibits skewness with longer left-hand tail, which suggests that there is a possibility that the model will encounter lower flutter speed as results from these parameters variation. The design sensitivity of each random parameters can be quantified using the sensitivity index analysis.

It is observed that the flutter speed varies due to uncertain in material properties and ply thickness. Based on the PDF plots in Figure 5.4, there is a high probability that the deterministic wing design will experience flutter due to the uncertain parameter in the model. The probability of failure (POF) can be estimated from the PDF plots as the cumulative probability below the design flutter speed ($V_{\text{f}}/V_{\text{f}_{\text{design}}} = 1$) or the area under the PDF plots. For example, consider the flutter response with uncertain in E_{11}, E_{22}, G_{12} and t_{ply} (using 4^{th} order 4-D PCE), the POF value at design flutter speed is 0.47. The results suggested that the deterministic optimal design is not sufficiently reliable for flutter instability with a 47% chance of failure. The use of probabilistic design optimisation approach in wing design for flutter can provide a better and more reliable design by optimising the design for lower POF, which will be introduced later in Chapter 6.

The sensitivity of the random parameters on the wing flutter response are evaluated using the PC-based Sobol indices defined in Section 5.3.4 (page 134). The sensitivity index (SU_i) for each random parameter and their interaction are given in Table 5.7. The

random parameters, E_{11}, E_{22}, G_{12} and t_{ply} are denoted as 1,2,3 and 4, respectively. The complete set of sensitivity index can be obtained using the 4^{th} order 4-D PCE model in which the sensitivity for the interaction of all random parameters can be found. For 4^{th} order 4-D PCE, the total expansion terms including β_0 is $\mathcal{A} = \binom{8}{4} = 70$.

Table 5.7: The sensitivity index, SU for flutter speed determined using PC-based Sobol indices.

Sensitivity Index	Order of PCE			
	$p=1$	$p=2$	$p=3$	$p=4$
SU_1	0.8296	0.8146	0.8134	0.9801
SU_2	0.0029	0.0015	0.0018	0.0018
SU_3	0.1524	0.0048	0.0007	0.0001
SU_4	0.0151	0.0007	0.0096	0.0001
$SU_{1,2}$		0.1597	0.0002	0.0086
$SU_{1,3}$		0.0003	0.0002	0.0022
$SU_{1,4}$		0.0000	0.0004	0.0008
$SU_{2,3}$		0.0184	0.1564	0.0010
$SU_{2,4}$		0.0000	0.0007	0.0004
$SU_{3,4}$		0.0000	0.0002	0.0018
$SU_{1,2,3}$			0.0159	0.0005
$SU_{1,3,4}$			0.0001	0.0005
$SU_{1,2,4}$			0.0003	0.0012
$SU_{2,3,4}$			0.0001	0.0009
$SU_{1,2,3,4}$				0.0001
SU_1^{T}	0.8296	0.9746	0.8306	0.9939
SU_2^{T}	0.0029	0.1797	0.1754	0.0145
SU_3^{T}	0.1524	0.0235	0.1736	0.0071
SU_4^{T}	0.0151	0.0007	0.0114	0.0057

In the flutter analysis, the flutter speed was largely influenced by E_{11} with $SU_1 = 0.9801$. The coefficients β_α that contribute to SU_1 correspond to the basis polynomials of the form ζ_1^q $(q = 1, \ldots, 4)$. The corresponding contribution are $\{0.8047, 0.0070, 0.1586, 0.0098\}$ respectively (which sums up to 0.9801). For 2^{nd} order sensitivity index, the interaction between E_{11} and E_{22} ($SU_{12} = 0.086$) provide a secondary influence on the wing flutter response which is evidenced from Figure 5.4(b) with longer end tail is observed. The corresponding contribution are $\{0.0000, 0.0000, 0.0009, 0.0009, 0.0037, 0.0030\}$ which are related to basis polynomial of the form $\zeta_1^r \zeta_2^s$ $(r, s = 1, \ldots, 3)$. The 3^{rd} and 4^{th} order sensitivity index, the influence of the interaction terms on the wing flutter response are minimal with $SU_{i\ldots d} < 0.012$. The overall influence of each of the random parameter is obtained from SU_i^T. For 4^{th} order 4-D PCE, E_{11} provides major influence on the flutter speed with $SU_1^T = 0.9939$ followed by E_{22} with $SU_2^T = 0.0145$.

5.4.2 Polynomial Chaos Expansion for Buckling Response

The buckling response due to the uncertainty in the composite material properties (longitudinal stiffness, E_{11}, transverse stiffness, E_{22} and shear modulus, G_{12}) and the ply thickness, t_{ply} are evaluated using the PCE model and validated with the MCSs. The buckling response was quantified in terms of the buckling critical load factor, λ_{crit} when subjected to a static manoeuvre load case. The buckling critical load factor variation due to random variables with properties defined in Table 5.1 (page 131) are evaluated using 4-D PCE model, and the results were given in Table 5.8. The analysis requires numbers of LHS samples given by $N_{\text{LHS}} = 3 \times \mathcal{A}$.

Table 5.8: The mean, $\frac{\mu_{V_f}}{V_{f,\text{Design}}}$ and standard deviation, σ of critical buckling load factor, λ_{crit} approximated with PCE and MCS for 4-dimension order of random parameters and MCSs.

	MCS (2500)	Order of PCE			
		$p=1$	$p=2$	$p=3$	$p=4$
Mean, $\frac{\mu_{V_f}}{V_{f,\text{Design}}}$	0.9873	1.0137	0.9886	1.0081	1.0103
Std. dev, σ	0.2307	0.2629	0.2806	0.2491	0.2553
RE (%) (μ)	-	2.6740	0.1317	2.1068	2.3296
$\mathcal{A}$	-	5	15	35	70
N_{LHS}	-	15	45	105	210

The PCE's results show an excellent agreement with the MCS data and only require a small number of data samples in comparison with MCSs (2500 runs). The lowest RE (mean value) of 0.13% was obtained from 2$^{\text{nd}}$ order PCE and the highest RE of 2.67% was calculated for 1$^{\text{st}}$ order PCE. Figure 5.5 shows the PDF plots for critical load factor obtained with PCE and MCSs. An excellent agreement with the MCS results can be seen from the plots with a small discrepancy shown when different order PCEs were used. The PDF's plot for 2$^{\text{nd}}$ order PCE exhibits longer tail sections in comparison with 1$^{\text{st}}$, 3$^{\text{rd}}$ and 4$^{\text{th}}$ order PCE as results from a larger response variance.

The sensitivity of the random parameters on the buckling response is evaluated using the PC-based Sobol' Indices. The sensitivity indices, SU_i for buckling response were tabulated in Table 5.9. Using 4$^{\text{th}}$ order 4-D PCE model, the complete set of sensitivity indices can be obtained from the expansion terms ($\mathcal{A} = 70$). Based on the first order sensitivity index, the buckling response are mainly influence by the random parameter, E_{11} denoted by SU_1 ($SU_1^{1^{\text{st}}} = 0.8994$, $SU_1^{2^{\text{nd}}} = 0.8960$, $SU_1^{3^{\text{rd}}} = 0.8967$ and $SU_1^{4^{\text{th}}} = 0.9986$).

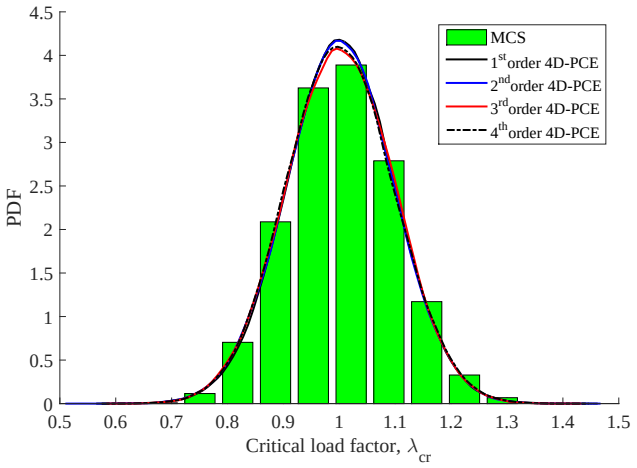

Figure 5.5: The PDFs for buckling critical load factor obtained with 1st, 2nd, 3rd, 4th order 4D-PCE model and MCSs.

Table 5.9: The sensitivity index, *SU* determined for the buckling critical load factor using PC-based Sobol' indices method.

Sensitivity Index	Order of PCE			
	$p=1$	$p=2$	$p=3$	$p=4$
SU_1	0.8994	0.8960	0.8967	0.9986
SU_2	0.0090	0.0002	0.0002	0.0001
SU_3	0.0036	0.0099	0.0000	0.0000
SU_4	0.0880	0.0000	0.0091	0.0000
$SU_{1,2}$		0.0043	0.0000	0.0010
$SU_{1,3}$		0.0000	0.0000	0.0001
$SU_{1,4}$		0.0000	0.0000	0.0000
$SU_{2,3}$		0.0888	0.0050	0.0000
$SU_{2,4}$		0.0006	0.0001	0.0000
$SU_{3,4}$		0.0000	0.0000	0.0000
$SU_{1,2,3}$			0.0883	0.0001
$SU_{1,3,4}$			0.0000	0.0000
$SU_{1,2,4}$			0.0005	0.0000
$SU_{2,3,4}$			0.0000	0.0000
$SU_{1,2,3,4}$				0.0000
SU_1^T	0.8994	0.9004	0.9856	0.9998
SU_2^T	0.0090	0.0940	0.0941	0.0013
SU_3^T	0.0036	0.0988	0.0935	0.0003
SU_4^T	0.0880	0.0007	0.0097	0.0002

5.4.3 Polynomial Chaos Expansion for Gust Response

The variation of gust response due to uncertainty in the composite material properties (E_{11}, E_{22} and G_{12}) and ply thickness, t_{ply} are evaluated using 4-D PCE model, and the results are validated with the MCSs. The gust responses are evaluated in terms of wing RBM value due to discrete gust load at $L_{\text{g}} = 216\,\text{m}$. The RBM variation due to random

variables is obtained using 1^{st}, 2^{nd}, 3^{rd} and 4^{th} order polynomial basis. The minimum number of LHS samples are used for the analysis given by $N_{\text{LHS}} = 3 \times \mathcal{A}$.

The mean, standard deviation and relative error (from MCSs data) for the RBM response are given in Table 5.10. The RBM responses obtained at different orders of PCE model are plotted with the MCS data as depicted in Figure 5.6. The number of training data used for the MCS model is 2500. Based on the results obtained (up to 4^{th} polynomial order), the lowest relative error for the mean value is 20.2% (1^{st} order PCE) with standard deviation value of 0.2611. As the order of polynomial increases, the resulting relative errors increase, with the highest value of 48.6% obtained from 2^{nd} order PCE. The results are inconsistent with the previous finding. This is thought due to more considerable difference (in order of 10^1 magnitude) in RBM values and insufficient number of LHS samples. Figure 5.6 provides a PDF plot of RBM at different polynomial order of 4-D PCE. There is a large discrepancy between the MCS and the PDF's plot obtained from PCE model (2^{nd} to 4^{th} order) at the peak value. However, a small discrepancy is noticed at the left-tail of the PDF's plot suggesting that the results are sufficient to provide information on the probability of failure at specific target design value.

Table 5.10: The mean, $\frac{\mu_{RBM}}{RBM_{\text{det}}}$ and standard deviation, σ_{RBM} of Root Bending Moment, RBM approximated with PCE and MCS for 4-dimension order of random parameters.

	MCS (2500)	Order of PCE			
		$p=1$	$p=2$	$p=3$	$p=4$
Mean, $\frac{\mu_{RBM}}{RBM_{\text{det}}}$	1.4662	1.1705	2.1787	1.9366	0.9442
Std. dev, $\frac{\sigma_{RBM}}{RBM_{\text{det}}}$	0.3211	0.2611	0.7857	0.7677	1.1879
RE (%) (μ)	-	20.1678	48.5950	32.0829	35.6022
$\mathcal{A}$	-	5	15	35	70
N_{LHS}	-	15	45	105	210

The sensitivity analysis was performed on the RBM responses to evaluate the uncertainty effects of the random parameters. The sensitivity indices, SU_i for RBM response are tabulated in Table 5.11. Based on the first-order sensitivity index,the RBM response are mainly influence by random parameter, E_{11} denoted by SU_1 except for 3^{rd} order polynomial where E_{22} is the major contributor to variation in RBM value. It is noticed from the higher-order sensitivity index; the combined contribution of several parameters also influences the RBM response. For example, based on the 1^{st} order polynomial ($p = 1$) data, the combined effect of all parameters is the second major influence on the RBM response with $SU_4^T = 0.2560$.

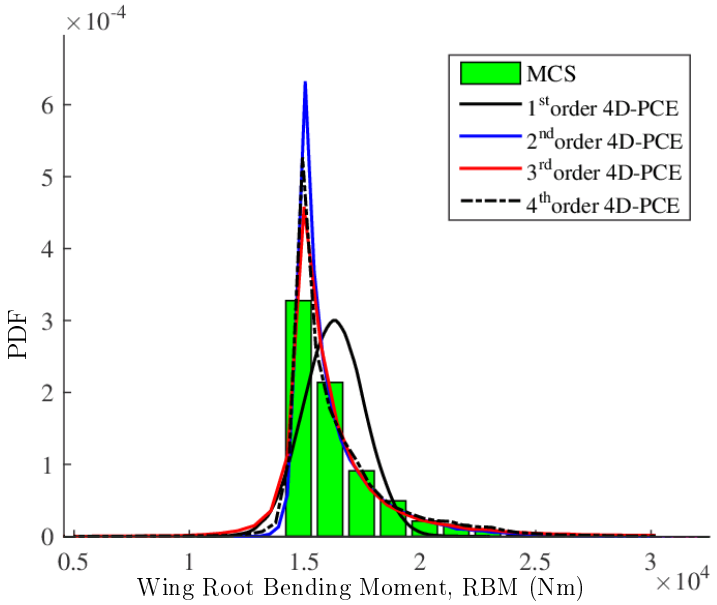

Figure 5.6: The PDFs for wing root bending moment (RBM) due to gust load obtained with 1^{st}, 2^{nd}, 3^{rd}, 4^{th} order 4D-PCE model. Results are compared with MCSs run using 2500 sample data.

Overall, the PCE model is capable of producing a reliable and accurate prediction of the wing responses due to the random parameters. An excellent agreement is obtained between the PCE data and MCSs in flutter and buckling analysis. However, a significant discrepancy is noticed for the RBM responses due to more considerable difference (in order of 10^1 magnitude) in RBM values and insufficient number of LHS samples.

5.5 Random Sampling High Dimensional Model Representation (RS-HDMR) Method

The High Dimensional Model Representation (HDMR) is another technique for uncertainty quantification introduced by Rabitz [152], which can be used to capture the input-output relationships for high dimensional random input variables. As mentioned in Section 5.3 (page 128), the efficiency of PCE for uncertainty quantification reduces as the dimensional order of the random variables increase. This disadvantage is often referred to as the *'curse of dimensionality'* of PCE [21]. The HDMR method employs low order correlations of the random variables to represent a response function, $f(\mathbf{x})$ with excellent accuracy. Hence, the method is capable of including higher dimensional order of random variables with acceptable computational expense. The HDMR method has been used

Table 5.11: The sensitivity index, SU for wing root bending moment (RBM) due to gust load using PC-based Sobol' indices.

Sensitivity Index	Order of PCE			
	$p=1$	$p=2$	$p=3$	$p=4$
SU_1	0.5084	0.2382	0.3541	0.4274
SU_2	0.0146	0.2943	0.1961	0.2178
SU_3	0.2210	0.0165	0.0040	0.0008
SU_4	0.2560	0.0158	0.0037	0.0022
$SU_{1,2}$		0.0956	0.0207	0.2780
$SU_{1,3}$		0.3030	0.0039	0.0036
$SU_{1,4}$		0.0007	0.0115	0.0148
$SU_{2,3}$		0.0143	0.1300	0.0057
$SU_{2,4}$		0.0202	0.2201	0.0151
$SU_{3,4}$		0.0015	0.0114	0.0015
$SU_{1,2,3}$			0.0134	0.0023
$SU_{1,3,4}$			0.0003	0.0008
$SU_{1,2,4}$			0.0292	0.0177
$SU_{2,3,4}$			0.0016	0.0123
$SU_{1,2,3,4}$				0.0001
SU_1^T	0.5084	0.6375	0.4331	0.7447
SU_2^T	0.0146	0.4244	0.6111	0.5490
SU_3^T	0.2210	0.3352	0.1646	0.0270
SU_4^T	0.2560	0.0381	0.2779	0.0643

in previous studies [155–157] to quantify the effect of random variables in composite materials.

There are three common types of HDMR expansion, namely, ANOVA-HDMR, cut-HDMR and random sampling HDMR (RS-HDMR) [153]. The RS-HDMR method is presented herein, and comparison is made with the PCE method. In the RS-HDMR method, the lower-order component functions are determined from the average value of the response function over the whole domain [27, 153] while the higher-order components are obtained from a Monte Carlo random sampling. Hence, the method is straightforward and applicable to many engineering problems.

The governing equation for the HDMR method is given by [152];

$$f(X) = f_0 + \sum_{i=1}^{n} f_i(x_i) + \sum_{1\leq i\leq j\leq n} f_{ij}(x_i, x_j) + ... + f_{1,2,...,n}(x_1, x_2, ..., x_n), \tag{5.27}$$

where f_0, $f_i(x_i)$, $f_{ij}(x_i, x_j)$ and $f_{1,2,...,n}(x_1, x_2, ..., x_n)$ are the zeroth, first, second and n^{th} order components. The input random parameters are rescaled such that $0 \leq x_i \leq 1$ for all i. The output function is defined in a unit hypercube, such that $K^N = \{(x_1, ..., x_n), i = 1, ..., n\}$.

The components of RS-HDMR function in Eqn. (5.27) can be evaluated using the sum of the integral function as [192]

$$f_0 = \int_{K^n} \prod_{i=1}^{n} w_i(x_i) f(\mathbf{x}) d\mathbf{x}, \tag{5.28}$$

$$f_i(x_i) = \int_{K^{n-1}} \prod_{\substack{k=1 \\ k \neq i}}^{n} w_k(x_k) f(\mathbf{x}) d\mathbf{x}^i - f_0, \tag{5.29}$$

$$f_{ij}(x_i, x_j) = \int_{K^{n-2}} \prod_{\substack{k=1 \\ k \neq ij}}^{n} w_k(x_k) f(\mathbf{x}) d\mathbf{x}^{ij} - f_i(x_i) - f_j(x_j) - f_0, \tag{5.30}$$

$$...,$$

where $d\mathbf{x}^i$ and $d\mathbf{x}^{ij}$ are the product of $dx_1, dx_2, ..., dx_n$ without dx_i and $dx_i dx_j$, respectively.

The zeroth order term, f_0 are estimated from the average value of response function, $f(\mathbf{x})$ for all $\mathbf{x}^{(s)} = (x_1^{(s)}, x_2^{(s)}, ..., x_n^{(s)}); s = 1, 2, ..., N$:

$$f_0 = \int_{K^n} \prod_{i=1}^{n} w_i(x_i) f(\mathbf{x}) d\mathbf{x} \approx \frac{1}{N} \sum_{s=1}^{N} f(\mathbf{x}^{(s)}), \tag{5.31}$$

where N is the number of sampling data.

The higher-order terms of HDMR component functions can be determined via two methods - direct determination and approximation using analytical basis function (i.e. Orthonormal polynomials). In the direct determination method, different set of the random samples of $f(x_i, x^i)$ are required to determine each of the component functions. If the input parameter, x_i is fixed at m distance values, mN numbers of the random samples are required and are computationally expensive. In the approximation method, only one set of random samples, N is necessary in order to determine all the component functions for RS-HDMR which inevitability reduces the sampling effort for computation. Herein, the approximation method is employed to determine the higher-order terms.

5.5.1 Approximation of Higher-Order Component Functions

For approximation of the higher order terms in HDMR function ($f_i(x_i)$, $f_{ij}(x_i, x_j)$, ... ,$f_{1,2,...,n}(x_1, x_2, ..., x_n)$), orthonormal polynomial basis functions are used to represent the

terms. The first and second order components can be formulated as

$$f_i(x_i) \approx \sum_{r=1}^{k} \alpha_r^i \varphi_r(x_i), \tag{5.32}$$

$$f_{ij}(x_i, x_j) \approx \sum_{p=1}^{l} \sum_{q=1}^{l'} \beta_{pq}^{ij} \varphi_p(x_i) \varphi_q(x_j), \tag{5.33}$$

....

where

- k, l, l' define the order of polynomial expansion.
- The order of polynomial basis function is given by r, p, q.
- α_r^i and β_{pq}^{ij} are the constant expansion coefficients that need to be determined.
- $\varphi_r(x_i)$, $\varphi_p(x_i)$ and $\varphi_q(x_j)$ are the orthonormal basis functions.

The expansion coefficients are determined by a minimisation process and Monte Carlo Integration [153] which leads to

$$\begin{aligned} \alpha_r^i &= \int_{K^n} \prod_{k=1}^{n} w_k(x_k) f(\mathbf{x}) \varphi_r^i(x_i^{(s)}) d\mathbf{x} \\ &\approx \frac{1}{N} \sum_{s=1}^{N} f(\mathbf{x}^s) \varphi_r(x_i^{(s)}), \end{aligned} \tag{5.34}$$

$$\begin{aligned} \beta_{pq}^{ij} &= \int_{K^n} \prod_{k=1}^{n} w_k(x_k) f(\mathbf{x}) \varphi_p^i(x_i^{(s)}) \varphi_q^j(x_j) d\mathbf{x} \\ &\approx \frac{1}{N} \sum_{s=1}^{N} f(\mathbf{x}^{(s)}) \varphi_p(x_i^{(s)}) \varphi_q(x_j^{(s)}) \\ &.... \end{aligned} \tag{5.35}$$

In most applications, lower-order polynomial approximation (up to third-order polynomial) is found to be sufficient although higher-order polynomials may be required for highly non-linear problems. However, using higher-order polynomial may results in sparse approximation due to more terms involved in the governing equation, and each has their own Monte Carlo integration errors. The errors are due to large variances in the integrands in Eqns. (5.34) to (5.35) and increase if a large number of basis functions

are involved (higher orders of polynomials are used). Hence, the Monte Carlo integration errors can be reduced by increasing the sample size N and by reducing the variance of integrands (Correlation method and Ratio control variate method).

5.5.2 Ratio Control Variate method

The Monte Carlo Integration errors related to approximation of higher-order terms in HDMR can significantly reduced by using Ratio Control Variate method [193]. In this method, consider Eqn. (5.34), the variance of the integrand $f(\mathbf{x})\varphi_r^i(x_i)$ in K^n can be reduced by seeking a control variate function $h(\mathbf{x})$ which satisfy two conditions:

- The response function $f(\mathbf{x})$ and $h(\mathbf{x})$ over the entire domain of $\mathbf{x}$ are very similar.
- The integrand $\int_{K^n} \prod_{k=1}^{n} w_k(x_k) h(\mathbf{x}) \varphi_r^i(x_i^{(s)}) d\mathbf{x}$ can be deduced analytically.

The analytical function is defined as

$$h(\mathbf{x}) = f_0 + \sum_{i=1}^{n}\sum_{r=1}^{k} \bar{\alpha_r^i}\varphi_r^i(x_i) + \sum_{1\le i<j\le n}\sum_{p=1}^{l}\sum_{q=1}^{l'} \bar{\beta_{pq}^{ij}}\varphi_p^i(x_i)\varphi_q^j(x_j), \tag{5.36}$$

where $\bar{\alpha_r^i}$ and $\bar{\beta_{pq}^{ij}}$ are the initial values obtained from direct Monte Carlo Integration.

Hence, the expansion coefficient, α and β can be determined by an iteration process involving $f(\mathbf{x})$ and $h(\mathbf{x})$ as

$$\alpha_r^i \approx \bar{\alpha_r^i} \frac{\sum_{s=1}^{N} f(\mathbf{x}^{(s)})\varphi_r^i(x_i^{(s)})}{\sum_{s=1}^{N} h(\mathbf{x}^{(s)})\varphi_r^i(x_i^{(s)})} \tag{5.37}$$

and

$$\beta_{pq}^{ij} \approx \bar{\beta_{pq}^{ij}} \frac{\sum_{s=1}^{N} f(\mathbf{x}^{(s)})\varphi_p^i(x_i^{(s)})\varphi_q^j(x_j^{(s)})}{\sum_{s=1}^{N} h(\mathbf{x}^{(s)})\varphi_p^i(x_i^{(s)})\varphi_q^j(x_j^{(s)})}. \tag{5.38}$$

The improved expansion coefficients are obtained when $h(\mathbf{x})$ is equal to $f(\mathbf{x})$ which give the ratio of summation terms in Eqns. (5.37) and (5.38) equals to one. The iteration process is stopped when the difference of two adjacent iterative values is below that of the specified tolerance value.

5.5.3 Optimisation for polynomial order

In many cases, the contribution of specific components of HDMR functions to $f(x)$ are relatively small and can be neglected. Ziehn & Tomling [27] proposed an optimisation approach based on the least-squares method to determine the optimal order of each component of RS-HDMR function. So that, any inactive components can be eliminated and further simplify the governing HDMR equation.

The optimum polynomial order can be determined from the smallest sum of square error of all component functions. The optimum order of first-order component function is determined such that

$$\min_{k_i \in \{0,1,2,3\}} \sum_{s=1}^{N} [f(\mathbf{x}^{(s)}) - (f_0 + f_i(x_i^{(s)}))]^2 \tag{5.39}$$

and where

$$f_i(x_i) = \begin{cases} \sum_{r=1}^{k_i} \alpha_r^i \varphi_r(x_i) : k_i \in \{1,2,3\}, \\ 0 : k_i = 0. \end{cases} \tag{5.40}$$

Similarly, the optimum polynomial order of second-order component function can be obtained using the optimal order for first-order component functions as follows

$$\min_{l_i = l'_j \in \{0,1,2,3\}} \sum_{s=1}^{N} [f(\mathbf{x}^{(s)}) - (\hat{f}(\mathbf{x}^{(s)}) + f_{ij}(x_i^{(s)}, x_j^{(s)}))]^2 \tag{5.41}$$

where

$$\hat{f}(\mathbf{x}^{(s)}) = f_0 + \sum_{i=1}^{n} \sum_{r=1}^{k_i} \alpha_r^i \varphi_r(x_i^{(s)}), \tag{5.42}$$

and

$$f_{ij}(x_i, x_j) = \begin{cases} \sum_{p=1}^{l_i} \sum_{q=1}^{l'_j} \beta_{pq}^{ij} \varphi_p(x_i) \varphi_q(x_j) : l_i, l_j \in \{1,2,3\} \\ 0 : l_i, l_j = 0. \end{cases} \tag{5.43}$$

By using the optimal polynomial order and the expansion coefficients, the response of the model for any value in the domain $\mathbf{x}$ can be approximated using the metamodel RS-HDMR equation (up to second-order components) given by

$$f(\mathbf{x}) = f_0 + \sum_{i=1}^{n} \sum_{r=1}^{k} \alpha_r^i \varphi_r^i(x_i) + \sum_{1 \le i < j \le n} \sum_{p=1}^{l} \sum_{q=1}^{l'} \beta_{pq}^{ij} \varphi_p^i(x_i) \varphi_q^j(x_j). \tag{5.44}$$

5.5.4 Global Sensitivity Analysis in RS-HDMR

The global sensitivity of the random parameters on the model response can be estimated by calculating the total and partial variances of the response [27]. The total variance, D can be calculated by

$$D = \int_{K^n} f^2(\mathbf{x}) d\mathbf{x} - f_0^2 \tag{5.45}$$

and the partial variance, $D_{i_1,\ldots,i_s}$ is given by

$$D_i = \int_0^1 f_i^2(x_i) dx_i, \tag{5.46}$$

$$D_{ij} = \int_0^1 \int_0^1 f_{ij}^2(x_i, x_j) dx_i dx_j, \tag{5.47}$$

....

In RS-HDMR, the partial variance can be obtained from the sum of expansion coefficients as follows [194];

$$D_i = \sum_{r=1}^{k_i} (\alpha_r^i)^2 \tag{5.48}$$

and

$$D_{ij} = \sum_{p=1}^{l_i} \sum_{q=1}^{l'_j} (\beta_{pq}^{ij})^2. \tag{5.49}$$

Once all the partial variance are obtained, the sensitivity index can be estimated by

$$S_{i_1,\ldots,i_s} = \frac{D_{i_1,\ldots,i_s}}{D}; \qquad 1 \leq i_1 < \ldots < i_s \leq n, \tag{5.50}$$

where

$$\sum_{i=1}^{n} S_i + \sum_{1 \leq i < j \leq n} S_{ij} + \ldots + S_{1,2,\ldots,n} = 1. \tag{5.51}$$

The main effect of the each random variable $(x_1, \ldots, x_n)$ on the model response is given by the first-order sensitivity index, S_i, while the interaction effect of the two random variables is evaluated from the second order sensitivity index, S_{ij} and so on.

5.6 Random Sampling - High Dimensional Model Representation (RS-HDMR) Case Study

In this case study, the efficiency of RS-HDMR method to quantify the effects of random input variables on the structural and aeroelastic responses of the FE composite wing are evaluated. The buckling and flutter responses due to variation in material properties (E_{11}, E_{22} and G_{12}) and composite ply thickness, t_{ply} are estimated using second-order RS-HDMR formulation given in Eqns. (5.32) and (5.33). The effectiveness of the method is determined in terms of its relative error, RE concerning MCSs. In this case, the RE is given by;

$$RE(\%) = \frac{|F - F'_{\text{RS-HDMR}}|}{F} \times 100, \tag{5.52}$$

where F is the response quantity obtained from MCSs and $F'_{\text{RS-HDMR}}$ is the approximate response obtained from the RS-HDMR method.

The mean and standard deviation of the random input variables are given in Table 5.1 (page 127) with the coefficient of variance (CV) of 0.1 for stiffness properties and 0.01 for the ply thickness. All other model parameters for buckling and flutter analysis have been defined in Section 5.2 (page 126).

5.6.1 Flutter Response

The flutter speed variations due to uncertainty in the composite material properties (E_{11}, E_{22} and G_{12}) and the composite ply thickness, t_{ply} are evaluated using the RS-HDMR model. The random sampling method is chosen due to its efficiency in determining the HDMR component function at less number of samples. The effect of these parameter variations are assessed individually, and their collective contribution on the flutter speed are studied. The outcomes from the case study are directly compared with MCSs and 4^{th} order PCE's results.

The wing's flutter response variation due to random input variables is predicted using the second-order RS-HDMR method formulated in Eqn. (5.44). The ratio control variate method is employed to determine the expansion coefficients with a maximum of ten iterations steps. The optimum polynomial order is obtained by an iteration process using the improved expansion coefficients to eliminate inactive terms in RS-HDMR formulation.

Table 5.12 provides the optimum polynomial order for the orthonormal basis function. The first-order, f_1 and second-order component, f_{12} of the RS-HDMR components are formulated using the first-order polynomial.

Table 5.12: The optimum polynomial's order for first and second-order RS-HDMR component functions in flutter analysis.

RS-HDMR component	f_1	f_2	f_3	f_4	f_{12}	f_{13}	f_{23}	f_{14}	f_{24}	f_{34}
Polynomial order	1	0	0	0	1	0	0	0	0	0

The outcomes from the RS-HDMR analysis are summarised in Table 5.13 together with the MCSs and PCE's results. In comparison with MCSs, the responses obtained show a small discrepancy in the maximum, minimum and mean flutter speed value which evidenced from the RE value. The RE obtained for these parameters are 0.491%, 0.307% and 0.401%, respectively. For standard deviation, σ_{V_f}, a RE value of 12.049% is obtained for the flutter speed. However, these values are smaller in comparison with the PCE's data (RE value of 21.935%). The number of samples required for RS-HDMR is 332 samples which are 58% more than the minimum number of samples for PCE method.

Nevertheless, the results obtained show better accuracy in comparison with PCE. Moreover, the number of samples required in the RS-HDMR is not dependent on the dimensional order of the random variables as in PCE. Hence, the method is thought to be more efficient when dealing with higher dimensional order of random parameters. The only disadvantage is that the optimum number of samples need to be determined for better accuracy.

Table 5.13: The statistical data of the flutter responses obtained from RS-HDMR method. The results obtained from MCSs and PCE are included for comparison.

	MCS	RS-HDMR	PCE	RE (%)
Max, $\frac{V_\mathrm{f}}{V_{\mathrm{f,Design}}}$	1.019	1.024	1.028	0.491
Min, $\frac{V_\mathrm{f}}{V_{\mathrm{f,Design}}}$	0.977	0.980	0.966	0.307
Mean, $\frac{\mu_{V_\mathrm{f}}}{V_{\mathrm{f,Design}}}$	0.998	1.002	0.997	0.401
Std., σ_{V_f}	4.299	4.817	5.242	12.049
N_{sample}	2500	332	210	-

The scatter plot of the flutter speed variation obtained from RS-HDMR, and original MCSs model is depicted in Figure 5.7. It can be seen that the response data obtained from the RS-HDMR is well-matched with the MCSs with only a small discrepancy being noticed. A direct correlation exists between both sets of data.

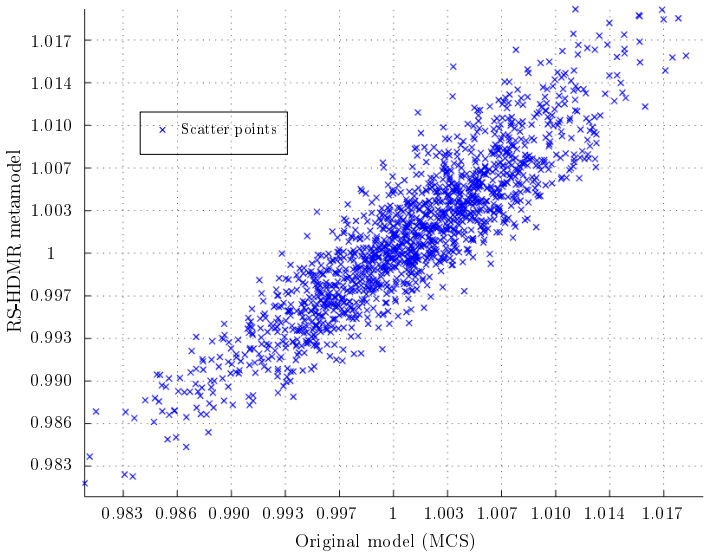

Figure 5.7: The scatter plot of the flutter speed obtained from RS-HDMR and original MCSs data.

The probability density function (PDF) of flutter response is plotted and depicted in Figure 5.8 together with the MCSs and PCE results. As expected, the PDF's curve for RS-HDMR is comparable with the bar plot of the MCSs. Small differences (a second peak) is noticed at the right tail of the RS-HDMR curve due to the inclusion of higher-order terms in the governing equation. In comparison with the PCE, the peak section of the RS-HDMR's curve is better suited with the MCS results whereas the PCE's curve is slightly offset to the right.

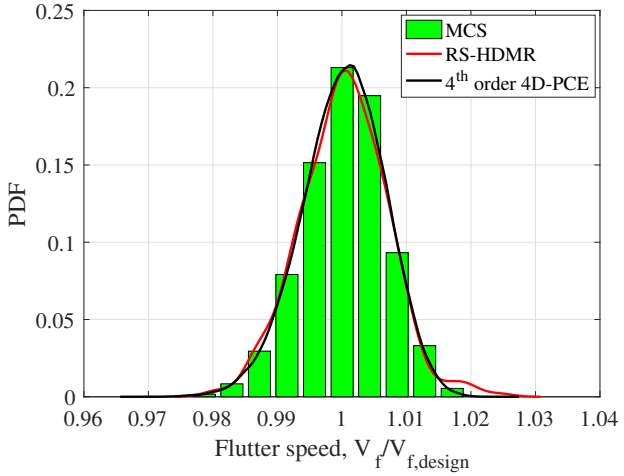

Figure 5.8: The plots of probability density function (PDF) against the flutter speed deduced from uncertainty quantification analysis using the RS-HDMR method, PCE method and MCSs.

The global sensitivity analysis is performed by calculating the partial variance as formulated in Eqn. (5.5.4). The first and second-order sensitivity indices (S_i and S_{ij}) are given in Table 5.14. The subscripts {1,2,3,4} are referred to E_{11}, E_{22}, G_{12} and t_{ply}, respectively. Based on the sensitivity index values, the main effects are contributed by E_{11} with $S_1 = 0.9804$. The interaction effects on the flutter response is contributed by E_{11} and E_{22} with $S_{12} = 0.0196$. The results are very similar to the sensitivity index, SU obtained from PC-based Sobol' Indices in which the main effects are contributed by E_{11} with $SU_1 = 0.9801$. The second-order PC-based Sobol' Indices is also contributed by E_{11} and E_{22} with $S_{12} = 0.0086$. These observations suggest that both methods are capable of producing accurate prediction with less computational expenses compared to convectional sensitivity analysis methods such as MCS-based Sobol' Indices which requires a more significant number of data samples.

Table 5.14: The first and second-order sensitivity indices calculated for flutter speed responses due to random input variables. The indices are obtained using the RS-HDMR method.

First Order Component		Second Order Component	
Sensitivity Index	Value	Sensitivity Index	Value
S_1	0.9804	S_{12}	0.0196
S_2	0.0000	S_{13}	0.0000
S_3	0.0000	S_{14}	0.0000
S_4	0.0000	S_{23}	0.0000
		S_{24}	0.0000
		S_{34}	0.0000

The variation of first-order RS-HDMR components due to uncertain in E_{11} is plotted in Figure 5.9. It can be seen that the component values increase proportionally as E_{11} is increased to 1. Notice that a unit scaled value of E_{11} is used in the plot. The $f_0 + f_1(E_1)$ values are normalised with $V_{\text{f,Design}}$. The results suggest that the flutter speed variation is mainly influence by E_{11} as the $f_0 + f_1(E_{11})$ value is approximately equals to $V_{\text{f,Design}}$.

The interaction effect of E_{11} and E_{22} on the second-order components of RS-HDMR function is visualised in a surface plot as shown in Figure 5.10. The $f_{12}(E_{11}, E_{22})$ are plotted using the actual value. From the plot, the highest effect is observed when E_{11} is at maximum/minimum value, and E_{22} is at minimum/maximum value. The second-order component equals zero when E_{11} or E_{22} is 0.5. However, the interaction effect of E_{11} and E_{22} on the flutter speed variation is minimal (only 2% of the total sensitivity

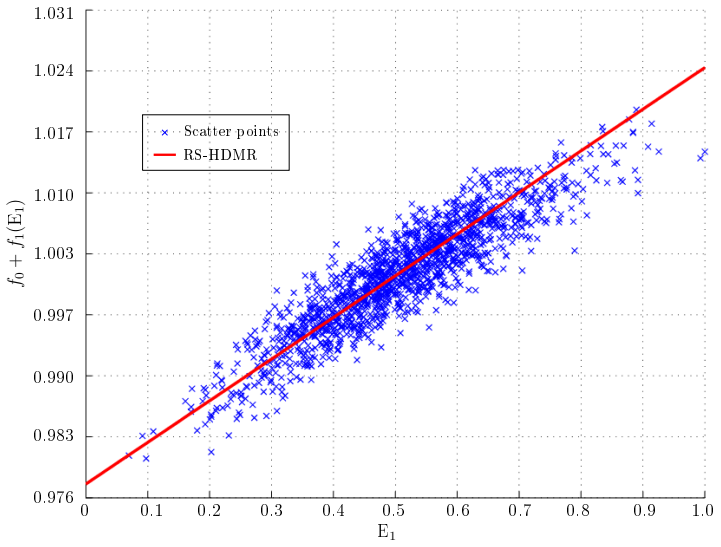

Figure 5.9: The scatter plot of first-order RS-HDMR components (flutter response) due to uncertain in E_{11}.

index). The response variation is mainly influenced by the uncertainty in the random parameter E_{11}.

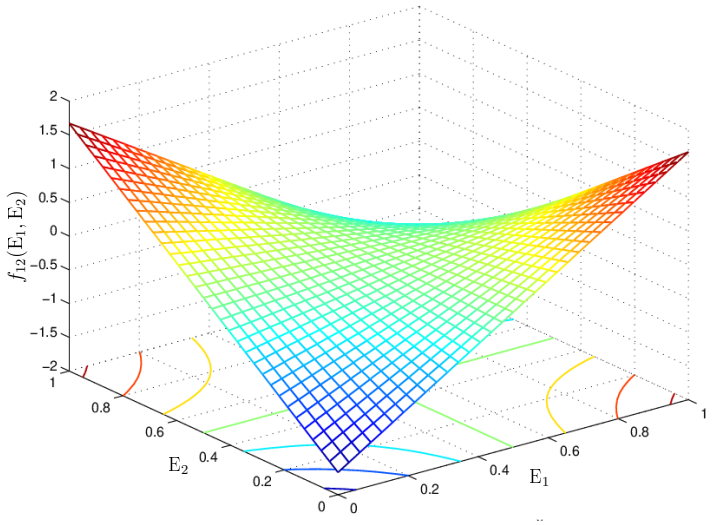

Figure 5.10: The surface plot of second-order RS-HDMR component due to interaction effect from input parameters E_{11} and E_{22}.

5.6.2 Buckling Response

The buckling response variation due to uncertainty in the composite material properties (E_{11}, E_2 and G_{12}) and composite ply thickness (t_{ply}) are evaluated using the RS-HDMR model and validated with the MCSs results. The buckling response is quantified in terms of the buckling critical load factor, λ_{crit} when subjected to a static manoeuvre load. The

properties of the random input variables are given in Table 5.1 (page 127). The effect of random input variables on the buckling response is quantified individually, and their interaction contribution on the responses are studied. A comparative study is performed to evaluate the effectiveness of the RS-HDMR method over the PCE method. The results obtained from 4^{th} order PCE method is used for comparison.

The output response due to random input variables is estimated using a second-order RS-HDMR formulation as in Eqn. (5.44). The ratio control variate method is used to determine the expansion coefficient with ten iteration steps. An iteration process determines the optimum polynomial order for the orthonormal basis functions to improve the estimation. The optimum polynomials order are given in Table 5.15. The first-order; f_1 and second-order RS-HDMR components; f_{14} and f_{23} are formulated using a first-order polynomial.

Table 5.15: The optimum polynomials order for the first and second-order RS-HDMR component functions in the buckling analysis.

RS-HDMR component	f_1	f_2	f_3	f_4	f_{12}	f_{13}	f_{23}	f_{14}	f_{24}	f_{34}
Polynomial order	1	0	0	0	0	0	1	1	0	0

The mean and standard deviation of the output response obtained from RS-HDMR model are summarised in Table 5.16. In general, the RS-HDMR method able to produce reliable data which well-matched with the MCSs data. The lowest relative error, RE of 0.151% is obtained for the maximum critical load factor, λ_{crit}. Similarly, a small RE of 1.766% is obtained for the mean value concerning MCSs. Higher RE values are recorded for the minimum λ_{crit} and the standard deviation value, $\sigma_{\lambda_{\text{crit}}}$ of 14.946% and 7.907%, respectively. In comparison with the PCE model, the RS-HDMR's output response produces lower RE for maximum λ_{crit} and standard deviation value. Both RS-HDMR and PCE methods produce an acceptable level of accuracy in comparison with the MCSs at smaller sampling sizes. The number of samples used for both method is 210 as opposed to MCSs which requires 2500 samples.

The scatter plot of the buckling critical load factor obtained from RS-HDMR metamodel and original MCSs model are depictured in Figure 5.11. An excellent correlation is observed for the estimated response as compared to the MCSs data. The PDF plot of RS-HDMR's output response is presented in Figure 5.12 together with MCSs and PCE plots. A good correlation is observed for the RS-HDMR's curve in comparison with the

Table 5.16: The statistical data of the buckling responses obtained from RS-HDMR method. The results obtained from MCSs and PCE are included for direct comparison.

	MCS	RS-HDMR	PCE	*RE* (%)
Max λ_{crit}	1.325	1.327	1.446	0.151
Min λ_{crit}	0.649	0.746	0.575	14.946
Mean, $\mu_{\lambda_{\text{crit}}}$	1.019	1.037	1.010	1.766
Std., $\sigma_{\lambda_{\text{crit}}}$	0.215	0.232	0.255	7.907
N_{sample}	2500	210	210	-

MCSs. A small discrepancy is noticed between the RS-HDMR and PCE's curve. A second peak is noticed at the right tail section of the curve which is thought to be a contribution from the second-order components in RS-HDMR function.

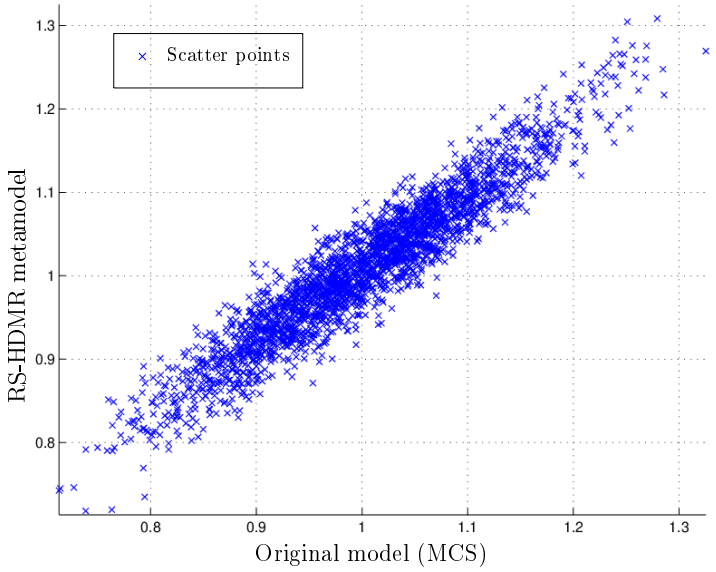

Figure 5.11: The scatter plot of the buckling critical load factors obtained from RS-HDMR and original MCSs data.

The first and second-order sensitivity indices (S_i and S_{ij}) are given in Table 5.17. Based on the sensitivity index values, the main effects are contributed by E_{11} with $S_1 = 0.9899$. Two second order sensitivity indices; SU_{14} and SU_{23} are obtained from the analysis which account for interaction effects of $\{E_{11}$,$t_{\text{ply}}\}$ and $\{E_{22}$,$G_{12}\}$. The corresponding values are $S_{14} = 0.0060$ and $S_{23} = 0.0041$, respectively. The results are slightly different from the PC-based Sobol' Indices. The second-order sensitivity indices, SU_{ij}^{PCE} are contributed by $\{E_{11}, E_{22}\}$ and $\{E_{11}, G_{12}\}$. A similar observation is obtained for first-order sensitivity indices where E_{11} is the main contributor to the buckling response variation. The PC-based Sobol's Indices for first order is $SU_1 = 0.9986$ and for second-order indices, the corresponding values are $SU_{1,2} = 0.0010$ and $SU_{13} = 0.0001$, respectively.

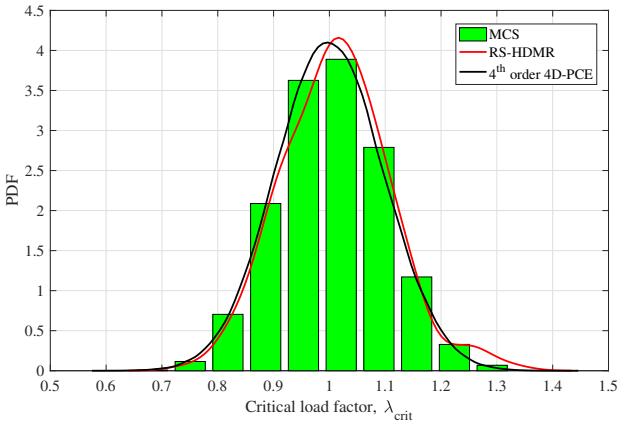

Figure 5.12: The PDF's plot of the buckling critical load factor, λ_{crit} obtained from RS-HDMR method, PCE method and MCSs.

Table 5.17: The RS-HDMR's first and second-order sensitivity indices obtained from the buckling analysis.

First Order Component		Second Order Component	
Sensitivity Index	Value	Sensitivity Index	Value
S_1	0.9899	S_{12}	0.0000
S_2	0.0000	S_{13}	0.0000
S_3	0.0000	S_{14}	0.0060
S_4	0.0000	S_{23}	0.0041
		S_{24}	0.0000
		S_{34}	0.0000

The variation of first-order RS-HDMR components (λ_{crit}) due to uncertain in E_{11} is plotted in Figure 5.13. From the plot, the $f_0 + f_1(E_{11})$ values seem to increase proportionally at higher E_{11} value.

The interaction effects on the second-order RS-HDMR components are visualised in a surface plot, as showed in Figure 5.14. Based on the plot, the highest interaction effect for $f_{14}(E_{11}, t_{\text{ply}})$ is noticed when $E_{11} = t_{\text{ply}} = 0$ and $E_{11} = t_{\text{ply}} = 1$. Conversely. the highest interaction effect for $f_{23}(E_2, G_{12})$ is obtained when E_{22} is at maximum/minimum value and G_{12} is at minimum/maximum value as shown in Figure 5.14(b) . The contribution of the second-order RS-HDMR components on the output response are relatively small which is one hundredth of the total response.

Overall, the RS-HDMR method is capable of producing an acceptable level of accuracy in predicting the output response due to random input variables. The results obtained from both case studies (flutter and buckling analysis) show an excellent correlation between RS-HDMR and MCSs output response at lower computational expenses.

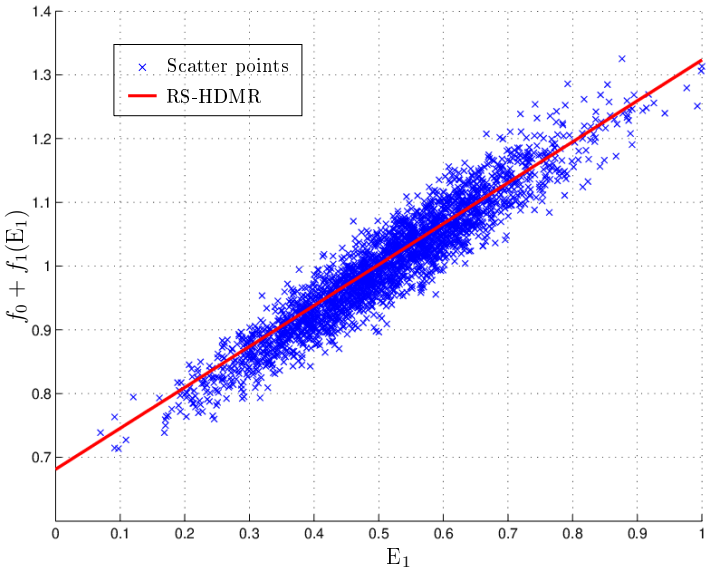

Figure 5.13: The scatter plot of first-order RS-HDMR components (buckling response) due to uncertain in E_{11}.

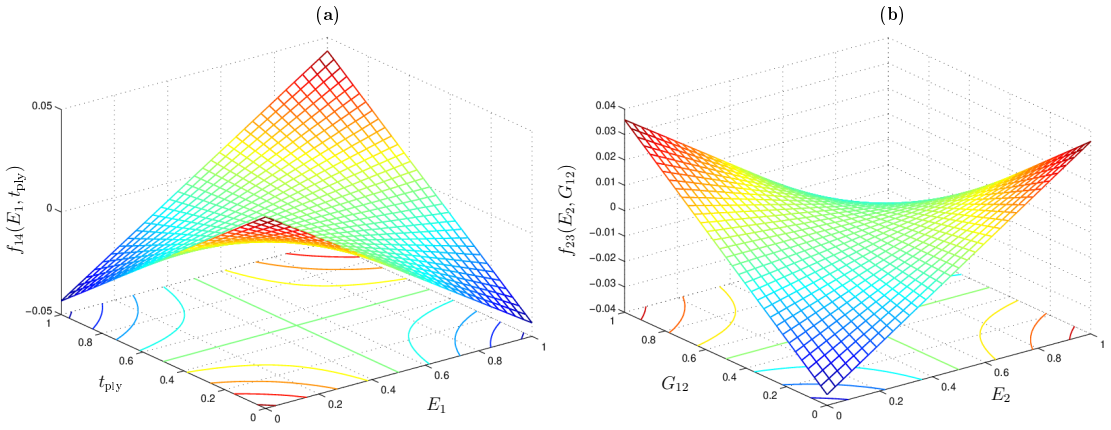

Figure 5.14: The surface plot of second-order RS-HDMR component(buckling response) due to interaction effect from input parameters; (a) E_{11} and t_{ply} (b) E_{22} and G_{12}.

5.7 Summary

The following conclusions can be drawn from the work in this chapter

1. The composite wing's structural and aeroelastic response variations due to uncertainty in model parameters are successfully evaluated using Polynomial Chaos Expansion (PCE) and Random Sampling High Dimensional Model Representation (RS-HDMR) methods. Both PCE and RS-HDMR capable of producing an accurate estimation that correlates well with conventional Monte Carlo Simulation method.

2. In reality, uncertainty exists and can be in the forms of parameter and geometry variations. The uncertainties in composite material properties and the ply thickness results in significant output response variation that may lead to catastrophic design failure. The uncertainty analysis performed in this chapter provides an essential insight into how composite wings response to the uncertainties structurally and aeroelastically.

3. PCE method is a surrogate model that employs polynomial basis function to represent the random input variables which result in better efficiency compared to other conventional methods. Different type of polynomial can be used to represent different types of random variables. In this work, Hermite polynomials were used to represent the Gaussian random variables.

4. In the PCE method, Latin Hypercube Sampling (LHS) is employed to determine the unknown expansion coefficient, β_i. LHS provides an efficient approach for sampling to ensure the output response is captured on all PDF's points and hence minimise the response variance.

5. The PC-based Sobol' indices method enables the determination of sensitivity index due to random input parameters at low computational cost. The sensitivity indices are obtained by evaluating the squared-sums of the PCE's expansion coefficients.

6. In flutter analysis using PCE, the output response variations due to uncertainty in E_{11}, E_{22}, G_{12} and t_{ply} are obtained in terms of probability density function. The output PDFs show an excellent correlation with the MCSs results. A small relative error, RE of 2.3% is obtained for the mean flutter speed using 4^{th} order 4D-PCE model. The flutter response is mainly effects by E_{11} with $SU_1 = 0.9801$.

7. In buckling analysis using PCE, the PDF's plot shows an excellent agreement with MCSs results. Different order polynomials used in the PCE model result in small differences which evidenced in the plots. Based on the first-order sensitivity index, the buckling responses are mainly influenced by the random variable, E_{11} with $SU_1 = 0.9986$.

8. In flutter and buckling analysis using PCE, the minimum number of samples required is 210 for 4^{th} order 4D-PCE model. The number of training data for MCSs is 2500.

9. In flutter analysis using RS-HDMR method, 332 samples are required in order to obtain an excellent agreement with MCSs results. The accuracy of the output response is improved in comparison with the PCE method. The method can be used efficiently for higher-dimensional order of random variables as the number of samples required is not dependent on the dimensional order. The sensitivity analysis in RS-HDMR reveals similar outcome with PCE-based Sobol' Indices method where the flutter response is mainly effected by E_{11}.

10. In buckling analysis using RS-HDMR, 210 samples are required to obtain an acceptable prediction of the output response concerning MCS. The output variation is primarily influenced by E_{11}, denoted by the first-order sensitivity index, S_1. The interaction effects are contributed by $\{E_{11}, t_{\text{ply}}\}$ and $\{E_{22}, G_{12}\}$.

11. Both PCE and RS-HDMR can be efficiently used to determine the wing's responses variation due to random input variables at lower computational expenses. The RS-HDMR method can be used for higher-dimensional order random input parameters using smaller number of training samples as opposed to PCE method. The number of samples required for PCE increases dramatically as the dimensional order increased which limits their application for uncertainty quantification of high-dimensional order input parameters.

Chapter 6

Reliability-based Design Optimisation for a Composite Aircraft Wing

6.1 Introduction

The current approaches for aeroelastic tailoring of aircraft structures employed deterministic optimisation methods to obtain the best design with minimum structural weight and optimum aeroelastic performance. In composite materials, aeroelastically-tailored designs can be achieved by altering the stiffness properties of the structure via the bending and the torsional coupling terms in the composite stiffness matrix. Recent work on aeroelastic tailoring is concerned with the optimisation of the wing structure for minimum structural weight subjected to multiple constraints that included structural and aeroelastic performance.

The deterministic approach, as presented in Chapter 4 for aeroelastic tailoring does not included uncertainty considerations within the optimisation process. Although in many cases, a safety factor is included in the design constraints to account for uncertainty in the model. In reality, uncertainty comes from various sources such as material properties, geometry and manufacturing defects. Aleatory uncertainty is the most common type of uncertainty encountered in many design problems and has been reported by various researchers. Aleatory uncertainty is classified as an irreducible uncertainty which is inherent in the system or model. The randomness in the model's parameter is a typical example of aleatory uncertainty. In Chapter 5, the effects of variability in composite material properties and ply thickness on the wing's structural and aeroelastic responses have been studied. The presence of parametric uncertainty in the model results in output response variation. These effects are needed to be appropriately quantified in the design to prevent catastrophic failure due parameter variation.

The effect of aleatory uncertainty on the model's response can be minimised by using improved modelling techniques, acquiring additional data or better parameter estimation. In this chapter, a reliability-based method [21, 172] is introduced to account for parametric uncertainty effects in aeroelastic tailoring procedures. The method requires a very efficient method for uncertainty quantification to rapidly evaluate the wing's response variation due to random input variables. Monte Carlo Simulation (MCS) [23, 24] is the conventional method used for uncertainty quantification, but it requires a large number of training data. Surrogate models, such as Polynomial Chaos Expansion (PCE) method [139, 140] presented in Chapter 5, can be used for this purpose as it employs a meta-modelling technique to evaluate the output response at low computational cost.

This chapter aims to introduce a reliability-based design optimisation (RBDO) method for the aeroelastic tailoring of a composite wing. The method is applied on a reference composite wing (benchmark wing) to obtain a reliable wing design that is insensitive to small changes in design parameters such as material properties and ply orientation.

6.2 Model Description

A detailed Finite Element (FE) wing box model of a regional jet airliner, as introduced in Chapter 3, was used for the analysis to demonstrate the effectiveness of the RBDO method. The aspect ratio of the wing model is 10. The wing geometry and the load-carrying wing box within the planform are depicted in Figure 3.4 (page 57). The structural entities including the spars, ribs and stringers sections are defined in the model. Three main spars and the ribs, including those at the root and tip are modelled and positioned equidistant in the spanwise direction aligned with the global x-axis. The stringers are included in the model as bar elements. The skin, ribs and spars are defined using composite material properties as in Table 3.3 (page 65) while others using massless aluminium properties. Further details on the wing model are given in Section 3.2 (page 54).

6.3 Reliability-based Design Optimisation (RBDO) method

The deterministic approach presented in Chapter 4 did not consider the effects of parameter variation in the optimisation process. The performance of the deterministic design can be overestimated or underestimated due to the presence of uncertainty. The probabilistic approach, such as Reliability-based design optimisation, can be used to ensure design reliability is satisfied. The probabilistic approach uses probability theory to include the effects of random parameters in the optimisation. The proposed RBDO method utilises the concept of maximising the reliability of the structures/model to improve the design's probability of survival at specific target values. In the context of aeroelastic tailoring, the RBDO method can be used to obtain a reliable design solution when uncertainty exists while satisfying the requirements for structural and aeroelastic performance. The uncertainty in the model can be in the form of parametric variations in the material properties and model geometry.

6.3.1 Probabilistic optimisation

The general concept of the probabilistic optimisation within the RBDO method is formulated as

$$\begin{aligned} \underset{\mathbf{x}}{\text{minimize}} \quad & f_{\text{obj,RBDO}}(P_{\text{f}}(\mathbf{x}, \mathbf{p})), \\ \text{subject to:} \quad & \mathbf{x}_{\text{L}} \leq \mathbf{x} \leq \mathbf{x}_{\text{U}}, \end{aligned} \tag{6.1}$$

where $f_{\text{obj,RBDO}}$ is the objective function; $\mathbf{p}$ is a vector of constant parameters in the optimisation; and $\mathbf{x}$ is the design variables that are bound between lower and upper limits, $\mathbf{x}_{\text{L}}$ and $\mathbf{x}_{\text{U}}$. The objective function is defined as the probability of failure, P_{f} for the response of interest at a specific target design value.

$$f_{\text{obj,RBDO}} = \frac{P_{\text{f}}}{P_{\text{allow}}}, \tag{6.2}$$

where P_{allow} is the allowable probability of failure. The P_{f} value is obtained from the probability density function (PDF) plot of the output response as the cumulative area under the plot up to target design value as shown in Figure 6.1. The objective of RBDO is to minimise the P_{f} so that the probability of the design to fail (any output response) before the target design value is reduced. This aim is illustrated in Figure 6.1 such that

the RBDO curve is shifted to the right of the deterministic curve to obtain lower P_f at a specific target of design response. The RBDO seeks for a reliable design that is insensitive to random variables in the model (minimum P_f values).

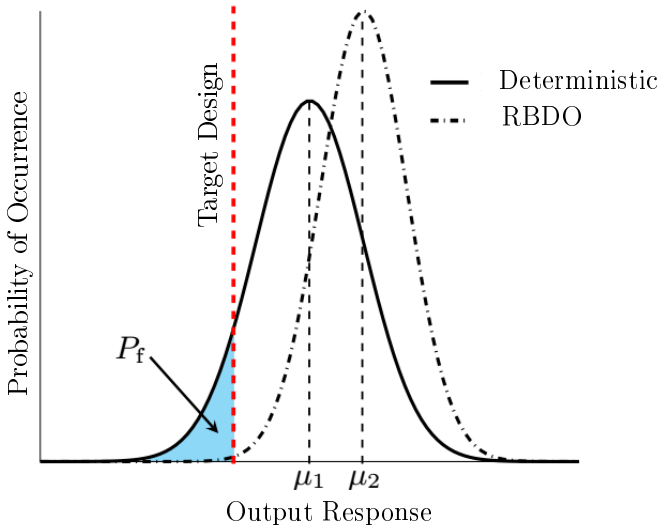

Figure 6.1: Reliability-based design optimisation approach.

The main challenge for the RBDO method is to perform a rapid evaluation of the wing's response due to random input variables. The RBDO method requires the determination of the output response at every iteration step, hence a surrogate model such as PCE is employed to obtain the wing response at a minimum number of samples data. As shown in previous chapter, PCE method is capable of producing results at reasonable accuracy compared to the conventional MCS method at lower computational cost.

6.3.2 Stochastic Modelling

The stochastic modelling using PCE is presented herein for reliability-based optimisation of the composite wing. The longitudinal Young's modulus, E_{11}, transverse in-plane Young's modulus, E_{22} and composite ply thickness, t_{ply} are chosen as the random input variables. The coefficient of variance (CV) for E_{11} and E_{22} is 0.1 and for t_{ply}, CV is 0.01. The mean and standard deviation for the random input variables are given in Table 6.1. Norbert Weiner [139] originally introduced the concept of Polynomial Chaos as part of homogeneous chaos formulations. The PCE formulation has been presented in Chapter

5. To recall, the general formulation is given by

$$u(\theta) = \sum_{i=0}^{\infty} \beta_i \psi_i(\zeta(\theta)), \tag{5.2}$$

where β_i is the expansion coefficient that needs to be determined from the sample data and ψ_i is the polynomial basis function. The type of polynomial basis used in the formulation depends on the type of distribution of the random input variables. If the input variables are Gaussian, Hermite polynomials are used to represent these variables. For other types of random input distributions, other orthogonal polynomials may be used such as Laguerre and Jacobi's polynomials given in Ref. [141]. For standard Gaussian random variables, the output of the system can be assumed to be Gaussian if only lower terms of the expansion coefficients are included. The output response obtained using higher terms may not be in the form of Gaussian distribution.

Table 6.1: The mean and standard deviation values for the random input variables used in the uncertainty analysis.

	E_{11} (GPa)	E_{22} (GPa)	Ply thickness, t_{ply} (m)
Mean, μ	148.0	10.3	1.83×10^{-4}
Std Dev.,σ	14.8	1.03	1.83×10^{-6}

The current work employed 1$^{\text{st}}$ to 4$^{\text{th}}$ polynomial orders in the PCE formulation. Higher polynomial order is not considered as it requires large sample size to determine the expansion coefficient as total-order expansion, $\mathcal{A}$ (Eqn. 5.16). The accuracy of the output responses obtained from this work is compared with the MCSs. To demonstrate, provided that the input random variables are continuous Gaussian consist of E_{11}, E_{22} and t_{ply}, the flutter response due to these variables can be estimated using 3$^{\text{rd}}$ order PCE formulation with $\mathcal{A} = \binom{6}{3} = 20$ as follows

$$\begin{aligned} V_{\text{f}}^{3rd} = {} & \beta_0 + \beta_1 E_1 + \beta_2 E_2 + \beta_3 t_{\text{ply}} + \beta_4 (E_1^2 - 1) + \beta_5 (E_2^2 - 1) + \beta_6 (t_{\text{ply}}^2 - 1) + \beta_7 E_1 E_2 + \\ & \beta_8 E_1 t_{\text{ply}} + \beta_9 E_2 t_{\text{ply}} + \beta_{10} (E_1^3 - 3E_1) + \beta_{11} (E_2^3 - 3E_2) + \beta_{12} (t_{\text{ply}}^3 - 3t_{\text{ply}}) + \\ & \beta_{13} E_1 (E_2^2 - 1) + \beta_{14} E_2 (E_1^2 - 1) + \beta_{15} E_2 (t_{\text{ply}}^2 - 1) + \beta_{16} E_1 (t_{\text{ply}}^2 - 1) + \\ & \beta_{17} t_{\text{ply}} (E_2^2 - 1) + \beta_{18} t_{\text{ply}} (E_1^2 - 1) + \beta_{19} E_1 E_2 t_{\text{ply}}, \end{aligned}$$

where $\beta_i, ..., \beta_n$; $i, ..., n = 0, ..., 19$ are determined from computed test data.

Figure 6.2 shows an overview of the PCE process to determine the PDF of the wing's response with Gaussian continuous random variables. The Latin Hypercube Sampling (LHS) technique [188] is used for data sampling to ensure that all test cases of the random variables are selected with equal probability. The random variables and fixed design variables are input in the FE model to obtain the sample response. The Hermite polynomial basis is constructed, and the expansion coefficients are obtained using a least-squares linear regression model, as presented in Chapter 5. The output response is emulated based on the combination of random parameters and the calculated expansion coefficients. Consequently, the statistical properties such as mean, standard deviation and probability of occurrence are obtained from the PDF of the emulated response.

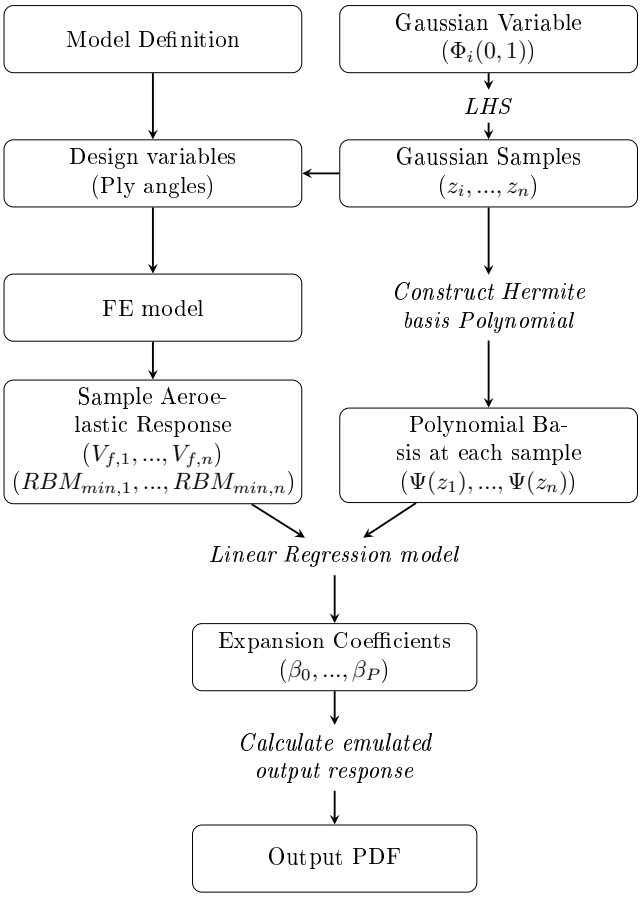

Figure 6.2: The PCE modelling process and FE modelling approach to obtain aeroelastic response distribution.

The convergence study is performed in order to obtain the minimum number of samples required for PCE. As the RBDO method requires the output response for each set of random variables to be determined in every iteration step, it is essential to establish the minimum number of data samples for PCE so that the computational cost can be

kept at a minimum. Figure 6.3 provides the PDF plots for PCE and MCS. MCS run is performed with 5000 training data. Note that the flutter speed is normalised concerning the maximum flutter speed. The output responses for flutter speed are determined using different polynomial order and different number of samples for 3^{rd} order PCE. The PDF plots of PCE at different polynomial as shown in Figure 6.3 (a) reveals an excellent agreement with the MCS results for 1^{st}, 2^{nd} and 3^{rd} order PCE. A small discrepancy is obtained from 4^{th} order PCE in comparison with the MCS. Based on the PCE run using a different number of sampled data, the PDF plot matched well with MCS as the number of samples increased to 30.

Further insight can be seen from Figure 6.4 where the Root Mean Square Error (RMSE) of the flutter speed relative to MCS is plotted against the number of LHS samples. It can be seen that the convergence occurs when number of samples ≤ 25. Hence, 30 samples are sufficient to obtain accurate approximation of the output response.

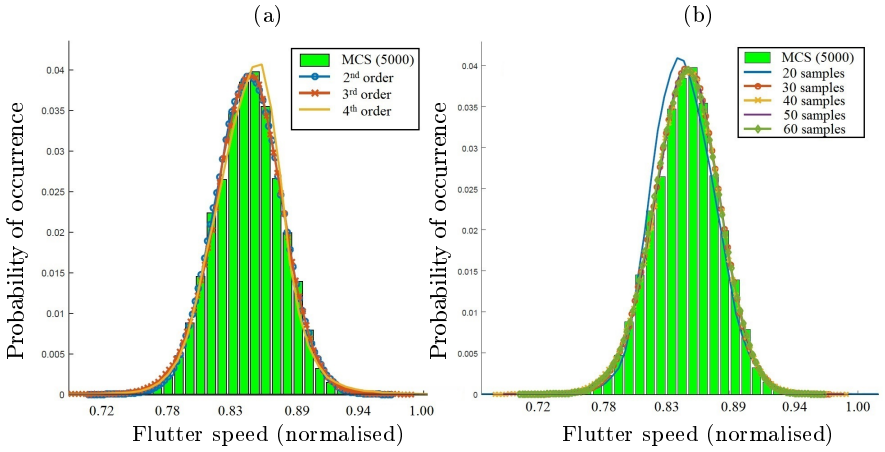

Figure 6.3: PDF plots for flutter response using; (a) Different order of PCE model and (b) Different number of samples data for 3^{rd} order PCE. The results are compared with output response from MCS.

6.4 Deterministic model

In the proposed RBDO procedure, the optimised deterministic model is used as the initial design for the probabilistic optimisation. In the deterministic optimisation, the composite wing structure is optimised for minimum structural weight with structural and aeroelastic responses as the design constraints. The strength and buckling responses are quantified for structural constraints. The aeroelastic instability behaviour of the wing is

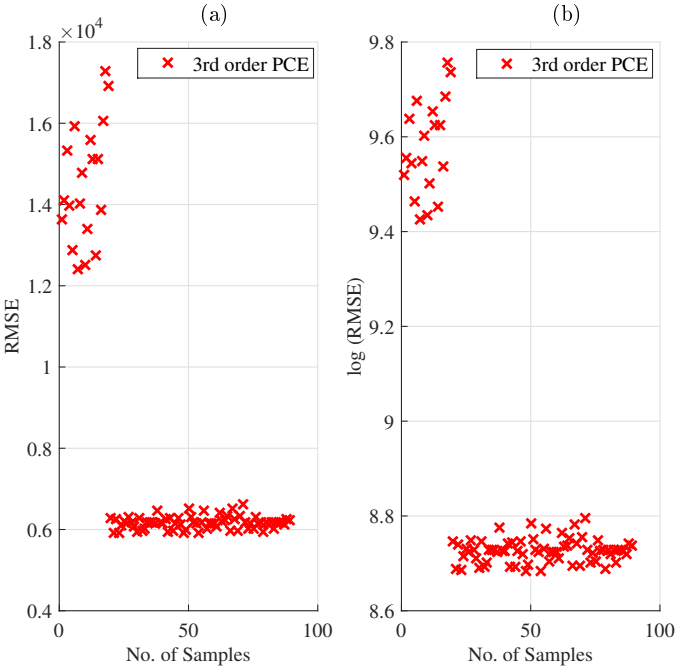

Figure 6.4: The root means square error (RMSE) of the flutter response against the number of LHS samples.

measured in terms of the flutter speed. The wing's response to gust loads is quantified in terms of the bending moment at the root (RBM). An idealised '1-cosines' discrete gust representation is assumed for the gust analysis. Only the top skin, bottom skin and the spar panels are optimised because of their active influence on the wing's structural strength and stiffness. In total, 41 panels are optimised for the deterministic model.

The deterministic design problem can be described as

$$
\begin{aligned}
\underset{\mathbf{x}}{\text{minimize}} \quad & f_{\text{obj,det}}(W(\mathbf{x}), f_{\text{cost,det}}(\mathbf{x})), \\
\text{subject to:} \quad & \text{Strain Failure Index,} \quad FI(\mathbf{x}) \leq 1 \quad \text{(Max. Strain)}, \\
& \text{Buckling critical load factor,} \quad \lambda_{\text{crit}}(\mathbf{x}) \geq 1, \\
& \text{Flutter speed,} \quad V_{\text{f}}(\mathbf{x}) \geq 1.15 V_{\text{D}} \quad (V_{\text{D}} = \text{Design dive speed}), \\
& \text{Wing Root Bending Moment,} \quad \max(RBM(\mathbf{x}, L_{\text{g}})) \leq \max(RBM_{\text{Benchmark}}(L_{\text{g}})), \\
& \mathbf{x} = [\xi_1^A, \ldots, \xi_4^A, \xi_1^D, \ldots, \xi_4^D, t_{\text{panel},1}, \ldots, t_{\text{panel},41}],
\end{aligned}
\tag{6.5}
$$

where $\mathbf{x}$ and L_{g} are the vector containing the design variables and gust wavelength, respectively. The strength performance of the composite panels is evaluated in terms of the maximum and minimum strain limit. The strain failure index is introduced to

quantify the strength performance by not exceeding a set allowable value and formulated as

$$FI_{\text{strain}} = \max\Big(\frac{\epsilon_{\text{min}}}{\epsilon_{\text{min,allowable}}}, \frac{\epsilon_{\text{max}}}{\epsilon_{\text{max,allowable}}}, \frac{\gamma_{\text{min}}}{\gamma_{\text{min,allowable}}}, \frac{\gamma_{\text{max}}}{\gamma_{\text{max,allowable}}}\Big), \tag{6.6}$$

where ϵ_{min} and ϵ_{max} are the principle strains for laminate under compression and tension, respectively. The allowable values are set to $\epsilon_{\text{min,allowable}} = -5900\mu\epsilon$ and $\epsilon_{\text{max,allowable}} = 7100\mu\epsilon$. The shear strains limit is defined in terms of maximum and minimum shear strains, with allowable values set to $\gamma_{\text{min,allowable}} = -4500\mu\epsilon$ and $\gamma_{\text{max,allowable}} = 4500\mu\epsilon$.

A static manoeuvre load case is considered for the analysis with Mach number, cruise altitude and acceleration of 0.82, 10 000 m and 2.5g, respectively. The upper boundary for FI is set as 1.0. The first ten buckling modes are computed from the buckling analysis to account for critical mode changes. The flutter speed, V_{f} is calculated from conventional $V-g$ plot, assuming Mach 0.82 and flight dive velocity, V_{D} at 10000m. V_{f} is assumed to be the lowest of 12 values (from 12 modes) at which the damping factor equals zero.

The objective function is defined as an aggregate of structural weight and a weighted cost function. The weighted cost penalty function is introduced to account for the influence of flutter and RBM responses on the optimised solution. The strength and buckling constraints are not included in the cost function but used to validate the design for structural performance. The objective function and the weighted cost penalty function are formulated as

$$f_{\text{obj,det}} = \frac{W(\mathbf{x})}{W_{\text{Benchmark}}} + f_{\text{cost,det}}(\mathbf{x}), \tag{6.7}$$

where W is the wing structural weight (skins and spars only) and

$$f_{\text{cost,det}} = w_{\text{f}} \times \Big|\frac{V_{\text{f}} - V_{\text{f,Design}}}{V_{\text{f,Design}}}\Big| + w_{\text{g}} \times \Big|\frac{RBM}{RBM_{\text{Benchmark}}}\Big|, \tag{6.8}$$

and where

$$w_{\text{constr}} = \{w_{\text{constr}_i} \in [0,1] : \sum_{\text{constr}_i} = 1, \text{constr}_i \in \{\text{f}, \text{g}\}\}. \tag{6.9}$$

For each set of weighting factors, the wing's responses are evaluated, and a Pareto front plot is constructed to determine the best design solution. The best solution is chosen

from the Pareto points based on the averaging principle to minimise $|\sum -2|$ where

$$\sum = \frac{V_{\mathrm{f}}}{1.15V_{\mathrm{D}}} + \frac{RBM}{RBM_{\mathrm{min}}} \tag{6.10}$$

and where the subscript 'min' is referred to the minimum value of RBM deduced from each combination of weighting factors.

In the deterministic optimisation, the lamination parameters and the laminate thickness are chosen as the design variables and input in the FE model as the stiffness component. The lamination parameters are derived from Classical Laminate Theory (CLT) as presented in Section 3.3.1 (page 59). The symmetric and unbalanced laminates are considered in the optimisation to avoid warping (upon cool down from the curing temperature) and to promote anisotropy (governed by the bending-torsion coupling parameter D_{16} and D_{26}) to the structures. This results in nine design variables (eight lamination parameters; $[\xi_1^A, \ldots, \xi_4^A, \xi_1^D, \ldots, \xi_4^D, t_{\mathrm{panel}}]$ and a thickness parameter) for each composite panel. Additionally, the lamination parameters are governed by the feasible region relationships derived from Fukunaga & Sekine [72] and are given in Eqn. (4.3). The deterministic optimisation is performed using the PSO algorithm with the maximum number of iteration is set to 50 with 20 particles in each iteration.

The flutter analysis is performed using MSc. Nastran's `SOL 145: Flutter analysis`. The frequency-matching *'p-k'* method is used to predict the flutter occurrence. Details on the flutter analysis is given in Section 3.4.4 (page 74).

The gust response constraint is determined in terms of minimum strain energy which is governed by the wing root bending moment (RBM) against discrete gust load. The aeroelastic dynamic response (`SOL 146`) in MSc. Nastran is used to evaluate the wing's gust response. Only the critical gust length is considered in the analysis which is defined as the maximum absolute value of RBM response. The gust length parameters, L_{g} are chosen in the range of 18 m to 216 m as to represent the critical gust length specified in CS-25 [181]. The design gust velocity, w_{g0} and the flight speed, V are 20 ms^{-1} and 253 ms^{-1}, respectively.

6.5 Reliability-based Design Optimisation for Flutter and Gust Response

The PCE based RBDO method is used to determine a reliable composite wing design for flutter and wing RBM due to gust with uncertainty in the material properties and ply thickness. A strategy is adopted whereby the probability of aeroelastic instability (flutter/divergence) occurrence at target design flutter speed is minimised, and the RBM response optimised below the specified target value. Here, the concept of maximising the reliability of the structure is used in terms of the probability of survival. For flutter response, the probability of survival is maximised such that the instability does not occur before a target design instability speed. For the RBM response, the optimisation aims to maximise the probability of occurrence at target RBM value so that the RBM value is minimised with the presence of uncertainty.

The RBDO method is visualised in Figure 6.5. The reliable design for flutter response is obtained by minimising the probability of failure for flutter occurrence at $V_{\text{f,Design}}$ or minimising the area under the deterministic's PDF curve. For the RBM response, the reliable design is obtained by maximising the probability of failure at RBM_{Design} so that the RBM response for the optimised design is below RBM_{Design} with uncertainty included in the model.

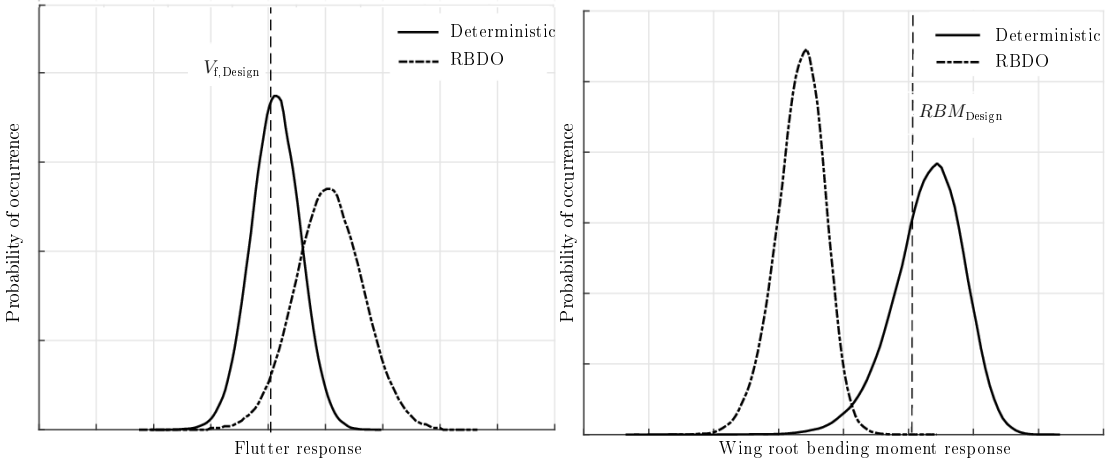

Figure 6.5: Overview of RBDO method for flutter response and RBM; (a) PDFs plot for flutter and (b) PDFs plot for wing's RBM.

The optimisation function in RBDO for the current work is given by;

$$f_{\text{obj,RBDO}} = \frac{P_{\text{f}}}{P_{\text{f,allow}}} + \frac{P_{\text{g,allow}}}{P_{\text{g}}}, \tag{6.11}$$

where P_{f} and P_{g} are the probability of failure for flutter and gust response. P_{allow} is the allowable probability of failure. In our case, probability of exceeding the target design response.

In the RBDO procedures, the design variable is the ply angle of the composite laminate in contrast with the deterministic optimisation where lamination parameters are used as the design variables. In the RBDO procedures, the variability in ply angles is treated as the random parameters as well as the material properties and the ply thickness. The improved design from the deterministic optimisation is used as the initial design configuration. The stacking sequence of the initial design (deterministic design) is determined from the lamination parameters and the laminate thickness of the deterministic solution. Here, three layup strategies are used. The first layup strategy involved only 0°, ±45° and 90° plies. The 0°, ±45° and 90° plies are often used to fabricate laminate in the industry as to carry the wing's structural axial, shear and transverse loads. Additional ±30° and ±60° plies are introduced in second layup strategy, and ±15° and ±75° plies in third layup strategy. The inclusion of additional ply angles in the layup strategies is to provide additional design spaces for the robust optimisation procedures and to evaluate their contribution on the wing's flutter behaviour.

To ensure a feasible stacking sequence, a ply contiguity constraint is enforced where no more than four plies of same orientation are used in the stacking. The ply angles are used as the discrete design variables in order to account for the stacking sequence variability. The particle swarm optimisation (PSO) algorithm is used for the optimisation with maximum of 50 iteration and 20 particles. The PSO is available from MATLAB optimisation toolbox.

6.5.1 Deterministic design

The structural weight, flutter speed and wing root bending moment for the optimised deterministic design are given in Table 6.2. The deterministic optimisations are performed using different combination of weighting factors, w_{f} and w_{g} which are chosen at random.

The weighting factors are assigned to flutter and RBM responses in order to evaluate the contribution of both response on the optimised design. It is observed that at the higher weighting factor, an optimal flutter speed is obtained ($V_\mathrm{f} \approx 1.15V_\mathrm{D}$). Similarly, for RBM, minimum RBM value is obtained when $w_\mathrm{g} \approx 1.0$.

The Pareto front plots of the deterministic optimum are depicted in Figure 6.6. The wing's responses (flutter speed and RBM) for all weighting combination are plotted against the weighting factor. It can be seen from Figure 6.6(a), the wing's flutter speed ($V_\mathrm{f}/1.15V_\mathrm{D}$) is converged towards the target value ($V_\mathrm{f}/1.15V_\mathrm{D} \approx 1$) as the weighting factor, w_f increases to unity. Similarly, the RBM responses converged towards minimum value as w_g increases to one as shown in Figure 6.6(b). It is also noticed from Figure 6.6(c) that the lowest RBM response can be obtained but with higher $V_\mathrm{f}/1.15V_\mathrm{D}$.

The best solution for the deterministic design is selected based on the averaging principle such that $|\sum -2|$ closed to 2. The values for $|\sum -2|$ are provided in Table 6.2. The corresponding flutter speed ($V_\mathrm{f}/1.15V_\mathrm{D}$) and RBM ($RBM/RBM_\mathrm{benchmark}$) for the best deterministic design are 1.1564 and 1.3741, respectively. The structural weight ($W/W_\mathrm{Benchmark}$) of the best deterministic design is 0.8866 which is 11.3% less than the benchmark wing. The maximum FI value of 0.76 is obtained at top skin panels at the proximity of engine pylon. The strain distribution of the best design is shown in Figure 6.7. The critical buckling load factor, λ_crit for the best deterministic design is 1.0473. The strain and buckling responses for all other deterministic design solutions satisfied the design requirement/constraints for the optimisation.

Table 6.2: The structural weight, flutter speed and wing root bending moment (RBM) obtained from the deterministic optimisation.

Run	w_f	w_g	$\frac{W}{W_\mathrm{Benchmark}}$	$\frac{V_\mathrm{f}}{1.15V_\mathrm{D}}$	$\frac{RBM}{RBM_\mathrm{Benchmark}}$	$\lvert\sum -2\rvert$
1	1.00	0.00	0.8619	1.1527	0.8249	9.4202
2	0.90	0.10	0.8769	1.1510	0.6389	7.5544
3	0.80	0.20	0.8592	1.1510	0.3378	4.5365
4	0.70	0.30	0.8384	1.2024	0.3385	4.5951
5	0.60	0.40	0.8922	1.1557	0.2046	3.2062
6	0.50	0.50	0.8799	1.1616	0.2184	3.3508
7	0.40	0.60	0.9029	1.1771	0.2451	3.6339
8	0.30	0.70	0.8854	1.1526	0.1673	2.8292
9	0.20	0.80	0.8866	1.1564	0.1371	2.5305
10	0.10	0.90	0.9390	1.5703	0.0998	2.5703
11	0.00	1.00	0.9519	1.9073	0.1171	3.0807

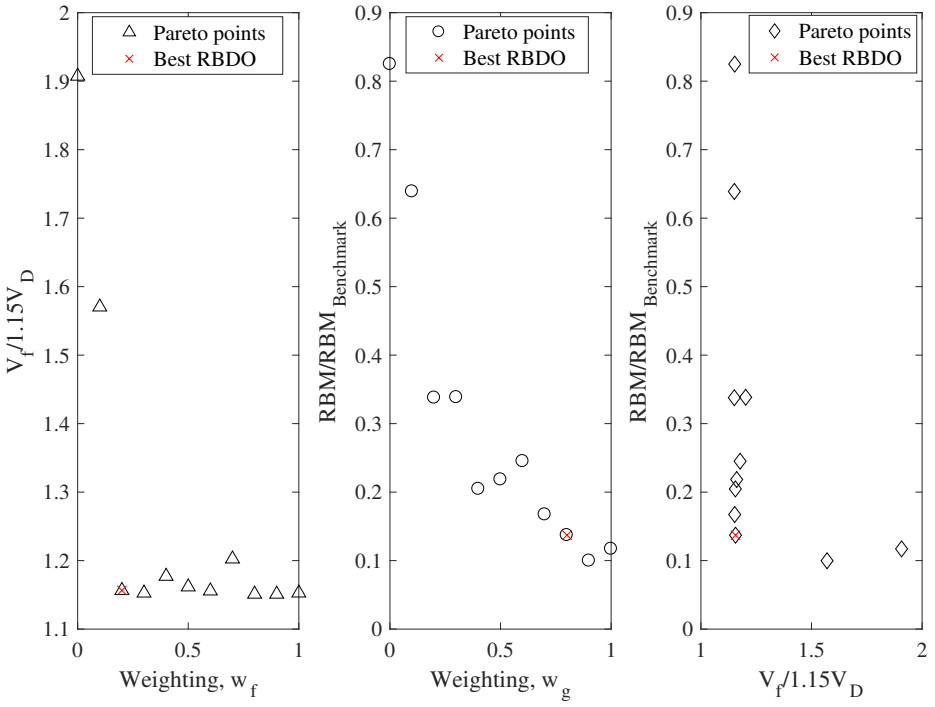

Figure 6.6: Pareto front plots deterministic optimum; (a) Weighting, w_{f} vs. Flutter speed, V_{f}, (b) Weighting, w_{g} vs. RBM and (c) Flutter speed, V_{f} vs. RBM.

6.5.2 Reliable design

The deterministic and RBDO designs based on three layup strategies are obtained at the design flutter speed, $V_{\mathrm{f,Design}} = 1.5$ and design root bending moment, $RBM_{\mathrm{Design}} = 0.15$. The mean value, standard deviation and probability of failure, P_{f} at design values are given in Table 6.3. Note that the deterministic design's responses given in the table differ from the responses provided in Section 6.5.1. This change is due to different design variables used in the analysis. Here, ply angles are used instead of lamination parameters. Hence, there is a slight difference in the response values. Moreover, the effect of random parameters (E_{11}, E_{22} and t_{ply}) are included in the deterministic design to obtain the mean, standard deviation and probability of failure at target design value. Figures 6.8 to 6.10 provide the PDF plots for the flutter speed and RBM of the deterministic design as well as the RBDO design evaluated at target design values.

For the deterministic design, the probability of flutter occurrence increases as additional ply angles is introduced in the laminate. The non-conventional ply angles impart more

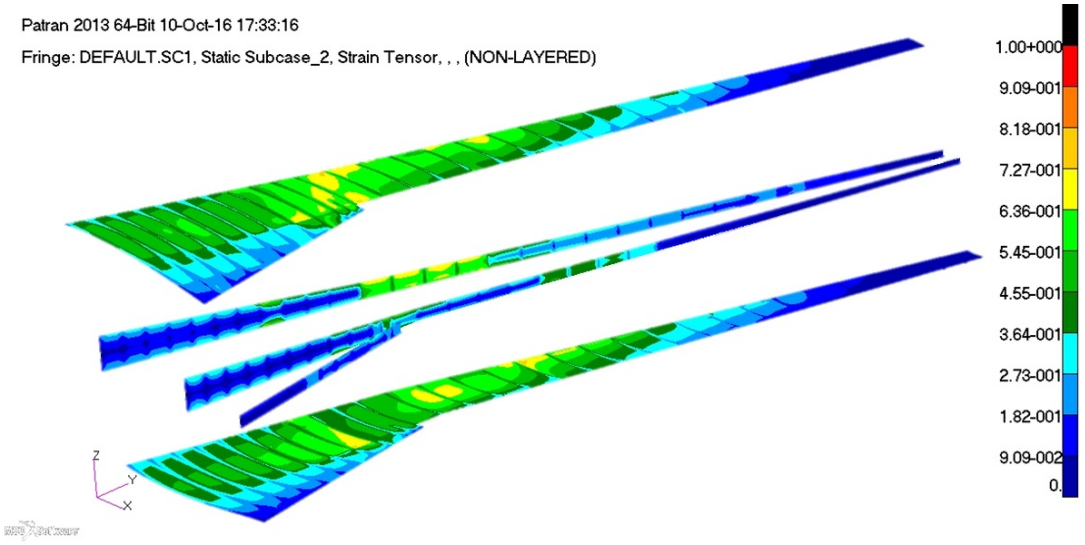

Figure 6.7: The longitudinal strain distribution (normalised) obtained from the deterministic optimised design.

Table 6.3: The flutter speed and wing root bending moment of the RBDO optimised designs.

Layup strategy	Design	Flutter speed, $\frac{V_f}{1.15V_D}$ ($V_{f,Design} = 1.5000$)			Wing root bending moment, $\frac{RBM}{RBM_{Benchmark}}$ ($RBM_{Design} = 0.1500$)		
		Mean	Std. Dev.	P_f	Mean	Std. Dev.	P_f
1	Deterministic	1.4203	0.3776	0.0089	5.2490	0.8163	0.0023
	RBDO	1.6383	0.2362	0.0060	4.8930	0.8664	0.0135
2	Deterministic	1.6360	0.1748	0.0096	4.3350	0.8460	0.4641
	RBDO	1.6333	0.1991	0.0005	2.5360	0.7365	1.0000
3	Deterministic	1.5762	0.4207	0.0319	3.6420	0.8239	0.9851
	RBDO	1.6544	0.1729	0.0177	2.6520	0.9512	1.0000

bending stiffness in the structure to resist the bending and twist deformation which results in higher flutter speed and the mean responses. A similar observation can be said for RBM response, as additional ply angles are included, lower RBM value is obtained from the deterministic design. The proposed RBDO method results in reliability improvement to the design as a lower probability of failure is obtained in comparison with the deterministic design.

From Table 6.3, a 32.6% reduction in terms of the probability of failure is evaluated from the RBDO design with only 0°, ±45° and 90° plies. A higher percentage of reductions is achieved with the inclusion of additional plies; 94.6% and 44.8% reliability improvement are obtained for the second and third layup strategy.

Similarly, for the gust responses, the mean values for root bending moment are reduced

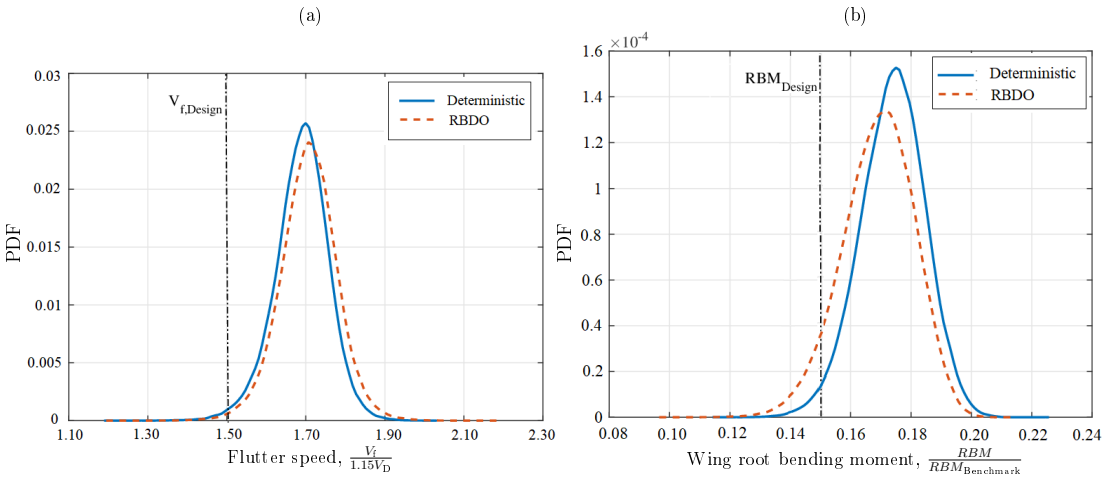

Figure 6.8: The PDF plots for deterministic and RBDO optimised design for first layup strategy (0°, ±45° and 90° plies); (a) Flutter response (b) RBM response.

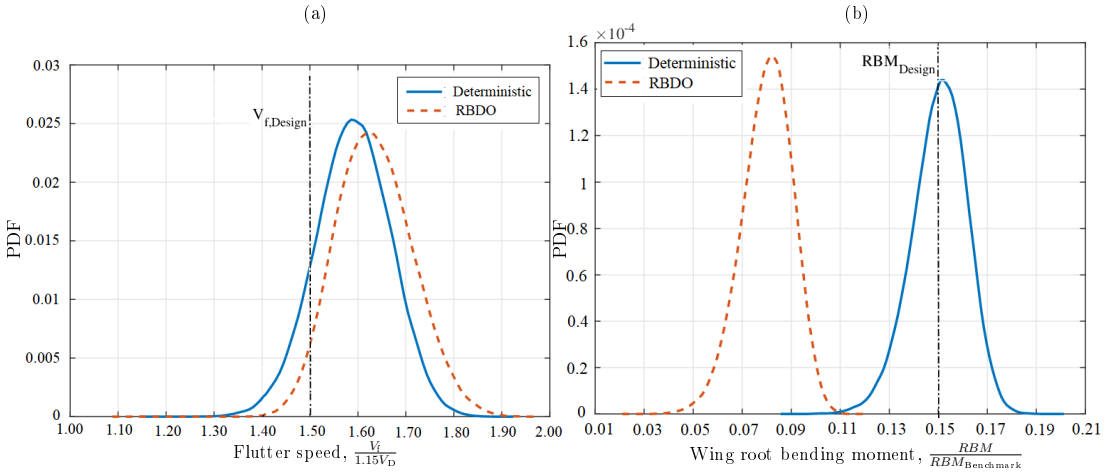

Figure 6.9: The PDF plots for deterministic and RBDO optimised design for second layup strategy (0°, ±30°, ±45°, ±60° and 90° plies); (a) Flutter response (b) RBM response.

for all layup strategies with the highest reduction of 41.5% are obtained from the second layup strategy as given in Table 6.3. More evidence can be found from Figure 6.9(b) and 6.10(b) where the PDF curves of RBM responses are shifted to the left. The results indicated that lower RBM responses could be obtained when additional ply angles are introduced.

It is also noted from Figure 6.10 that the RBDO's flutter response obtained from the third layup strategy is shifted to the left and has a higher peak value compared to the deterministic design. However, it is noticed that the skewness of the PDF curve is reduced, thereby lowering the probability of failure.

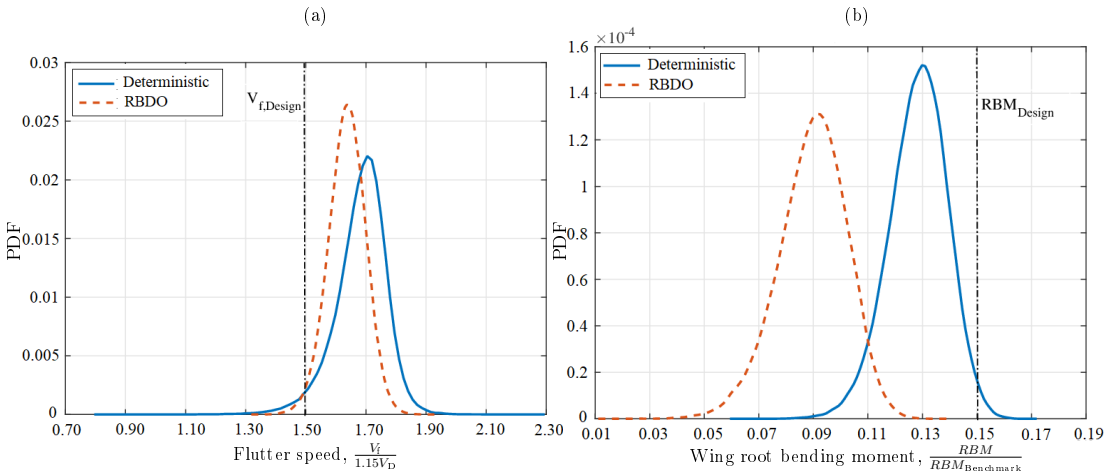

Figure 6.10: The PDF plots for deterministic and RBDO optimised design for third layup strategy (0°, ±15°, ±30°, ±45°, ±60°, ±75° and 90° plies); (a) Flutter response (b) RBM response.

The layup strategy with 0°, ±30°, ±45°, ±60° and 90° plies provides the optimal RBDO solution for both flutter and root bending moment responses. Figure 6.11 shows the ply configuration for the optimal RBDO design obtained from the second layup strategy. Note that, layup obtained is symmetric and only half of the layup is depictured in Figure 6.11.

In comparison with the deterministic model, a small reliability improvement is achieved from the first layup strategy, which is evidenced in Table 6.3. There is minimal discrepancy observed in terms of the stacking sequences of the optimised and deterministic model. The results are expected as the layup strategy limited to 0°, ±45° and 90° plies. The layup consists of 0°, ±45° and 90° plies able to resist bending and twisting motion of the structure and hence results in larger mean flutter speed. The additional ±30° and ±60° plies in the second layup strategy promote higher mean flutter speed as opposed to first layup strategy. This is thought due to greater design space in finding the optimal ply sequences, which also promotes additional stiffnesses to the structure for better bending and twisting resistance. The best reliable design is obtained from the second layup strategy with ±30° and ±60° plies in the stacking sequence.

The optimised stacking sequence obtained from the RBDO method is obtained with the inclusion of several manufacturing constraints as follows;

- The ply contiguity constraint is enforced such that there is no more than four plies with the same orientation are used in the stacking sequences.

		PLY NO																													
	Panel No.	1	2	3	4	5	6	7	8	9	10	11	12	13	14	15	16	17	18	19	20	21	22	23	24	25	26	27	28	29	30	31	32
TOP SKIN 1	1	45	90	-45	90	-30	30	90	-60	90	90																						
	2	45	90	-45	0	30	90	-30	30	60	-60	90	-60	-60	90																		
	3	45	90	-45	0	-30	0	60	45	-60	90	-60	-60	-60	90	90																	
	4	45	90	-45	0	0	45	0	45	60	60	-60	30	-60	60	-60	60	60	90														
	5	45	90	-45	0	30	30	30	60	90	90	-45	-60	90	90	-60																	
	6	45	90	-45	0	0	-60	90	90	90	-60	60	90																				
	7	45	90	-45	0	30	-45	30	90	90	90	90	-60	90																			
	8	45	90	-45	0	90	-60	90																									
TOP SKIN 2	9	45	90	-45	0	30	30	-60	90	90	90	-60	90	-60																			
	10	45	90	-45	0	30	30	0	30	30	0	45	90	60	30	90	30	45	60	45	45	-30	30	60	90								
	11	45	90	-45	90	90	0	-60	90																								
BOTTOM SKIN 1	1	45	90	-45	30	30	60	0	-60	30	90	-45	-30	90	-60	60	90																
	2	45	90	-45	0	30	-45	90	90	60	90	-60	90																				
	3	45	90	-45	90	0	30	30	45	0	30	30	0	-60	30	45	0	30	30	30	0	0	-30	0	30	0	0	0	0	90	30	-30	30
	4	45	90	-45	0	30	30	60	0	0	0	60	30	90	45	45	30	-45	30	60	45	-30	30	60	60	30							
	5	45	90	-45	30	0	45	90	-30	90	-60	90	90	-60																			
	6	45	90	-45	0	0	30	30	30	90	60	60	-60	-60	60	-60	60	90															
	7	45	90	-45	0	0	30	30	30	60	60	90	60	90	90	-60	90	-60															
	8	45	90	-45	0	30	30	0	90	45	30	0	30	45	30	30	30	60	90	-45	60	60	-60	60									
BOTTOM SKIN 2	9	45	90	-45	0	30	30	0	0	90	45	-60	30	45	30	-30	60	30	-60	60	90	60	90										
	10	45	90	-45	30	30	0	90	30	0	0	30	45	30	30	0	45	60	0	30	60	-60	60	-60	30	0	-30	-60					
	11	45	90	-45	30	0	30	0	30	0	90	30	45	-60	60	45	90	60	60	45	60	-60											
SPAR 1	1	45	90	-45	30	0	30	0	30	30	0	45	30	90	30	90	45	90	30	30	90	-30	60	60	0	90	-30						
	2	45	90	-45	0	30	-60	-45	90	30	90	-60	90	90																			
	3	45	90	-45	0	30	30	30	0	45	30	60	30	0	90	0	30	30	-45	90	0	90	0	45	0	60	60	-30	60	30	90	30	-60
	4	45	90	-45	0	0	30	30	30	60	0	45	30	60	-60	90	-60	90	-60	0	60	-60	90										
	5	45	90	-45	-30	0	90	-45	30	60	90	90	-60	90																			
	6	45	90	-45	0	-30	45	90	60	90	-60	90	90																				
	7	45	90	-45	0	30	0	30	30	0	30	30	0	45	-60	30	90	90	30	-60	-60	60	45	90	30	-45	60	-60	0	30	0	30	-60
	8	45	90	-45	0	30	0	-45	0	90	45	60	45	45	60	60	-60	-30	90	60													
SPAR 2	1	45	90	-45	30	30	0	60	60	0	60	60	30	-45	60	-45	90	45	-60														
	2	45	90	-45	60	30	0	0	30	0	30	60	30	90	0	30	30	-45	30	0	45	30	0	30	30	90	-45	30	60	90	0		
	3	45	90	-45	0	90	90	-60	90																								
	4	45	90	-45	0	30	30	0	90	30	30	30	30	-45	30	30	90	-60	90	60	90	60	45										
	5	45	90	-45	45	-30	0	90	-60	90	90	-60	90																				
	6	45	90	-45	0	0	30	30	60	0	30	30	60	45	90	45	45	90	-60	-60	-60	30	90										
	7	45	90	-45	-60	0	-60	90	60	90	90																						
	8	45	90	-45	0	30	30	45	0	45	-60	90	90	90	-45	60	90	60															
SPAR 3	1	45	90	-45	-60	0	90	90																									
	2	45	90	-45	0	90	90	-60																									
	3	45	90	-45	-30	90	30	30	-30	-60	90	90	-60	90																			

Figure 6.11: The stacking sequence for RBDO design obtained from second layup strategy with 0°, ±30°, ±45°, ±60°, and 90° plies.

- A 45 deg, 90 deg and −45 deg sequence is specified at the outer surface of the laminate to provide damage resistant and helps prevent delamination under loading.

However, the ply drop constraint is not considered in the layup configuration. In reality, the ply drop constraint allows for continuity and to avoid high-stress concentration area on the laminate due to sharp change in the thickness of the adjacent laminate. From the results presented in this chapter, it can be remarked that the design reliability of the laminate panel is driven by the inclusion of additional ply angle in the layup strategy which imparts higher bending stiffness on the wing structures.

6.6 Summary

The following conclusions can be drawn from the work in this chapter.

1. A computationally efficient approach has been presented for improved design reliability of composite wings subjected to multiple constraints with uncertain in material properties and ply thickness. The Polynomial Chaos Expansion method

provides an efficient tool to estimate the wing's responses due to the random parameters at a lower computational cost.

2. Polynomial Chaos Expansion method provides sufficient accuracy for uncertainty quantification with fewer model runs compared to Monte Carlo Simulation.

3. The reliability-based design optimisation (RBDO) method is capable of producing a reliable design based on the minimum probability of failure for flutter and root bending moment responses. Different level of design reliability can be achieved with three layup strategies suggested. The first layup strategy consists of 0°, ±45° and 90° plies. Additional ply angles of ±30°, ±60°, ±15° and ±75° are included in the second and third layup strategies.

4. The deterministic design provides a structural weight reduction of 11.3% in comparison with the benchmark wing. The structural weight saving is not considered in the RBDO as only ply angles are used as the design variables.

5. The composite manufacturing constraints such as composite ply drops are not considered in the analysis, which may provide more feasible stacking sequence for RBDO design.

6. An improvement of 32.6% in terms of structure reliability for flutter response is obtained from RBDO design with 0°, ±45° and 90° plies. The highest reduction in the RBM value is obtained from the second layup strategy consists of ±30° and ±60° plies.

7. The second layup strategy with 0°, ±30°, ±45°, ±60° and 90° plies produce an optimal RBDO design for flutter and wing root bending moment responses.

Chapter 7

Multi-level Robust and Reliability-Based Aeroelastic Tailoring Framework

7.1 Introduction

Traditionally, aircraft wing structures are designed using deterministic approaches for minimum structural weight, while satisfying multiple constraints for performance and certification. Designers, however, are aware that deterministic optimisations, being unable to account for probabilistic uncertainties in material and structural parameters, may lead to unreliable or unrealistic designs. When dealing with composite structures, stochastic uncertainties arise from geometric and material properties, and from manufacturing processes. If one were to design for reliability and robustness, parameter variations in the model should be quantified accurately. Hence, the growing interest in improving or replacing deterministic optimisation procedures for robust and reliability-based structural design methods.

A probabilistic design concept, Reliability-based Design Optimisation (RBDO) has been introduced in a previous chapter (Chapter 6) which employs the probability of failure to determine the level of design reliability in the aeroelastic tailoring. The method aims to optimise a design whilst having a particular risk or target reliability/performance as a constraint. Another probabilistic design concept known as Robust Design Optimisation (RDO) method is introduced in this chapter. The method seeks for optimal designs about a mean response value to maximise the design robustness via minimisation of the sensitivity to random parameter variations [29]. Later on in this chapter, a mixed RBDO-RDO approach is introduced which employs features of both RDO and RBDO in aeroelastic tailoring of composite wings within a multi-level optimisation framework. The mixed approach is thought to be a more effective means to search for robust optimum that also satisfy reliability constraints.

There are very few studies [21, 30, 172] that have been done using probabilistic optimisation approaches such as RBDO and RDO for the aeroelastic tailoring of composite structures. Scarth *et al.* [21] and Manan *et al.* [172] used simplified analytical models for aeroelastic stability with uncertainty arising from composite material properties. These works employed a PCE model for uncertainty evaluation, together with a singly-constrained RBDO approach, to obtain a reliable design for maximum instability speed. Paiva *et al.* [29] used a mixed RDO-RBDO approach for the preliminary design of aircraft wings. Their multidisciplinary approach employs a Kriging surrogate model to account for uncertainty in parameters of the flight condition. To the knowledge of the author, the current work is the first to perform probabilistic optimisation approach using a combination of robust and reliability-based design methods within a multi-level aeroelastic tailoring framework for structural and aeroelastic response constraints.

The work presented in this chapter introduces a multi-level aeroelastic tailoring optimisation approach to determine minimum structural wing weight, subject to multiple structural and aeroelastic constraints. The optimisation procedure is divided into two levels: a deterministic optimisation and a combined implementation of robust and reliability-based design optimisations (RRBDO). The current work employs a detailed finite element wing box model, together with a PCE surrogate model for uncertainty quantification, to solve for a multi-constrained aeroelastic tailoring optimisation problem. Composite material properties and ply thickness variations are chosen as the parameters carrying uncertainty, with different levels of variation. A comparison between the RDO, RBDO and RRBDO approaches for aeroelastic tailoring is presented.

7.2 Model definition and analysis methods

A detailed Finite Element (FE) model for the high aspect ratio wing box of a reference regional jet airliner as described in Section 3.2.1 (page 56) is used for the analyses in this work. All parts of the primary structure are modelled with intermediate modulus carbon/epoxy composite (Hexcel 8552 IM7 [179]), with material properties listed in Table 3.3 (page 65). For dynamic and aeroelastic analyses, engine and fuel weight are modelled as concentrated masses, with locations as shown in Figure 3.4 (page 57). The fuel mass is distributed spanwise along the tank centroid line, with point masses

positioned between each spar-rib bay. Fuel load is included to provide a realistic representation of the wing model. The wing's secondary masses that included pylon, nacelle and engine part are modelled as point masses. Only the skin and spar sections are included in the optimisation procedures, where a total of 41 panels are created, with 11 panels for the top and bottom skins, eight panels for spar 1 and 2, and three panels for spar 3, as shown in Figure 3.6 (page 63). The wing model is optimised for a minimum weight with consideration of robustness and reliability, when subject to multiple constraints including strain, buckling, aeroelastic stability and extreme gust loads. Lamination parameters and laminate thickness are chosen as design variables and translated into stiffness components to be input into the FE model.

The lamination parameters are also governed by the feasible region relationships which act as an additional set of constraints to reduce the design spaces towards convergence solution. The feasible regions of the four in-plane and out-of-plane lamination parameters given by Eqn. (3.10) in Section 3.3.1 (page 59). To recall, the feasible regions are governed by

$$\begin{aligned} &-1 \leq \xi_k^j \leq 1, \\ &(\xi_1^j)^2 + (\xi_3^j)^2 \leq 1, \\ &2(1+\xi_2^j)(\xi_3^j)^2 - 4\xi_1^j\xi_3^j\xi_4^j + (\xi_4^j)^2 - (\xi_2^j - 2(\xi_1^j)^2 + 1)(1-\xi_2^j) \leq 0, \end{aligned} \tag{3.10}$$

where ξ_k^j are the lamination parameters with $k = 1, 2, 3, 4$ and $j = A, D$.

In this work, symmetric laminates and unbalanced laminates are considered. The unsymmetrical laminates tend to warp upon cool down from the curing temperature. For balanced laminates, the extension-shear coupling terms, A_{16} and A_{26}, are zero. These will reduce the influence of anisotropy (extension-shear coupling) on the response of composite structures [137], thereby reducing the design spaces for aeroelastic tailoring. The unbalanced, symmetric laminates are considered in this work. This decision results in nine design variables for each composite panel in the wing box model (eight lamination parameters plus one laminate thickness), giving a cumulative total of 369 design variables for each level of optimisation.

7.2.1 Aeroelastic analysis

The aeroelastic stability of the wing box is assessed using MSc. Nastran's `SOL 145`, which relies on the frequency matching *'p-k'* method to predict the flutter speed, V_{f}. In Nastran, a matched flutter analysis is specified (`PKNL` in `FLUTTER` input command). Further details can be found in [182]. Structural frequencies, as well as their modal amplitudes and damping, are obtained from the analysis as functions of air speed. The flutter speed at each mode is found as the value at which the damping equal to zero. A total of 12 modes are considered in the flutter analysis to allow for mode switching during the optimisation process.

7.2.2 Gust analysis

The wing's responses due to gust load were analysed by considering discrete gusts or continuous turbulence as specified by aeronautical authorities (CS-25 [181]). Herein, the wing's response to turbulence is evaluated in terms of root bending moment (RBM) for discrete *'1-cosine'* gusts [22, 23]. The governing equations for *'1-cosine'* gust profile are given by Eqns. (3.30) and (3.31) in Section 3.4.5 (page 78). To recall

$$w_g(t) = \frac{w_{g0}}{2}(1 - \cos\frac{2\pi V}{L_g}t), \tag{3.30}$$

where

$$w_{g0} = U_{\mathrm{ref}}\, F_{\mathrm{g}} \left(\frac{H}{107}\right)^{\frac{1}{6}}. \tag{3.31}$$

In the current work, the reference gust velocity, U_{ref} is 13.41 ms^{-1} and the flight speed is set to 253 ms^{-1}. The gust length is chosen to vary from 18 m to 216 m. MSc. Nastran's `SOL 146` is used to evaluate the wing box dynamic aeroelastic response to discrete gusts. The details on the analysis are explained as per Section 3.4.5 (page 78). The input gust velocity as a function of time at reference gust velocity used in the analysis is shown in Figure 3.17 (page 80).

7.2.3 Structural analysis

The structural responses of the composite wing are evaluated in terms of strain and buckling responses subjected to static manoeuvre load case at a Mach 0.82, cruise altitude of 10000 m and acceleration $2.5g$. The load distributions on the wing due to the aerodynamic loading is initially obtained from a trim analysis performed with MSc. Nastran's `SOL 144`. The buckling and static analyses were performed with MSc. Nastran's `SOL 105`. The strength of the laminate panels for top skin, bottom skin and spars are evaluated in terms of laminate strain. The buckling performances are assessed by computing the crtitical buckling load factor, λ. The first ten buckling modes are computed to include the possibility of mode changes.

7.3 Multi-level aeroelastic Tailoring

A multi-level optimisation method is proposed for the aeroelastic tailoring of the composite wing box of a reference regional jet airliner. The optimisation methodologies, algorithms and strategy are detailed in this section.

The optimisation's objective is to minimise the structural weight, subject to multiple constraints, including strength and aeroelastic stability. Thickness and lamination parameters of the wing box composite panels are used as design variables. The design's robustness and reliability, when considering stochastic variations of composite ply material properties and thickness, are also assessed.

The optimisation framework comprises two levels, as illustrated in Figure 7.1. Matlab's implementation of the Particle Swarm Optimisation (PSO) algorithm and MSc. Nastran are used to solve the optimisation problem. PSO is a heuristic search method based on simple analogues of collaborative behaviour and swarming in biological populations [58]. Similar to a Genetic Algorithm (GA), PSOs perform population-based searches that depend on exchanges of information between individuals for search progression. PSO is reported to be computationally more efficient than GAs, because the algorithm requires fewer function evaluations [52].

The PCE, as presented in Section 5.3, is used as a surrogate models to quantify model uncertainty for robust and reliability-based design optimisation. In the first level opti-

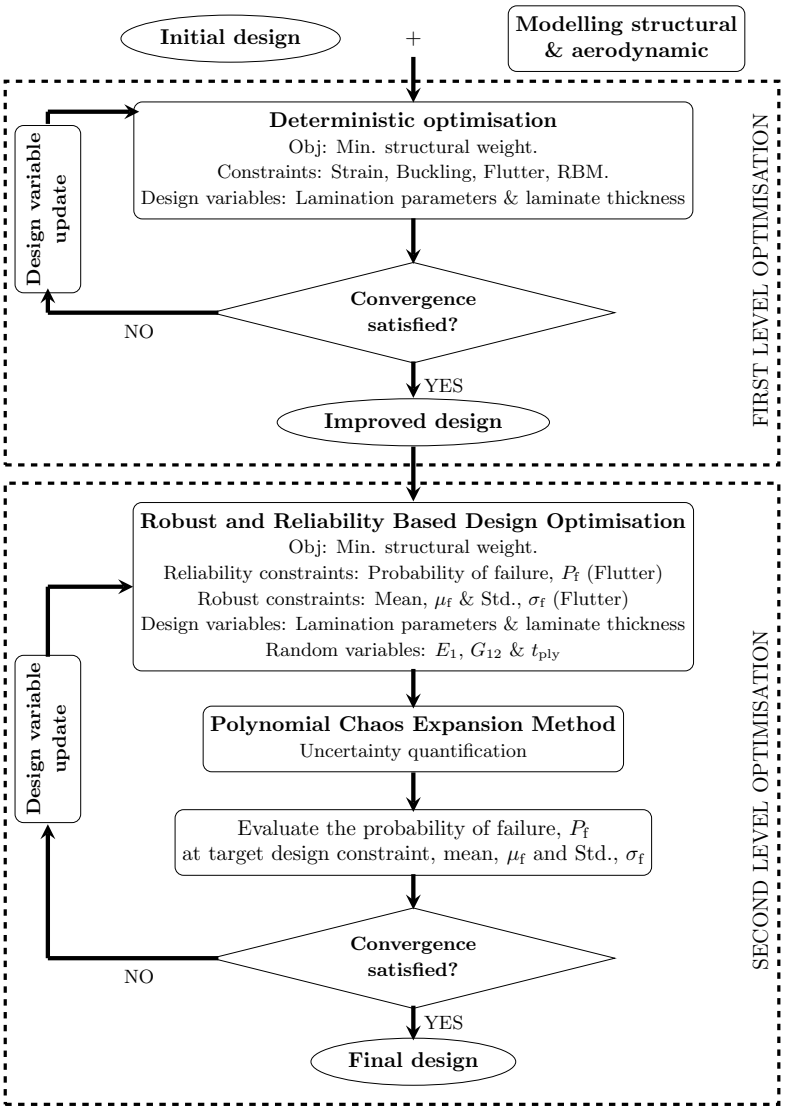

Figure 7.1: The multi-level optimisation approach.

misation, the wing structure is optimised subjected to a static manoeuvre load and optimised for minimum weight with strain, buckling, flutter and gust response constraints. A weighted cost function is used to account for the influence of multiple constraints.

Results from the first level are fed to the second level to optimise the design further for robustness and reliability. The effect of uncertainties is considered in terms of probability density functions (PDF), mean and variance of the flutter responses. To keep computational time to acceptable levels, the effect of uncertainties on other first level constraints is not quantified explicitly. However, for consistency, first level responses are imposed as design constraints in the second level.

7.3.1 First level: Deterministic optimisation

The first level optimisation problem is formulated as follows:

$$
\begin{aligned}
\underset{\mathbf{x}}{\text{minimize}} \quad & f_{\text{obj}}(W(\mathbf{x}), f_{1,\text{cost}}(\mathbf{x})), \\
\text{subject to:} \quad & \text{Strain Failure Index,} \quad FI(\mathbf{x}) \leq 1 \quad \text{(Max. Strain)}, \\
& \text{Buckling critical load factor,} \quad \lambda(\mathbf{x}) \geq 1, \\
& \text{Flutter speed,} \quad V_{\text{f}}(\mathbf{x}) \geq 1.15 V_{\text{D}} \quad (V_{\text{D}} = \text{Design dive speed}), \\
& \text{Wing Root Bending Moment,} \quad \max(RBM(\mathbf{x}, L_{\text{g}})) \leq \max(RBM_{\text{Benchmark}}(L_{\text{g}})), \\
& \mathbf{x} = [\xi_1^A, \ldots, \xi_4^A, \xi_1^D, \ldots, \xi_4^D, t_{\text{panel},1}, \ldots, t_{\text{panel},41}],
\end{aligned}
\tag{7.1}
$$

where

- $\mathbf{x}$ is vector containing the design variables.
- λ is the lowest buckling load factor (ten modes are computed to account for mode switching).
- FI is the strain Failure Index defined as

$$
FI = \max\Big(\frac{\epsilon_{\text{min}}}{\epsilon_{\text{min,allowable}}}, \frac{\epsilon_{\text{max}}}{\epsilon_{\text{max,allowable}}}, \frac{\gamma_{\text{min}}}{\gamma_{\text{min,allowable}}}, \frac{\gamma_{\text{max}}}{\gamma_{\text{max,allowable}}}\Big), \tag{7.2}
$$

  where ϵ_{min} and ϵ_{max} are the principle strains for laminate under compression and tension, respectively. The allowable values are set to $\epsilon_{\text{min,allowable}} = -5900\mu\epsilon$ and $\epsilon_{\text{max,allowable}} = 7100\mu\epsilon$. The shear strains limit is defined in terms of maximum and minimum shear strains, with allowable values set to $\gamma_{\text{min,allowable}} = -4500\mu\epsilon$ and $\gamma_{\text{max,allowable}} = 4500\mu\epsilon$.

- The flutter speed, V_{f}, is calculated from a conventional V-g plot as per Section 7.2.1. A matched method is employed with Mach 0.82 at varied altitude. Since 12 modes are considered, V_{f} is assumed to be the lowest of 12 values at which the damping factor equals zero.
- For the gust constraint, six different values of L_{g} are used in order to compute the maximum RBM. The values are indicated in Section 7.2.2 (page 179).

Finally, the objective function in Eqn. (7.1) is given as

$$f_{\text{obj}} = \frac{W(\mathbf{x})}{W_{\text{Benchmark}}} + f_{1,\text{cost}}(\mathbf{x}), \tag{7.3}$$

where W is the wing structural weight (skins and spars only); $f_{1,\text{cost}}(\mathbf{x})$ is a cost penalty function defined to account for constraint violations as

$$f_{1,\text{cost}} = w_{\text{f}} \times \left|\frac{V_{\text{f}} - V_{\text{f,Design}}}{V_{\text{f,Design}}}\right| + w_{\text{g}} \times \left|\frac{RBM}{RBM_{\text{Benchmark}}}\right| + w_{\text{EIG}} \times \left|\frac{\lambda - \lambda_{\text{Design}}}{\lambda_{\text{Design}}}\right| + w_{\text{FI}} \times \left|\frac{FI - FI_{\text{Design}}}{FI_{\text{Design}}}\right|, \tag{7.4}$$

and where

$$w_{\text{constr}} = \{w_{\text{constr}_\text{i}} \in [0,1] : \sum_{\text{constr}_\text{i}} w_{\text{constr}_\text{i}} = 1,\ \text{constr}_\text{i} \in \{\text{f}, \text{g}, \text{EIG}, \text{FI}\}\} \tag{7.5}$$

is the set of weighting coefficients relative to each of the constraints, and the subscript 'Design' denotes desired or allowable values.

By variation of the weighting coefficients, a Pareto front of optimised solutions is obtained. Following the averaging principle defined in [187], the overall best deterministic design is chosen as the Pareto point minimising the expression ($|\Sigma - 1|$), where

$$\Sigma = c_1 \frac{W}{W_{\text{min}}} + c_2 \frac{V_{\text{f}}}{V_{\text{f,max}}} + c_3 \frac{RBM}{RBM_{\text{min}}} + c_4 \frac{\lambda}{\lambda_{\text{min}}} + c_5 \frac{FI}{FI_{\text{max}}}, \tag{7.6}$$

and

- The subscripts 'min' and 'max' indicate the minimum and maximum values obtained for each parameter from all possible weighting combinations.
- c_1, c_2, c_3, c_4 and c_5 are the constant parameters each having a value of 0.2.

7.3.2 Second level: Robust and reliability-based design approaches

The need for a multi-level optimisation strategy is justified by considerations of computational feasibility. Evaluating full wing box designs, for multiple performance/constraint metrics and by means of finite element models, can be costly and take many minutes per attempted solution. Aiming to quantify the effect of parameter uncertainty on the

robustness and reliability of optimised designs, one would have to run a statistically relevant number of stochastic variations for every tentative solution trialled by the optimiser. This requirement makes "all-at-once", single level approaches computationally impractical. A potential alternative to alleviate the computational burden is to recur to surrogate models to approximate system behaviour with functions that are quick to interrogate and evaluate. However, training the surrogates to capture a variety of responses to multiple parameters is similarly computationally expensive and impractical.

To overcome these limitations, the approach adopted in this work is to run a deterministic optimisation first and then pass the output to a second level, to account for uncertainty. In the second level, PCE is used to quantify the effect of uncertainties on some responses only, using the optimised values of the remaining ones as design constraints. This approach guarantees that the second level output, i.e. the final optimised design, is robust and reliable in terms of chosen responses, whilst still meeting all of the constraints imposed on and met by the deterministic optimum.

Reliability-based design optimisation and robust design optimisation are the two main methodologies reported in the literatures for probabilistic design optimisation [25, 29–31, 172]. The work presented herein employed a combination of both methods to quantify the parameter variations in material properties and composite ply thickness. In particular, and unless stated otherwise, the longitudinal, E_{11} and shear modulus, G_{12} as well as t_{ply}. The coefficient of variation (CV) of 0.1 is chosen for E_{11} and G_{12}, while for t_{ply}, the CV is assumed to be 0.01. The mean and standard deviation values for the random parameters are given in Table 7.1. For completeness, additional numerical analyses have been performed with different sets of coefficients of variations. These analyses aimed at testing the robustness of the proposed computational framework, as well as the generality of the ensuing results and conclusions.

Table 7.1: Mean and standard deviation for the parameters carrying uncertainties.

	E_{11} (GPa)	G_{12} (GPa)	t_{ply} (m)
Mean, μ	148.0	5.90	1.83×10^{-4}
Std Dev., σ	14.8	0.59	1.83×10^{-6}

The concepts of reliability-based design optimisation, robust design optimisation and a mixed approach of robust and reliability-based design optimisation are presented in following sections.

7.3.2.1 Reliability-Based Design Optimisation (RBDO)

In RBDO, the goal is for a structure to achieve a target performance whilst attaining a prescribed level of design reliability [29]. Reliability is measured in terms of probability of failure, P_f, i.e. constraint violation, or occurrence of a particular response. P_f is calculated as the area between the PDF and the target design constraint.

In the context of aeroelastic tailoring, designers typically aim to minimise aircraft weight whilst maximising reliability. Reliability is maximised by minimising P_f [25, 172], that is by shifting the failure PDF to the right and/or shrinking it. The generalised form of the RBDOs performed in this work is expressed as

$$\begin{aligned} \underset{\mathbf{x}}{\text{minimize}} \quad & f_\mathrm{rbdo}(W(\mathbf{x},\mathbf{p}), P_\mathrm{f}(\mathbf{x},\mathbf{p})), \\ \text{subject to:} \quad & g_\mathrm{rc}(\mathbf{x},\mathbf{p}) \leq 0, \\ & \mathbf{g}_\mathrm{d}(\mathbf{x},\mathbf{p}) \leq 0, \\ & \mathbf{x}_\mathrm{L} \leq \mathbf{x} \leq \mathbf{x}_\mathrm{U}, \end{aligned} \tag{7.7}$$

where f_rbdo is the objective function; $g_\mathrm{rc}(\mathbf{x})$ is the reliability constraint; $\mathbf{g}_\mathrm{d}(\mathbf{x})$ is the vector set of design constraints for which a reliability target is not established; $\mathbf{p}$ is a vector of constant parameters that do not vary in the optimisation; and $\mathbf{x}$ is bound between lower and upper limits, $\mathbf{x}_\mathrm{L}$ and $\mathbf{x}_\mathrm{U}$.

The objective function is defined as an aggregate of the structural weight and the probability of failure

$$f_\mathrm{rbdo} = w_W \times \frac{W}{W_\mathrm{det}} + w_{P_\mathrm{f}} \times \frac{P_\mathrm{f}}{P_\mathrm{allow}}, \tag{7.8}$$

where W_det is the structural weight from the deterministic optimisation, and w_W and w_{P_f} are weighting coefficients chosen so that $w_W + w_{P_\mathrm{f}} = 1$. Here, the reliability constraint takes the form

$$g_\mathrm{rc} = P_\mathrm{f} - P_\mathrm{allow}, \tag{7.9}$$

where P_allow is the allowable probability of failure. In our case, the probability of exceeding the design flutter speed.

7.3.2.2 Robust Design Optimisation (RDO)

The RDO method aims at optimising a structure placing the targeted performance around a mean value and maximising robustness by minimising sensitivity to random parameter variations [29]. This aim is achieved by minimising the variance and optimising the mean of the response in question. The generalised form of the RDOs performed in this work is

$$\begin{aligned} \underset{\mathbf{x}}{\text{minimize}} \quad & f_{\text{rdo}}(W(\mathbf{x},\mathbf{p}), \mu_{\text{f}}(\mathbf{x},\mathbf{p}), \sigma_{\text{f}}(\mathbf{x},\mathbf{p})), \\ \text{subject to:} \quad & g_{\text{upper}}(\mu_{\text{f}}(\mathbf{x},\mathbf{p}), \sigma_{\text{f}}(\mathbf{x},\mathbf{p})) \leq USL \quad \text{or} \quad g_{\text{lower}}(\mu_{\text{f}}(\mathbf{x},\mathbf{p}), \sigma_{\text{f}}(\mathbf{x},\mathbf{p})) \geq LSL, \\ & \mathbf{g}_{\text{d}}(\mathbf{x},\mathbf{p}) \leq 0, \\ & \mathbf{x}_{\text{L}} \leq \mathbf{x} \leq \mathbf{x}_{\text{U}}, \end{aligned} \tag{7.10}$$

where f_{rdo} is the objective function defined in terms of weight, weighting coefficients ($\{w_W, w_\mu, w_\sigma\} : w_W + w_\mu + w_\sigma = 1$), mean response, μ_{f}, and standard deviation, σ_{f},

$$f_{\text{rdo}} = w_W \times \frac{W}{W_{\text{det}}} + w_\mu \times \left| \frac{\mu_{\text{f}} - \mu_{\text{det}}}{\mu_{\text{det}}} \right| + w_\sigma \times \frac{\sigma_{\text{f}}}{\sigma_{\text{det}}}, \tag{7.11}$$

and where $g_{\text{upper}} = \mu_{\text{f}} + n\sigma_{\text{f}}$ and $g_{\text{lower}} = \mu_{\text{f}} - n\sigma_{\text{f}}$ are design constraints used to define the solution's robustness. These constraints are bounded by their upper and lower statistical limits, USL and LSL, which are given as functions of the mean and standard deviation of the deterministic optimisation design, μ_{det} and σ_{det}, as

$$USL = \mu_{\text{det}} + n\sigma_{\text{det}} \qquad \text{and} \qquad LSL = \mu_{\text{det}} - n\sigma_{\text{det}}, \tag{7.12}$$

entailing that feasibility is maintained within n standard deviations of the optimised mean. In this work, $n = 6$ in line with a 6σ design philosophy [195].

7.3.2.3 Robust and Reliability-based Design Optimisation (RRBDO)

A combined approach, mixing robust and reliability-based design optimisations (RRBDO), is thought to be more comprehensive than RBDO and RDO individually. Particularly when, as in the case of aeroelastic tailoring, design reliability and robustness are sought together. An RRBDO approach is expected to: (a) improve on the RDO solutions by bringing additional reliability; and (b) improve on RBDO with increased robustness. In

aeroelastic terms, RRBDO should ensure minimum mean weight with mean constrained responses, such as flutter or stresses, all close to the boundary of failure. Mathematically, this is obtained by combining RDO and RBDO constraints as follows:

$$\begin{aligned}
\underset{\mathbf{x}}{\text{minimize}} \quad & f_{\text{rrbdo}}(W(\mathbf{x},\mathbf{p}),\mu_{\text{f}}(\mathbf{x},\mathbf{p}),\sigma_{\text{f}}(\mathbf{x},\mathbf{p})),\\
\text{subject to:} \quad & g_{\text{rc}}(\mathbf{x},\mathbf{p}) \leq 0,\\
& g_{\text{upper}}(\mu_{\text{f}}(\mathbf{x},\text{p}),\sigma_{\text{f}}(\mathbf{x},\text{p})) \leq USL \quad \text{or} \quad g_{\text{lower}}(\mu_{\text{f}}(\mathbf{x},\mathbf{p}),\sigma_{\text{f}}(\mathbf{x},\mathbf{p})) \geq LSL,\\
& \mathbf{g}_{\text{d}}(\mathbf{x},\mathbf{p}) \leq 0,\\
& \mathbf{x}_{\text{L}} \leq \mathbf{x} \leq \mathbf{x}_{\text{U}},
\end{aligned} \tag{7.13}$$

where the objective function, f_{rrbdo}, is

$$f_{\text{rrbdo}} = w_W \frac{W}{W_{\text{det}}} + f_{1,\text{cost}} + f_{2,\text{cost}}, \tag{7.14}$$

and the cost penalty functions, $f_{1,\text{cost}}$ and $f_{2,\text{cost}}$ are defined as

$$f_{1,\text{cost}} = w_\mu \times \left|\frac{\mu_{\text{f}} - \mu_{\text{det}}}{\mu_{\text{det}}}\right| + w_\sigma \times \frac{\sigma_{\text{f}}}{\sigma_{\text{det}}} \qquad \text{and} \qquad f_{2,\text{cost}} = w_{P_{\text{f}}} \times \frac{P_{\text{f}}}{P_{\text{allow}}}, \tag{7.15}$$

where w_W, w_μ,w_σ and $w_{P_{\text{f}}}$ are weighting factors ($w_W + w_\mu + w_\sigma + w_{P_{\text{f}}} = 1$) and all other quantities are defined previously.

7.4 Stochastic Modelling

For reasons of computational cost, the Polynomial Chaos Expansion (PCE) method is used to quantify the effect of random parameter variations in the optimisation algorithms. The used of PCE provided a significant reduction in the number of samples required for accurate estimations of the responses. Moreover, the probabilistic optimisation approach introduced here requires quantification of uncertainty in each iteration steps. Hence, the use of an efficient method such as PCE is crucial to reduce computational costs. The details of modelling using PCE are presented in Chapter 5.

A general overview of the PCE method is illustrated in Figure 7.2. The Latin Hypercube Sampling (LHS) technique [188] is used for sampling to ensure all these points are sampled with equal probability so that the response are captured on all PDF's points, hence, the

response's variance are kept at minimum. The least-square linear regression model is fitted to calculate the expansion coefficients, β_i based on sampling data. The resulting coefficients are then fed back to the PCE formulation to emulate the system response for any combination of random variables and to estimate the statistical properties of the system at a reduced computational cost.

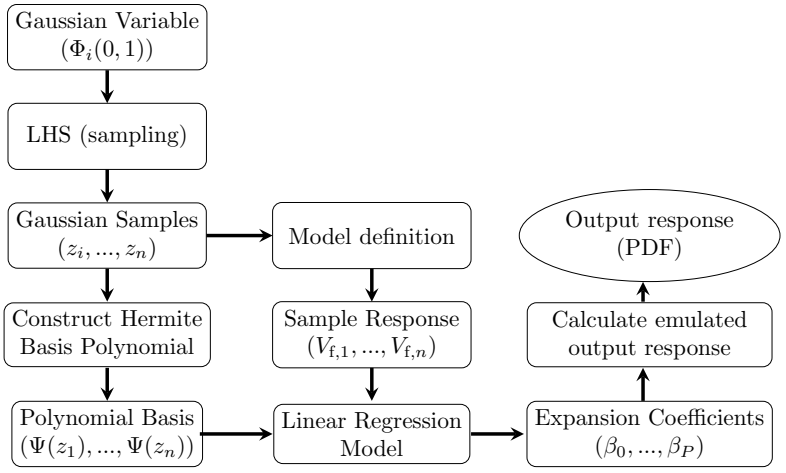

Figure 7.2: Overview of the stochastic modelling process using Polynomial Chaos Expansion.

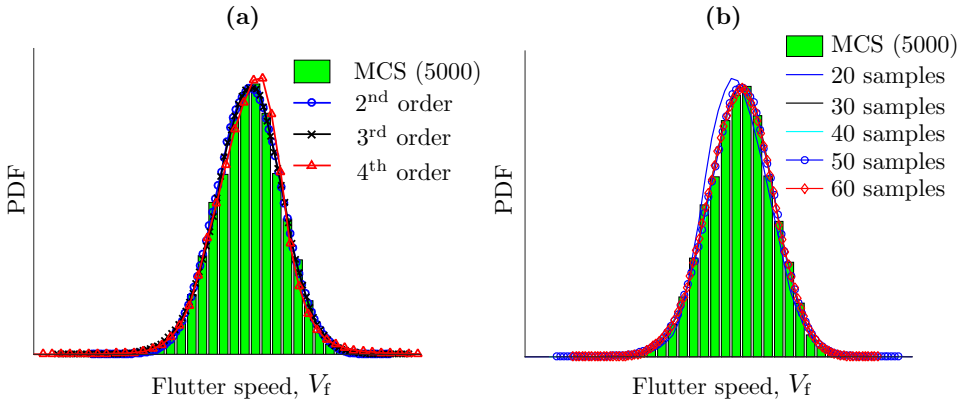

Figure 7.3: Flutter speed responses obtained using MCS and PCE: (a) MCS and PCE using polynomials of different order; (b) MCS and 3rd order PCE using different number of sample runs.

To ensure the accuracy of the PCE method, a convergence study is performed using different order PCE models and different number of samples. In comparison with MCS, the convergence study proves that 30 sample runs are sufficient which is a 100× less than MCS. Figure 7.3 shows a comparison of the flutter speed distribution obtained 5000 MCS runs and using PCE models of different order (with random composite material properties as defined in Section 7.3.2). An adequate agreement is obtained using 1st, 2nd

and 3^{rd} order PCE with 30 samples, with a small discrepancy observed for a 4^{th} order PCE due to an insufficient number of sample runs. These results suggest that sufficiently accurate uncertainty quantifications can be obtained using low order PCE models, i.e. 3^{rd} order, and a small number of sample runs, which contains overall computational cost. In consequence, a 3^{rd} order PCE model with 30 samples is used in the second level optimisation.

7.5 Case study on multi-level aeroelastic tailoring framework

Results obtained using the optimisation framework detailed in previous sections are presented herein, where the benchmark wing model is tailored deterministically as per Section 7.3.1 using different combinations of the weighting factors for each of the responses in the cost function. An ideal deterministic optimum is then selected from the Pareto front generated. Subsequently, by following the methods detailed in Section 7.3.2, RBDO, RDO and RRBDO are employed to optimise the design for added reliability and/or robustness with minimal structural weight penalty. The effect of uncertainties is quantified for flutter speed and weight. All of the other responses of the deterministic design are kept in the second level optimisation as additional design constraints ($\mathbf{g}_{\text{d}}$) to ensure no deterioration in performance from the first level optimisation.

Henceforth, it is assumed that the random parameters are Gaussian continuous variables. Hermite polynomials are used to construct the polynomial basis in the stochastic model.

7.5.1 First level: Deterministic optimisation

A total of 20 optimisation runs were performed, with the weighting factors for each of the responses (as defined in Eqn. (7.4)) assuming values in $[0, 1]$. These values are chosen using LHS to respect Eqn. (7.5) and are shown in Table 7.2.

Table 7.3 presents a summary of the results. The notations DET1, DET2, ..., DET20 refered to individual optimisation run in the precedures. In comparison to the benchmark wing, the optimisation reduces structural weight by at least 16.4% (DET9) and up to a maximum of 35.7% (DET8). Interestingly, the lightest solution has a buckling load

Table 7.2: Weighting coefficient values used for deterministic optimisation runs.

Run	Weighting coefficients			
	w_{f}	w_{g}	w_{EIG}	w_{FI}
DET1	0.3655	0.3785	0.1164	0.1396
DET2	0.3347	0.2375	0.3102	0.1176
DET3	0.0654	0.3063	0.2832	0.3451
DET4	0.1227	0.2073	0.1127	0.5572
DET5	0.1568	0.7270	0.0804	0.0358
DET6	0.3061	0.4243	0.1713	0.0983
DET7	0.1724	0.1069	0.2595	0.4611
DET8	0.5348	0.0863	0.3324	0.0464
DET9	0.1828	0.1574	0.3638	0.2960
DET10	0.2546	0.4689	0.0721	0.2044
DET11	1.0000	0.0000	0.0000	0.0000
DET12	0.0000	1.0000	0.0000	0.0000
DET13	0.0000	0.0000	1.0000	0.0000
DET14	0.0000	0.0000	0.0000	1.0000
DET15	0.7500	0.1250	0.0625	0.0625
DET16	0.1250	0.7500	0.0625	0.0625
DET17	0.1250	0.1250	0.7500	0.0000
DET18	0.0500	0.3000	0.0500	0.6000
DET19	0.8000	0.1000	0.0500	0.0500
DET20	0.4000	0.4000	0.1000	0.1000

Table 7.3: Deterministic optimisation results at different weighting factors.

Run	$\frac{W}{W_{\mathrm{Benchmark}}}$	$\frac{V_{\mathrm{f}}}{V_{\mathrm{f,Design}}}$	$\frac{RBM}{RBM_{\mathrm{Benchmark}}}$	λ	FI	$f_{1,\mathrm{cost}}$	$\lvert\Sigma - 1\rvert$
DET1	0.669	1.007	0.004	1.006	0.823	0.030	0.027
DET2	0.646	1.001	0.145	1.042	0.601	0.095	9.381
DET3	0.681	1.019	0.032	1.057	0.993	0.030	1.944
DET4	0.676	1.009	0.043	1.022	0.976	0.026	2.663
DET5	0.647	1.007	0.030	1.062	0.859	0.033	1.771
DET6	0.698	1.026	0.026	1.020	0.913	0.031	1.527
DET7	0.683	1.015	0.201	1.029	0.935	0.062	13.193
DET8	0.643	1.001	0.207	1.000	0.589	0.038	13.503
DET9	0.836	1.081	0.180	1.008	0.915	0.071	11.845
DET10	0.654	1.001	0.039	1.029	0.922	0.037	2.379
DET11	0.681	1.000	0.088	1.052	0.725	0.000	5.619
DET12	0.661	1.008	0.003	1.024	0.758	0.003	0.052
DET13	0.709	1.030	0.450	1.001	0.740	0.001	29.759
DET14	0.736	1.048	0.030	1.212	1.000	0.000	1.865
DET15	0.663	1.006	0.321	1.000	0.763	0.060	21.145
DET16	0.772	1.059	0.012	1.095	0.783	0.036	0.612
DET17	0.712	1.036	0.086	1.002	0.860	0.016	5.519
DET18	0.645	1.007	0.037	1.010	1.000	0.012	2.256
DET19	0.646	1.001	0.005	1.408	0.878	0.028	0.177
DET20	0.663	1.006	0.012	1.028	0.952	0.015	0.588

factor equal to one, suggesting that the buckling resistance is critical for minimum weight designs.

Intuitively, cost penalties are incurred when the optimiser is tasked with satisfying multiple constraints. Indeed, the cost function reaches its lowest values for singly constrained optimisations (DET11 to DET14), with the relative reserve factors converging approximatively to the design allowable. A clear example is DET12, for which $w_{\mathrm{g}} = 1$ and $RBM/RBM_{\mathrm{Benchmark}}$ is minimum. Similarly, the lowest flutter speed is obtained when $w_{\mathrm{f}} = 1$, i.e. for DET11. Although, it is noted that V_{f} varies marginally across optimisations, the maximum value deviating only 8.1% from $V_{\mathrm{f,Design}}$ (DET9).

Further insight into the results can be gained from Figure 7.4, where the reserve factors are plotted against the corresponding weighting factor. In theory, the higher the weighting factor, the closer the response should be to its allowable value. This proves to be the case here, which gives confidence into the validity of the underlying calculations.

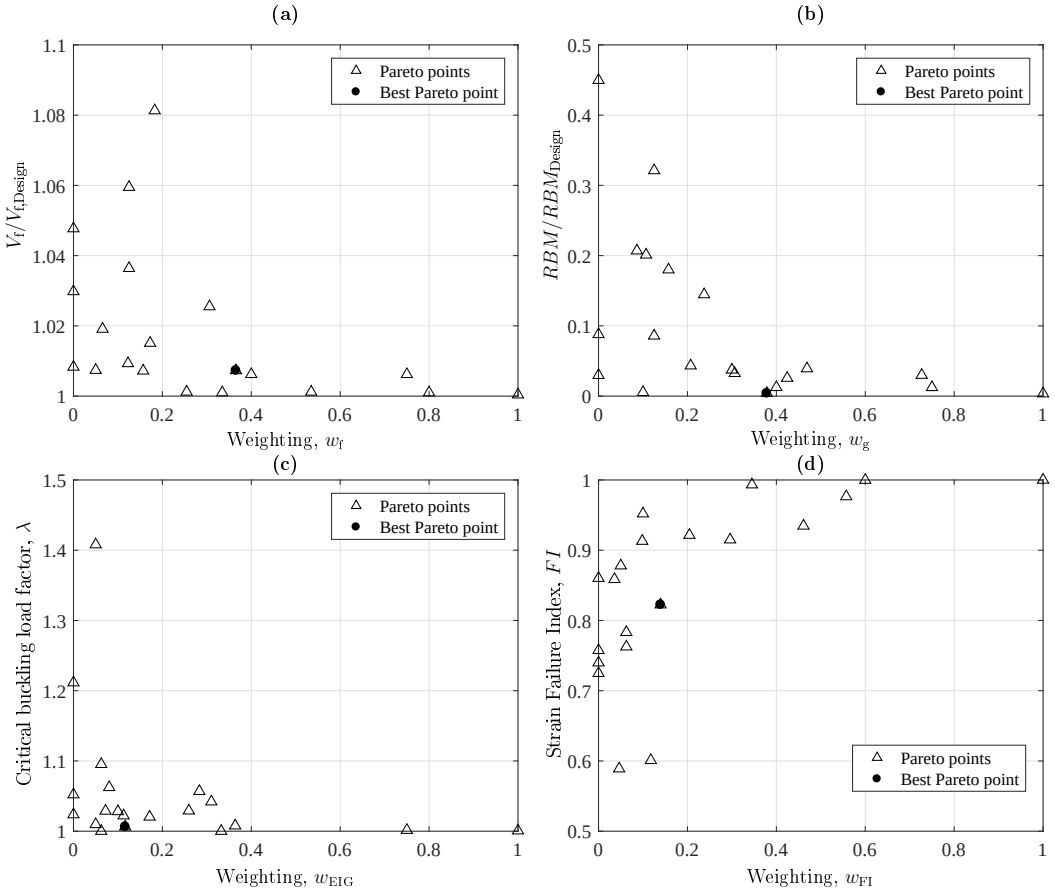

Figure 7.4: Pareto plots for (a) Flutter constraint against weighting, w_{f}, (b) RBM constraint against weighting, w_{g}, (c) Buckling constraint against weighting, w_{EIG} and (d) Strain constraint against weighting, w_{FI}.

The overall best design is chosen utilising the averaging principle defined in Eqn. (7.6). The selection is based on the Pareto point which produced a minimum value of expression $(\Sigma - 1)$. The value of Σ for each optimisation run are given in Table 7.3. DET1 is found to be overall best deterministic design to be used as the starting point for the second level optimisation. The corresponding wing box-sizing parameters are shown in Figure 7.5, where they are also compared to the benchmark model. Naturally, thickness values are discontinuous and multiples of t_{ply}. For simplicity, blending constraints were not applied at this stage of the study. Alternatively, in order to ensure panel contiguity, no more than two plies were allowed to be dropped between adjacent panels.

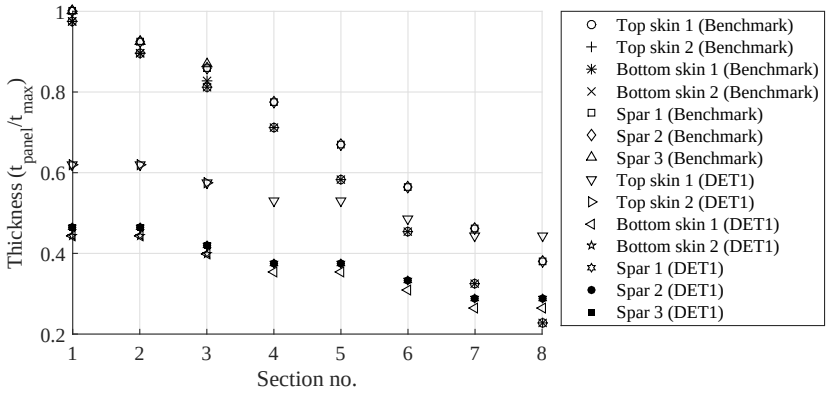

Figure 7.5: Thickness variation for skin and spar sections for benchmark and deterministic optimum design (DET1).

7.5.2 Second level: Reliability-Based Design Optimisation (RBDO)

Following on from the first level, the overall best deterministic design (DET1) is further optimised for reliability, by assuming stochastic variations of material properties (E_{11} and G_{12}) and composite ply thickness (t_{ply}). Here, similar properties of the random parameters given in Section 7.3.2 (Table 7.1) are used. The 3$^{\text{rd}}$ order PCE model is used for uncertainty quantification, utilising 30 data samples selected using LHS as it is proven to be sufficient to gain acceptable level of results accuracy in comparison with the MCSs. Reliability is evaluated in terms of the probability of failure, P_{f}, of trialled designs to exceed the minimum flutter speed ($V_{\text{f}}/V_{\text{f,Design}} > 1$) requirement.

The RBDO objective function is formulated in terms of structural weight and probability of failure as indicated by Eqn. (7.8). The allowable probability of failure is set to be equal to the probability of failure of DET1. Hence, $P_{\text{allow}} = 8.5 \times 10^{-3}$. Eleven combinations

of the weighting factors, w_{W} and $w_{P_{\mathrm{f}}}$, are used, as indicated in Table 7.4 to evaluate the contribution of individual response towards the optimised solution.

A design is deemed to be more reliable than the baseline when the probability of failure, P_{f} or the occurrence of flutter at the design speed, is reduced. To ensure overall design feasibility, the first level responses, for which the effect of uncertainties is not evaluated (strain, buckling and gust wing root bending moment), are quantified here as additional design constraints, g_{d}. The RBDO design solutions are checked for any design constaints violation as given in Eqn. (7.1).

The responses evaluated from the RBDO solutions are given in Table 7.4. The wing's structural weight, mean flutter speed, standard deviation and the probability of failure at target design values are evaluated for each trialled design with different weighting coefficient values. For all combinations of weighting coefficients, the wing design is lighter than the benchmark with P_{f} values are lower than P_{allow}. Except, of course, for RUN 1, for which $w_{P_{\mathrm{f}}} = 0$. The overall best RBDO design is determined by minimising the expression, $|\Sigma - 1|$, where $\Sigma = d_1(W/W_{\mathrm{min}}) + d_2(P_{\mathrm{f}}/P_{\mathrm{f,min}})$. The constant parameters, d_1 and d_2 are added to balanced the contribution of each design constraints and each parameter is equal to 0.5. In this case, only the contribution of structural weight and probability of failure are included in determining the ideal design as we seek for the design with the lowest weight and minimum P_{f} value. This condition is met by RUN 10 in Table 7.4, which is 31.8% lighter than the benchmark model and only 1.9% heavier than the best deterministic design. The P_{f} value evaluated for the best RBDO design is 2.448×10^{-7} which is 99.9% improvement in reliability.

Table 7.4: RBDO solutions obtained using different weighting factors for structural weight and probability of failure.

Run	Weightings		Responses				
ID	w_{W}	$w_{P_{\mathrm{f}}}$	$\frac{W}{W_{\mathrm{Benchmark}}}$	$\frac{\mu_{\mathrm{f}}}{V_{\mathrm{f,Design}}}$	σ_{f}	P_{f}	$\lvert\Sigma - 1\rvert$
1	1.00	0.00	0.669	1.010	2.654	8.500×10^{-3}	17346.447
2	0.90	0.10	0.658	1.013	3.176	2.100×10^{-3}	4285.214
3	0.80	0.20	0.678	1.019	3.684	6.623×10^{-5}	134.678
4	0.70	0.30	0.739	1.026	6.244	4.833×10^{-5}	98.194
5	0.60	0.40	0.689	1.034	5.938	5.001×10^{-6}	9.730
6	0.50	0.50	0.679	1.015	3.046	2.645×10^{-4}	539.312
7	0.40	0.60	0.729	1.025	5.706	9.974×10^{-6}	19.909
8	0.30	0.70	0.689	1.021	3.805	8.318×10^{-6}	16.499
9	0.20	0.80	0.682	1.023	4.087	2.922×10^{-6}	5.482
10	0.10	0.90	0.682	1.023	3.974	2.448×10^{-7}	0.018
11	0.00	1.00	0.679	1.017	3.451	2.010×10^{-4}	409.720

The improved design reliability are further evidenced from Figure 7.6(a) where the flutter PDFs are shifted to the right of deterministic design which results in reduction of P_f value. However, lower P_f values are accompanied by increases in the mean flutter speed and standard deviation values, suggesting that reliability is obtained at the expense of robustness. Further observations on the structural weight PDFs resulting from RBDO revealed higher mean value for majority of the trialled designs as shown in Figure 7.6(b). The observation suggest that a weight penalty is generally necessary for greater reliability. It is interesting to note that the distribution of the structural weight obtained for RUN 2 has a lower mean value compared to the deterministic design, hence indicating that it is possible to minimise structural weight whilst improving design reliability.

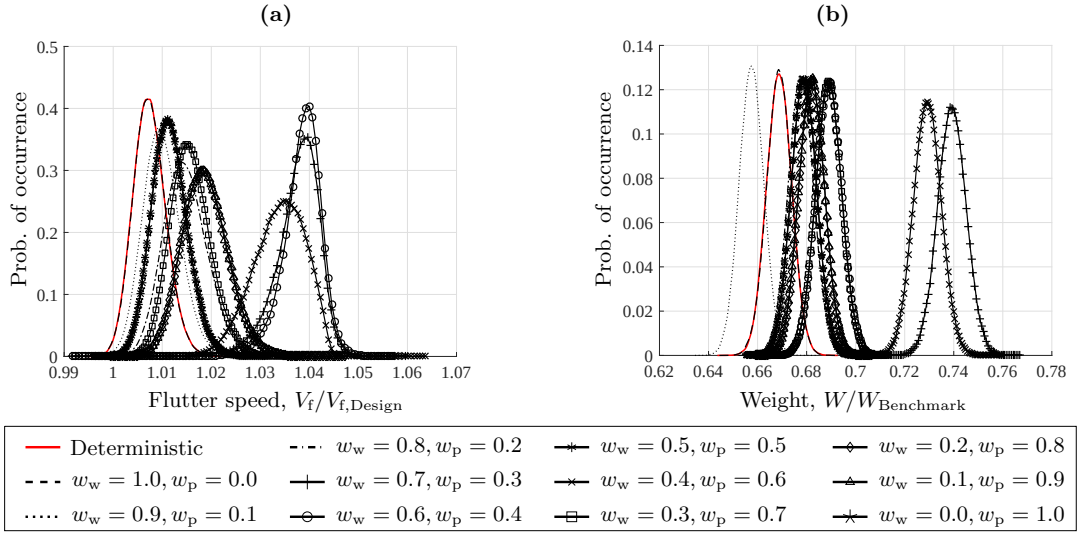

Figure 7.6: PDF plots of RBDO solutions for different weighting factors: (a) Flutter speed and (b) Structural weight.

7.5.3 Second level: Robust Design Optimisation (RDO)

The best deterministic design (DET1) obtained from first level is further optimised for robustness following the procedure described in Section 7.3.2.2. In particular, the optimisation seeks for a wing box configuration of minimal weight and whose flutter speed distribution, arising from uncertainties in material properties, has mean as close as possible to the deterministic value and minimum standard deviation.

The responses in terms of the structural weight, mean and standard deviation of the RDO trialled designs are given in Table 7.5. From the tabulated responses, it is observed that all design solutions are characterised by weight reductions in comparison to the

benchmark model and mean flutter speeds above the target design value. Moreover, an increase in robustness is demonstrated by smaller standard deviations in comparison to both deterministic design and reliability-based design solutions. The minimum reduction from $\sigma_{\text{det}} = 2.766$ occurs for RUN 1 ($w_\sigma = 0$) and is 2.6%; the maximum one being 24.9% and occurring for RUN 3 ($w_\sigma = 1$). Similarly, the overall best RDO design is selected based on an averaging principle by minimising the expression, $|\Sigma - 1|$, with $\Sigma = g_1(W/W_{\text{min}}) + g_2(\mu_{\text{f}}/\mu_{\text{f,min}}) + g_3(\sigma_{\text{f}}/\sigma_{\text{f,min}})$. g_1, g_2, g_3 are the constant parameters where the summation of the terms is equal to 1. In this case, the contribution of structural weight, mean and standard deviation of the flutter speed distribution are included in determining the best design. Based on the $|\Sigma - 1|$ values given in Table 7.5, the best RDO design corresponds to RUN 8 which features lower structural weight and mean flutter speed, and smaller standard deviation in comparison to the overall best RBDO solution.

Table 7.5: RDO solutions obtained using different weighting factors for weight, flutter speed mean and standard deviation.

Run	Weightings			Responses			
ID	w_{W}	w_μ	w_σ	$\frac{W}{W_{\text{Benchmark}}}$	$\frac{\mu_{\text{f}}}{V_{\text{f,Design}}}$	σ_{f}	$\lvert\Sigma - 1\rvert$
1	1.000	0.000	0.000	0.669	1.010	2.694	0.116
2	0.000	1.000	0.000	0.669	1.009	2.668	0.111
3	0.000	0.000	1.000	0.782	1.065	2.077	0.094
4	0.750	0.125	0.125	0.666	1.004	2.564	0.091
5	0.125	0.750	0.125	0.669	1.009	2.598	0.100
6	0.125	0.125	0.750	0.802	1.061	2.088	0.105
7	0.500	0.250	0.250	0.739	1.047	2.564	0.143
8	0.250	0.500	0.250	0.639	1.004	2.352	0.043
9	0.250	0.250	0.500	0.800	1.051	2.570	0.178
10	0.340	0.330	0.330	0.669	1.009	2.632	0.105

Having used $V_{\text{f,Design}}$ as an optimisation target, mean flutter speeds cluster uniformly around it as shown in Figure 7.7. Conversely, all but one RDO solutions have similar or greater weight in comparison to the best deterministic optimum, thus suggesting that an increase in design robustness is likely to be achieved at the expense of weight. Interestingly, some RDO solutions are also sufficiently reliable but these are substantially heavier than their RBDO counterparts.

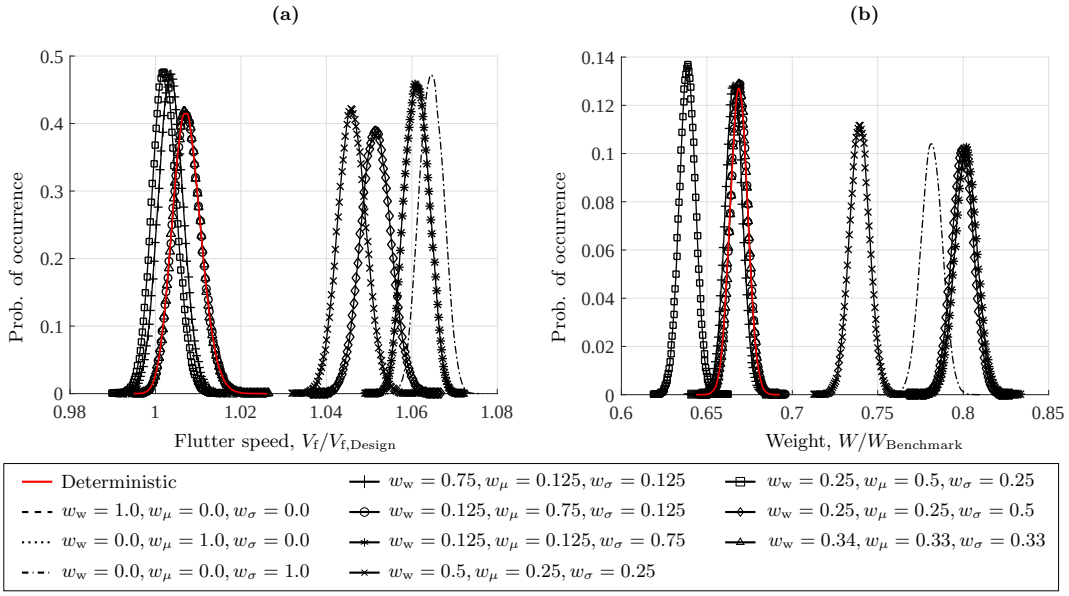

Figure 7.7: PDF plots of RDO solutions: (a) Flutter speed and (b) Structural weight.

7.5.4 Second level: Robust and Reliability-based Design Optimisation (RRBDO)

The RBDO and RDO results in Section 7.5.2 and 7.5.3 show the following trends: 1) As expected, RBDO solutions tend to be more reliable and less robust than RDO ones, and vice versa; 2) Mean flutter speeds are close to but consistently above the design allowable. With RBDO, these values are also consistently above the mean flutter speed of the overall best deterministic design (DET1). While, with RDO, they are uniformly distributed around it; 3) Reliability or robustness are generally achieved at the expenses of weight, the latter imposing greater penalties. An RRBDO approach is thought to be able to provide a better compromise between weight and design robustness and reliability.

The results in terms of structural weight, mean flutter speed, standard deviation and probability of failure at the target design flutter speed are presented in Table 7.6. Notably, most flutter speed PDFs cluster closely, with mean values approximatively 1% above the allowable. Similarly, all runs result in probabilities of failure below P_{allow}. The lowest value is 2.344×10^{-4} which is a 97.2% improvement in comparison to the deterministic design. In terms of robustness, RRBDO results, although generally worse, are comparable with RDO solutions ($\sigma_{\text{f,rdo}} \in [2.077, 2.694]$ vs $\sigma_{\text{f,rrbdo}} \in [2.555, 2.788]$). A slight increase in minimum structural weight is observed for RRBDO designs in comparison

to both RDO and RBDO ones ($W^{\min}_{\text{rbdo}}/W_{\text{Benchmark}} = 0.658$, $W^{\min}_{\text{rdo}}/W_{\text{Benchmark}} = 0.639$, $W^{\min}_{\text{rrbdo}}/W_{\text{Benchmark}} = 0.669$).

Table 7.6: RRBDO solutions for different weighting values for weight, flutter speed mean and standard deviation, and probability of failure.

Run	Weighting coefficients				Responses				
ID	w_{W}	w_μ	w_σ	$w_{P_{\text{f}}}$	$\frac{W}{W_{\text{Benchmark}}}$	$\frac{\mu_{\text{f}}}{V_{\text{f,Design}}}$	σ_{f}	P_{f}	$\lvert\Sigma - 1\rvert$
1	1.000	0.000	0.000	0.000	0.669	1.011	2.788	8.359×10^{-3}	8.704
2	0.000	1.000	0.000	0.000	0.669	1.010	2.683	7.989×10^{-3}	8.298
3	0.000	0.000	1.000	0.000	0.679	1.015	2.727	2.344×10^{-4}	0.022
4	0.000	0.000	0.000	1.000	0.669	1.010	2.561	8.126×10^{-3}	8.432
5	0.250	0.250	0.250	0.250	0.669	1.010	2.663	8.214×10^{-3}	8.536
6	0.500	0.250	0.125	0.125	0.669	1.010	2.688	8.264×10^{-3}	8.592
7	0.250	0.500	0.125	0.125	0.679	1.014	2.555	2.446×10^{-4}	0.016
8	0.250	0.125	0.125	0.500	0.669	1.010	2.741	8.011×10^{-3}	8.327
9	0.125	0.250	0.500	0.125	0.669	1.010	2.633	7.923×10^{-3}	8.223
10	0.100	0.300	0.300	0.300	0.669	1.009	2.584	7.720×10^{-3}	8.001

The increase in structural weight is thought to be due to the increase in mean flutter speed and the decrease in its standard deviation. These variations are necessary to shift flutter PDFs to the right and to shrink them, which enhances design reliability and robustness as shown in Figure 7.8. RRBDO results further support the finding that a weight penalty is necessary to impart some level of robustness and reliability to the design. The overall best RRBDO solutions is deduced by finding the minimum value of expression, $|\Sigma - 1|$, where $\Sigma = h_1(W/W_{\min}) + h_2(\mu_{\text{f}}/\mu_{\text{f,min}}) + h_3(\sigma_{\text{f}}/\sigma_{\text{f,min}}) + h_4(P_{\text{f}}/P_{\text{f,min}})$. The constant parameters, h_1, h_2, h_3 and h_4 are set to 0.25. The $|\Sigma - 1|$ values for each trialled designs are given in Table 7.6. The best RRBDO design corresponds to RUN 7 with $W^{\text{best}}_{\text{rrbdo}}/W_{\text{Benchmark}} = 0.679$) and $|\Sigma - 1| = 0.016$.

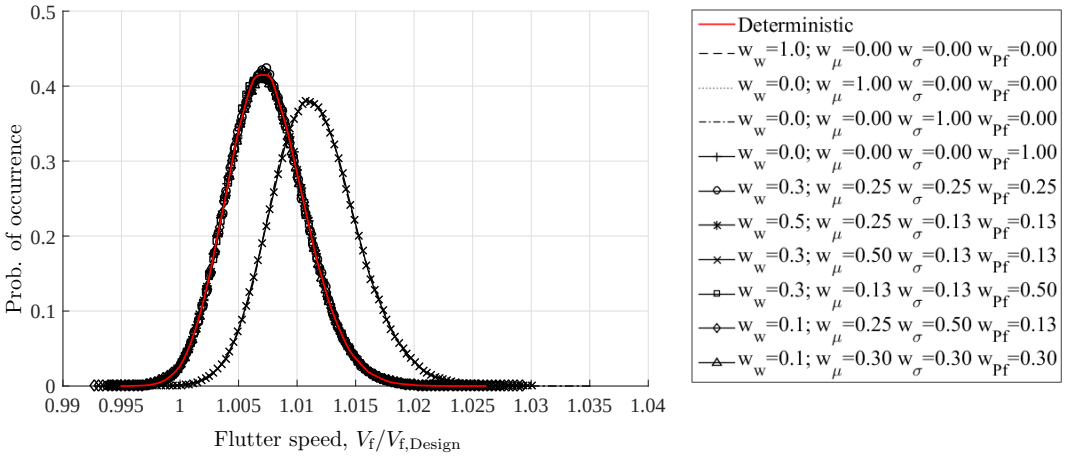

Figure 7.8: PDF plots of RRBDO solutions.

Tables 7.7 and 7.8 provide the stiffnesses terms calculated from the lamination properties of the deterministic, RBDO, RDO and RRBDO best optimised design. Both RBDO and RDO designs show a reduction in terms of the bending stiffness values (D_{16} and D_{26}) due to smaller thickness value in comparison with the deterministic design. The observation suggests that by incorporating some level of robustness and reliability in the design, allow for more substantial bending and torsion motion due to lower bending stiffness. The lower bending stiffness values result in lower mean flutter speed which is evidenced in Table 7.4 and 7.5. The RRBDO design shows higher bending stiffness value closer to the deterministic design, which translates into higher mean flutter speed value (i.e. more reliable). For the in-plane stiffnesses components (A_{16} and A_{26}), the stiffness values for RBDO, RDO and RRBDO designs show insignificant changes compared to the deterministic design. Overall, the results suggest that the robustness and reliability of the composite wing design are driven by the bending stiffness of the laminated panels.

Table 7.7: The extension-shear coupling terms (A_{16} and A_{26}) and bending-twisting coupling terms (D_{16} and D_{26}) of the top skin panels deduced from the best deterministic and RBDO optimised design.

	Deterministic design				RBDO design			
	A_{16} (10^7 N/m)	A_{26} (10^7 N/m)	D_{16} (N.m)	D_{26} (N.m)	A_{16} (10^7 N/m)	A_{26} (10^7 N/m)	D_{16} (N.m)	D_{26} (N.m)
Panel 1	-2.54	-6.08	-178.18	-198.12	1.83	0.75	102.09	102.85
Panel 2	-12.10	-3.74	63.01	99.00	1.72	4.31	93.74	82.89
Panel 3	-10.60	-4.39	-165.26	-124.19	-2.41	0.72	-81.26	-45.31
Panel 4	6.21	5.95	-165.68	-51.03	7.25	4.91	-136.98	-49.09
Panel 5	-2.28	-4.59	-71.80	-161.80	-6.40	-4.24	-25.66	-72.99
Panel 6	0.85	2.84	29.38	38.10	3.77	5.96	3.39	29.60
Panel 7	5.52	4.61	-103.77	-37.60	3.21	5.06	-56.78	-32.85
Panel 8	1.77	6.62	55.82	53.29	-2.56	-3.92	34.13	-7.99
Panel 9	1.37	9.69	-67.06	115.00	-6.58	1.41	-79.43	-67.36
Panel 10	-8.78	-3.01	-143.87	-199.99	0.60	2.26	-59.74	-72.84
Panel 11	1.65	1.13	30.72	-29.56	-1.42	-7.45	-7.43	-60.02

7.6 Case study on different coefficient of variation.

In this section, the RBDO, RDO and RRBDO designs are presented when evaluated at different coefficient of variation values for random parameters, E_{11} and G_{12}. The robustness and reliability of the designs are measured in terms of flutter speed variation, while other design constraints (root bending moment, buckling and strain) are quantified to satisfy the overall design requirements. Three design cases are considered; 1) CV=0.05

Table 7.8: The extension-shear coupling terms (A_{16} and A_{26}) and bending-twisting coupling terms (D_{16} and D_{26}) of the top skin panels deduced from the best RDO and RRBDO optimised design.

	RDO design				RRBDO design			
	A_{16} (10^7 N/m)	A_{26} (10^7 N/m)	D_{16} (N.m)	D_{26} (N.m)	A_{16} (10^7 N/m)	A_{26} (10^7 N/m)	D_{16} (N.m)	D_{26} (N.m)
Panel 1	-2.09	-5.31	-80.28	-134.71	0.23	-3.53	-271.27	-131.62
Panel 2	-9.71	-2.88	54.19	37.90	-13.00	-4.37	180.78	164.00
Panel 3	-9.05	-3.44	37.19	93.73	-8.28	-6.82	-161.42	-136.61
Panel 4	5.06	4.56	-70.71	-13.82	4.56	8.10	-196.54	-66.96
Panel 5	-2.23	-1.71	-9.21	-54.72	-7.64	-8.19	-89.38	-186.73
Panel 6	-2.08	1.25	13.48	20.34	2.59	9.06	-125.87	-35.70
Panel 7	1.97	5.63	-43.81	-15.82	7.82	2.82	-120.23	-43.42
Panel 8	-0.17	3.50	23.01	24.70	-0.37	4.99	40.96	51.76
Panel 9	-3.61	3.22	12.06	112.82	-3.23	5.39	22.38	224.65
Panel 10	-8.76	-3.34	-101.37	-113.05	-7.24	-3.26	-267.60	-163.37
Panel 11	3.05	-0.11	-8.71	-66.63	-5.34	-11.80	81.59	-15.46

for E_{11} and G_{12}, 2) CV=0.1 for E_{11} and G_{12} and 3) CV=0.25 for E_{11} and G_{12}. Note that the CV value for t_{ply} is kept constant at 0.01.

The wing's responses obtained for each design case are given in Table 7.9. Note that the probability of failure for flutter responses are evaluated at target design value of $V_{\text{f}}/V_{\text{f,Design}} = 1$. For Design Case 1, RRBDO design has a similar structural weight as the deterministic design of $W/W_{\text{Benchmark}} = 0.669$. However, the flutter response shows mean flutter speed closed to the deterministic mean value ($\mu_f^{\text{RRBDO}} = 1.010$; $\mu_f^{\text{Deterministic}} = 1.011$) and has lower standard deviation ($\sigma_f^{\text{RRBDO}} = 2.705$; $\sigma_f^{\text{Deterministic}} = 2.816$) which indicate an improvement in robustness of the design. In terms of design reliability, the RRBDO design in Case 1 shows slight improvement in reliability in comparison to the deterministic design ($P_{\text{f}}^{\text{Deterministic}} = 8.7 \times 10^{-3}$; $P_{\text{f}}^{\text{RRBDO}} = 8.547 \times 10^{-3}$). Meanwhile, the RBDO design shows 98.54% reliability improvement in comparison with the deterministic design.

On the other hand, the P_{f} value of RDO design increases as the flutter response distributed at lower mean values. The high probability of failure for RDO design suggests that it is not sufficient to prevent flutter failure although the design produces lower structural weight and lower response variance. The structural weight for RDO designs is heavier compared to the RRBDO and deterministic design due to the stiffer structure, which is evidenced by higher mean flutter speed values.

For Design Cases 2 and 3, the structural weight of all designs is higher in comparison to the deterministic solution resulting from improved design robustness and reliability.

Table 7.9: Design optimum with different CV values of random parameters E_{11} and G_{12}. For each design case, the optimised designs are obtained using deterministic, RBDO, RDO and RRBDO approaches.

Design Case 1				
CV for $E_{11} = 0.05$; CV for $G_{12} = 0.05$; CV for $t_{\text{ply}} = 0.01$				
	Deterministic	RBDO	RDO	RRBDO
Weight, $\frac{W}{W_{\text{Benchmark}}}$	0.669	0.739	0.659	0.669
Flutter speed, $\frac{V_{\text{f}}}{V_{\text{f,Design}}}$				
Mean, $\mu_{\text{f}}/V_{\text{f,Design}}$	1.011	1.027	1.005	1.010
Std. deviation, σ_{f}	2.816	7.241	2.501	2.705
Prob. of failure, P_{f}	8.700×10^{-3}	1.267×10^{-4}	1.293×10^{-1}	8.547×10^{-3}
Root Bending Moment, $\frac{RBM}{RBM_{\text{Benchmark}}}$	0.004	0.003	0.004	0.014
Critical buckling factor, λ	1.006	1.440	1.054	1.015
Strain Failure Index, FI	0.823	0.974	0.760	0.843
Design Case 2				
CV for $E_{11} = 0.1$; CV for $G_{12} = 0.1$; CV for $t_{\text{ply}} = 0.01$				
	Deterministic	RBDO	RDO	RRBDO
Weight, $\frac{W}{W_{\text{Benchmark}}}$	0.669	0.682	0.739	0.679
Flutter speed, $\frac{V_{\text{f}}}{V_{\text{f,Design}}}$				
Mean, $\mu_{\text{f}}/V_{\text{f,Design}}$	1.010	1.023	1.047	1.014
Std. deviation, σ_{f}	2.766	3.974	2.164	2.255
Prob. of failure, P_{f}	8.500×10^{-3}	2.448×10^{-7}	0.00	2.446×10^{-4}
Root Bending Moment, $\frac{RBM}{RBM_{\text{Benchmark}}}$	0.004	0.505	0.227	0.077
Critical buckling factor, λ	1.006	1.436	1.109	1.033
Strain Failure Index, FI	0.823	0.683	0.792	0.844
Design Case 3				
CV for $E_{11} = 0.25$; CV for $G_{12} = 0.25$; CV for $t_{\text{ply}} = 0.01$				
	Deterministic	RBDO	RDO	RRBDO
Weight, $\frac{W}{W_{\text{Benchmark}}}$	0.669	0.689	0.732	0.679
Flutter speed, $\frac{V_{\text{f}}}{V_{\text{f,Design}}}$				
Mean, $\mu_{\text{f}}/V_{\text{f,Design}}$	1.011	1.022	1.056	1.015
Std. deviation, σ_{f}	2.771	3.8566	2.0171	2.343
Prob. of failure, P_{f}	7.400×10^{-3}	2.636×10^{-7}	0.00	3.00×10^{-4}
Root Bending Moment, $\frac{RBM}{RBM_{\text{Benchmark}}}$	0.004	0.1868	0.5174	0.039
Critical buckling factor, λ	1.006	1.163	1.392	1.033
Strain Failure Index, FI	0.823	0.661	0.5615	0.860

A 1.49% increase in structural weight is evidenced from RRBDO design for both design case. The highest structural weight is evaluated from RDO designs at a higher mean flutter speed values. The probability of failure of RRBDO designs in both design cases significantly reduced which suggest improvement in the design reliability. The sensitivity to random parameters of RRBDO design is also reduced which evidenced from lower response variances concerning deterministic design. The sensitivity of random parameters dispersion on the output responses are minimal which can be seen from small discrepancy in structural weight and flutter speed properties.

The improvement in terms of design's reliability and robustness can be clearly seen from Figure 7.9. From the figure, the RBDO designs show significant reliability improvement in comparison with other design solutions as the PDF curves of the flutter response are shifted to the right of deterministic PDF. The reliability is deduced at target design value of $V_{\mathrm{f}}/V_{\mathrm{f,Design}} = 1$. The PDF of RRBDO designs are plotted in between RBDO and RDO which suggest an improvement in both design robustness and reliability.

In general, although there is an increase in structural weight for RRBDO designs, the gains in terms of improved design's reliability and robustness are thought to be more crucial for composite structural design. In reality, uncertainties are exists and the capability to include uncertainty quantification in design process is thought to be beneficial to obtain a more realistic design for composite aircraft wings.

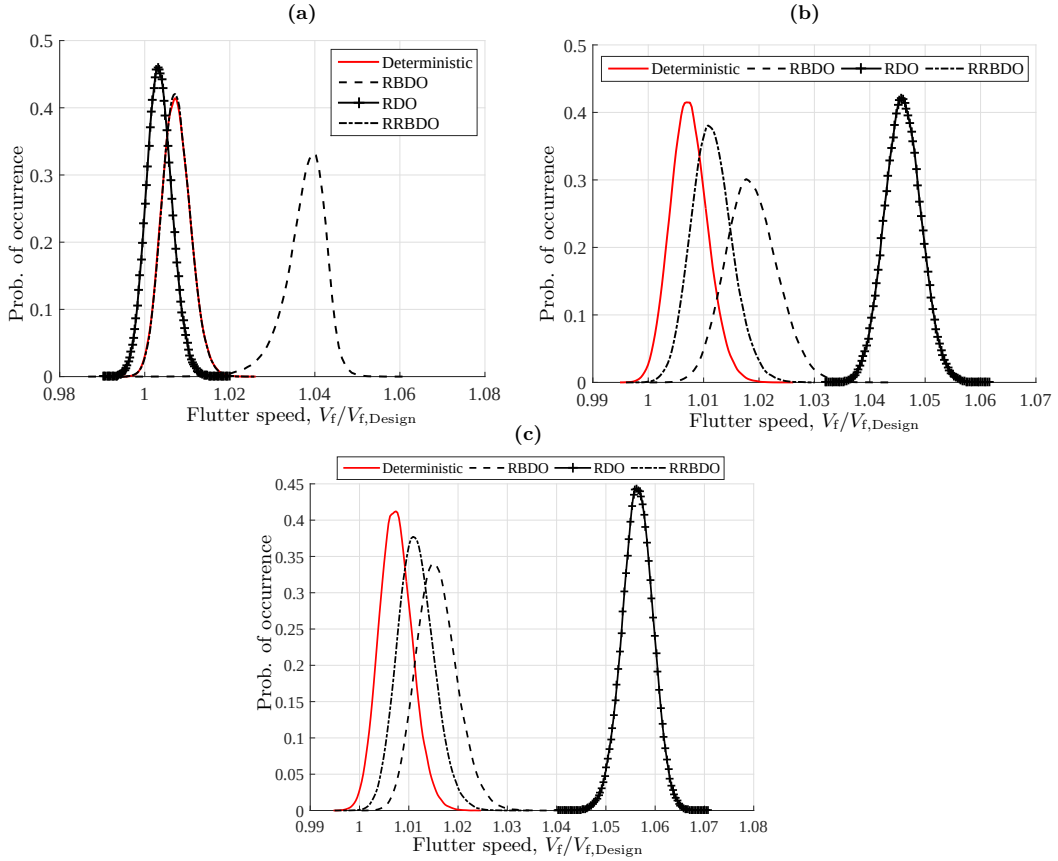

Figure 7.9: PDF plots of optimised design obtained from deterministic, RBDO, RDO and RRBDO for (a) Design Case 1 (b) Design Case 2 (c) Design Case 3.

7.7 Summary

A multi-level optimisation approach for the robust and/or reliability-based aeroelastic tailoring of a wing box structure is presented. The optimisation objective is to minimise weight subject to multiple constraints, including strength, buckling and flutter margin. The procedure accounts for stochastic variations in input material design parameters. Based on grounds of computational cost, surrogate modelling with Polynomial Chaos Expansion (PCE) is preferred to Monte Carlo Simulation (MCS) for the quantification of the effect of uncertainties on structural weight and flutter speed. The results presented in this chapter support the following conclusions:

1. PCE is capable of quantifying the effects of uncertainties with sufficient accuracy and fewer model runs in comparison to MCS, thus enabling probabilistic design optimisation of a full Finite Element wing box model.

2. Reliability-based design optimisation (RBDO) shows that reducing the model's probability of failure entails a weight penalty and a loss of design robustness.

3. Optimising for robustness successfully reduces the design sensitivity to stochastic variations at the cost of additional weight. Robust designs can also be sufficiently reliable, but generally at a greater weight penalty in comparison to designs optimised for reliability only.

4. In general, the model can be optimised for minimal weight and a desired level of reliability or robustness or both. However, enhanced reliability and robustness result in a weight penalty in comparison to the deterministic optimum design.

5. Simultaneous robust and reliability-based design optimisation successfully provides the best compromise between weight, reliability and robustness.

6. In comparison to the benchmark wing, the framework produces an overall weight reduction of 32.1%, with a 1.5% increase from the first to the second level optimisation to account for stochastic design variations.

Results follow the same pattern when the framework is trialled on other design problems with different values of coefficient of variation.

Chapter 8

Conclusions and future work

Conclusions

The use of composite materials in many aircraft structures are driven by the attractive strength-to-weight ratio of composite materials and their anisotropic properties. Consequently, an aeroelastically-tailored aircraft structure is made possible that offer an improved design with minimum structural weight and optimum aeroelastic performances. This goal can be achieved through material tailoring (altering the composite panel ply configuration) to promote bending-torsional couplings in the structures.

For aircraft wing structures, a deterministic approach is used to determine an optimised design for aeroelastic tailoring. However, the deterministic approach does not account the probabilistic uncertainties in the design which lead to unreliable or unrealistic designs. An improved aeroelastic tailoring approach is introduced in this thesis in which uncertainty quantification is included as a measure for design robustness and reliability.

A novel multi-level aeroelastic tailoring framework for a '*robust*' and '*reliable*' design of the composite aircraft wing is successfully introduced in the current work. The framework employs two optimisation levels that consist of deterministic and probabilistic design optimisation approaches. The framework is capable of producing an optimised composite wing design for minimum structural weight while satisfying multiple design constraints that included structural, aeroelastic and parametric variation. The optimised model obtained from the framework shows the best compromise between structural weight, design robustness and reliability.

The work presented in this thesis employs an idealised *'box-like'* wing model as a benchmark wing (EBW). The model is capable of producing a realistic approximation of the wing's performance with a reasonable computational cost. The initial analyses suggest

that there is a potential for design improvement and weight-saving via aeroelastic tailoring due to ample safety margin measured from its performance and design requirement for certification.

An improved method for aeroelastic tailoring of the composite wings is successfully introduced for design problems with multiple design constraints and different static manoeuvre load conditions. The aeroelastic tailoring performed on the EBW model produced a significant structural weight saving with all the design constraints satisfied. The EBW model is optimised subjected to multiple static manoeuvre load cases with multiple constraints that included strength and aeroelastic responses. The introduction of a weighted cost function in the objective function of the optimisation algorithm enables the contribution of each design constraints on the optimised solution to be quantified adequately.

Two optimisation approaches are applied to solve for an aeroelastic tailoring procedure with multiple design constraints. The Single-point optimisation is used for design problems subjected to single static manoeuvre load case. Similarly, the Multi-point optimisation method is applicable for design problems subjected to multiple static manoeuvre load cases. The optimised solution obtained from the Multi-point method is more realistic as multiple critical load cases are considered in the optimisation. However, the multi-point method requires a longer time to solve as opposed to the Single-point method. Hence, single-point method is preferable, provided that the pre-established critical load case is available.

The existence of aleatory uncertainty in the model results in significant output response variation and may lead to catastrophic failure if not quantified directly in the design process. The deterministic optimised design can be overly estimated or underestimate due to lack of uncertainty consideration. The PCE and RS-HDMR method introduced in the current work are capable of quantifying the uncertainty effects on the wing's performances in effective manner. The efficiency of both methods is evidenced by the case studies performed with uncertain material properties and ply thickness. Both PCE and RS-HDMR methods are capable of performing rapid quantification of uncertainty effects on the wing's responses compared to conventional MCS method. However, the capability of the PCE is limited to the dimensional order of random parameters. As the dimensional order increases, the number of runs requires in PCE increase significantly. On the other hand, RS-HDMR is not dependent on the dimensional order of random

parameters, and hence it can be applied to stochastic problems with higher dimensional order.

Two theoretical probabilistic optimisation approaches namely, Reliability-based Design optimisation (RBDO) and Robust Design Optimisation (RDO) method are used to obtain an optimised design with improved design reliability/robustness subjected to multiple constraints with uncertain in material properties and ply thickness. The methods coupled with the efficiency of PCE, are capable of producing a reliable/robust design for flutter and wing root bending moment responses. However, the enhanced reliability and robustness in the model result in a weight penalty in comparison to the deterministic design. Robust designs can also be sufficiently reliable, but generally at a more significant weight penalty in comparison to the designs optimised for reliability only.

A new probabilistic approach; Robust and Reliability-based design optimisation (RRBDO) is successfully introduced to obtain an optimised design with both improved design reliability and robustness. The design robustness is incorporated in the design by obtaining the target performance around a mean value and maximising the robustness by minimising the response variance. The reliability is improved by minimising the probability of failure at target design value. The improved design robustness and reliability are obtained with the expenses of higher structural weight in comparison with deterministic designs.

Future work

The scope of work performed in this thesis is limited to aleatory uncertainty and focused on the effect of variation in material properties. The effect of uncertain in E_{11}, E_{22}, G_{12} and t_{ply} on the wing's responses are covered in the current work. The effect of epistemic uncertainty or the combination of them on the wing's response needs to be explored using other quantification methods such as possibility theory or interval analysis.

Uncertainty in the structural geometry (i.e. spars and ribs geometry) may be incorporated in the analysis to explore their effect on the wing's responses. The aerolastically-tailored structure can also be achieved by structural tailoring which has been studied by Refs. [15, 115, 116]. The study of uncertainty in structural geometry can be done to predict the variation in wing performance.

The use of High Dimensional Model Representation (HDMR) in probabilistic optimisation procedure needs to be explored. It is known that HDMR can be utilised for uncertainty quantification involving high dimensional order of random parameters efficiently. In current work, the study only considered up to four random parameters; hence, PCE is used for the analysis. The use of HDMR may overcome the issues with PCE related to modelling efficiency when involving high dimensional order of random parameters.

In probabilistic optimisation (Multi-level aeroelastic framework), the possibility of using discrete design variables in terms of ply angle needs to be explored to obtain a feasible stacking sequence. The method of retrieving the ply configuration, such as blending method can be incorporated in the framework, together with the manufacturing feasibility constraints. These will eliminate the needs for another optimisation step in order to obtain the ply configuration as in the current method.

The uncertainty quantification methods presented in this thesis, such as PCE can be used to predict failure of the aircraft structures due to cyclic loading such as creep or fatigue in efficient manners. The defects on the composite panel can be modelled using the variation in material properties.

References

[1] J. R. Wright and J. E. Cooper. *Introduction to Aircraft Aeroelasticity and Loads.* John Wiley & Sons, 2007.

[2] M. H. Shirk, T. J. Hertz, and T. A. Weisshaar. *Aeroelastic tailoring — Theory, practice, and promise.* Journal of Aircraft, Jan 1986. 23(1): p. 6–18.

[3] F.E. Eastep, V. A. Tischler, V. B. Venkayya, and N. S. Khot. *Aeroelastic Tailoring of Composite Structures.* Journal of Aircraft, 1999. 36(6): p. 1041–1047.

[4] T.A. Weisshaar, C. Nam, and A. B. Rodriguez. *Aeroelastic tailoring for improved UAV performance.* In 39th AIAA/ASME/ASCE/AHS/ASC Structures, Structural Dynamics, and Materials Conference and Exhibit, Reston, Virigina, Apr 1998. American Institute of Aeronautics and Astronautics.

[5] G.A.A. Thuwis, R.D. Breuker, M. M. Abdalla, and Z. Gürdal. *Aeroelastic tailoring using lamination parameters :Drag reduction of a Formula One rear wing.* Structural and Multidisciplinary Optimization, 2010. 41(4): p. 637 –646.

[6] W. E. Triplett. *Aerolastic Tailoring Studies in Fighter Aircraft Design.* Journal of Aircraft, 1979. 17(7): p. 508–513.

[7] J. K. S. Dillinger, T. Klimmek, M. M. Abdalla, and Z. Gürdal. *Stiffness Optimization of Composite Wings with Aeroelastic Constraints.* Journal of Aircraft, 2013. 50(4): p. 1159–1168.

[8] J. K. S. Dillinger, M. M. Abdalla, T. Klimmek and Z. Gürdal. *Static Aeroelastic Stiffness Optimization and Investigation of Forward Swept Composite Wings.* 10th World Congress on Structural and Multidisciplinary Optimization, 2013: p. 1-10.

[9] C. Cesnik, D. Hodges, and M. Patil. *Aeroelastic analysis of composite wings.* 37th Structure, Structural Dynamics and Materials Conference, 1996: p. 1–11.

[10] M. Y. Harmin and J. E. Cooper. *Aeroelastic Tailoring Using Ant Colony Optimization.* 50th AIAA/ASME/ASCE/AHS/ASC Structures, Structural Dynamics and Materials Conference, 4-7 May 2009: p. 1–17.

[11] O. Stodieck, J. E. Cooper, P. M. Weaver, and P. Kealy. *Improved aeroelastic tailoring using tow-steered composites.* Composite Structures, Dec 2013. 106: p. 703–715.

[12] M. K. Abbas, H. M. Negm, and M. A. Elshafei. *Flutter and Divergence Characteristics of Composite Plate Wing.* International Journal of Engineering and Innovative Technology (IJEIT), 2014. 4(2): p. 105–115.

[13] J. A. Green. *Aeroelastic tailoring of aft-swept high-aspect-ratio composite wings.* {Journal of Aircraft}, 1987. 24(11): p. 812–819.

[14] S. Guo, D. Li, and Y. Liu. *Multi-objective optimization of a composite wing subject to strength and aeroelastic constraints.* Proceedings of the Institution of Mechanical Engineers, Part G: Journal of Aerospace Engineering, Oct 2011. 226(9): p. 1095–1106.

[15] G. Vio, G. Georgiou, and J.E. Cooper. *Design of Composite Structures to Improve the Aeroelastic Performance.* In *53rd AIAA/ASME/ASCE/AHS/ASC Structures, Structural Dynamics and Materials Conference
20th AIAA/ASME/AHS Adaptive Structures Conference
14th AIAA*, Reston, Virigina, Apr 2012. American Institute of Aeronautics and Astronautics.

[16] G. Georgiou, A. Manan, and J.E. Cooper. *Modeling composite wing aeroelastic behavior with uncertain damage severity and material properties.* Mechanical Systems and Signal Processing, Oct 2012. 32: p. 32–43.

[17] S. Sriramula and M. K. Chryssanthopoulos. *Quantification of uncertainty modelling in stochastic analysis of FRP composites.* Composites Part A: Applied Science and Manufacturing, 2009. 40(11): p. 1673–1684.

[18] C. L. Pettit. *Uncertainty Quantification in Aeroelasticity: Recent Results and Research Challenges.* Journal of Aircraft, 2004. 41(5): p. 1217–1229.

[19] M. Allen and K. Maute. *Reliability-based design optimization of aeroelastic structures.* Structural and Multidisciplinary Optimization, June 2004. 27(4): p. 228–242.

[20] K. V. N. Gopal. *Product design for advanced composite materials in aerospace engineering.* In Sohel Rana and Raul Fangueiro, editors, Advanced Composite Materials for Aerospace Engineering, 2016, Woodhead Publishing: p. 413–428.

[21] C. Scarth, J. E. Cooper, P. M. Weaver and G. H.C. Silva. *Uncertainty quantification of aeroelastic stability of composite plate wings using lamination parameters.* Composite Structures, Sept 2014. 116: p. 84–93.

[22] A. Manan and J.E. Cooper. *Uncertainty of Composite Wing Aeroelastic Behaviour.* 12th AIAA/ISSMO Multidisciplinary Analysis and Optimization Conference, 2008.

[23] T.-U. Kim and I. H. Hwang. *Optimal design of composite wing subjected to gust loads.* Computers & Structures, July 2005. 83(19-20): p. 1546–1554.

[24] T. Ali, Member, ASCE, and E. P. Wiser. *Monte Carlo Technique with Correlated Random Variables.* Journal of Construction Engineering and Management, 1992. 118(2): p. 258–272.

[25] C. Scarth, P.N. Sartor, and J.E. Cooper. *Robust Aeroelastic Design of Composite Plate Wings.* 17th AIAA Non-Deterministic Approaches Conference, 2015. (January): p. 1–13.

[26] A. Manan. *Uncertainty and Robust Design in Aeroelastic Tailoring.* PhD thesis, University of Liverpool, 2009.

[27] T. Ziehn and A.S. Tomlin. *GUI–HDMR – A software tool for global sensitivity analysis of complex models.* Environmental Modelling & Software, 2009. 24(7): p. 775–785.

[28] A. Manan and J.E. Cooper. *Design of Composite Wings Including Uncertainties: A Probabilistic Approach.* Journal of Aircraft, 2009. 46(2): p. 601–607.

[29] R. M. Paiva, C. Crawford, and A. Suleman. *Robust and Reliability-Based Design Optimization Framework for Wing Design.* AIAA Journal, Jan 2014. 52(4): p. 711–724.

[30] M. Nikbay and M. N. Kuru. *Reliability Based Multidisciplinary Optimization of Aeroelastic Systems with Structural and Aerodynamic Uncertainties.* Journal of Aircraft, Apr 2013. 50(3): p. 708–715.

[31] Y. Liang, X.Q. Cheng, Z.N. Li, and J.W. Xiang. *Robust Multi-Objective Wing Design Optimization Via CFD Approximation Model.* Engineering Applications of Computational Fluid Mechanics, 2011. 5(2): p. 286–300.

[32] A. A. B. Baker and D. W. Kelly. *Composite Materials for Aircraft Structures.* AIAA education series. American Institute of Aeronautics & Astronautics, 2004.

[33] H. T. Hahn and S. W. Tsai. *Introduction to Composite Materials.* Taylor & Francis, 1980.

[34] L. P. Kollár and G. S. Springer. *Mechanics of Composite Structures.* Cambridge University Press, 2009.

[35] H. Ghiasi, D. Pasini, and L. Lessard. *Optimum stacking sequence design of composite materials Part I: Constant stiffness design.* Composite Structures, 2009. 90(1): p. 1–11.

[36] M. Miki and Y. Sugiyamat. *Optimum Design of Laminated Composite Plates Using Lamination Parameters.* AIAA, May 1993. 31(5): p. 921–922.

[37] M.W. Bloomfield, C.G. Diaconu, and P.M. Weaver. *On feasible regions of lamination parameters for lay-up optimization of laminated composites.* Proceedings of the Royal Society A: Mathematical, Physical and Engineering Sciences, 2009. 465(2104): p. 1123–1143.

[38] D. Peeters and M. Abdallah. *Optimization of Ply Drop Locations in Variable-Stiffness Composites.* AIAA Journal, 2016. 54(5): p. 1760–1768. (January):1–13, 2015.

[39] F. Aymerich and M. Serra. *Optimization of laminate stacking sequence for maximum buckling load using the ant colony optimization (ACO) metaheuristic.* Composites Part A: Applied Science and Manufacturing, Feb 2008. 39(2): p. 262–272.

[40] Z. Jing, Q. Sun, and V. V. Silberschmidt. *A framework for design and optimization of tapered composite structures. Part I: From individual panel to global blending structure.* Composite Structures, 2016. 154: p. 106–128.

[41] K. D. Potter, M. Campbell, C. Langer, and M. R. Wisnom. *The generation of geometrical deformations due to tool/part interaction in the manufacture of composite components.* Composites Part A: Applied Science and Manufacturing, 2005. 36(2 SPEC. ISS.): p. 301-308.

[42] K. Potter, C. Langer, B. Hodgkiss, and S. Lamb. *Sources of variability in uncured aerospace grade unidirectional carbon fibre epoxy preimpregnate.* Composites Part A: Applied Science and Manufacturing, 2007. 38(3): p. 905–916.

[43] K. Potter, B. Khan, M. Wisnom, T. Bell, and J. Stevens. *Variability, fibre waviness and misalignment in the determination of the properties of composite materials and structures.* Composites Part A: Applied Science and Manufacturing, 2008. 39(9): p. 1343-1354.

[44] D. J. Lekou and T. P. Philippidis. *Mechanical property variability in FRP laminates and its effect on failure prediction.* Composites Part B: Engineering, 2008. 39(7-8): p. 1247–1256.

[45] B. Liu and R. Haftka. *Composite wing structural design optimization with continuity constraints.* 19th AIAA Applied Aerodynamics Conference, 2001.

[46] S. Guo, W. Cheng, and D. Cui. *Aeroelastic Tailoring of Composite Wing Structures by Laminate Layup Optimization.* AIAA Journal, 2006. 44(12): p. 3146–3150.

[47] T.U. Kim, J. W. Shin, and I. H. Hwang. *Stacking sequence design of a composite wing under a random gust using a genetic algorithm.* Computers & Structures, May 2007. 85(10): p. 579–585.

[48] R.L. Riche and R. T. Haftka. *Optimization of laminated stacking sequence for buckling load maximization by genetic algorithm. Aiaa*, 1992. 31(5): p. 951–956.

[49] M. Walker and R. E. Smith. *A technique for the multiobjective optimisation of laminated composite structures using genetic algorithms and finite element analysis.* Composite Structures, 2003. 62(1): p. 123–128.

[50] V. V. Toropov, R. Jones, T. Willment and M. Funnell. *Weight and manufacturability optimization of composite aircraft components based on a genetic algorithm.* 6th World Congresses of Structural and Multidisciplinary Optimisation. June 2005.

[51] J. E. Herencia, P. M. Weaver, and M. I. Friswell. *Morphing Wing Design via Aeroelastic Tailoring.* 48th AIAA/ASME/ASCE/AHS/ASC Structures, Structural Dynamics & Materials Conference, 2007. (April): p. 1–19.

[52] R. Hassan, B. Cohanim, O. D. Weck, and G. Venter. *A Comparison of Particle Swarm Optimization and the Genetic Algorithm.* 46th AIAA/ASME/ASCE/AHS/ASC Structures, Structural Dynamics and Materials Conference, 2005. (April): p. 1–13.

[53] N. Chang, W. Wang, W. Yang, and J. Wang. *Ply stacking sequence optimization of composite laminate by permutation discrete particle swarm optimization.* Structural and Multidisciplinary Optimization, 2010. 41(2): p. 179–187.

[54] T.A. Sebaey, C.S. Lopes, N. Blanco, and J. Costa. *Ant Colony Optimization for dispersed laminated composite panels under biaxial loading.* Composite Structures, Dec 2011. 94(1): p. 31–36.

[55] W. Wang, S. Guo, N. Chang, and W. Yang. *Optimum buckling design of composite stiffened panels using ant colony algorithm.* Composite Structures, Feb 2010. 92(3): p. 712–719.

[56] S. Baluja. Population-Bases Incremental Learning: A Method for Integrating Genetic Search Based Function Optimization and Competitive Learning, 1994.

[57] J. Kennedy and R. Eberhart. *A new optimizer using particle swarm theory.* Micro Machine and Human Science, 1995. MHS '95., Proceedings of the Sixth International Symposium on, Nagoya, 1995: p. 39–43.

[58] R. Poli, J. Kennedy, and T. Blackwell. *Particle swarm optimization.* Swarm Intelligence, 2007. 1(1): p. 33–57.

[59] J. Kennedy and R.C. Eberhart. *A discrete binary version of the particle swarm algorithm.* 1997 IEEE International Conference on Systems, Man, and Cybernetics. Computational Cybernetics and Simulation, 1997. 5: p. 4–8.

[60] M. W. Bloomfield, J. E. Herencia, and P. M. Weaver. *Optimization of Anisotropic Laminated Composite Plates Incorporating Non-Conventional Ply Orientations.* 49th AIAA/ASME/ASCE/AHS/ASC Structures, Structural Dynamics and Materials Conference, 2008. (April): p. 1–15.

[61] M. Dorigo, M. Birattari, and T. Stutzle. *Ant colony optimization.* IEEE Computational Intelligence Magazine, 2006.

[62] R. M. Koide and M. A. Luersen. *Ant colony optimization applied to laminated composite plates.* In 20th International Congress of Mechanical Engineering, Nov 2009.

[63] A Rama Mohan Rao. *Lay-up sequence design of laminate composite plates and a cylindrical skirt using ant colony optimization.* Proceedings of the Institution of Mechanical Engineers, Part G: Journal of Aerospace Engineering, 2009. 223(1): p. 1–18.

[64] R. M. Koide, G.Von Zeska De Franca, and M. A. Luersen. *An Ant Colony Algorithm Applied to Lay-up Optimization of Laminated Composite Plates.* Latin American Journal of Solids and Structures, 2013. 10: p. 491–504.

[65] O. Seresta, Z. Gürdal, D. B. Adams, and L. T. Watson. *Optimal design of composite wing structures with blended laminates.* Composites Part B: Engineering, 2007. 38(4): p. 469–480.

[66] D. Liu, V. V. Toroporov, O. M. Querin, and D. C. Barton. *Bilevel Optimization of Blended Composite Wing Panels.* Journal of Aircraft, 2011. 48(1): p. 107–118.

[67] W. Liu and R. Butler. *Optimum Buckling Design of Composite Wing Cover Panels.* Optimization, 2007. (April): p. 1–11.

[68] Z. Jing, X. Fan, and Q. Sun. *Global shared-layer blending method for stacking sequence optimization design and blending of composite structures.* Composites Part B: Engineering, 2014. 69: p. 181–190.

[69] Z. Jing, Q. Sun, and V. V. Silberschmidt. *Sequential permutation table method for optimization of stacking sequence in composite laminates.* Composite Structures, 2016. 141: p. 240–252.

[70] S.W. Tsai, J.C. Halpin, and N.J. Pagano. *Composite materials workshop.* Stamford, CT: Technomic Publishing Co., Inc., 1968.

[71] M. Miki. *Material design of composite laminates with required in-plane elastic properties.* In T Hayashi, K Kawada, and S Umekawa, editors, *Progress in science and engineering of composite*, pages 1725–1731. Japan Society for Composite Materials, 1982.

[72] H. Fukunaga and H. Sekine. *Stiffness design method of symmetric laminates using lamination parameters.* AIAA Journal, Nov 1992. 30(11): p. 2791–2793.

[73] J. L. Grenestedt and P. Gudmundson. *Layup Optimization of Composite Material Structures.* In P. Pederson, editor, Optimal Design with Advanced Materials, Elsevier Science Publishers B.V., 1993: p. 311–336.

[74] C. G. Diaconu, M. Sato, and H. Sekine. *Feasible region in general design space of lamination parameters for laminated composites.* AIAA Journal, 2002. 40(3): p. 559–565.

[75] C. G. Diaconu, M. Sato, and H. Sekine. *Buckling characteristics and layup optimization of long laminated composite cylindrical shells subjected to combined loads using lamination parameters.* Composite Structures, 2002. 58(4): p. 423–433.

[76] C. G. Diaconu and H. Sekine. *Layup optimization for buckling of laminated composite shells with restricted layer angles.* Aiaa Journal, 2004. 42(10): p. 2153–2163.

[77] S. Setoodeh, M. M. Abdalla, and Z. Gürdal. *Approximate feasible regions for lamination parameters.* {Collection of Technical Papers - 11th AIAA/ISSMO Multidisciplinary Analysis and Optimization Conference}, 2006. (September): p. 814–822.

[78] B. Liu, R.T. Haftka, and M. A. Akgün. *Composite wing structural optimization using genetic algorithms and response surfaces.* AIAA Journal, 1998: p. 4854.

[79] A. Todoroki and R.T. Haftka. *Lamination prameters for efficient genetic optimization of the stacking sequences of composite panels.* 7th AIAA/USAF/-NASA/ISSMO Symposium on Multidisciplinary Analysis and Optimization, 1998: p. 870–879.

[80] M. Abouhamze, M. Shakeri, B. Liu, R. T. Haftka, M. A. Akgün, Y. Hirano, A. Todoroki, T. Ishikawa, and Y. Terada. *Multi-objective stacking sequence optimization of laminated cylindrical panels using a genetic algorithm and neural networks.* Composite Structures, 2004. 48(2): p. 65–72.

[81] A. Todoroki and T. Ishikawa. *Design of experiments for stacking sequence optimizations with genetic algorithm using response surface approximation.* Composite Structures, 2004. 64(3-4): p. 349–357.

[82] R. Rikards, H. Abramovich, J. Auzins, A. Korjakins, O. Ozolinsh, K. Kalnins, and T. Green. *Surrogate models for optimum design of stiffened composite shells.* Composite Structures, 2004. 63(2): p. 243–251.

[83] S. Jeong, M. Murayama, and K. Yamamoto. *Efficient Optimization Design Method Using Kriging Model.* Journal of Aircraft, 2005. 42(2): p. 413–420.

[84] A. Todoroki and Y. Terada. *Improved Fractal Branch and Bound Method for Stacking-Sequence Optimizations of Laminates.* AIAA Journal, 2004. 42(1): p. 141–148.

[85] Y. Hirano and A. Todoroki. *Stacking-Sequence Optimization of Composite Delta Wing to Improve Flutter Limit Using Fractal Branch and Bound Method.* JSME International Journal Series A, 2005. 48(2): p. 65–72.

[86] M. Abouhamze and M. Shakeri. *Multi-objective stacking sequence optimization of laminated cylindrical panels using a genetic algorithm and neural networks.* Composite Structures, 2007. 81(2): p. 253–263. doi: 10.1016/j.compstruct.2006.08.015.

[87] Z. Gurdal and R. Olmedo. *In-plane response of laminates with spatially varying fiber orientations - Variable stiffness concept.* AIAA Journal, 1993. 31(4):p. 751–758.

[88] C. Waldhart. *Analysis of Tow-Placed , Variable-Stiffness Laminates.* Master Thesis, Virginia Polytechnic Institute and State University, 1996: p. 11–15.

[89] S. Setoodeh, M. M. Abdalla, and Z. Gürdal. *Design of variable-stiffness laminates using lamination parameters.* Composites Part B: Engineering, 2006. 37(4-5): p. 301–309.

[90] S. T. Ijsselmuiden, M. M. Abdalla, and Z. Gürdal. *Optimization of Variable-Stiffness Panels for Maximum Buckling Load Using Lamination Parameters.* AIAA Journal, 2010. 48(1): p. 134–143.

[91] A. Khani, S. T. Ijsselmuiden, M. M. Abdalla, and Z. Gürdal. *Design of variable stiffness panels for maximum strength using lamination parameters.* Composites Part B: Engineering, 2011. 42(3): p. 546–552.

[92] H. Ghiasi, K. Fayazbakhsh, D. Pasini, and L. Lessard. *Optimum stacking sequence design of composite materials Part II: Variable stiffness design.* Composite Structures, 2010. 93(1): p. 1–13.

[93] I. E. Garrick and W. H. Reed. *Historical Development of Aircraft Flutter.* Journal of Aircraft, 1981. 18(11): p. 897–912.

[94] D. H. Hodges and G. A. Pierce. *Introduction to Structural Dynamics and Aeroelasticity.* Cambridge Aerospace Series. Cambridge University Press, 2 edition, 2011.

[95] N. J. Krone. *Divergence Elimination with Advanced Composites.* {AIAA} paper, 1975: p. 75-1009.

[96] C. Jutte and B. K. Stanford. *Aeroelastic Tailoring of Transport Aircraft Wings: State-of-the-Art and Potential Enabling Technologies.* (April): p. 34, 2014.

[97] T. A. Weisshaar and D. K. Duke. *Induced Drag Reduction Using Aeroelastic Tailoring with Adaptive Control Surfaces.* Journal of Aircraft, 2006. 43(1): p. 157–164.

[98] B. K. Stanford, C. D. Wieseman and C. V. Jutte. Aeroelastic Tailoring of Transport Wings Including Transonic Flutter Constraints. 56th AIAA/ASCE/AHS/ASC Structures, Structural Dynamics, and Materials Conference. 2015.(January): p. 1–22.

[99] T. A. Weisshaar and R. J. Ryan. *Control of aeroelastic instabilities through stiffness cross-coupling.* Journal of Aircraft, 1986. 23(2): p. 148–155.

[100] J. M. Houslaer and M. Stein. *Flutter Analysis of Swept Wing Subsonic Aircraft With Parameter Studies of Composite Wings.* NASA Technical Note, NASA TN0-7539.(September), 1974.

[101] V. C. Sherrer, T. J. Hertz, and M. H. Shirk. *Wind Tunnel Demonstration of Aeroelastic Tailoring Applied to Forward Swept Wings.* Journal of Aircraft, 1981. 18(11): p. 976–983.

[102] S. J. Hollowell and J. Dugundji. *Aeroelastic flutter and divergence of stiffness coupled, graphite/epoxy cantilevered plates.* Journal of Aircraft, Jan 1984. 21(1): p. 69–76.

[103] T. A. Weisshaar and B. L. Foist. *Vibration tailoring of advanced composite lifting surfaces.* Journal of Aircraft, 1985 22(2): p. 141–147.

[104] I. Lottati. *Flutter and Divergence Aeroelastic Characteristics for Composite Forward Swept Cantilevered Wing.* Journal of Aircraft, 1985. 22(11): p. 1001–1007.

[105] M. Kameyama and H. Fukunaga. *Optimum design of composite plate wings for aeroelastic characteristics using lamination parameters.* Computers and Structures, 2007. 85: p. 213–224.

[106] M. J. Patil. *Aeroelastic Tailoring of Composite Box Beams.* 21st Congress of International Council of the Aeronautical Sciences, Melbourne, Australia, September, 1998.

[107] S. J. Guo, J. R. Bannerjee, and C. W. Cheung. *The effect of laminate lay-up on the flutter speed of composite wings. Proceedings of the Institution of Mechanical Engineers, Part G: Journal of Aerospace Engineering*, 2003. 217(3): p. 115–122.

[108] R. T. Haftka and J. H. Jr. Starnes. *WINDOWAC (Wing Design Optimization With Aeroelastic Constraints): Program manual.* Oct 1974.

[109] K. Wilkinson, J. Markowitz, E. Lerner, D. George, and S. M. Batill. *FASTOP: A Flutter and Strength optimization Program for Lifting-Surface Structures.* Journal of Aircraft, 1977. 14(6): p. 581–587.

[110] D. J. Neill, E. H. Johnson, and R. Canfield. *ASTROS - A multidisciplinary automated structural design tool.* Journal of Aircraft, 1990. 27(12): p. 1021–1027.

[111] A. Attaran, D. L. Majid, S. Basri, A. S. Mohd Rafie, and E. J. Abdullah. *Structural optimization of an aeroelastically tailored composite flat plate made of woven fiberglass/epoxy.* Aerospace Science and Technology, 2011. 15(5): p. 393–401.

[112] N. Chang, W. Yang, J. Wang, and W. Wang. *Design optimization of composite wing box for flutter and stiffness.* 48th AIAA Aerospace Sciences Meeting, January 2010.

[113] J. K. S. Dillinger, T. Klimmek, M. M. Abdalla, and Z. Gürdal. *Stiffness Optimization of Composite Wings with Aeroelastic Constraints.* Journal of Aircraft, 2013. 50(4): p. 1159–1168.

[114] A. Abdelkader, M. Y. Harmin, J. E. Cooper, and F. Bron. *Aeroelastic Tailoring of Metallic Wing Structures.* 52nd AIAA/ASME/ASCE/AHS/ASC Structures, Structural Dynamics and Materials Conference, Denver, Colorado, United States Of America, Apr 2011. (April): p. 1–19.

[115] D. Locatelli, S. B. Mulani, and R. K. Kapania. *Wing-Box Weight Optimization Using Curvilinear Spars and Ribs (SpaRibs).* Journal of Aircraft, 2011. 48(5): p. 1671–1684.

[116] G.Francois, J.E. Cooper, and P.M. Weaver. *Aeroelastic Tailoring using Rib / Spar Orientations :.* 56th AIAA/ASME/ASCE/AHS/ASC Structures, Structural Dynamics and Materials Conference, 2015. (January): p. 1–22.

[117] B. K. Stanford and C. V. Jutte. *Aeroelastic Tailoring via Tow Steered Composites.* NASA/TM-2014-218517, September 2014.

[118] E. L. Walker and T. K. West Iv. *Integrated Uncertainty Quantification for Risk and Resource Management : Building Confidence in Design (Invited).* 53rd AIAA Aerospace Sciences Meeting, AIAA SciTech, 2015. (January):1–17.

[119] R. E. Melchers and A. T. Beck. *Structural Reliability Analysis and Prediction.* Wiley, 2018.

[120] W. L. Oberkampf, J. C. Helton, and K. Sentz. *Mathematical representation of uncertainty.* Non-Deterministic Approaches Forum, 2001. (April): p. 1–23.

[121] L.A. Zadeh. *Fuzzy sets as a basis for a theory of possibility.* Fuzzy Sets and Systems 100 Supplement, 1999: p. 9–34.

[122] R. E. Moore and F. Bierbaum. *Methods and Applications of Interval Analysis (SIAM Studies in Applied and Numerical Mathematics).* Soc for Industrial & Applied Math, 1979.

[123] G. Shafer. *A Mathematical Theory of Evidence.* Limited paperback editions. Princeton University Press, 1976.

[124] H. R. Bae, R. Grandhi, and R. Canfield. *Uncertainty Quantification of Structural Response Using Evidence Theory.* AIAA Journal, 2003. 41(10): p. 2062–2068.

[125] H. R. Bae, R. V. Grandhi, and R. A. Canfield. *An approximation approach for uncertainty quantification using evidence theory.* Reliability Engineering & System Safety, 2004. 86(3): p. 215–225.

[126] C. C. Chamis. *Probabilistic simulation of multi-scale composite behavior.* Theoretical and Applied Fracture Mechanics, 2004. 41(1-3): p. 51–61.

[127] G. V. Vinckenroy and W.P. de Wilde. *The use of Monte Carlo techniques in statistical finite element methods for the determination of the structural behaviour of composite materials structural components.* Composite Structures, 1995. 32(1-4): p. 247–253.

[128] J. Kuttenkeuler and U. Ringertz. *Aeroelastic tailoring considering uncertainties in material properties.* Structural Optimization, 1998. 15(3-4): p. 157–162.

[129] R. L. Harrison. *Introduction to Monte Carlo Simulation.* AIP Conf. Proc., 2010. 1204: p. 17–21.

[130] S. Raychaudhuri. *Introduction to Monte Carlo simulation.* 2008 Winter Simulation Conference, 2008: p. 91–100.

[131] H.K. Jeong and R.A. Shenoi. *Probabilistic strength analysis of rectangular FRP plates using Monte Carlo simulation.* Computers & Structures, 2000. 76(1-3): p. 219–235.

[132] A. K. Onkar, C. S. Upadhyay, and D. Yadav. *Probabilistic failure of laminated composite plates using the stochastic finite element method.* Composite Structures, 2007. 77(1): p. 79–91.

[133] S. C. Lin. *Reliability predictions of laminated composite plates with random system parameters.* Probabilistic Engineering Mechanics, 2000. 15(4): p. 327–338.

[134] S. C. Castravete and R. A. Ibrahim. *Effect of Stiffness Uncertainties on the Flutter of a Cantilever Wing.* AIAA Journal, Apr 2008. 46(4): p. 925–935.

[135] N. J . Lindsley, P. S. Beran, and C. L. Pettit. *Effects of Uncertainty on Nonlinear Plate Aeroelastic Response. AIAA*, 2002. 1271(April): p. 1–10.

[136] S. H. Crandall. *Perturbation Techniques.* The Journal of the Acoustical Society of America, 1962. 34(12): p. 2000.

[137] J. L. Grenestedt. *A study on the effect of bending-twisting coupling on buckling strength.* Composite Structures, 1989. 12(4): p. 271–290.

[138] I. Elishakoff, Y.J. Ren, and M. Shinozuka. *Improved finite element method for stochastic problems.* Chaos, Solitons & Fractals, 1995. 5(5): p. 833–846.

[139] N. Wiener. *The Homogeneous Chaos.* American Journal of Mathematics, 1938. 60 (4): p. 897–936.

[140] R. Ghanem and P. D. Spanos. *Polynomial Chaos in Stochastic Finite Elements.* Journal of Applied Mechanics, 1990. 57(1): p. 197.

[141] D. Xiu and G. E. Karniadakis. *The Wiener–Askey Polynomial Chaos for Stochastic Differential Equations.* SIAM Journal on Scientific Computing, 2002. 24(2): p. 619–644.

[142] S. K. Choi, R. V. Grandhi, and R. A. Canfield. *Structural reliability under non-Gaussian stochastic behavior.* Computers and Structures, 2004. 82(13-14): p. 1113–1121.

[143] M. Eldred and J.Burkardt. *Comparison of Non-Intrusive Polynomial Chaos and Stochastic Collocation Methods for Uncertainty Quantification.* 47th AIAA Aerospace Sciences Meeting including The New Horizons Forum and Aerospace Exposition, January 2009.

[144] C. L. Pettit and P. S. Beran. *Polynomial Chaos Expansion Applied to Airfoil Limit Cycle Oscillations Polynomial Chaos Expansion Applied to Airfoil Limit Cycle Oscillations.* 45th AIAA/ASME/ASCE/AHS/ASC Structures, Structural Dynamics & Materials Conference, April 2004.

[145] P. S. Beran, C. L. Pettit, and D. R. Millman. *Uncertainty quantification of limit-cycle oscillations.* Journal of Computational Physics, 2006. 217(1): p. 217–247.

[146] X. Wan and G. E. Karniadakis. *An adaptative multi-element generalized polynomial chaos method for stochastic differential equations.* J. Comput. Phys., 2005. 209 (March 2005): p. 617–642.

[147] S. Sarkar, J. A. S. Witteveen, A. Loeven, and H. Bijl. *Effect of uncertainty on the bifurcation behavior of pitching airfoil stall flutter.* Journal of Fluids and Structures, 2009. 25(2): p. 304–320.

[148] R. G. Ghanem and P. D. Spanos. *Stochastic Finite Elements: A Spectral Approach.* Springer-Verlag, New York., 1991.

[149] L. Mathelin, M. Yousuff Hussaini, and A. Thomas Zang. *Stochastic approaches to uncertainty quantification in CFD simulations.* Numerical Algorithms, 2005. 38: p. 209–236.

[150] L. Mathelin and M. Y. Hussaini. *A Stochastic Collocation Algorithm for Uncertainty Analysis.* NASA STI Report Series (NASA/CR-20030212153), (February), 2003.

[151] G.J.A. Loeven, J.A.S. Witteveen, and H. Bijl. *Probabilistic Collocation: An Efficient Non-Intrusive Approach for Arbitrarily Distributed Parametric Uncertainties.* 45th AIAA Aerospace Sciences Meeting and Exhibit, 2007. (January): p. 1–14.

[152] H. Rabitz, Ö Alis, and Ömer F. Alış. *General foundations of high-dimensional model representations.* J. Math. Chem., 1999. 25(2-3): p. 197–233.

[153] G. Li, C. Rosenthal, and H. Rabitz. *High dimensional model representations.* Journal of Physical Chemistry A, 2001. 105(33): p. 7765–7777.

[154] R. C. Smith. *Uncertainty Quantification: Theory, Implementation, and Applications.* Computational Science and Engineering. Society for Industrial and Applied Mathematics, 2013.

[155] S. Murugan, R. Chowdhury, S. Adhikari, and M. I. Friswell. *Helicopter aeroelastic analysis with spatially uncertain rotor blade properties.* Aerospace Science and Technology, 2012. 16(1): p. 29–39.

[156] T. Mukhopadhyay, T. K. Dey, R. Chowdhury, A. Chakrabarti, and S. Adhikari. *Optimum design of FRP bridge deck: an efficient RS-HDMR based approach.* Structural and Multidisciplinary Optimization, 2015. 52(3): p. 459–477.

[157] S. Dey, T. Mukhopadhyay, and S. Adhikari. *Free vibration analysis of angle-ply composite plates with uncertain properties.* 17th AIAA Non-Deterministic Approaches Conference, 2015. (January): p. 5–9.

[158] C. Zang, M. I. Friswell, and J. E. Mottershead. *A review of robust optimal design and its application in dynamics.* Computers and Structures, 2005. 83(4-5): p. 315–326.

[159] G. Taguchi, E. A. Elsayed, and T. C. Hsiang. *Quality engineering in production systems.* McGraw-Hill series in industrial engineering and management science. McGraw-Hill, 1989.

[160] T. P. Bagchi. *Taguchi Methods Explained. Paractical Steps to Robust Design.* Prentice Hall of India Private Limited, 1993.

[161] K. H. Lee, I. S. Eom, G. J. Park, and W. I. Lee. *Robust design for unconstrained optimization problems using the Taguchi method.* AIAA Journal, 1996. 34(5): p. 1059–1063.

[162] K. H. Hwang, K. W. Lee, and G. J. Park. *Robust optimization of an automobile rearview mirror for vibration reduction.* Structural and Multidisciplinary Optimization, 2001. 21(4): p. 300–308.

[163] M. Dodson and G. T. Parks. *Robust Aerodynamic Design Optimization Using Polynomial Chaos.* Journal of Aircraft, 2009. 46(2):p. 635–646.

[164] S. Sundaresan, K. Ishii, and D. R. Houser. *A robust optimization procedure with variations on design variables and constraints.* Engineering Optimization, 1995. 24 (2): p. 101–117.

[165] J. M. Mulvey, R. J. Vanderbei, and S. A. Zenios. *Robust Optimization of Large-Scale Systems.* Operations Research, 1995. 43(2): p. 264–281.

[166] I. Das and J. E. Dennis. *A closer look at drawbacks of minimizing weighted sums of objectives for Pareto set generation in multicriteria optimization problems.* Structural Optimization, 1997. 14(1): p. 63–69.

[167] W. Chen, M. M. Wiecek, and J. Zhang. *Quality Utility—A Compromise Programming Approach to Robust Design.* Journal of Mechanical Design, 1999. 121(2): p. 179.

[168] S. K. Choi, R. A. Canfield, and R. V. Grandhi. *Reliability-based structural design.* Reliability-based Structural Design, 2007: p. 1–306.

[169] E. Nikolaidis and R. Burdisso. *Reliability based optimization: a safety index approach.* Computers & Structures, 1988. 28(6): p. 781–788.

[170] A. M. Hasofer and N. C. Lind. *Exact and invariant second-moment code format.* Journal of the Engineering Mechanics Division, 1974. 100: p. 111–121.

[171] J. S. Yang, E. Nikolaidis, and R. T. Haftka. *Design of aircraft wings subjected to gust loads: A system reliability approach.* Computers and Structures, 1990. 36(6): p. 1057–1066.

[172] A. Manan and J.E. Cooper. *Design of Composite Wings Including Uncertainties: A Probabilistic Approach.* Journal of Aircraft, 2009. 46(2): p. 601–607.

[173] B.N. Rao and R. Chowwdhury. *Enhanced high-dimensional model representation for reliability analysis.* International Journal for Numerical Methods in Engineering, 2009. 77: p. 719–750.

[174] N. P. M.Werter and R. De Breuker. *Aeroelastic Tailoring and Structural Optimisation using an Advanced Dynamic Aeroelastic Framework.* International Forum on Aeroelasticity and Structural Dynamics, 2015: p. 1–20.

[175] M. T. Bordogna, T. Macquart, D. Bettebghor, and R. De Breuker. *Aeroelastic Optimization of Variable Stiffness Composite Wing with Blending Constraints.* In 17th AIAA/ISSMO Multidisciplinary Analysis and Optimization Conference, AIAA AVIATION Forum. American Institute of Aeronautics and Astronautics, Jun 2016.

[176] Embraer 195 Specifications. URL `https://www.airlines-inform.com/commercial-aircraft/Embraer-195.html`.

[177] Embraer. E195, 2017. URL `https://www.embraercommercialaviation.com/commercial-jets/e195/`.

[178] Z. Gürdal, R. T. Haftka, and P. Hajela. *Design and Optimization of Laminated Composite Materials.* A Wiley-Interscience publication. Wiley, 1999.

[179] K. Marlett. *Hexcel 8552 IM7 Unidirectional Prepreg 190 gsm & 35% RC Qualification Material Property Data Report.* 2011: p. 238.

[180] S. S. Rao. *Vibration of Continuous Systems.* Wiley, 2007.

[181] EASA. *Certification Specifications for Large Aeroplanes.* CS-25, (September):750, 2008.

[182] E. H. Johnson. *MSc. Nastran Version 68 Aeroelastic Analysis User's Guide*. Structure, 1994.

[183] S. S. Rao. *Optimization of airplane wing structures under taxiing loads*. Computers and Structures, 1987. 26(3): p. 469–479.

[184] S. S. Rao and L. Majumder. *Optimization of Aircraft Wings for Gust Loads: Interval Analysis-Based Approach*. AIAA Journal, 2008. 46(3): p. 723–732.

[185] MSC Software Corporation. *MSC Nastran 2012 Dynamic Analysis User's Guide*. 2011.

[186] A. Manan, G. A. Vio, M. Y. Harmin, and J. E. Cooper. *Optimization of aeroelastic composite structures using evolutionary algorithms*. Engineering Optimization, 2010. 42(2): p. 171–184.

[187] Z. P. Mourelatos and J. Liang. *A Methodology for Trading-Off Performance and Robustness Under Uncertainty*. Journal of Mechanical Design, 2006. 128(July 2006): p. 856.

[188] S. K. Choi, R. V. Grandhi, R. A. Canfield, and C. L. Pettit. *Polynomial Chaos Expansion with Latin Hypercube Sampling for Estimating Response Variability*. AIAA Journal, Jun 2004. 42(6): p. 1191–1198.

[189] L. P. Swiler and G. D. Wyss. *A User ' s Guide to Sandia ' s Latin Hypercube Sampling Software*. SAND Report, 1998. (July): p. 88.

[190] Loïc L. Le Gratiet, S. Marelli, and B. Sudret. *Metamodel-based sensitivity analysis: Polynomial chaos expansions and gaussian processes*. Handbook of Uncertainty Quantification, 2017: p. 1289–1325.

[191] B. Sudret. *Global sensitivity analysis using polynomial chaos expansions*. Reliability Engineering and System Safety, 2008. 93(7): p. 964–979.

[192] G. Li, J. Hu, S. W. Wang, P. G. Georgopoulos, J. Schoendorf, and H. Rabitz. *Random Sampling-High Dimensional Model Representation (RS-HDMR) and orthogonality of its different order component functions*. Journal of Physical Chemistry A, 2006. 110(7): p. 2474–2485.

[193] G. Li and H. Rabitz. *Ratio control variate method for efficiently determining high-dimensional model representations.* Journal of Computational Chemistry, 2006. 27 (10): p. 1112–1118.

[194] G. Li, S. W. Wang, H. Rabitz, S. Wang, and P. Jaffé. *Global uncertainty assessments by high dimensional model representations (HDMR).* Chemical Engineering Science, 2002. 57(21): p. 4445–4460.

[195] G. J. Park, T. H. Lee, K. H. Lee, and K. H. Hwang. *Robust design: an overview.* AIAA journal, 2006. 44(1): p. 181–191.

[196] E. Albano and W. P. Hodden. *A doublet-lattice method for calculating lift distributions on oscillating surfaces in subsonic flows.* AIAA Journal, 1969. 7(2): p. 279–285.

[197] T. P. Kalman, W. P. Rodden, and J. P. Giesing. *Application of the Doublet-Lattice Method to Nonplanar Configurations in Subsonic Flow.* Journal of Aircraft, 1971. 8(6): p. 406–413.

[198] *MSC.Nastran Aeroelastic Analyis User's Guide.* In MSC.Nastran Aeroelastic Analyis User's Guide. MSC Software Corporation, version 68 edition, 2009.

[199] I. Lee, H. Miuraf, and M. K. Charging. *Static Aeroelastic Analysis for Generic Configuration Wing.* Journal of Aircraft, 1991. 28(12): p. 801–802.

Appendix A

Classical Laminate Theory (CLT)

In CLT [34], it is assumed that if there is no applied force acting on the out-of-plane direction, the stress component in that direction are zero. Hence, the stress-strain relations for orthotropic lamina can be expressed as

$$\begin{Bmatrix} \sigma_1 \\ \sigma_2 \\ \tau_{12} \end{Bmatrix} = \begin{bmatrix} Q_{11} & Q_{12} & 0 \\ Q_{12} & Q_{22} & 0 \\ 0 & 0 & Q_{66} \end{bmatrix} \begin{Bmatrix} \mathcal{E}_1 \\ \mathcal{E}_2 \\ \gamma_{12} \end{Bmatrix}, \tag{A.1}$$

where Q_{ij} are the reduced stiffness terms which can be obtained using composite material properties such that

$$\begin{aligned} Q_{11} &= \frac{E_1}{1-\mathcal{V}_{12}\mathcal{V}_{21}}, \quad Q_{22} = \frac{E_2}{1-\mathcal{V}_{12}\mathcal{V}_{21}}, \\ Q_{12} &= \frac{\mathcal{V}_{12}E_2}{1-\mathcal{V}_{12}\mathcal{V}_{21}} = \frac{\mathcal{V}_{21}E_2}{1-\mathcal{V}_{12}\mathcal{V}_{21}}, \\ Q_{66} &= G_{12}. \end{aligned} \tag{A.2}$$

The stress-strain relationship from Eqn. (A.1) is given in the local material properties directions. Since each layer of the lamina are generally rotated with respect to reference coordinate system (x-y), the stress and strain must be transformed to the reference axes such that

$$\begin{Bmatrix} \sigma_1 \\ \sigma_2 \\ \tau_{12} \end{Bmatrix} = \mathbf{T} \begin{Bmatrix} \sigma_x \\ \sigma_y \\ \tau_{xy} \end{Bmatrix} \quad \text{and} \quad \begin{Bmatrix} \mathcal{E}_1 \\ \mathcal{E}_2 \\ \gamma_{12} \end{Bmatrix} = \mathbf{T} \begin{Bmatrix} \mathcal{E}_x \\ \mathcal{E}_y \\ \gamma_{xy} \end{Bmatrix}, \tag{A.3}$$

where the transformation matrix, $\mathbf{T}$ is given by

$$\mathbf{T} = \begin{bmatrix} m^2 & n^2 & 2mn \\ n^2 & m^2 & -2mn \\ -mn & mn & m^2 - n^2 \end{bmatrix}, \quad m = cos(\theta) \quad \text{and} \quad n = sin(\theta) \tag{A.4}$$

In order to obtain the engineering strain from the tensor strain notation, the transformation matrix, $\mathbf{T}$ is pre- and post-multiplied by a matrix $\mathbf{R}$ and $\mathbf{R}^{-1}$ such that

$$\begin{Bmatrix} \mathcal{E}'_x \\ \mathcal{E}'_y \\ \gamma'_{xy} \end{Bmatrix} = \mathbf{R} \begin{Bmatrix} \mathcal{E}_x \\ \mathcal{E}_y \\ \gamma_{xy} \end{Bmatrix}, \quad \text{and} \quad \mathbf{R} = \begin{bmatrix} 1 & 0 & 0 \\ 0 & 1 & 0 \\ 0 & 0 & 2 \end{bmatrix}. \tag{A.5}$$

Hence, the transformation matrix for engineering strain is given by

$$\mathbf{T}_e = \begin{bmatrix} m^2 & n^2 & mn \\ n^2 & n^2 & -mn \\ -2mn & 2mn & m^2 - n^2 \end{bmatrix}. \tag{A.6}$$

By using the transformation relations for the stresses and engineering strains Eqn. (A.1) can be rewritten as

$$\begin{Bmatrix} \sigma_x \\ \sigma_y \\ \tau_{xy} \end{Bmatrix} = \mathbf{T}^{-1}\mathbf{Q}\mathbf{R}\mathbf{T}\mathbf{R}^{-1} \begin{Bmatrix} \mathcal{E}_x \\ \mathcal{E}_y \\ \gamma_{xy} \end{Bmatrix}. \tag{A.7}$$

Hence,

$$\begin{Bmatrix} \sigma_x \\ \sigma_y \\ \tau_{xy} \end{Bmatrix} = \begin{bmatrix} \bar{Q}_{11} & \bar{Q}_{12} & \bar{Q}_{16} \\ \bar{Q}_{12} & \bar{Q}_{22} & \bar{Q}_{26} \\ \bar{Q}_{16} & \bar{Q}_{26} & \bar{Q}_{66} \end{bmatrix} \begin{Bmatrix} \mathcal{E}_x \\ \mathcal{E}_y \\ \gamma_{xy} \end{Bmatrix}, \tag{A.8}$$

where $\bar{Q}_{ij}$ is are the transformed reduced stiffnesses which are given by

$$\begin{aligned}
\bar{Q}_{11} &= Q_{11}\cos^4\theta + 2(Q_{12}+2Q_{66})\sin^2\theta\cos^2\theta + Q_{22}\sin^4\theta,\\
\bar{Q}_{12} &= (Q_{11}+Q_{22}-4Q_{66})\cos^2\theta\sin^2\theta + Q_{12}(\sin^4\theta+\cos^4\theta),\\
\bar{Q}_{22} &= Q_{11}\sin^4\theta + 2(Q_{12}+2Q_{66})\sin^2\theta\cos^2\theta + Q_{22}\cos^4\theta,\\
\bar{Q}_{16} &= (Q_{11}-Q_{12}-2Q_{66})\sin\theta\cos^3\theta + (Q_{12}-Q_{22}+2Q_{66})\sin^3\theta\cos\theta,\\
\bar{Q}_{26} &= (Q_{11}-Q_{12}-2Q_{66})\sin^3\theta\cos\theta + (Q_{12}-Q_{22}+2Q_{66})\sin\theta\cos^3\theta,\\
\bar{Q}_{66} &= (Q_{11}+Q_{22}-2Q_{12}-2Q_{66})\sin^2\theta\cos^2\theta + Q_{66}(\sin^4\theta+\cos^4\theta).
\end{aligned} \tag{A.9}$$

The composite laminates are normally made of layers that are bonded together to form a laminate as shown in Figure A.1. In CLT, it is assumed that the N layers of a laminate are perfectly bonded together with infinite thin bond line and the in-plane deformation across the bond-line are continuous. For symmetric laminate which is normally the case in most application, the reference plane is chosen as the mid-plane of the laminate as shown in Figure A.1. By implying these assumption, the strain distribution is therefore given by

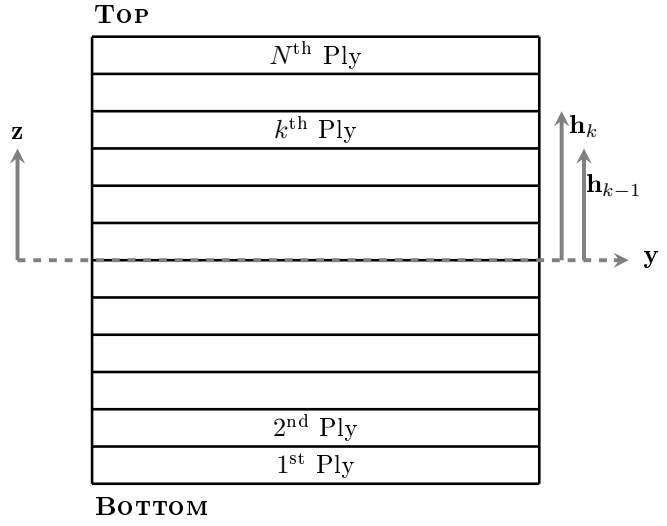

Figure A.1: Symmetric stacking representation of N plies laminate.

$$\begin{Bmatrix} \mathcal{E}_x \\ \mathcal{E}_y \\ \gamma_{xy} \end{Bmatrix} = \begin{Bmatrix} \mathcal{E}_x^o \\ \mathcal{E}_y^o \\ \gamma_{xy}^o \end{Bmatrix} + z \begin{Bmatrix} \kappa_x \\ \kappa_y \\ \kappa_{xy} \end{Bmatrix}, \tag{A.10}$$

where $\mathcal{E}_x^o$, $\mathcal{E}_y^o$ and $\mathcal{E}_{xy}^o$ are the mid-plane strains and the curvature, κ are constant through the thickness. Therefore, by substituting Eqn. (A.10) into the stress-strain relationship

derived in Eqn. (A.8), the stress in the Nth ply can be expressed in terms of reduced stiffness as

$$\begin{Bmatrix} \sigma_x \\ \sigma_y \\ \tau_{xy} \end{Bmatrix}_{(k^{\text{th}}\text{ply})} = \begin{bmatrix} \bar{Q}_{11} & \bar{Q}_{12} & \bar{Q}_{16} \\ \bar{Q}_{12} & \bar{Q}_{22} & \bar{Q}_{26} \\ \bar{Q}_{16} & \bar{Q}_{26} & \bar{Q}_{66} \end{bmatrix}_{(k^{\text{th}}\text{ply})} \left(\begin{Bmatrix} \mathcal{E}_x^o \\ \mathcal{E}_y^o \\ \gamma_{xy}^o \end{Bmatrix} + z \begin{Bmatrix} \kappa_x \\ \kappa_y \\ \kappa_{xy} \end{Bmatrix} \right). \tag{A.11}$$

The in-plane forces and moments acting on small element are obtained through-the-thickness integration of the stress in each ply such that

$$\begin{Bmatrix} N_x \\ N_y \\ N_{xy} \end{Bmatrix} = \int_{-h/2}^{h/2} \begin{Bmatrix} \sigma_x \\ \sigma_y \\ \tau_{xy} \end{Bmatrix}_{(k^{\text{th}}\text{ply})} dz = \sum_{k=1}^{N} \int_{h_{k-1}}^{h_k} \begin{Bmatrix} \sigma_x \\ \sigma_y \\ \tau_{xy} \end{Bmatrix} dz \tag{A.12}$$

and

$$\begin{Bmatrix} M_x \\ M_y \\ M_{xy} \end{Bmatrix} = \int_{-h/2}^{h/2} \begin{Bmatrix} \sigma_x \\ \sigma_y \\ \tau_{xy} \end{Bmatrix}_{(k^{\text{th}}\text{ply})} zdz = \sum_{k=1}^{N} \int_{h_{k-1}}^{h_k} \begin{Bmatrix} \sigma_x \\ \sigma_y \\ \tau_{xy} \end{Bmatrix} zdz, \tag{A.13}$$

By substituting the stress-strain relations from Eqn. A.11, the constitutive relations for the laminate are obtained as follow

$$\begin{Bmatrix} N_x \\ N_y \\ N_{xy} \end{Bmatrix} = \begin{bmatrix} A_{11} & A_{12} & A_{16} \\ A_{12} & A_{22} & A_{26} \\ A_{16} & A_{26} & A_{66} \end{bmatrix} \begin{Bmatrix} \mathcal{E}_x^o \\ \mathcal{E}_y^o \\ \gamma_{xy}^o \end{Bmatrix} + \begin{bmatrix} B_{11} & B_{12} & B_{16} \\ B_{12} & B_{22} & B_{26} \\ B_{16} & B_{26} & B_{66} \end{bmatrix} \begin{Bmatrix} \kappa_x \\ \kappa_y \\ \kappa_{xy} \end{Bmatrix} \tag{A.14}$$

and

$$\begin{Bmatrix} M_x \\ M_y \\ M_{xy} \end{Bmatrix} = \begin{bmatrix} B_{11} & B_{12} & B_{16} \\ B_{12} & B_{22} & B_{26} \\ B_{16} & B_{26} & B_{66} \end{bmatrix} \begin{Bmatrix} \mathcal{E}_x^o \\ \mathcal{E}_y^o \\ \gamma_{xy}^o \end{Bmatrix} + \begin{bmatrix} D_{11} & D_{12} & D_{16} \\ D_{12} & D_{22} & D_{26} \\ D_{16} & D_{26} & D_{66} \end{bmatrix} \begin{Bmatrix} \kappa_x \\ \kappa_y \\ \kappa_{xy} \end{Bmatrix}, \tag{A.15}$$

where $N = \{N_x, N_y, N_{xy}\}^T$ and $M = \{M_x, M_y, M_{xy}\}^T$ are the resultant forces and moments per unit length, $\mathcal{E} = \{\mathcal{E}_x, \mathcal{E}_y, \gamma_{xy}\}^T$ and $\kappa = \{\kappa_x, \kappa_y, \kappa_{xy}\}^T$ are the in-plane deformation and twist curvature terms. The stiffness matrix $[A]$, $[B]$ and $[D]$ are given as

$$
\begin{aligned}
A_{ij} &= \sum_{k=1}^{N} (\bar{Q}_{ij})_{(k)} (h_k - h_{k-1}), \\
B_{ij} &= \frac{1}{2} \sum_{k=1}^{N} (\bar{Q}_{ij})_{(k)} (h_k^2 - h_{k-1}^2), \\
D_{ij} &= \frac{1}{3} \sum_{k=1}^{N} (\bar{Q}_{ij})_{(k)} (h_k^3 - h_{k-1}^3).
\end{aligned} \tag{A.16}
$$

Appendix B

Aerodynamic Modelling

B.1 Doublet Lattice Method (DLM)

The Doublet Lattice Method (DLM) theory is first presented by Albano & Hodden [196] and Kalman *et al.* [197] which has been widely used for interfering lifting surface in subsonic flow. The theory is based on a linearised potential flow theory in which the undisturbed flow is uniform and it is assumed that all the lifting surfaces are arranged in columns parallel to the flow [196]. The DLM is an extension of vortex-lattice method DLM for unsteady case and used to calculate the aerodynamic parameters (i.e. Aerodynamic influence coefficient) in subsonic flow.

In DLM, the lifting surfaces is divided into small trapezoidal panels or *'boxes'* in a manner such that the boxes are arranged in columns (strips) parallel to the flow as shown in Figure 3.9. The $\frac{1}{4}$-chord line of each box contains the unknown lifting pressure distributions. For each box, there is one control point positioned at mid-span and on the $\frac{3}{4}$-chord line of the box such that the normal wash boundary condition is satisfied [198]. From Refs. [196, 199], the relation between the pressure and the normal velocity at the lifting surface is given as

$$w(x,s) = \frac{1}{8\pi} \iint K(x,\xi;s,\sigma)\, \bar{p}\,(\xi,\sigma)\, d\xi\, d\sigma, \tag{B.1}$$

where

w = normal velocity

(x,s) = orthogonal coordinates on the lifting surface, S as shown in Figure 3.9

$\bar{p}$ = complex amplitude of lifting pressure coefficient

K = kernel function which is defined in Ref. [196]

The basic relationships between the lifting pressure and downwash (normal wash) is written as

$$\{w_i\} = \frac{1}{q}\,[A_{ij}]\,\{P_j\}, \tag{B.2}$$

where

w_i = downwash (normalwash)

P_j = pressure on lifting element j

A_{ij} = aerodynamic influence coefficient matrix which is a function of Mach number and reduced frequency

q = flight dynamic pressure

The aerodynamic influence coefficient matrix, A_{ij} is the normal velocity magnitude at control point, i, with j^{th} singularity of unit strength and can be determined from the following equation [199]

$$A_{ij} = \frac{\Delta C_j}{8\pi} \int_{-d}^{d} K\, d\eta, \tag{B.3}$$

where

ΔC_j = centerline chord of the j^{th} panel

d = j^{th} panel semiwidth

K = kernel function at the $\frac{1}{4}$-chord load line

In the MSC. NASTRAN static aeroelasticity analysis, the calculated aerodynamic influence matrix from DLM is used to determine the pressures, forces and moments at subsonic speed.

B.2 Geometry Interpolation using Surface Spline

In MSC. NASTRAN, the aerodynamic is defined as two set degree of freedoms. The first set is the *'j'*-set, which is a set of degree of freedom for aerodynamics. There are two

variables in this set which are w_j and f_j^a. The downwash velocity, angle of attack, or camber can be included in the variable w_j. The variable f_j^a can be the pressure, moment and the generalised forces. From the aerodynamic theory, the j-set of degree of freedom can be written as

$$w_j = \frac{1}{q} A_{jj} f_j^a. \tag{B.4}$$

The second set of aerodynamic degree of freedom is the *'k'*-set which act as interface between the j-set and the structural degree of freedom. The variables for k-set degree of freedom are the displacement, u_k and the forces, F_k^a. The transformation of k-set to j-set can be performed using

$$w_j = D_{jk} u_k \tag{B.5}$$

and

$$F_k^a = S_{kj} f_j^a, \tag{B.6}$$

where

D_{jk} = substantial derivative matrix

u_k, F_k^a = displacement and the forces at the aerodynamic grid points

S_{kj} = integration matrix

f_j^a = pressure on the lifting element

Two displacement values are chosen as u_k degree of freedom for each of aerodynamic element which located at the centre of pressure ($\frac{1}{4}$-chord) and the downwash centre ($\frac{3}{4}$-chord). Thus, the k-set is the normal displacement at the centre of pressure and at the downwash centre. The j-set is the downwash at $\frac{3}{4}$ chord and pressure at the centre of pressure. Hence, the integration matrix, S_{kj} is given by

$$\begin{Bmatrix} F_{k1}^a \\ F_{k2}^a \end{Bmatrix} = \begin{bmatrix} S \\ 0 \end{bmatrix} \left\{ f_j^a \right\}, \tag{B.7}$$

where F^a_{k1} and F^a_{k2} are the forces at the centre of pressure and at downwash centre, respectively and S is the aerodynamic element area. The substantial derivative matrix is given by

$$[D_{jk}] = \left[\frac{1}{\Delta x} - \left(\frac{1}{\Delta x} + i\frac{k}{b}\right)\right], \tag{B.8}$$

where Δx is the distance between the centre of pressure and the downwash center, b is the reference length and k is the reduced frequency ($k = \frac{b\omega}{V}$). Hence, Eqn. (B.5) becomes

$$\{w_j\} = \left[\frac{1}{\Delta x} - \left(\frac{1}{\Delta x} + i\frac{k}{b}\right)\right] \begin{Bmatrix} u_{k1} \\ u_{k2} \end{Bmatrix}. \tag{B.9}$$

where u_{k1} and u_{k2} are the normal displacement at centre of pressure and at the downwash centre, respectively.

In the MSc. Nastran static aeroelasticity, the displacement sets are the dependent aerodynamic-displacement set, u_k and independent structural-displacement set, u_g. The dependent displacements, u_k are obtained from interpolation using the structural displacement, u_g such that

$$\{u_k\} = [G_{kg}]\{u_g\}, \tag{B.10}$$

where the interpolation matrix $[G_{kg}]$ is obtained using splining methods that included linear splines, surface splines and explicit user-defined interpolation. For current work, a surface spline is used for the interpolation. A surface spline method is used to find a surface function $u(x, y)$ for all points (x, y) when u is known for a discrete set of points ($i.e\ u_i = u(x_i, y_i)$). The surface spline is considered as an infinite plate that solves for its deformation due to a set of point loads. The formulation in surface spline method and derivation for the interpolation matrix determination are given in Ref. [199].

The aerodynamic forces at aerodynamic control points can be determined by combining Eqns. (B.4) to (B.6) which lead to

$$\{F^a_k\} = q[S_{kj}][A_{jj}]^{-1}[D_{jk}]\{u_k\}. \tag{B.11}$$

The total work for two displacement set (g-set or k-set) should be the same and satisfied the following equation

$$\{u_k\}^T \{F_k^a\} = \{u_g\}^T \{F_g^a\}. \tag{B.12}$$

From Eqn. (B.10)

$$\{u_k\}^T = [G_{kg}]^T \{u_g\}^T. \tag{B.13}$$

The relationship between the aerodynamic force at aerodynamic control points and the aerodynamic forces at the structural grid points is derived from Eqns. (B.12) and (B.13) such that

$$\{F_g^a\} = [G_{kg}]^T \{F_k^a\}. \tag{B.14}$$

Hence, by rewriting Eqn.(B.14) with Eqn. (B.11), the aerodynamic forces at the structural grid points are given by

$$\{F_g^a\} = q\,[G_{kg}]^T [S_{kj}] [A_{jj}]^{-1} [D_{jk}] [G_{kg}] \{u_g\}. \tag{B.15}$$